Scott. M. Shemwell · Jia'en Lin *Editors*

Proceedings of the International Petroleum and Petrochemical Technology Conference 2018

Springer

Proceedings of the International Petroleum and Petrochemical Technology Conference 2018

Scott. M. Shemwell · Jia'en Lin
Editors

Proceedings of the International Petroleum and Petrochemical Technology Conference 2018

Springer

Editors
Scott. M. Shemwell
Rapid Response Institute
Houston, TX, USA

Jia'en Lin
School of International Education
Xi'an Shiyou University
Xi'an, Shaanxi, China

ISBN 978-981-13-2172-6 ISBN 978-981-13-2173-3 (eBook)
https://doi.org/10.1007/978-981-13-2173-3

Library of Congress Control Number: 2018953024

This Springer imprint is published by the registered company Springer Nature Singapore Pte Ltd.
The registered company address is: 152 Beach Road, #21-01/04 Gateway East, Singapore 189721, Singapore

Contents

Applications of AVO Attributes in the Prediction of Tight Gas Reservoirs and Optimization of Horizontal Well Trajectory in Xihu Sag of the East China Sea 1
Hongyan Gao, Dewen Qin, Bing Cao, Chuangxin Liu, and Tao Zhong

Estimation of Formation Damage Along Lateral Formation Using Ordinary Kriging Method 21
Rui Zhang and Kehao Bo

Development and Evaluation of Ne: A Microemulsion Lubricant for Drilling Fluids 29
Bingqiang Dong, Ye Zhang, Zhengsong Qiu, Zhaohui Lu, Junyi Liu, Linhua Pan, and Pei He

Flow Characteristics of Two Temperature-Tolerant and Salt-Resistant Polymers in Porous Media 38
Fulin Yang

Analysis and Study on Operating Trend of the Rotor System of Oil Pump Unit 49
Wencai Liu, Qihua Wang, and Qiyong Peng

Torsional Impact Tool Based on the Problem of Stick-Slip Vibration and Its Application 57
Xin Ling and Wei Li

Resin Application as Permanent Well Barrier for Wells with Sustainable Casing Pressure in Sichuan 68
Xin Zheng, Minh Vo, San Su, Xiao Chaohong, and Da Wang

Water Disposal Management in a Sour Gas Field Development in Sichuan 80
Yan Xue, Minh Vo, Yue Yu, Frank Singleton, and Junliang Zhang

Ultrasonic Flow Metering Device and Field Trial Success at Sour Gas Field Development 94
Yue Yu, Minh Vo, Sihe Zheng, and Junliang Zhang

Effect of Additives on Viscosity of Sulfonate Gemini Surfactant Solution 108
Yahui Zheng, Shanfa Tang, Mingzheng Pu, Jiaxin Wang, and Tianyuan Zhou

Detection and Assessment of Natural Gas Pipeline Slip 117
Ke Cai, Zhixin Chen, Fengping Yang, and Jiangang Lai

Experimental Study on Wall Sticking Occurrence Temperatures of High Water Cut Crude Oil Gathered and Transported at Normal Temperatures 128
Xiong-yi Hu, Xue-ling Zhao, Chun-Yan Ma, Zai-xing Wang, Yi-chi Liu, Jie Liu, Jin Cao, Tao Zou, and Jiao Li

Numerical Analysis for Water Annulus Transportation of High-Viscosity Oil Under the Opening Ball Valve 136
Fan Jiang, Sijie Li, Yongcheng Xu, and Jiangdong Chen

Study of the Method Laying Fiber Optic Cable in the Same Trench with Pipeline in Permafrost Region 152
Guizhi Liu

Lessons Learnt in Annuli Cure of Gas Storage Well 159
Lunjie Chang, Shouwu Qiao, Yong Liu, Yongbin Shan, and Xiaohu Jin

Research on the Design Concept and Key Technology of a New Topology Gas Station 169
Mingjun Du, Jiaqiang Jing, Xinqiang Xiong, Zhigui Zhang, and Cheng Wu

Defoaming Characteristics of Crude Oil Foams Containing CO_2 178
Xiaokai Xing, Heng Zhou, and Xuhui Guo

Analysis on the Cause of the Defects of the Weld Seam in a Butt Welded Flange Ring 187
Xiang Zhang, Ke Cai, and Tingting Qu

Relationship Between Microstructure and Mechanical Properties of X90 Pipeline Steel 196
Xiang Zhang and Fang Yang

Determination of Titanium, Chromium, Magnesium, and Aluminum in Chromium-Based Polyethylene Catalysts by Inductively Coupled Plasma Atomic Emission Spectrometry (ICP-AES) with Microwave Digestion 202
Li-li Rong, Li-na Zhu, Tie-kai Zhao, Yan Liu, and Yan Zhang

Investigation on Heat Transfer Characteristics of Hot Water Thermal Tracing with Thermal Cement 213
Yuqin Zhu, Yaqian Guan, and Feng Xu

Attaining and Sustaining Operational Excellence: A Best Practice POC 224
Scott. M. Shemwell

Applications of AVO Attributes in the Prediction of Tight Gas Reservoirs and Optimization of Horizontal Well Trajectory in Xihu Sag of the East China Sea

Hongyan Gao[1,2], Dewen Qin[2(✉)], Bing Cao[2], Chuangxin Liu[2], and Tao Zhong[2]

[1] State Key Laboratory of Marine Geology, Tongji University, Shanghai 200092, China
gaohy3@cnooc.com.cn
[2] Shanghai Branch of CNOOC (China) Ltd., Shanghai 200335, China
{gaohy3,qindw}@cnooc.com.cn

1 Introduction

Tight gas reservoir is defined as one whose overburden permeability is less than or equal to 0.1 mD, and is generally of no natural production capacity or of a natural capacity lower than the lower limit of industrial gas flow. Nevertheless, under certain economic conditions and technical measures, industrial natural gas production can achieve (PRC National Standard, GB/T 30501-2014). Horizontal well technology is an important means of developing such tight gas [1]. Reservoir prediction accuracy is particularly important for the optimization of horizontal well trajectories.

Methods commonly used for the prediction of tight gas reservoirs by seismic data mainly include post-stack seismic attribute analysis, post-stack inversion [1–6], geostatistical inversion [7, 8], pre-stack synchronous inversion [9–12], amplitude variation with offset (AVO) analysis [13–18], and so on. These methods have achieved good results in the prediction of tight gas reservoirs. Each method, however, has certain application conditions. In the sandstone and the shale series with little impedance contrast, the post-stack seismic is difficult to identify the lithology. The pre-stack synchronous inversion and geostatistical inversion techniques constrained by well logging data are susceptible to modeling effects, which reduces the lateral resolution and are difficult to meet the requirements of horizontal well deployment. AVO technique uses pre-stack to gather information to predict lithology and to detect gas [13, 19]. However, AVO has been used extensively over the years for identification of fluid effect [20, 21], and its use in lithology determination is neglected [22]. Case studies from tight gas reservoir characterization are rare. By doing so, AVO intercept and gradient attributes are normally used. AVO gradient attribute contains important lithological information, which can be used to characterize lithology, porosity, and gas-bearing characteristics in areas with small impedance differences between sandstone and shale [16, 23], and the process of the attribute calculation is involved without well, it is suitable for reservoir prediction in less well area and sand and shale acoustic

S. M. Shemwell and J. Lin (eds.), *Proceedings of the International Petroleum and Petrochemical Technology Conference 2018*,
https://doi.org/10.1007/978-981-13-2173-3_1

impedance overlay area. But the AVO gradient attribute contains intercept term, which does not give the formation concept, and then it is difficult to indicate reservoir thickness and other information [24].

The optimization of horizontal well trajectory should be built on accurate reservoir prediction. In this paper, we integrate forward modeling and AVO attributes to characterize and predict the deeply buried tight sandstone gas reservoirs of the lower Huagang Formation in the Xihu Sag of the East China Sea, with the aim to optimize the trajectory of the potential horizontal wells (Figs. 1 and 2). It is found that the acoustic impedance value of sand and shale in this area is close to each other by petrophysical analysis, and it is difficult to identify the reservoir effectively using conventional seismic attribute and post-stack inversion technique. Some authors [25–28] applied well-constraint pre-stack inversion techniques in this area to reservoir prediction and achieved good results. But here, a more difficult problem need address: because of sparse well pattern in offshore gasfield and characterized with rapid change of the

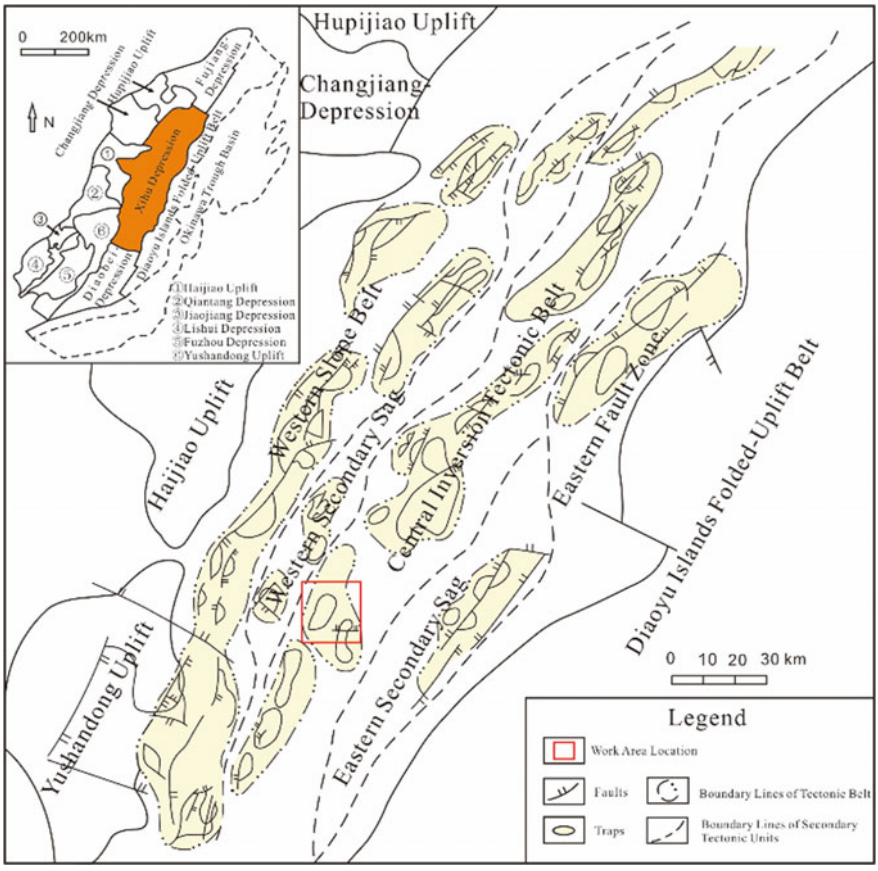

Fig. 1. Location map, structural zoning map of Xihu sag of the East Sea basin (modified from Zhang et al. [38, 39]). The box indicates the study area

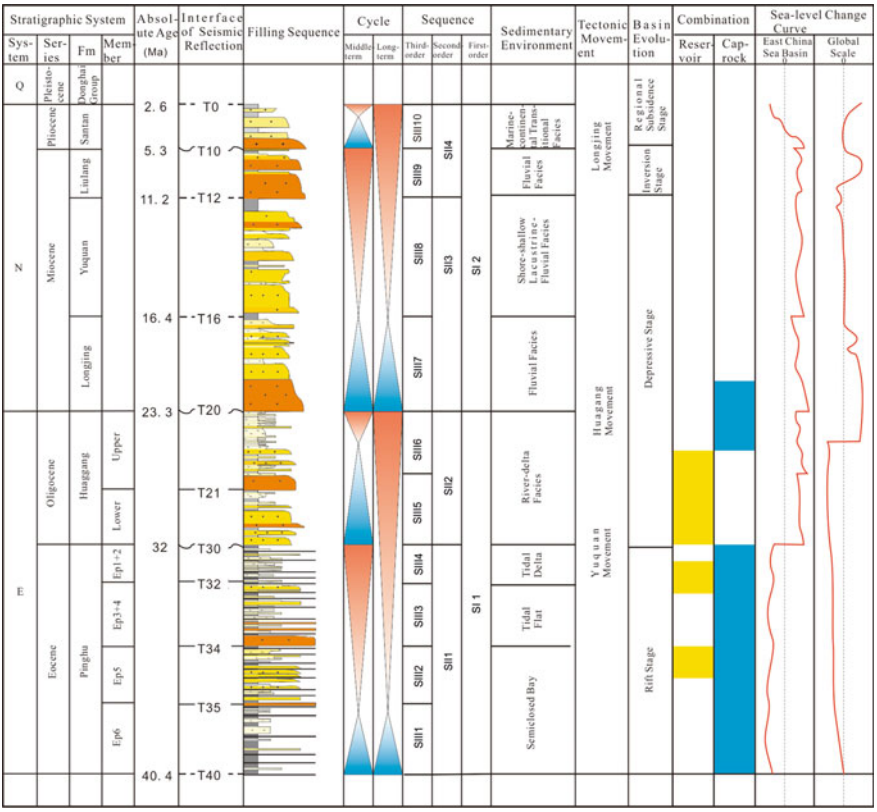

Fig. 2. Stratigraphic column showing the lithology, tectonic history, sequences, sedimentary facies, and source–reservoir–seal combination of the study area

reservoir facies, the pre-stack inversion is difficult to obtain good prediction results due to the introduction of the low-frequency model reducing the lateral prediction accuracy. The AVO analysis technique, which does not need well involvement, can maintain the lateral resolution of the seismic and the higher lateral prediction accuracy.

In this paper, we use the relative Poisson ratio reflectivity attribute from the AVO analysis to predict tight gas-bearing reservoirs. In order to realize the quantitative characterization of sandstone thickness, the stored filtering techniques are used to obtain the relative Poisson ratio, the reservoir interpretation is more accuracy, and the amplitude and thickness are approximately linearly correlated in the tuning thickness. Based on the AVO characteristics of the tight reservoirs, the seismological facies study is carried out using the strata slicing technique [29–36]. The spatial distribution of sandstone is analyzed by fine sedimentary facies and sedimentary evolution, and then searching the area where the sandstone development is stable to optimize the horizontal well trajectory, in order to develop the middle-deep tight reservoirs effectively.

2 Geologic Setting

The Xihu sag is located in the middle of the East China Sea continental shelf (Fig. 1) with a total area of about 5.9 × 104 km^2 [28, 37]. It experienced three major stages of geologic evolution, which are the rifting during the Paleocene to Eocene, depression during the Oligocene to Miocene, and regional subsidence during the Pliocene and Quaternary, respectively. Stratigraphy of the sag consists from the bottom upward of Pre-Eocene, Eocene Pinghu Formation, Oligocene Huagang Formation, Miocene Longjing, Yuquan and Liulang Formations, Pliocene Santan Formation, and Quaternary Donghai Group (Fig. 2).

The study area is located in the central south of Central Anticlinal Zone of the Xihu sag (highlighted in the box in Fig. 1) [38, 39]. Hydrocarbon reservoirs are predominantly distributed in the Huagang Formation (hereinafter referred to as H), which is unconformable contact with the underlying Pinghu Formation. The Huagang Formation, developed in shallow-water delta environments, is subdivided into two parts: the lower and the upper members (Fig. 2). Our target interval is the HB layer in the lower member of the Huagang Formation. It is currently buried at a depth of nearly 4000 m, consists of sandstones dominated by delta plain facies, and has experienced strong deep burial diagenesis [38, 39]. Sedimentation and diagenesis processes together caused the tight sandstone reservoirs of Huagang Formation [40]; Zhang et al. [38, 39]. Two drilled wells, wells W1 and W2, reveal that the HB layer, about 100 m thick, consists of light-gray sandstone interbedded with gray-black carbonaceous mudstone and coal. The HB layer contains two reservoir intervals, named HBa at the top and HBb at the bottom. HBb can be further subdivided into four reservoir beds, named HBab-1 to HBb-4, respectively. Where the HBb reservoir intervals are multistage sandstone overlap, drilling results indicate that the HBb sandstones are 25–32 m in thickness, with porosity between 6 and 10%, and permeability less than 0.5 mD. The reservoir gas content is better, and the average gas saturation is about 55%. Exploration well W1 got the commercial gas findings. And a horizontal well WH3 is designed to develop it.

3 Data and Methods

3.1 Data

Three-dimensional pre-stack time migration seismic data are available. Bin size of the seismic dataset is 12.5 × 25.0 m. Sampling rate of the three-dimensional data is 2 ms. Dominant frequency for the target interval is approximately 25 Hz, allowing a vertical resolution (tuning thickness) of ca. 42 m.

Core and well logging data from two wells are obtained. The core data include 8.9 m cores. Well logs available are natural gamma, resistivity, resistivity logging while drilling, neutron, density, and array sonic. These core and well logging data are used to calibrate the seismic data and to identify the geological significance of related seismic attribute parameters.

3.2 Principle of AVO Reservoir Prediction

The changes of lithology and fluid properties of the reservoirs will have certain influence on seismic amplitude and AVO attributes. The theoretical basis of the AVO is based on the Zoeppritz equation, which establishes the relationship between the reflection coefficient, the incident angle, and the elasticity parameters. Geophysicists have shown different approximated forms of the Zoepprize equations to simplify it. Shuey [41] showed that the variations of the Poisson ratio will have a great influence on the reflection coefficient variation versus the angle of incidence. When the angle of incidence is less than 30°, the approximate equation is given as below [41]:

$$\begin{aligned} R(\theta) &\approx A + B * \sin^2\theta \\ A &= \frac{1}{2}\left(\frac{\Delta\alpha}{\overline{\alpha}} + \frac{\Delta\rho}{\overline{\rho}}\right), \quad B = B_0 A + \frac{\Delta\sigma}{(1-\overline{\sigma})^2}, \\ B_0 &= D - 2*(1+D)\frac{1-2\overline{\sigma}}{1-\overline{\sigma}}, \quad D = \frac{\frac{\Delta\alpha}{\overline{\alpha}}}{\frac{\Delta\alpha}{\overline{\alpha}} + \frac{\Delta\rho}{\overline{\rho}}} \end{aligned} \tag{1}$$

where θ is the incident angle; $R(\theta)$ is the reflection coefficient of the PP wave, and changes with the angles θ; $\Delta\alpha$, $\Delta\rho$, and $\Delta\sigma$ represent the relative change rates of compressional wave velocity, density, and Poisson ratio of the medium on both sides of the interface, respectively; and $\bar{\alpha}$, $\bar{\rho}$, *and* $\bar{\sigma}$ denote the average values of compressional wave velocity, density, and Poisson ratio of the medium on both sides of the reflection interface, respectively. Parameter A is the reflection coefficient at the time of vertical incidence of the compressional wave, which is the intercept term, and parameter B is the gradient term, assuming that the background value of σ is σ = 1/3 (the compressional wave velocity is 2 times the shear wave velocity), then put the σ background value into the gradient item B to get as follows:

$$B = -A + \frac{9}{4}\Delta\sigma \tag{2}$$

$$\Delta\sigma = \frac{4}{9}(A + B) \tag{3}$$

Equation 2 shows that when the acoustic impedance of sandstone and shale is constant, the $\Delta\sigma$ will have a great influence on the amplitude variation with offset. In the gas-bearing sandstone, the value of Poisson ratio was significantly reduced, causing $\Delta\sigma$ of the two sides of the medium to increase, resulting in abnormal AVO. Equation 3 shows that variations of $\Delta\sigma$ can be inferred from the intercept and gradient attributes by summing the intercept and the gradient. However, the intercept and gradient attributes are relative values and dimensionless, which can be given by the well calibration in the calculation process for $\Delta\sigma$.

3.3 AVO Forward Modeling

AVO is a comprehensive response of lithology, physical, and gas-bearing properties of reservoirs. The reflection amplitude is the comprehensive response of the multifactors including lithology, thickness, porosity, and saturation. Under certain circumstances, one or more factors may play a leading role. Tight gas reservoirs have different reflection characteristics and influencing factors relative to the conventional reservoirs. Here, the effects of variations of gas saturation and porosity, and sandstone thickness on AVO characteristics are, respectively, studied by one-dimensional and two-dimensional seismic forward modeling, on which reservoir characteristics are qualitatively described.

3.3.1 One-Dimensional Forward Modeling

The forward process. A conventional reservoir model with a porosity of 17% and a tight reservoir model with a porosity of 9% were designed, respectively. Then, well logs of reservoirs with different gas saturations (from 5 to 95%) are obtained by fluid replacement, based on the original log curves (compressional wave velocity, shear wave velocity, and density). The synthetic well logs are used for AVO forward modeling. The seismic amplitude values are extracted along the layer and are used to analyze the AVO type, and associated the intercept and gradient changes.

Another reservoir model with gas saturation of 55% is designed, equal to the average gas saturation value of target layer. AVO forward modeling is carried out through changing its porosity from 3 to 21%. Then, the amplitude values are extracted along the layer, which are used to analyze the AVO type, and associated intercept and gradient changes.

Effects of gas saturation on AVO characteristics. Figure 3a, b shows the results of AVO forward modelings of the conventional reservoir at a depth of approximately 3000 m, and of the tight reservoir, the middle-deep layer at a depth of approximately 3950 m, respectively. For the conventional reservoir case, the near-zero reflection amplitude (intercept attribute) decreases and the gradient changes little with the increase of gas saturation; and for the tight reservoir case, the AVO intercept and gradient attributes are almost unchanged with the increase in gas saturation.

It is suggested that AVO used for the fluid indicators may not be useful in tight gas sand plays because tight gas has low porosity and thus little change when water is replaced with gas [16].

Effect of porosity on AVO characteristics. Figure 3c shows the AVO forward modeling results with porosity variation with the gas saturation of 55%. It can be seen that the porosity has a great influence on seismic amplitude. As porosity increases, the AVO intercept becomes smaller. The reason for this is that the sandstone density decreases with the increase of porosity. The difference of the impedance value between the sandstone and the shale decreases. The absolute value of the AVO gradient increases gradually as porosity increases, and the gas content of the sandstone increases, and the difference of the impedance value between the sandstone and the shale increases. Thus, relatively high-porosity sandstones in tight reservoirs are characterized by low intercept and high gradient values.

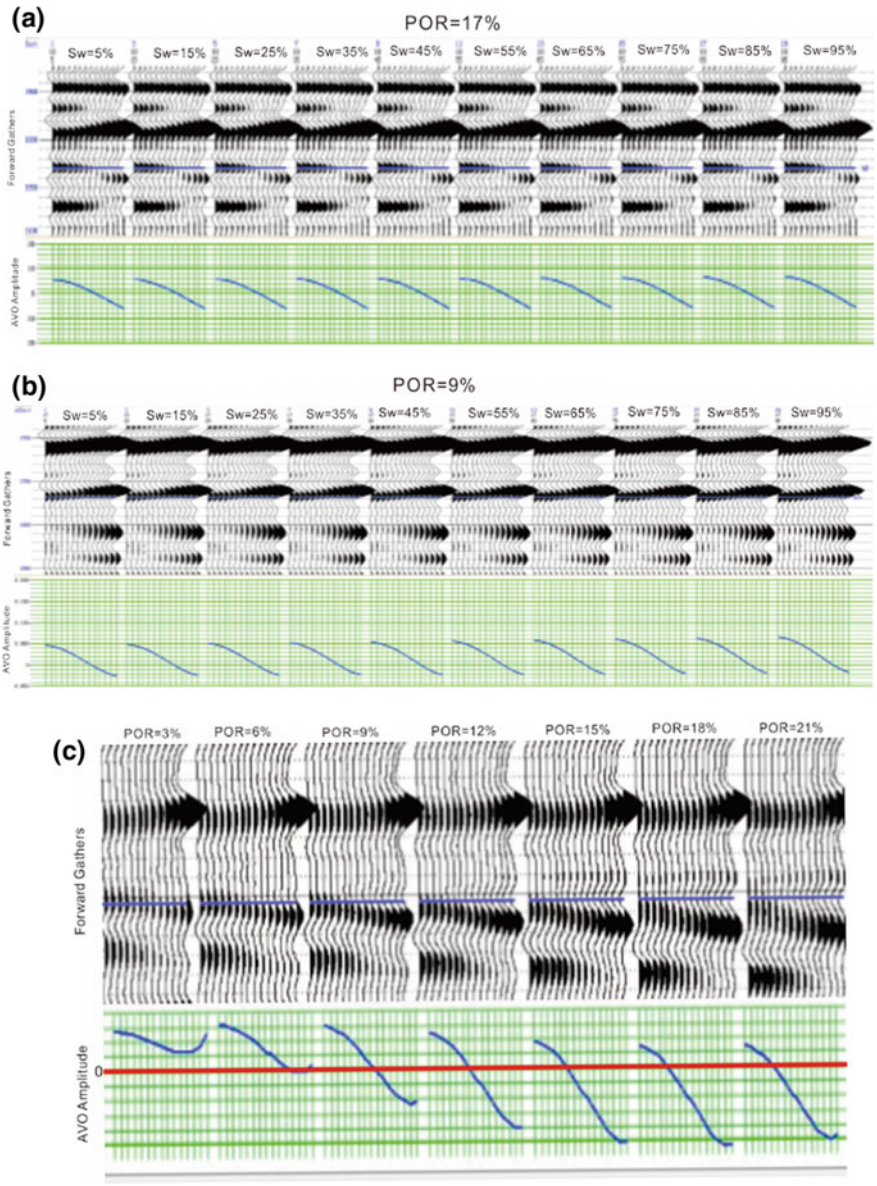

Fig. 3. AVO with different water saturations of conventional reservoir (where porosity is 17%) (**a**). Compared to tight reservoir (where porosity is 9%) (**b**). The peak amplitude related to the reservoir is plotted in below each gather, and from left to right a total of 10 tracks, water saturation from 5% gradually increased to 95%. The near-zero reflection amplitude (intercept attribute) of the conventional reservoir decreases and the gradient changes little with the increase of gas saturation; and the AVO intercept and gradient attributes of the tight reservoir are almost unchanged with the increase in gas saturation. AVO with different porosities (where gas saturation is 55%) (**c**). The peak amplitude related to the reservoir is plotted in below each gather, and from left to right a total of 7 tracks, porosity from 3% gradually increased to 21%. As the porosity becomes larger, the reflection characteristic is the AVO intercept that becomes smaller and the absolute value of the AVO gradient increases gradually

3.3.2 Two-Dimensional Forward Modeling

A simple wedge model is created to evaluate the effect of sandstone thickness on the AVO characteristics based on the compress wave velocity, shear wave velocity, and density values of the drilled target layer. The compress wave velocity of the sandstone is 4615 m/s, the shear wave velocity is 2818 m/s, the density is 2.3 g cm^3, the porosity is 8%, and the gas saturation is 55%; and the compress velocity of the shale is 4300 m/s, the shear wave velocity is 2400 m/s, and the density is 2.38 g cm^3.

The effect of sandstone thickness on AVO characteristics. According to Widess [42], the seismic reflection amplitude of a subtuning bed is dependent on the impedance and thickness of that bed. When the thickness of the sandstone is equal to one-quarter of the wavelength, the seismic stack amplitude is the strongest. When the wavelength is less than the quarter wavelength, the thickness and the amplitude show a positive linear correlation. When the wavelength is greater than a quarter wavelength, the top and bottom interfaces appear as simple peaks or troughs, and the reflection amplitude is an equation of the reflection coefficient, which is not affected by the tuning effect (Fig. 4a, b).

The seismic reflection amplitude is influenced by the angle of incidence (AVO) in addition to the influence of the thickness of the sandstone.

Figure 4c shows the AVO forward modeling results with sandstone thickness variation. The three coordinates are the sandstone thickness, the incident angle, and the reflection amplitude, and the tuning thickness is 18 m. The AVO amplitude shows obvious variations with the thickness and incident angle of the formation. The AVO reflection characteristic is influenced by the tuning effect. When the thickness of the formation is larger than the tuning thickness, the AVO reflection is stable and is not affected by the tuning effect. When the thickness of the formation is close to the tuning thickness, the influence of the tuning effect on AVO and reflection characteristics is significantly enhanced, and the reflection amplitude is enhanced. When the thickness of the formation is less than the tuning thickness, influence of the tuning effect on AVO reflection characteristics is weakened, and the reflection amplitude is weakened.

The effect of sandstone thickness on the variation of AVO reflection characteristics and amplitude can be characterized by the intercept and gradient attributes. The intercept and gradient values with different thicknesses show that the thickness of the gas reservoir reduces from 50 m to the tuning thickness of 18 m, and the intercept and gradient values are gradually increased, reaching the largest at the tuning thickness. When the thickness of the gas layer gradually decreases from the tuning thickness of 18 m, the intercept and gradient values are gradually weakened (Fig. 4d).

3.3.3 AVO Characteristics of the Tight Reservoir in the East China Sea

The forward modeling shows that the AVO gradient and intercept attributes of the tight reservoirs are sensitive to the changes in the thickness and porosity of the sandstone and are almost irrelevant to the gas saturation. When the sandstone thickness is less than the quarter length, the AVO intercept and the gradient attribute increase with the increase of the sandstone thickness. When the sand thickness is more than the quarter wavelength, the AVO intercept and the gradient attribute decrease with the increase of the sandstone thickness. As the sandstone porosity increases, AVO intercept property decreases, and AVO gradient attribute increases.

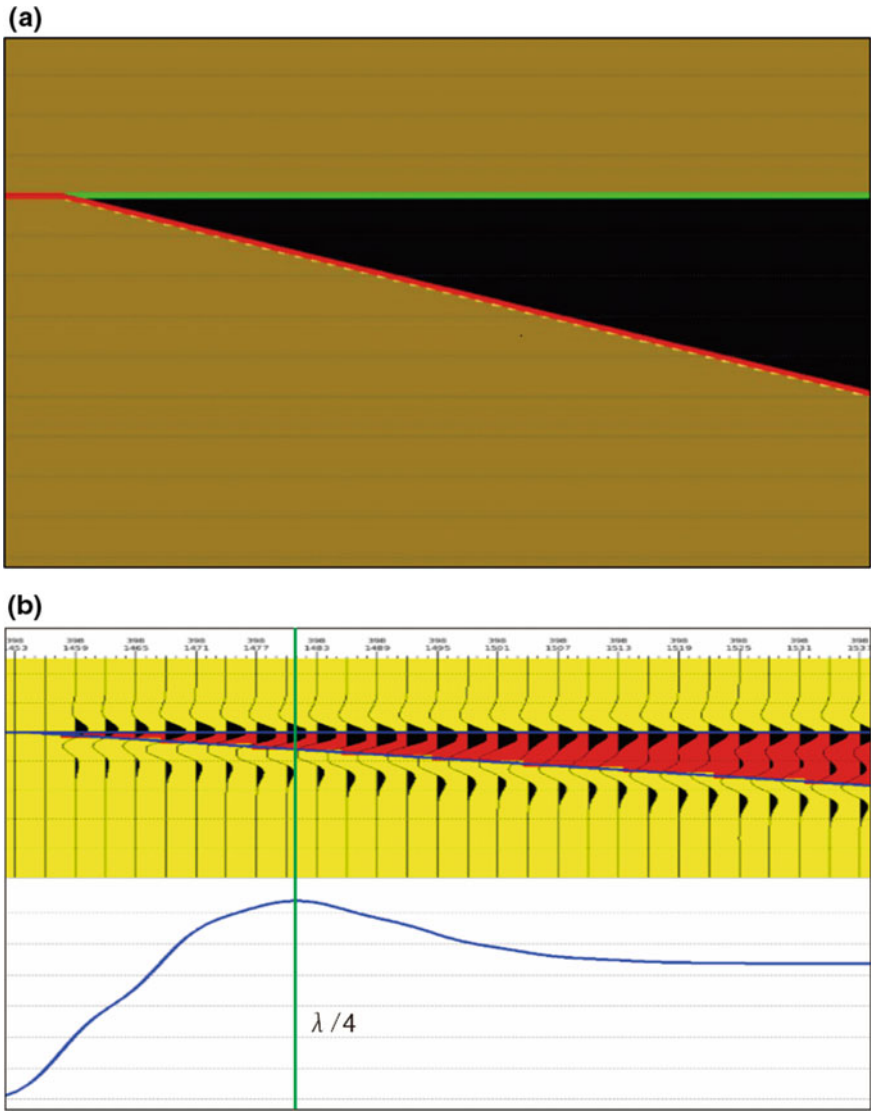

Fig. 4. A simple wedge model is created to evaluate the effect of sandstone thickness on the AVO characteristics. Where **a** is wedge model, the compress wave velocities, shear wave velocities and density characteristic value come from the drilled target layer, the tuning thickness is 18 m. **b** is two-dimensional forward results of the wedge model; the seismic superposition amplitude is the strongest while the thickness of the sandstone is equal to one-quarter of the wavelength when the sandstone is less than the quarter wavelength, and the thickness and the amplitude show a positive linear correlation. When the wavelength is greater than a quarter wavelength, the top and bottom interfaces appear as simple peaks or troughs, and the reflection amplitude is a function of the reflection coefficient, which is not affected by the tuning effect. **c** is three-dimensional forward results; *x*, *y*, *z* coordinates represent the sandstone thickness, incident angle, and reflection amplitude, respectively. When the thickness of the formation is larger than the tuning thickness, the AVO reflection is stable and is not affected by the tuning effect. When the thickness of the formation is close to the tuning thickness, the influence of the tuning effect on

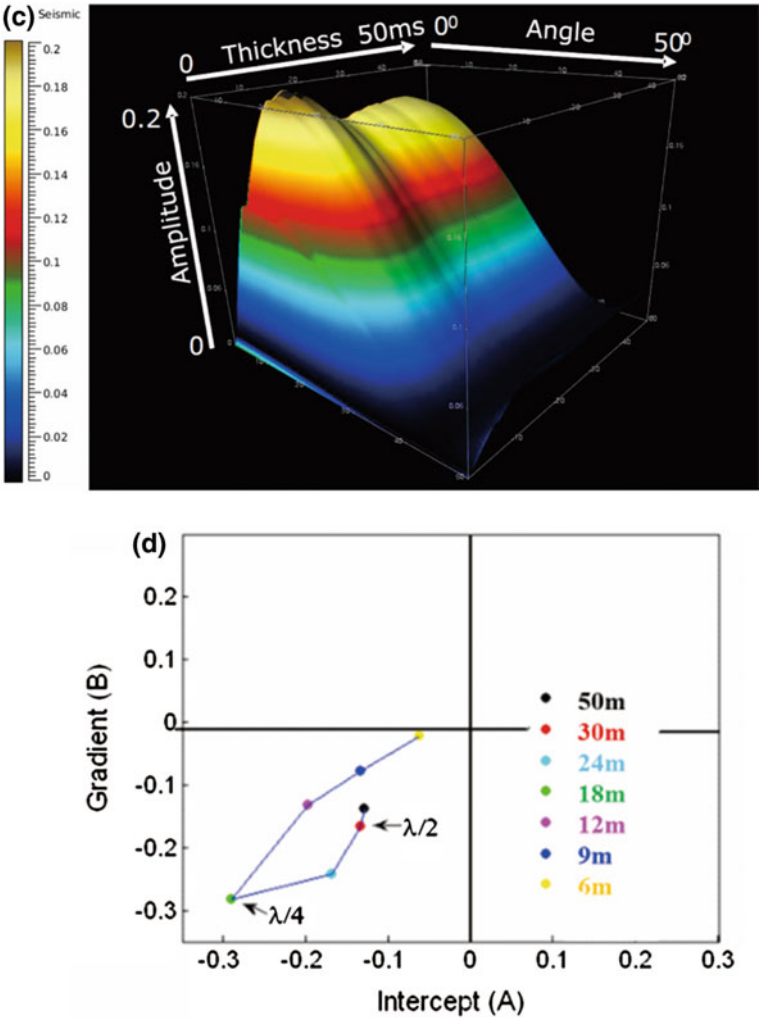

AVO reflection characteristic is significantly enhanced and the reflection amplitude is enhanced. When the thickness of the formation is less than the tuning thickness, influence of the tuning effect on AVO reflection characteristic is weakened and the reflection amplitude is weakened. **d** indicates the variation of intercept and gradient attributes with different thicknesses. When the thickness of the gas layer is reduced from 50 m to the tuning thickness of 18 m, the intercept and gradient absolute values are gradually increased, reaching the strongest at the tuning thickness. When the thickness of the gas layer gradually decreases from the tuning thickness of 18 m, the intercept and gradient absolute values are gradually weakened

Phase Conversion and Frequency Division Based on Stored Filter

Interface information can be transformed to layer information by the so-called ninety-degree phase transform technology of seismic data [43]. Through the ninety-degree phase transforming, the Poisson ratio reflectivity is converted to the relative Poisson

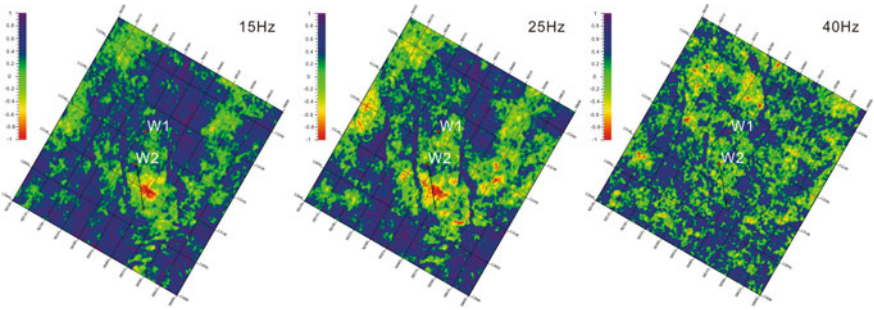

Fig. 5. The results obtained by stored filtering from left to right with 15, 25, and 40 Hz wavelet filters, respectively, where the 25 Hz stored filter results weaken the interference effects of the wavelet

ratio attribute, which makes the lithology interpretation more clear. However, this method does not take into account the problems of sandstone thickness, wavelet frequency, and actual seismic phase. The results are often the same as those of sandstone thickness not consistent and non-true 90° phase section. In this paper, a stored filter technique is proposed, by which phase transformation and frequency division interpretation are done by one step in the form of a wavelet filter by the filter factor Ricker (f, (p-90)), where p is the actual seismic phase, the filtered result is a true 90° phase profile, f is the target layer wavelet frequency within the tuning thickness, and the amplitude and thickness are approximately linearly related.

As drilled in the study area, the thickness of HBb is about 30 m wavelet tuning and frequency is 25 Hz. Figure 5 shows the results obtained by stored filtering with 15, 25, and 40 Hz wavelet filters, respectively. Where the 25 Hz result due to the influence of wavelet interference is weakened, it can better reflect the main sandstone lateral distribution characteristics and more accurate for the thickness of sandstone prediction. In contrast to the results of the stored filter (Fig. 6 left) (f = 25 Hz, p = 10) and −90° phase transforming results (Fig. 6 right), it can be found that the stored filter result is in good agreement with the actual drilled sandstone (white box) and higher vertical resolution (black box).

Strata Slicing Technique The top and bottom boundaries of the lower member of the Huagang Formation, HA and HC, correspond to the stable seismic reflection horizons, T21 and T30, respectively (Fig. 7). HB exhibits a continuous and stable peak reflection in the seismic section (Fig. 7). Therefore, HA and HC are chosen as the upper and lower bounds of the isochronal surfaces, and HB is used as the constraint surface.

Petrophysical analysis shows that the relative Poisson ratio is a good attribute sensitive to lithology. The distribution characteristics of sedimentary bodies are analyzed by strata slices of the relative Poisson's ratio attribute data. As shown in the stratal slices of the HBb in Fig. 8, shape and boundary of the sandstone, especially the distributary channel patterns, can be clearly identified.

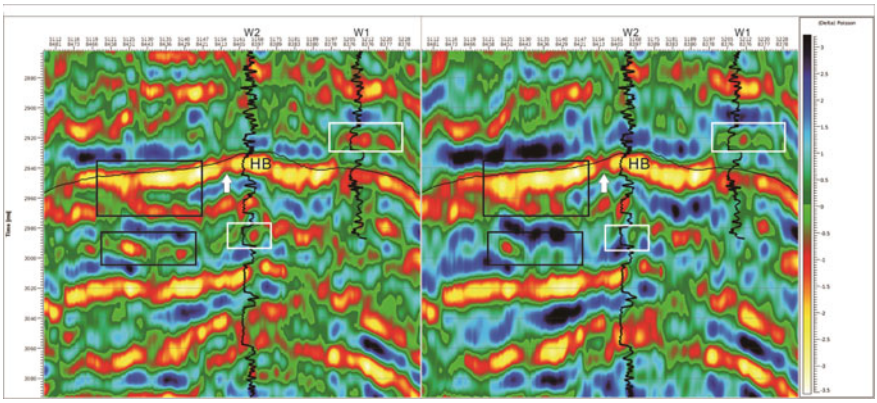

Fig. 6. Sections of AVO attributes and the reflectivity of the contrast of apparent Poison's ratio calculated from HB formation (**a**). Relative Poisson ratio results were calculated with different methods (**b**). The left is the method of storage filter, and the right is the method ninety-degree phasing of seismic data. The black curves in the figure are the gamma ray (GR) curve of the drilled wells. The left is in good agreement with the actual drilled sandstone (white box) and higher vertical resolution (black box)

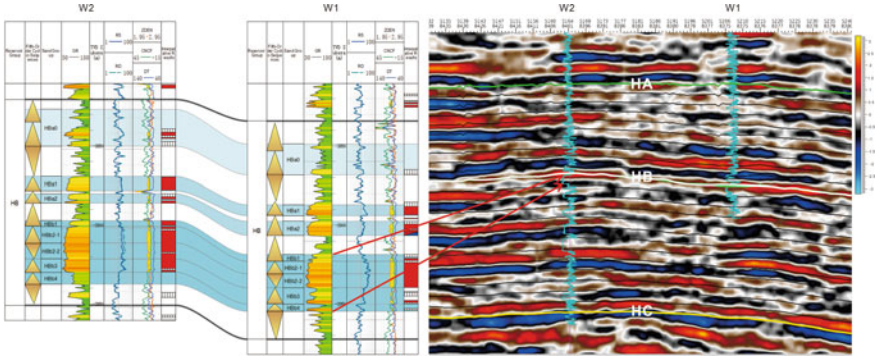

Fig. 7. Isochronous stratigraphic framework for constraining stratigraphic sections. The left profile shows stratigraphic division and comparison results of HB formation. On the seismic section of the right, the green line is tracked to the HA formation top interface, and yellow line tracked to the HC formation top interface. The HA and HC are the top and bottom boundaries of the lower part of the Huagang formation, respectively, and correspond to the stable seismic reflection interfaces T21 and T30. White line corresponds to the target layer HB formation top interface, and HB layer is continuous and stable in the seismic section peak reflection

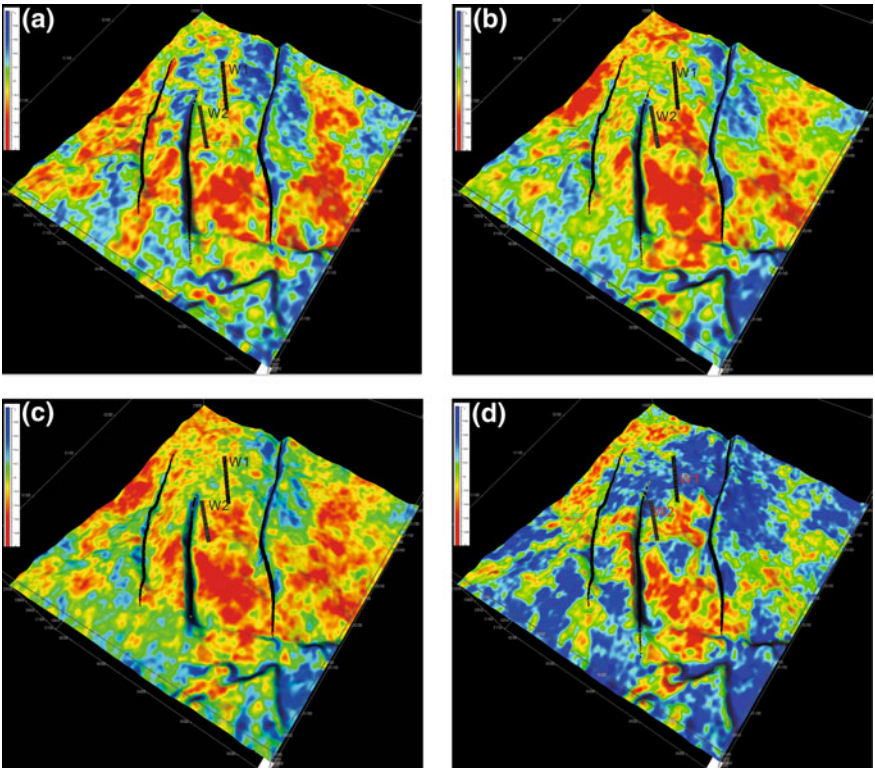

Fig. 8. H8b relative Poisson ratio attribute slices, **a**, **b**, **c**, and **d** represent the sections of HBb-4, HBb-3, H8b-2, and HBb-1, respectively. The red color indicates the sandstone and the blue color indicates the shale. Sandstone shape and boundary description are more clear and can better reflect the distribution of river channel sandstone characteristics

4 Results

4.1 Qualitative Analysis of HBb Reservoir

The AVO reflection amplitude is influenced by thickness, porosity, and gas saturation of the sandstone reservoirs. The gas saturation of the tight gas reservoirs has little effect on the reflection amplitude, while the effect of porosity and thickness of sandstone reservoirs on the reflection amplitude is obvious. In Fig. 6, the HBb layer has a weak seismic amplitude region (at the white arrow), which could be caused by variations in porosity or thickness of the sandstone reservoirs. Through the AVO influencing factors and regular characteristics, qualitative judgments can be made.

The layer velocity is 4200 m/s, tuning thickness is 42 m, and HBb sand thickness is less than the tuning thickness. According to AVO influencing factors and changes in the study results, when the thickness of the sandstone is thinner than the tuning thickness, the intercept and the gradient attribute increases with the increase of the

sandstone thickness, and the gradient increases with the porosity increases. It can be seen from Fig. 6a that the intercept and gradient properties of the weak amplitude region of the HBb layer are reduced. Therefore, it is inferred that the weak amplitude region could be caused by the thickness reduction, not by porosity increase, and the relative Poisson ratio is stronger, which represents the thickness of sandstone would be thicker.

4.2 Quantitative Analysis of HBb Reservoir

The time domain thickness of the sandstone can be obtained by the relative Poisson ratio data volume, and the depth domain thickness of the sandstone can be obtained by time–depth conversation. The results show that the sandstone of HBb reservoir is more

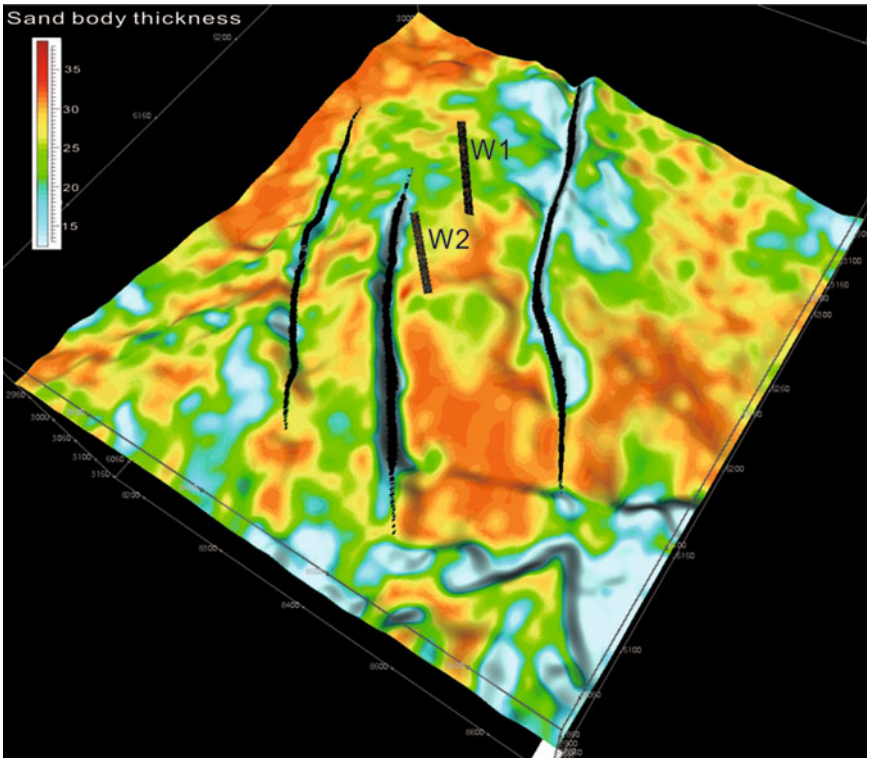

Fig. 9. Sandstone thickness prediction results of HBb layer. The relatively low value (red) mainly represents the longitudinal overlay of the multistage distributary channel, which is the relatively high-quality reservoir with thicker sandstone thickness and better porosity. The thicker the color characterizes, the thicker the sandstone. The relative medium value (light yellow and light blue) represents the sandstone on the side of the distributary channel, in which thickness is relatively thin, the clay content is higher, and the porosity is relatively lower. The relatively high value (blue) mainly represents the interdistributary bay microfacies, shale, and non-reservoir

developed in the region between wells W1 and W2 and its southern part, with the predicted maximum thickness over 35 m (Fig. 9).

4.3 Characterization of HBb Sandstone Reservoirs

The results of the study on the sedimentary facies of the study area show that the sedimentary facies of the HB are mainly sedimentary in the delta plain. The distributary channel is mainly composed of light-gray sandstone, and GR curve of the distributary channel facies is characterized with box-typed or box- and bell-typed log facies, showing an abrupt basal and an abrupt or gradual top contact. The natural levee is dark gray siltstone, in which GR curve is the high value, serrated, or straight. The crevasse spray is light-gray silty sandstone, in which GR curve is the low value, finger, or bell type. The swamp is dark gray mudstone, in which GR curve is low and high, straight, or zigzag type.

The value of the relative Poisson ratio (Fig. 8) shows a good correspondence with the sedimentary facies and lithology, with relatively lower values (red) predominantly correspond to the vertically stacked distributary channel bodies, which are the relatively high-quality reservoirs of larger sandstone thickness and better porosity. Medium relative Poisson ratio values (light yellow and light blue) characterize the sandstones deposited on the margins of the distributary channels, which are normally of relatively thinner thickness, higher clay content, and lower porosity. High relative Poisson ratio values (blue) are shale dominated and are interpreted as the interdistributary bay facies.

The sedimentary facies and sedimentary evolution of HBb are interpreted using the drilled data and previous research results, combined with seismic geomorphology and seismic lithology characteristics (Fig. 10). During the deposition of the HBb layer, river channels trending predominantly in the northwest–southeast direction were developed. In the area between wells W1 and W2, lateral stacking of river channel bodies is noted, and the sandstone lateral distribution is more or less stable. To the south of well W2, thickness could be decreased.

From HBb-4 to HBb-1, several sets of sandstone sublayers are developed and show good inheritance, in which the HBb-4 deposition period is the early stage of the delta construction, and the characteristics of the single channel in the north are obvious. The sandstone bodies are mainly developed in the south of well W2, and well W2 is located in the main passage of the river channel.

HBb-3 and HBb-2 deposition periods witnessed the highly building of the delta system, during which the size of the braided distributaries increased. The sand supply capacity of the delta is obviously enhanced, the distribution of sandstone is widened, W1 and W2 are in the main part of the river channel, sandstone continuous distributes in lateral, thickness is stability, and there is less risk of reservoir changes.

HBb-1 deposition period is the abandoned period, transition to meandering river. Wells W1 and W2 are at the margins of the river system, and the sandstone distribution is narrowed due to the reduced capacity of the delta sand proving, but the sandstone between wells W2 and W1 and the south of well W2 is still developed.

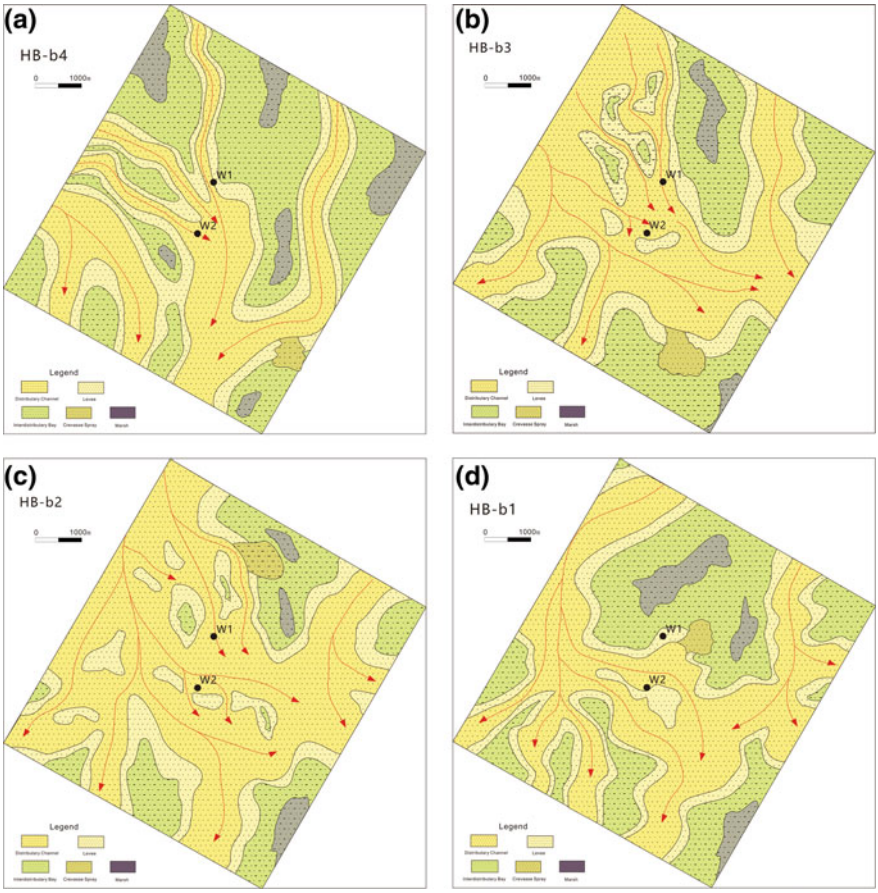

Fig. 10. The sedimentary microfacies and sedimentary evolution of HBb layer in the study area, **a**, **b**, **c**, and **d** are the sedimentary microfacies of HBb-4 sublayer, HBb-3 sublayer, H8b-2 sublayer, and HBb-1 sublayer, respectively. The black arrow indicates the direction of the flow, and distributary river is the most developed in HBb-2 sublayer

4.4 Horizontal Well Trajectory

The results show that the HBb-2 sandstones are the most stable, and the main body of the distributary channel is favorable sedimentary facies. Thick and continuous sandstones are distributed in between wells W1 and W2, and the southern part of our study area. Taking into account the predicted reservoir distribution, the horizontal segment trajectory of well Wh3 is designed to avoid the bottom water and possible faulting. The HBb-2 sublayer is mainly targeted in the vertical direction, and the area between W2 and W1 wells is the target in the horizontal direction (Fig. 11). Meanwhile, it is

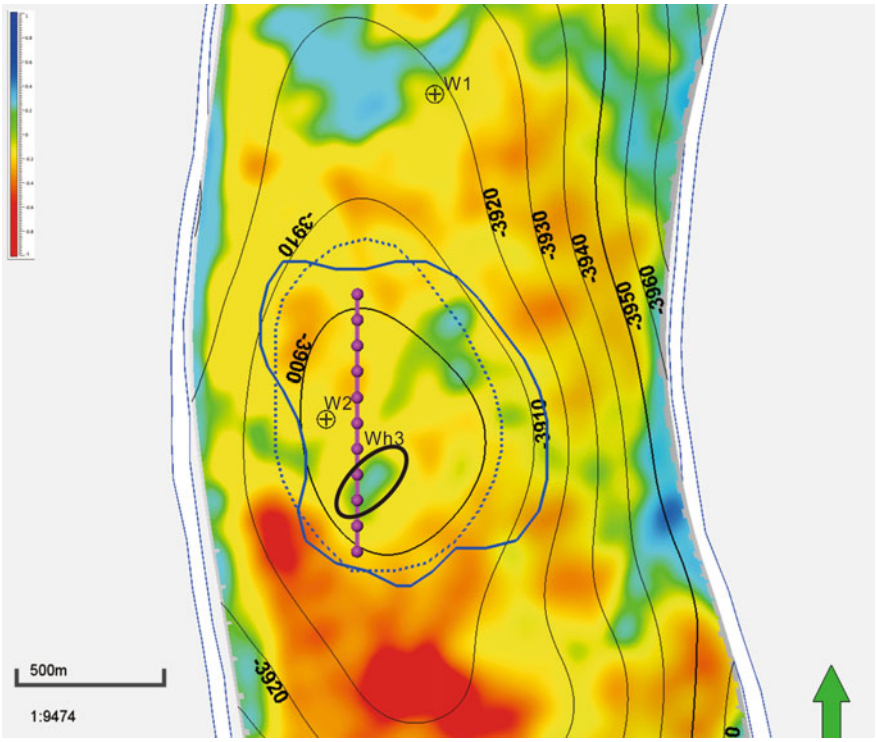

Fig. 11. HBb-2 sublayer reservoir distribution superposition structure contour map and horizontal well Wh3 plane trajectory, where the dashed line and the thicker solid line are the two co-operative companies explaining the explained gas boundary separately, and the black oval circle indicates the risk of reservoir thinning or lithology deterioration

suggested that the weak amplitude in the southern section of the horizontal section has the risk of drilling the sand thinning zone (Fig. 11 black oval circle).

The drilling results of the well confirmed the reliability of reservoir prediction: the encountering rate of sandstone is 100% in the horizontal segment (Fig. 12). However, there are two spikes in GR curve in the southern section (Fig. 12), indicating that the shale content is increased and the lithology is finer, and the rock samples also confirm this, which is the boundary zone where the two sandstones overlap. And the GR value of the horizontal segment between the two spikes is slightly higher than the GR value

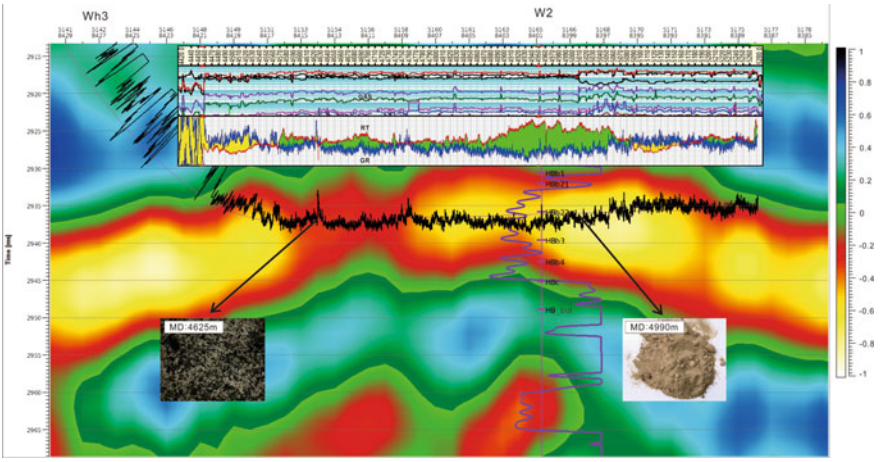

Fig. 12. Reservoir prediction section and real drilling horizontal segment trajectory of the well wh3. The brighter the color indicates the more developed the sandstone where the black curve is the GR curve of the well wh3, and purple curve is the GR curve of the well w1. The red arrows are indicated for logging cuttings, and the arrow at GR peak indicates that the corresponding cuttings show high shale content, and the arrow at the GR straight indicates that the corresponding cuttings show sandstone purity

of the other parts, and the construction pressure of this part is obviously higher than that of the other parts during the fracturing construction, confirming that the lithology is thinner and the reservoir thinning of the part of the previous study is reliable.

Acknowledgements. We would like to thank Professor Zhong Guangfa of Tongji University, Guo Shisheng and Shan Lijun (CNOOC Shanghai Branch) for their help. This work is funded by the National Science and Technology Major Project of China (2016ZX05027-003). And thanks CNOOC Shanghai Branch for permission to publish this paper.

References

1. Yuan SJ (2008) Study on technique of Lower Shihezi Formation reservoir prediction in Daniudi gasfield of Ordos Basin by seismic and application. Oil Geophys Prospect 43:48–52
2. Dong N, Liu ZF, Zhou XY, Wang JB, Liu JZ, Xia HM, She G (2008) Seismic detection and prediction of tight gas reservoirs in the Ordos Basin. Oil Gas Geol 29:668–675
3. Qiao SR, Zhang H, Zhao S (2008) Reservoir prediction techniques and their application to tight sandstones of the Xujiahe Formation in DY area, western Sichuan Basin. Oil Gas Geol 29:774–780
4. Sheng J (2016) The reservoir comprehensive study and horizontal well development countermeasures of tight sandstone gas. PhD thesis, Northwest University
5. Zhang J, Wang YC, Zhao F, Yang L, Zeng YJ (2008) Multi-parameters joint inversion technology predicts gas-bearing tight sandstone. Nat Gas Geosci 19:864–869

6. Wu HZ, Ye TR, Zhao D, Ma RH (2015) Fine characterization technique and its application to channel sandstone in continental tight gas reservoirs of western Sichuan depression. Oil and Gas Geology 36:230–239
7. Pang CY, Zhang YD, Zhang HR, Zhang X, Duan J, Huang XH, Xia M (2017) The application of geostatistics inversion to prediction of compact and thin sand body in Sulige gas field. Geophys Geochem Explor 41:16–21
8. Xu J, Dong N, Zhu ChH, Liu JZ, Chen TSh (2012) Application of seismic data to the design of horizontal well trajectory in tight sandstone gas reservoirs. Oil Gas Geol 33:909–913
9. Close D, Stirling S, Cho D, Horn F (2010) Tight gas geophysics: AVO inversion for reservoir characterization. J Aoac Int 93:434–441
10. Fan R, Liu LH, Shi WB, Zhang GC, Zeng T (2015) Tight reservoir prediction of lower subsection of Xu_2 member in western Yuanba area. Geophys Prospect Petrol 54:83–89
11. Qin GP, Li Y, Jiang L, Wang HL, Li Y (2013) EEI inversion for detection and mapping of sweet spots in tight gas glutenites—an example from Northeastern China. Presented at the 75th EAGE conference and exhibition incorporating, SPE EUROPEC
12. Zhang SS, Liu YJ, Liu XH (2015) Prediction technique of high-quality reservoir in tight reservoir of the sixth member of Xujiahe Formation in Jiannan area. Lithologic Reservoirs 27:98–102
13. Guo SY (2014) Research on geophysical characterization method of tight gas reservoir. MS thesis, Yangtze University
14. Jin JN, Pan RF, Zhou Y, Liu HT, Gong Q (2015) Predicting tight gas-bearing sandstone reservoir of the 4th Xujiahe formation in Jiannan area. Sci Technol Eng 15:150–156
15. She YW (2015) Study on seismic reservoir prediction and hydrocarbon detection technology in 8th he formation in 59 area of Sulige Gas Field. MS thesis, Southwest Petroleum University
16. Tyiasning S, Cooke D (2015) A comparison of competing amplitude variation with offset techniques applied to tight gas sand exploration in the Cooper Basin of Australia. Interpretation 3:SZ15–SZ26
17. Wang ZM (2010) Fluvial facies tight sandstone gas reservoirs characterization and effective sandstone prediction in Sulige Gasfield. Ph.D. thesis, China University of Geosciences
18. Wu FR, Li YL, Wang D, Chen HF, Yao MW (2011) Application of AVO attribute to the detection of tight sandstone reservoirs. Nat Gas Ind 31:55–57
19. Goodway W (2001) AVO and lame constants for rock parameterization and fluid detection. CSEG Recorder 26:39–60
20. Castagna TR, Swan HW (1996) Principles of AVO crossplotting. Lead Edge 16:337–342
21. Castagna JP (1998) Framework for AVO gradient and intercept interpretation. Geophysics 63:948–956
22. Waters KD, Kemper MAC (2014) Find the rocks and the fluids will flow—AVO as a tool for lithology classification. Interpretation 2:SC77–SC91
23. Liu LH, Li JH, Yang X, Ding Y, Hu C (2013) Exploration and practice of seismic lithology of prestack AVO attributes. Geophys Prospect Petrol 52:247–252
24. Chen XG, Xu R, Mu X, Gao WY (2007) Application of relative poisson ration analysis technique to the detection in gas reservoir with middle-deep sandstones in Pinghu area. Pet Geol Recovery Effi 14:63–65
25. Jiang Y, Tu QC (2015) The reservoir prediction of tight gas sandstone by using petrophysical analysis and prestack inversion technology. Mar Geol Frontiers 31:36–42
26. Jiang Y, Zhang L, Zou W, Hou ZQ (2015) Technology for prediction of underwater distributary channel reservoir and application in B structure, Xihu sag. Offshore Oil 35:35–39

27. Qin DW, Jiang Y, Hou ZQ, Cheng C, Sun YZ, Hu W (2015) Application of prestack synchronous inversion technology in "sweet spot" prediction of low porosity and permeability reservoir in Xihu sag. Reservoir Eval Dev 5:12–15
28. Zhang JP, Yu YF, Zhang T, Zhang SL, Tang XJ (2013) A discussion on the exploration potential of deep basin gas in Xihu sag, East China Sea. China Offshore Oil Gas 25:24–29
29. Dong CM, Zhang XG, Lin ANDCY (2006) Conception method and technology of the seismic sedimentology. Acta Sedimentol Sin 24:698–704
30. Dong CM, Zhang XG, Lin ANDCY (2006) Discussion on several issues about seismic sedimentology. Oil Geophys Prospect 41:405–409
31. Lin CY, Zhang XG (2006) The discussion of seismic sedimentology. Adv Earth Sci 21:1140–1144
32. Zeng HL, Henry SC, Riola JP (1998) Stratal slicing, partII: real 3-D seimic data. Geophysics 63:514–522
33. Zeng HL (2011) Seismic sedimentology in China: a review. Acta Sedimentol Sin 29:417–426
34. Zeng HL, Zhu XM, Zhu RK, Zhang QS (2012) Guidelines for seismic sedimentologic study in non-marine postrift basins. Petrol Explor Dev 39:275–284
35. Zhang HF, Zeng HL, Zhang WX (1988) Regional seismic stratigraphic method for fault-depressed basins in land. Oil Gas Geol 9:231–241
36. Zhu XM, Li Y, Dong YL, Zhao DN, Wang X, Zhu M (2013) The program of seismic sedimentology and its application to Shahejie formation in Qikou depression of North China. Geol China 40:152–162
37. Zhang GH (2013) Origin mechanism of high formation pressure and its influence on hydrocarbon accumulation in Xihu sag. China Offshore Oil Gas 25:1–8
38. Zhang W, Xu F, Xu GS, Gao WZ, Tang JC (2012a) Diagenesis and pore evolution of Huagang formation tight sandstone reservoir in a structure of Xihu sag in East China Sea basin. J Chendu Univ Technol (Science & Technology Edition) 39:122–129
39. Zhang JP, Xu F, Zhong T, Zhang T, Yu YF (2012b) Sequence stratigraphic models and sedimentary evolution of Pinghu and Huanggang formation in Xihu sag. Mar Geol Quatern Geol 35–41
40. Liu JS, Cao B, Xu ZX, Qin LZ, Xu FH, Tang JC (2012) Sedimentary facies and the characteristics of tight sandstone reservoirs of Huagang formation in Xihu sag in East China Sea basin. J Chendu Univ Technol (Science & Technology Edition) 39:130–136
41. Shuey RT (1985) A simplification of the Zoeppritz equations. Geophysics 50:337–342
42. Windess MB (1973) How thin is a thin bed? Geophysics 38:1176–1180
43. Zeng HL (2007) Seismic imaging for seismic geomorphology beyond the seabed: potentials and challenges. Geol Soc, London, Special Publications, 277:15–28

Estimation of Formation Damage Along Lateral Formation Using Ordinary Kriging Method

Rui Zhang(✉) and Kehao Bo

School of Petroleum Engineering, China University of Petroleum (East China), Qingdao, China
zhangrui@upc.edu.cn, ll02l6l5@s.upc.edu.cn

1 Introduction

During drilling and production operations, the original balance of oil and gas reservoirs can be interfered near the wellbore with movement of inevitably break original balance state of reservoirs in varying degrees such as pressure and temperature alteration of near wellbore and thermo-kinetics movement of chemical balance, which results in formation damages. They occur throughout the drilling and production process [1, 2]. Since 1930s, studies were conducted on the description and experimental analysis [3–7], as well as modeling and simulation of the damage phenomenon [8–16]. It was learned that the most effective method of avoiding formation damage was prevention rather than treatment [5]. Therefore, it was particularly important to forecast potential formation damage in advance that may be caused by operations. Currently, the relevant studies are focused on damage prediction methods especially in China [17–19], while the prediction of damage differences in the same formation is often ignored. The research claimed that the damage of the same block within the same formation is all the same, ignoring the damage differences along lateral direction. For reservoir development, the general well spacing between vertical wells and the directional well lengths is much larger than the reservoir thickness. Therefore, if the differences in damage are ignored in the lateral direction, the drilling operation whose design is based on the data of adjacent wells is more likely to cause damage. Thus, the ordinary Kriging estimation method is used to predict the damage of formation along the lateral direction, according to the information of drilled wells.

2 Methodology

2.1 Principle of Kriging Estimation

Considering the sample shape, size, the spatial distribution of the area to be estimated, and the spatial structure of variables, Kriging estimate [20–24] gives each observation value a certain weight and uses weighted means to interpolate the value at an

S. M. Shemwell and J. Lin (eds.), *Proceedings of the International Petroleum and Petrochemical Technology Conference 2018*,
https://doi.org/10.1007/978-981-13-2173-3_2

unobserved location nearby in order to achieve linear no deviation and minimum variance of unobserved location.

$Z(u)$ is defined as a regionalized variable of point burdening and is second-order smooth. Z_i is the average of the scatter regionalized variable that is defined at point burdening u_i or burden in v_i whose center u_i or v_i is different from V. The linear estimation of $Z_V(u_0) = \int_V Z(u)\mathrm{d}u/V$ which is the average of $V(u_0)$ is

$$Z_V^* = \sum_{i=1}^{n} \lambda_i Z_i \tag{1}$$

where Z_V^* is the regionalized variable estimation at area V, and λ_i is a group of weight coefficient with given discrete regionalized variables defined on point burdening.

The ordinary Kriging estimation [25–29] is an unbiased estimate with minimal variance of Eq. (1) in the condition that $E[Z(u)] = m$ is unknown.

If Z_V^* is the unbiased estimation of Z_V, then

$$E\left[Z_V^* - Z_V\right] = 0 \tag{2}$$

In the assumption of equability

$$E[Z_v] = E\left[Z_V^*\right] = m \tag{3}$$

and

$$E\left[Z_V^*\right] = E\left[\sum_{i=1}^{n} \lambda_i Z_i\right] = \sum_{i=1}^{n} \lambda_i \cdot E[Z_i] = \sum_{i=1}^{n} \lambda_i \cdot m \tag{4}$$

The non-biased condition that Z_V^* is the unbiased estimation of Z_V is

$$\sum_{i=1}^{n} \lambda_i = 1 \tag{5}$$

Based on statistics, the formula of calculating estimate variance σ_E^2 is

$$\sigma_E^2 = \bar{C}(V,V) - 2\bar{C}(V,v_i) + \bar{C}\left(v_i,v_j\right) \tag{6}$$

where $\bar{C}(V,V)$ denotes the covariance average of regionalized variables in block V, $\bar{C}(V,v_i)$ denotes the covariance average of regionalized variables in block V and at observation point v_i, $\bar{C}\left(v_i,v_j\right)$ denotes the covariance average of regionalized variables at observation point v_i and v_j.

For Z_V^* to be the unbiased estimate of Z_v and the demand of variance to be minimum, the optimum estimate of Eq. (1) is translated to calculate the condition extreme value for the purpose of obtaining minimum estimate variance in non-biased condition.

$$\begin{aligned} &\min \quad \sigma_E^2 \\ &s.t. \quad \sum_{i=1}^{n} \lambda_i = 1 \end{aligned} \tag{7}$$

So the ordinary Kriging equation group is

$$\begin{cases} \sum_{j=1}^{n} \lambda_j \bar{C}(v_i, v_j) - \mu = \bar{C}(V, v_i) \\ \sum \lambda_i = 1 \end{cases} \tag{8}$$

μ is the half of Lagrangian multiplier.

Based on the known observational values and Eq. (8), weight coefficients λ_i and μ are calculated. Then, regionalized variable estimation and variance of block V can be calculated using Eqs. (1) and (6).

2.2 Regionalization Character of Formation Damage

The premise of using ordinary Kriging estimates is that the variable to be estimated is regionalized. Regionalized variable refers to $Z(x_u, x_v, x_w) = Z(u)$ whose independent variables are in the rectangular coordinate system (x_u, x_v, x_w). And it is structural and random in the space. It is random before observation, and it is a space point function after observation.

Formation damage is determined by the pore characteristics, rock type, and the content of sensitive ions in the formation water on the condition that the other parameters, such as the performance of drilling and completion fluid, remain unchanged. But the reservoir properties such as the original porosity, the original permeability, rock mineral content, and sensitive ion content of formation water are geological variables. It falls into the category of regionalized variables (Ion content of formation water can be regarded as a special case of regional variables). After a certain point in the reservoir is determined, the parameters can be expressed as a random variable, for example, the random variable of a parameter is $Z_i(u), i = 1, Ln$.

Formation damage is caused by various parameters affecting permeability together in the external condition, so it is a general representation of various parameters affecting permeability. The damage $I(\mu)$ at the position μ of the reservoir can be expressed as a linear function of random variables.

$$I(\mu) = F(Z_1(\mu), LZ_n(\mu)) \quad i = 1, L\, n \tag{9}$$

$I(\mu)$ indicates the degree of reservoir damage and is called reservoir damage index. It can be calculated by core flow test and $I(\mu) = (K_{\text{Initial}} - K_{\text{Recovered}})/K_{\text{Initial}}$.

As is shown in Eq. (9), $I(\mu)$ is a linear combination of $Z_1(\mu), L, Z_n(\mu)$, so $I(\mu)$ is a random variable according to principles of statistics and possesses randomness. When μ is a space variable in Eq. (9), $Z_i(u), i = 1, Ln$ is a function that changes when space point changes, so $I(\mu)$ is a function that changes when space point changes too and is structural. So reservoir damage $I(\mu)$ can be regarded as a regionalized variable in

space, it is random before observation, and it is a function whose independent variable is μ.

The randomness of reservoir damage is due to the uncertainty during the deposition process when the reservoir was created. During the deposition process and later crustal movement, there are different physical, chemical, and biological reactions. The randomness of deposition and anadiagenesis caused the variations in permeability and mineral content. As a result, the damage is random and so is the reservoir damage index. The reservoir damage is structural because of the same depositional environment and later geology movements caused in relation with space of affecting parameters and their determinative damage. Although the damage indexes at the different positions of the same reservoir are different, they are relative and compliance, and the damage fluctuates around a degree.

2.3 Estimating Formation Damage Along Lateral Direction of Formation

We use the rock core at the same formation of different wells in the same reservoir to do damage flow test, measure the gas permeability before and after drilling, completion fluid damage is introduced, and calculate the damage index. Based on ordinary Kriging estimation method and the structural performance and randomness between the known and uncertain parameters, we calculate the damage index. The workflow is shown in Fig. 1.

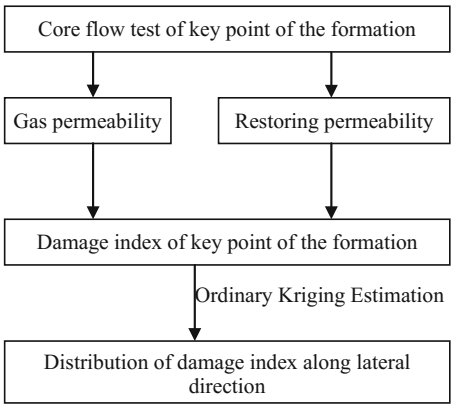

Fig. 1. Damage estimation process along lateral direction of formation

3 Field Application and Analysis

Taking layer Es3 of Shengli Oilfield, for example, we analyze the water sensitivity index of 17 wells. We assume that the differences in the small angle and depth of the 17 wells do not affect the results. The results show that the average water sensitivity index is 0.24, with a standard deviation of 0.06, a bias of −0.175, and a peakedness of −0.751. Figure 2 shows the frequency distribution histogram.

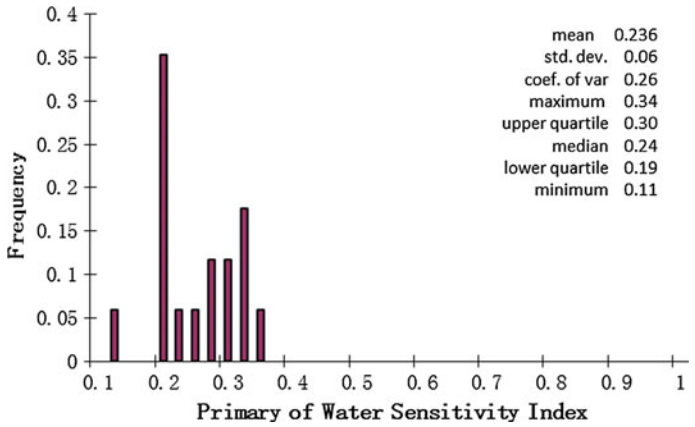

Fig. 2. Histogram of water sensitivity

Figure 2 shows that most of the water sensitivity indexes are between 0.2 and 0.3. Frequency is partial distribution not normal distribution. So before the ordinary Kriging estimation, the normal transformation is required. In addition, there is an outlier near 0.1. This should be a small probability event in real situation.

We obtained the basic parameters of variogram of 17 data points according to the theoretical spherical model, established on a 50 m × 60 m planar grid, with a grid spacing of 10 m. Based on ordinary Kriging estimation, we obtained the estimation of water sensitivity index along bedding surface of reservoir. The results are shown in Fig. 3.

In Fig. 3, black dots represent wells; lines are contours; the warmer color represents greater water sensitivity index; and the colder color represents smaller water sensitivity index. According to Fig. 3, the distribution area is biggest when the water sensitivity index is about 0.2, followed by the water sensitivity index of about 0.3. The distribution area of other values is smaller. The results are consistent with the statistical law of frequency distribution histogram. Predictions are consistent with experimental results.

We use the remaining 16 water sensitivity indexes to crosscheck and calculate the error after removing the water sensitivity index alternatively. The results are shown in Table 1.

Table 1 shows that the error is no more than ±0.08 except for small probability events; the average relative error is 21.25%. The accuracy of estimate is above 75%, so it meets the criterion for the accuracy of prediction in engineering and the method is valid. In addition, the table also shows that the estimated values fluctuate around the average values. The large deviations appear at the position of high value or low value. This also indirectly reflects that the method shows the average trend.

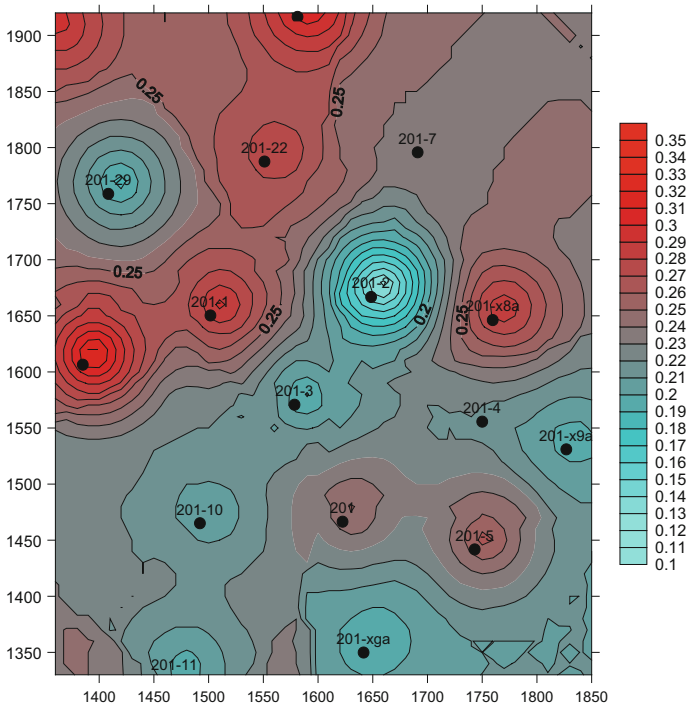

Fig. 3. Isogram of water sensitivity index estimated

Table 1. Result of crosscheck to ordinary Kriging estimation

True value	Predictive value	Error	Relative value%
0.273	0.213	−0.06	22.0
0.189	0.221	0.032	16.9
0.259	0.214	−0.045	17.4
0.189	0.229	0.04	21.2
0.282	0.248	−0.034	12.1
0.322	0.244	−0.078	24.2
0.302	0.243	−0.059	19.5
0.177	0.253	0.076	42.9
0.236	0.234	−0.003	1.3
0.298	0.224	−0.074	24.8
0.108	0.244	0.136	125.9
0.301	0.229	−0.072	23.9
0.341	0.223	−0.118	34.6
0.18	0.246	0.066	36.7
0.216	0.222	0.006	2.8
0.19	0.225	0.035	18.4
0.197	0.223	0.026	13.2

4 Conclusion

(1) The regional characteristics of formation damage show that formation damage is the combination of characteristic parameters and a function in space. It is stochastic and structural, and is a regionalized variable.
(2) Taking the water sensitivity index in Shengli Oilfield as an example, ordinary Kriging estimation is used for estimating formation damage along bedding planes of reservoir and giving the accurate distribution along bedding planes of water sensitivity index. It also shows that the method is valid.
(3) The statistical analysis and ordinary Kriging estimation of water sensitivity index in Shengli Oilfield show that the probability of water sensitivity was the greatest at 0.2 followed by 0.3. The accuracy was over 75%.
(4) Because formation damage is a regionalized variable with randomness and structural features, it is closely related to geological properties. Based on this study, it is recommended that future work should be performed to predict potential damage along lateral formation even for formation space in pre-drilling combined with precision geological model for a reservoir.

Acknowledgements. This research is financially supported by the National Natural Science Foundation of China (No. 51674283).

References

1. Fan SZ, Yan JN, Zhou DC (1996) Drilling fluid & completion fluid and technique of formation damage prevention (in Chinese). University of Petroleum Press, Dongying, pp 409–584
2. Xu TT, Zhao ZJ (2004) Technique of drilling fluid & completion fluid applied in foreign country (in Chinese). Petroleum Industry Press, pp 32–78
3. Ohen HA, Civan F (1993) Simulation of formation damage in petroleum reservoirs. Soc Petrol Eng J 1(1):27–35
4. Chang F, Civan F (1991) Modeling of formation damage due to physical and chemical interactions between fluids and reservoir rocks. In: Proceeding of the 66th annual technical conference and exhibition of the society of petroleum engineers, Dallas, TX, October 1991, pp 6–9
5. Civan F (2003) Reservoir formation damage—fundamentals, modeling, assessment and mitigation. Petroleum Industry Press, pp 131–422
6. Khilar KC, Fogler HS (1983) Water sensitivity of sandstones. Soc Pet Eng J 55–64
7. Civan F (1994) A multi-phase mud filtrate invasion and well bore filter cake formation model. In: Proceeding of international petroleum conference & exhibition of Mexico, Veracruz, Mexico, October 1994, pp 10–13
8. Liu XH, Civan F (1995) Formation damage by fines migration including effects of filter cake, pore compressibility, and non-darcy flow—a modeling approach to scaling from core to field. In: Proceeding of international symposium on oilfield chemistry, San Antonio, TX, February 1995, pp 14–17
9. Civan F (1996) A multi-purpose formation damage model. In: Proceeding of formation damage control symposium, Lafayette, Louisiana, February 1996, pp 14–15

10. Civan F (1996) Convenient formulations for immiscible displacement in porous media. In: Proceeding of the 1996 SPE annual technical conference and exhibition, Denver, Colorado, October 1996, pp 6–9
11. Schneider GW (1997) A geochemical model of the solution-mineral equilibria within a sandstone reservoir. M.S Thesis, The University of Oklahoma
12. Mansoori GA (1997) Modeling of asphaltene and other heavy organic depositions. J Petrol Sci Eng 17:101–111
13. Leontaritis KJ. Asphaltene near-wellbore formation damage modeling. In: Proceeding of the 1998 SPE formation damage control conference, Lafayette, Louisiana, February 1998, pp 18–19
14. Ali MA, Islam MR (1998) The effect of asphaltene precipitation on carbonate-rock permeability: an experimental and numerical approach. SPE Prod Facil J 178–183
15. Wang SJ, Civan F, Strycker AR (1999) Simulation of paraffin and asphaltene deposition in porous media. In: Proceeding of the 1999 SPE international symposium on oilfield chemistry, Houston, Texas, February 1999, pp 16–19
16. Kalam MZ, Al-Alawi SM, Al-Mukheini M (1996) Assessment of formation damage using artificial neural networks. In: Proceeding of the 1996 SPE formation damage control symposium, Lafayette, Louisiana, February 1996, pp 14–15
17. Zhang R, Wang RH, Qiu ZS (2005) Exploring research on conceptual models of formation damage. Prog Geophys (in Chinese) 20(2):308–313
18. Zhang R, Wang RH, Yu SH (2009) Prediction method of formation potential damage in pre-drilling based on geological statistics. Chin J Geophys (in Chinese) 52(6):1657–1662
19. Dong SL (2001) Technique study and intellectual method for drilling fluid programming (in Chinese). Ph.D. dissertation, University of Petroleum
20. Deutsch CV, Journel AG (1992) GSllB: geostatistical software library and user's guide. Oxford University Press
21. He KT, Gu HL (interpret), Xia LX (Check) (1997) Estimation technique and conditional simulation of geostatistics. World Geol (in Chin) 16(3):83–100
22. Hou JR (1998) The practical geostatistics (in Chinese). Geological Publishing House
23. Peng XJ, Wang K, Li Q (2014) A new power mapping method based on ordinary kriging and determination of optimal detector location strategy. Ann Nucl Energy 68:118–123
24. Ali-Akbar D (2012) Reserve estimation of central part of Choghart north anomaly iron ore deposit through ordinary kriging method. Int J Min Sci Technol 22(4):573–577
25. Pesquer L, Cortés A, Pons X (2011) Parallel ordinary kriging interpolation incorporating automatic variogram fitting. Comput Geosci 37(4):464–473
26. Dai FQ, Zhou QG, Lv ZQ, Wang XM, Liu GC (2014) Spatial prediction of soil organic matter content integrating artificial neural network and ordinary kriging in Tibetan Plateau. Ecol Ind 45:184–194
27. Wackernagel H (2003) Multivariate Geostatistics, 3rd edn. Springer-Verlag Berlin Heidelberg, pp 416–429
28. Davis JC (2002) Statistics and data analysis in geology, 3rd edn. Wiley, pp 57–61
29. Su Z, Lin AW, Liu QH (1999) Ordinary kriging algorithm applied for interpolation. J South Yangtze Univ (Natural Science Edition) (in Chinese) 11(6) 525–529

Development and Evaluation of Ne: A Microemulsion Lubricant for Drilling Fluids

Bingqiang Dong[1,2], Ye Zhang[1,2], Zhengsong Qiu[3], Zhaohui Lu[1,2(✉)], Junyi Liu[4], Linhua Pan[1,2], and Pei He[1,2]

[1] Key Laboratory of Shale Gas Exploration, Ministry of Land and Resources Chongqing Institute of Geology and Mineral Resources, Chongqing, China
dbqsl23@163.com
[2] Chongqing Engineering Research Center for Shale Gas Resource & Exploration, Chongqing Institute of Geology and Mineral Resources, Chongqing, China
[3] College of Petroleum Engineering, China University of Petroleum (East China), Qingdao, China
[4] Drilling Technology Research Institute of Sinopec Shengli Oilfield Service Corporation, Dongying, China

1 Introduction

Higher requirements have been exerted on the lubricating property of drilling fluids in the past few years, with the continual technical development of the directional well, highly deviated well, and extended-reach horizontal well [1–4]. Much progress has been made in developing more amounts and types of drilling fluid lubricants [5–8]. The liquid drilling fluid lubricant is at present the most widely used lubricant, mainly including the mineral oil, vegetable oil, surfactant, bitumen, etc. [9, 10]. It lubricates the borehole wall and the drilling tool by forming lubricating films on the rock or drilling tool surfaces through adsorption [11, 12]. However, all of the currently available liquid lubricants for drilling fluids suffer from low thermal stability, high complexity in preparation, proneness to foaming, and high fluorescence grade [13–15]. Moreover, as the horizontal wellbore section of the horizontal well continuously extends, the current liquid lubricant mostly fails to sufficiently meet the practical application requirement of drilling fluids used in the field. This paper, on the basis of the latest progress in research on liquid lubricants, developed a microemulsion lubricant referred to as NE, with the help of the small-size effect and surface effect of nanoparticles [16–18].

S. M. Shemwell and J. Lin (eds.), *Proceedings of the International Petroleum and Petrochemical Technology Conference 2018*,
https://doi.org/10.1007/978-981-13-2173-3_3

2 Preparation and Basic Characteristics of Microemulsion Lubricant NE

2.1 Preparation of Microemulsion Lubricant NE

1. Raw materials: Chemically pure Span 80 and Tween 80 as well as analytically pure n-butyl alcohol, manufactured by the Sinopharm Chemical Reagent Co., Ltd; Industrial-grade liquid paraffin (No. 5 white oil), made by the Zhengzhou Ruibo Chemical Engineering Co., Ltd; Industrial Gemini Quaternary ammonium compound-based (QAC) surfactant GTN, from the Henan Titaning Chemical Technology Co., Ltd.
2. Preparation: The mixture of Span 80 and Tween 80 was used as the primary surfactant (with hydrophilic–lipophilic balance of about 10.5), and n-butyl alcohol, as the secondary surfactant. The Gemini QAC surfactant GTN served as the electrical regulator of the emulsion, and the liquid paraffin (No. 5 white oil) as the oil phase in this research. 20–30% primary surfactant, 5–10% secondary surfactant, 30–40% oil phase, and 1–2% emulsion electrical regulator were successively put into water and stirred thoroughly. The resultant faint yellow mixture was the water-in-oil (W/O) microemulsion high-efficiency lubricant, NE, as is shown in Fig. 1.

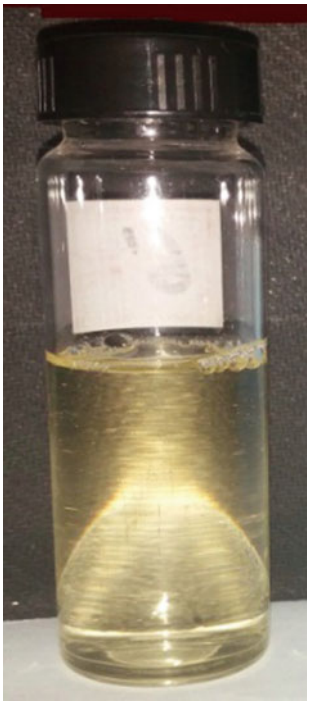

Fig. 1. High-efficiency microemulsion lubricant NE

2.2 Basic Characteristics of Microemulsion Lubricant

Massive nanodroplets were created from the diluted lubricant NE in the drilling fluid, which lubricated the borehole wall and the drilling tool through adsorption on the clay particle or the drilling tool surface with the help of the electrostatic effect. Hence, the particle size of the created nanodroplet from the diluted lubricant NE as well as the particle electric property was the key to the high-efficiency lubrication of the drilling fluid. The average size and zeta potential of droplets created by the microemulsion lubricant NE diluted in water at various concentrations were measured at 25 °C, using the Malvern Zetasizer Nano ZS90. Results are shown in Fig. 2 and Table 1. It was demonstrated that with the increasing concentration of the microemulsion lubricant NE, the average size of the created droplet grew, while the measured zeta potential, which was always positive and gradually increased. As the W/O micriemulsion was mixed with water, the hydrophilicity of the surfactant boundary layer at the oil–water interface sharply intensified, due to the significant growth of the water content. Under such circumstances, the dispersed liquid paraffin in the microemulsion rapidly nucleated and evolved into O/W nanodroplets with expanded sizes. Moreover, larger nanodroplets generally corresponded to more adsorbed electrical regulator GTN and higher electropositivity.

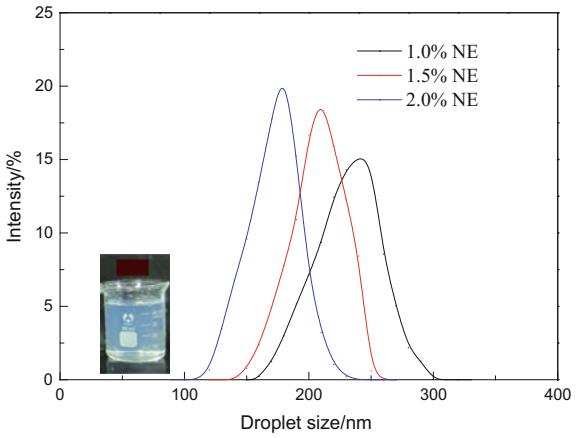

Fig. 2. Size distribution of nanoparaffin particles created in differentially diluted microemulsion

Table 1. Particle size and zeta potential measurement of the nanoemulsion lubricant

Specimen	Average particle size/nm	Zeta potential/mV
0.5% NE	187	34.3
1.0% NE	224	37.9
2.0% NE	258	44.0

3 Performance Evaluation of the Microemulsion Lubricant NE

3.1 Lubrication Performance

With reference to Petroleum and Natural Gas Industry Standard SY/T 6094-94, this study evaluated the effects of the lubricant NE with different concentrations on the coefficient of friction (K_f) and mud cake adhesion factor (F) of the drilling fluid containing 5% of bentonite (400 mL of water + 20 g of bentonite + 0.8 g of Na_2CO_3, denote as BDF) so as to assess the lubrication performance of the lubricant NE. The mud cake adhesion factor was measured at the room temperature and under the pressure of 3.5 MPa. Experimental results are displayed in Table 2.

Table 2. Evaluation of the lubrication performance of the lubricant NE

Volumetric fraction of NE (%)	K_f	ΔK_f/% (%)	F	ΔF/% (%)
0	0.44	–	0.16	–
1.0	0.15	65.8	0.063	60.4
1.5	0.11	74.3	0.052	69.2
2.0	0.072	83.8	0.041	74.2
2.5	0.070	84.2	0.038	76.1

Table 2 indicates the excellent lubrication performance of the bentonite drilling fluid with the presence of the lubricant NE. With the increasing concentration of the lubricant NE, both the coefficient of friction and the factor of mud cake adhesion significantly declined. In the case with the lubricant concentration of 2.0%, the coefficient of friction dropped by 83.8% and the mud cake adhesion factor by 74.2%.

3.2 Thermal Stability

Test samples used in this study included bentonite, inorganic salt, polysulfonate, and polymer drilling fluids. Lubrication performances of different drilling fluids before and after being aged at 120 °C for 16, 32, and 48 h were experimentally assessed in order to investigate the thermal stability of the lubricant NE. Experiment results are presented in Table 3, which indicate rare changes of both the coefficient of friction and the factor of mud cake adhesion varied types of drilling fluids, and thus suggest good thermal stability of lubricant NE.

Drilling fluid compositions: (1) Inorganic drilling fluid (IDF): 2.0% bentonite + 3.0% SMP-II + 2.5% SPNH + 2.0% sulfonated bitumen + 0.30% PF-XC + 5.0% KCl + 15.0% NaCl + 3.0% ultrafine calcium; (2) Polysulfonate drilling fluid (PFDF): 4.0% bentonite + 0.15% NaOH + 0.35% K-PAM + 0.2% DBF-2 + 5% SMP-2 + 3.0% SPNH + 2.5% GLA; (3) Polymer drilling fluid (PMDF): 4.0% bentonite + 0.15% NaOH + 2% ultrahib + 0.3% ultracap + 2.0% PF-PAC + 0.3% XC + 5.0% ultrafine calcium carbonate.

Table 3. Evaluation of thermal stability of the lubricant NE

Drilling fluid	Aging duration/h	K_f	F
Bentonite drilling fluid + 2% NE	16	0.072	0.041
	32	0.071	0.041
	48	0.076	0.043
Inorganic drilling fluid + 2% NE	16	0.091	0.054
	32	0.093	0.055
	48	0.092	0.054
Polysulfonate drilling fluid + 2% NE	16	0.074	0.044
	32	0.078	0.046
	48	0.076	0.045
Polymer drilling fluid + 2% NE	16	0.087	0.056
	32	0.088	0.056
	48	0.092	0.057

3.3 Anti-high Temperature

The lubrication effect of the conventional lubricant could be compromised by the degradation induced by the high temperature, and thus fails to meet the drilling requirement [13]. The variations of coefficients of friction of the four drilling fluids mentioned above with the addition of 2.0% of the lubricant NE were measured after 16 h hot rolling at 120, 140, and 160 °C (Fig. 3).

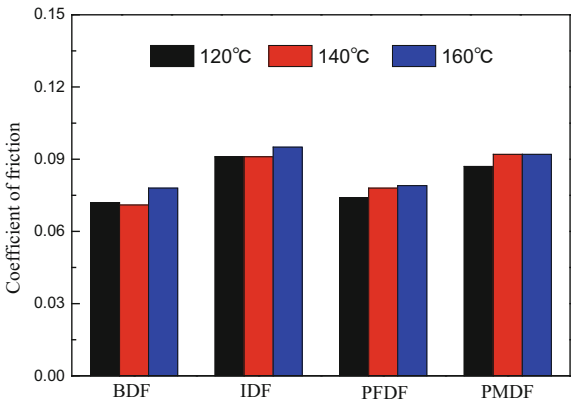

Fig. 3. Anti-high temperature measurement of the lubricant NE

It is illustrated that coefficients of friction of the four types of drilling fluids with the addition of 2% of the lubricant NE after being aged at varied temperatures (respectively, 120, 140, and 160 °C) barely changed. Moreover, the coefficients of friction were small in all cases. Hence, it is safe to say that the lubricant NE is of excellent anti-high temperature.

3.4 Foaming Ratio

Conventional lubricants are relatively vulnerable to drilling fluid density reduction due to the foaming effect, which impacts the drilling fluid column pressure and can even lead to well control risks [19]. On the basis of the laboratory experiment, the volume and density variations of the bentonite drilling fluids with the lubricant NE at different concentrations after 8000 rpm stirring were measured so as to determine the foaming capacity of the lubricant NE. Measurement results are presented in Table 4.

Table 4. Foaming capacity of the lubricant NE

Drilling fluid	NE/%	Density ρ/(g/cm^3)		Change Percentage/%	Volume V/mL		Foaming ratio/%
		Before high-RPM stirring	After high-RPM stirring		Before high-RPM stirring	After high-RPM stirring	
Bentonite	0.0	1.028	1.027	0.1	400	400	0.0
	1.0	1.028	1.007	2.0	400	408	2.0
	2.0	1.027	0.9814	4.4	400	419	2.2
	3.0	1.027	0.9791	4.7	400	427	4.9

Table 4 shows that with the increasing addition of the lubricant NE resulted in very small variations of the bentonite drilling fluid density and volume after high-RPM stirring. In the case with the NE dosage of 3.0%, the density of the bentonite drilling fluid dropped by 0.0479 g/cm^3, and the corresponding foaming ratio was 4.9%, far less than the value prescribed in the enterprise standard *Q/SY 1088-2012 Specifications of Liquid Lubricants Used in Drilling Fluids* proposed by the China National Petroleum Corporation (CNPC) (density variation $\leq \pm 0.08$ g/cm^3). Therefore, it can be concluded that the effect of the lubricant NE on the foaming capacity of the drilling fluid is relatively slight, which fulfills the field application requirement of the drilling engineering.

3.5 Fluorescence Grade

The drilling fluid used in exploration wells should have lower fluorescence intensity, in order not to disturb the result of fluorescence analysis in cutting logging [14]. Consequently, the lubricant also should have a lower fluorescence grade. In terms of the fluorescence grade determination method of CNPC's enterprise standard *Q/SY 1088-2012 Specifications of Liquid Lubricants Used in Drilling Fluids*, the fluorescence grade of the lubricant NE was determined through comparison with the standard chromatic series based on the crude oil from the Dagang Oilfield. Results showed that the lubricant NE had Grade-2 fluorescence and met the requirement for geological fluorescence logging in exploration wells.

3.6 Compatibility with Drilling Fluids

The compatibility of the microemulsion lubricant NE with varied drilling fluids was investigated by measuring the rheological property, fluid loss performance, yield point, and lubrication performance of the four types of drilling fluids mentioned above before and after the addition of 2.0% NE. Experimental results are presented in Table 5.

Table 5. Compatibility of the lubricant NE with various drilling fluids

Drilling fluid	NE/ %	Experimental condition	AV/ (mPa·s)	PV/ (mPa·s)	YP/Pa	F_{API}/ mL	F_{HTHP}/ mL	K_f
Bentonite	0.0	Pre-aging	6.5	4	2.5	32	–	
		Post-aging	6	5	1	37	38.5	0.42
	2.0	Pre-aging	8	5	3	30	–	
		Post-aging	6.5	6	0.5	24	22	0.071
Inorganic salt	0.0	Pre-aging	45	35	10	1.4	–	–
		Post-aging	41	32	10	1.6	8.9	0.23
	2.0	Pre-aging	45.5	35	10.5	1.2	–	–
		Post-aging	40	32	8	1.4	8.2	0.091
Polysulfonate	0.0	Pre-aging	30.5	26	4.5	3.2	–	–
		Post-aging	29.5	24	5.5	3	15	0.19
	2.0	Pre-aging	31.5	27	4.5	3.0	–	–
		Post-aging	30	25	5	2.8	13.6	0.074
Polymer	0.0	Pre-aging	45	31	14	3.8	–	–
		Post-aging	39.5	27	12.5	3.2	12.8	0.23
	2.0	Pre-aging	46	31	15	3.4	–	–
		Post-aging	39	28	11	2.8	10.2	0.088

On the basis of Table 5, it is safe to draw the conclusion that the lubricant NE is well compatible with various drilling fluids. The pre- and post-aging drilling fluids with 2.0% of the lubricant NE, compared with the drilling fluid without the lubricant, show considerable reduction in the coefficient of friction (K_f), with slight variations observed in the apparent viscosity (AV), plastic viscosity (PV), and yield point (YP). This suggests that the lubricant NE has rare effects on the rheology of the drilling fluid. In addition, the medium-pressure filter loss as well as the high-temperature high-pressure filter loss of each type of drilling fluids declines with different.

Aging conditions, 120 °C and 16 h magnitudes, indicate the capacity of lubricant NE to effectively improve the mud cake quality and enhance the plugging ability of the drilling fluid.

4 Conclusions

(1) With the raw materials of the liquid paraffin, Span 80, Tween 80, and the Gemini quaternary ammonium compound-based surfactant GTN, this study developed a microemulsion lubricant NE through mixing and stirring. This lubricant produced positively charged nanodroplets with an average size of 187–258 nm.
(2) The invented lubricant NE was demonstrated to have good lubrication performance, strong thermal stability, and favorable anti-high temperature. Addition of 2.0% NE could decrease the coefficient of friction of the bentonite drilling fluid over 80%, and the mud cake adhesion factor over 70%. At 8000 RPM, the lubricant presented a foaming ratio of 2.2%, and it had Grade-2 fluorescence. Moreover, the proposed lubricant was verified to be remarkably compatible with various drilling fluids.

Acknowledgements. This work is supported by the National Natural Science Foundation of China (Project Nos. 51604050, 51474236, and U1562101), "Science and Technology Innovation Leading Talent Support Program of Chongqing City" (No. CSTCCXLJRC201712), and Basic Science and Cutting-Edge Technology Research (key projects) of Chongqing City (No. CSTC2017JCYJBX0076).

References

1. Meng M, Qiu Z (2018) Experiment study of mechanical properties and microstructures of bituminous coals influenced by supercritical carbon dioxide. Fuel 219:223–238
2. Meng M, Qiu Z, Liu J et al (2016) Study progress of coalbed methane development technology withs supercritical CO2 injection. Coal Sci Technol 44(1):187–195
3. Han C, Qiu Z, Meng M et al (2015) The experimental research of the surface abrasion of steel N80 through different weight material. Science Technology and Engineering 15(3):61–65
4. Huang W, Jia J, Li S et al (2015) Development of low molecular polymer (KGDP) with high-temperature resistance and its application in drilling fluid for deep wells. Journal of Southwest Petroleum University (Science and Technology Edition) 30(3):72–76
5. Lescure J, Teng J, Degouy D et al (2013) Development and field trial of a non-aqueousbased mud lubricant. In: SPE Offshore Europe oil and gas conference and exhibition. Society of Petroleum Engineers
6. Liu J, Liu X, Wang B (2016) Performance of low fluorescence and high efficiency extremepressure lubricant BDLU-100L for drilling fluid. Oilfield Chem 33(2):200–203
7. Wang W, Qiu Z, Zhong H et al (2016) Preparation and properties of nanoparticle-based lubricant SD-NR for drilling fluids. Fault-Block Oil Gas Field 1:113–116
8. Atabani AE, Silitonga AS, Ong HC et al (2013) Non-edible vegetable oils: a critical evaluation of oil extraction, fatty acid compositions, biodiesel production, characteristics, engine performance and emissions production. Renew Sustain Energy Rev 18:211–245
9. Skalle P, Backe KR, Lyomov SK et al (1999) Microbeads as lubricant in drilling muds using a modified lubricity tester. In: SPE annual technical conference and exhibition. Society of Petroleum Engineers

10. Qi Y, Lv Z, Yan B et al (2015) Study and application of new vegetable lubricant used in drilling fluid. Drilling Fluid Completion Fluid 32(3):39–41
11. Wang Z, Li R, Zhu K et al (2016) The development and field application of JZLU-1 highefficiency lubricants. Petrol Drilling Tech 5:79–83
12. Jin J (2017) Research advances of the lubricants for drilling fluid. Appl Chem Industry 46(4):770–774
13. Mousavi P, Wang D, Grant CS et al (2005) Measuring thermal degradation of a polyol ester lubricant in liquid phase. Ind Eng Chem Res 44(15):5455–5464
14. Liu A (2003) Understanding and pondering over fluorescence problem of drilling fluid additives. Drilling Fluid Completion Fluid 20(2):9–12
15. Lu Y (2017) Preparation and performance evaluation of environmentally friendly efficient lubricant NH-HPL for drilling. J Xi'an Shiyou University (Nat Sci Edition) 32(5):85–89
16. Qiu Z, Dong B, Zhong H et al (2015) Preparation of oil-in-water nanoemulsions used for protection of shale gas reservoirs. J. CIESC 66(11):4565–4571
17. Dong B, Qiu Z, Wang W et al (2015) Preparation and performance of novel reservoir protection agent SDME-2 used for shale gas reservoirs. Journal of Petrochemical Universities 28(6):61–65
18. Wang W, Qiu Z, Zhong H et al (2015) Preparation and properties of thermosensitive poly (NIPAm-co-AA)/nano-SiO_2 composite blocking agent for shale gas reservoir. Acta Petrolei Sinica 36(3):378–384
19. Lv X, Yan J, Yue X (2005) Preparation of silicone defoaming agent. Fine Chem 22(9):688–690

Flow Characteristics of Two Temperature-Tolerant and Salt-Resistant Polymers in Porous Media

Fulin Yang(✉)

College of Petroleum and Chemical Engineering, Qinzhou University, 535011 Qinzhou, People's Republic of China
fulinyang@sina.com

1 Introduction

Following primary and secondary recovery processes, at least half of the original oil in place is still trapped in reservoirs [1]. Numerous technologies of enhanced oil recovery (EOR) have been proposed and studied in the past decades [2–4]. Among these EOR technologies, polymer flooding is one of the several large-scale industrial applications. Partially hydrolyzed polyacrylamide (HPAM) and Xanthan gum, which is a biologically produced polysaccharide, are the most widely used polymers to date in polymer flooding process. The performance of two kinds of polymers in EOR is significantly affected by harsh reservoir conditions such as high temperature and salinity. Xanthan gum is the good tolerance to salinity and mechanical shear, but susceptible to high temperature [5, 6]. To obviate the limitations, numerous studies are focused on a series of the modified HPAM polymers including comb copolymer, sulfonated polyacrylamide (S-HPAM), and hydrophobic associating polyacrylamide (A-HPAM) [7–10]. Because of the availability in large quantity and low manufacturing cost, the comb copolymer now is widely used in many mature oilfields such as Shengli, Daqing, and Huabei in China [11]. And several small-scale pilots of A-HPAM flooding were reported [12, 13]. However, some arguments are still focusing on A-HPAM molecular forming effective viscosity in limited porous space, especially low and ultralow permeability reservoirs. In recent years, extensive studies on S-HPAM are implemented and several pilots with good increased oil recovery effect are reported in oilfields such as Shengli and Henan [14, 15].

Numerous studies were carried out on the flow behavior of EOR polymers in porous media [16–20], which is closely associated with their solution properties. Wang explored the mechanism of polymer flooding by micro-seepage experiment [21] finding that polymer solution is able to mitigate viscous fingers. Recent polymer flooding experiments [22–26] showed that may improve micro-displacement efficiency at different extents. In the literature, no detailed studies have been reported on the flow characteristics of the comb copolymer and S-HPAM in porous media. Therefore, this work selected the two types of temperature-tolerant and salt-resistant polymers, and carried out studies on the rheological properties, flow characteristics, and EOR performance. The objective of this study is attempting to relate the bulk solution properties

S. M. Shemwell and J. Lin (eds.), *Proceedings of the International Petroleum and Petrochemical Technology Conference 2018*,
https://doi.org/10.1007/978-981-13-2173-3_4

to the flow behavior in porous media. The study also provides a theoretical reference for the choice and development of polymer flooding of high-temperature and high salt reservoir.

2 Experimental

2.1 Materials

S-HPAM polymer and the comb polymer (KYPAM6210) were provided by Beijing Research Institute of Chemical Industry (BRICI) and Jiangsu Oilfield Company of SINOPEC, respectively. The basic properties of two polymers are listed in Table 1. In laboratory of BRICI, the S-HPAM (Fig. 1) with micro-branched structure was synthesized by solution polymerization of acrylamide (AM), 2-acrylamide-2-methylpropanesulfonic acid (AMPS) with ammonium persulfate (APS)/*N, and N*-dimethylaminoethyl methacrylate (DEMAEMA) as initiating system.

Table 1. Properties of the evaluated polymer systems

Name	Molecular weight (10^6g/mol)	Hydrolysis (%)	Shear viscosity (mpa.s)	Solid content (%)	Filtration factor
S-HPAM	1020	21.6	7.8	88.0	0.99
KYPAM6210	980	22.6	5.1	89.5	1.06

Remarks the viscometer rotate speed of 6r/min, 0# rotor, test temperature of 78 °C, polymer concentration of 1000 mg/L, and formation brine

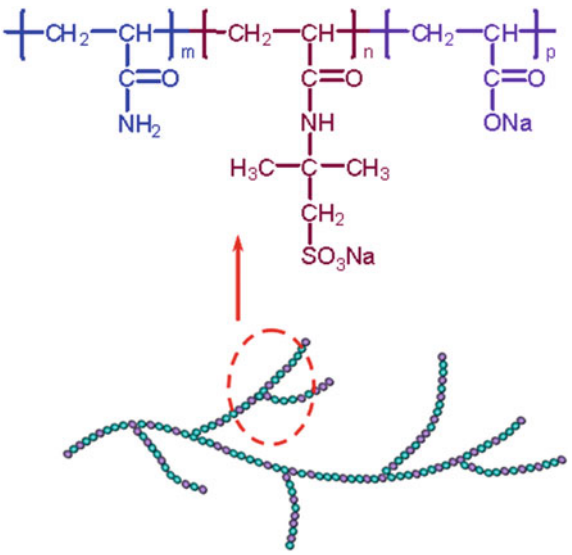

Fig. 1. Molecular structures of S-HPAM-1 used in this study

The two synthetic brines were prepared with the inorganic salt of NaCl, $CaCl_2$, $MgCl_2$, $NaHCO_3$, and Na_2SO_4 in laboratory. The ionic concentrations of the salts are listed in Table 2. The total salinity is the sum of the ionic concentrations. All chemicals were of analytical grade and were used as received without further purification. Distilled water was used in all experiments.

Table 2. Composition of the synthetic brine

Brine name	Ionic concentration/(mg/L)						Total salinity/(mg/L)
	K^++Na^+	Ca^{2+}	Mg^{2+}	Cl^-	SO_4^{2-}	HCO_3^-	
Formation brine	6274	46	21	8083	556	1820	16,800
Injection brine	131	36	34	59	41	475	776

2.2 Rheology

The polymers were dissolved under gentle stirring till complete hydration, and then left to stand for 1 day prior to test. All rheological measurements were carried out using a rotary viscometer Haake RS6000 with concentric cylinder at 78 °C. Dynamical measurements were performed with the viscometer at 78 °C to determine the elastic(G') and viscous(G'') moduli of polymer solutions as a function of frequency ranging from 0.01 to 10 Hz under stress of 0.02 Pa.

2.3 Flow Behavior of Polymer Solution in Porous Media

The polymer solution was injected through approximate $130 \times 10^{-3}\mu m^2$ artificial cores (10×2.5 cm) until the differential pressure between the inlet and outlet (ΔP) leveled off. Afterward, the synthetic formation brine was resumed until ΔP values held constant. The expressions of the resistance coefficient (RF) and residual resistance coefficient (RRF) are given in Eqs. (1) and (2)[6].

$$RF = \frac{\Delta P_{polymer}}{\Delta P_{brine}} \tag{1}$$

$$RRF = \frac{\Delta P_{brine\ after\ polymer\ injection}}{\Delta P_{brine\ before\ polymer\ injection}} \tag{2}$$

2.4 Core Food Test

An HA-II system for displacing hydrocarbons from a core operates at high temperature and pressure (Jiangsu Hua An Co., Ltd). The experiments were carried out on artificial cores reproducing the petrology properties of the formation. The core was evacuated from two to three hours, and then saturated by several pore volumes (PVs) of synthetic formation brine injection. The average permeability to brine can be calculated using Darcy's Law. We used crude oil obtained from the Jiangsu Oilfield. The oil sample was

filtered through 0.045 mm stainless steel mesh, and then the oil was dehydrated to residual water content below 0.5%. The viscosity of the degassed oil at a temperature of 78 °C was 6.2 mPa s. Under the reservoir temperature, the core was saturated with the oil sample until the water cut of the outlet is less than 2%, and aged for 1 day. And then the core was flooded by synthetic injection brine until the water cut of the outlet is higher than 98%. Finally, the injection of 0.43 PVs (slug size) of KYPAM62210 or S-HPAM solution with similar apparent viscosity and a subsequence waterflooding (injection brine) were followed. All the fluids were injection at 0.31 mL/min.

3 Results and Discussion

3.1 Rheological Behavior of Polymer Solutions

Steady Rheological Behaviors

In polymer flooding process, the viscous behavior of polymer solution can prevent viscous fingering. Thus, it is necessary to study the viscous behavior of polymer solution before core flooding test. The comparative steady-shear rheological results of the two types of polymer solutions at 78 °C are presented in Fig. 2. It is clear that with the increase in the shear rate, the viscosity of both two polymer solutions gradually decreases and the characteristics of pseudoplastic fluid are presented. Within the whole shear rate range examined, the viscosity of S-HPAM solution is always higher than that of the KYPAM6210 solution. These rheological observations can be generally attributed to the conformational status of polymer systems. The molecules of S-HPAM and KYPAM6210 tend to orderly associate through the weak hydrogen bonding and chain entanglement, which therefore results in a high viscosity at low shear rate. However, at high shear rate, the formed associations would be easily broken, which led to an obvious shear-thinning trend.

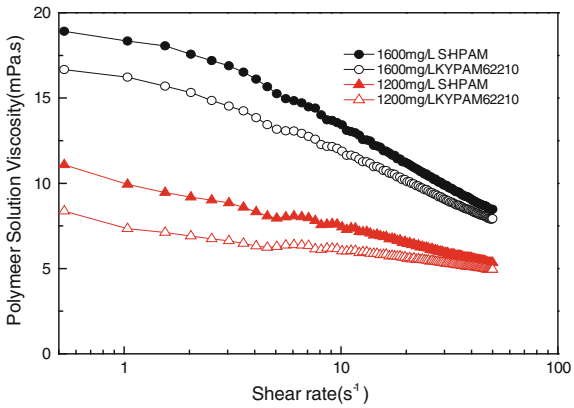

Fig. 2. Steady-shear viscosity of polymer solutions versus shear rate. Test conditions: 78 °C, salinity 16,800 mg/L

Environmental scanning electron microscope (ESEM) is an effective technology for reflecting the microstructure of polymer chains in solution, especially S-HPAM and KYPAM6210. In Fig. 3, two typical micromorphologies of S-HPAM and KYPAM6210 sample solutions are displayed. Among these images, it can be seen clearly that compared with KYPAM6210, and more compact and much denser networks could be found in S-HPAM, which could be the proof of high viscosity of S-HPAM.

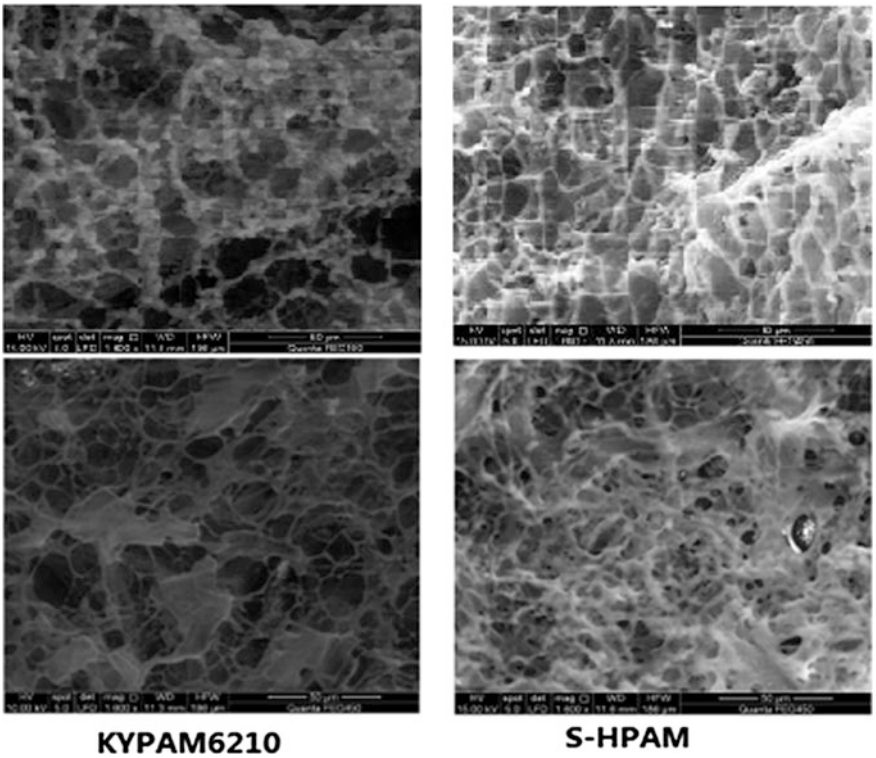

Fig. 3. The SEM images of two polymer solutions at 50 μm, 1600 × Test conditions: concentration 1200 mg/L, salinity 16,800 mg/L

Figure 4 plots the viscosity of the S-HPAM and KYPAM6210 solutions as a function of age time. As the age time increases from 0 to 90 days, it is clearly found that the viscosities of the S-HPAM and KYPAM6210 solutions are initially on the rise and then decrease. The increase in the viscosity of polymer solutions could be explained by polymer hydrolysis. And the decrease in the viscosity of polymer solutions is mainly attributed to the degradation of polymer molecule. Compared with KYPAM6210, it is found that the antiaging property of S-HPAM is more excellent than KYPAM6210. The experimental results showed that the viscosity of S-HPAM increased from 16.3 to 18.3 mPa s and the viscosity retention rate is 112.3%, while KYPAM6210 declined from 16.2 to 12.9 mPa s and the viscosity retention rate is 79.6%. This result is quite attractive. Such a comparison clearly shows that the antiaging property of S-HPAM is

more excellent than that of KYPAM, which is favorable for keeping a long-term high viscosity of the polymer solution in reservoir with high temperature and salinity, thus improving sweep efficiency and mobility control.

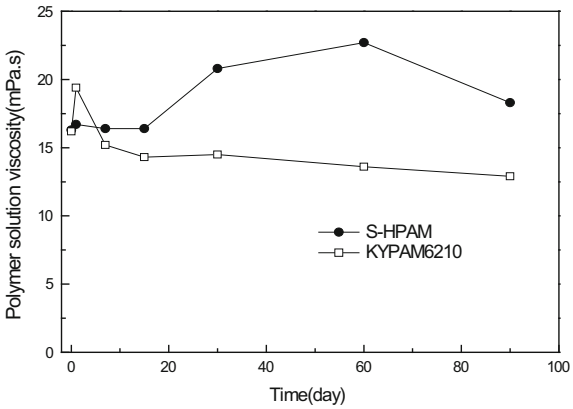

Fig. 4. Apparent viscosity of polymer solutions versus aging time: Test conditions: 78 °C, concentration 1600 mg/L, salinity 16,800 mg/L

To gain insight into the mechanism behind the behaviors of antiaging property, IR spectrometry was employed to demonstrate difference between the S-HPAM and KYPAM6210 molecular structures. Figure 5 shows the IR images of the S-HPAM and KYPAM6210. From the curve of S-HPAM, the bands observed at 1195.64, 1045.79 and 1657.25 cm^{-1} were attributed to the stretching vibration peaks of sulfonic groups (S = O and S–O) and carboxyl group(C = O). And then from the curve of KYPAM6210, the bands observed at 1199.31, 1031.52, and 1655.90 cm^{-1} were attributed to the stretching vibration peaks of ether groups (C–O–C) and carboxyl group(C = O). It can be verified that S-HPAM and KYPAM6210 molecular structures have sulfonic groups and ether groups, respectively. Therefore, the behaviors of anti-aging property can probably be explained by the difference between S and HPAM and KYPAM6210, in which the hydrolysis resistance of polymer enhanced by sulfonic group is higher than that of ether group.

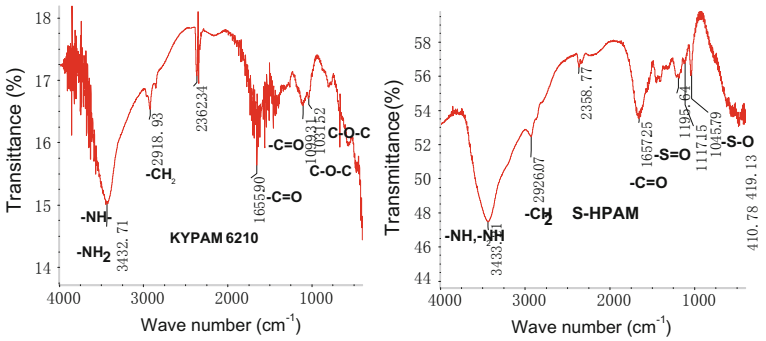

Fig. 5. IR images of S-HPAM and KYPAM6210

Dynamic Viscoelastic Behaviors

In recent years, more and more people believe that the elasticity of polymer solutions may improve micro-displacement efficiency. Figure 6 shows the elastic (G') and viscous (G'') moduli of polymer solutions versus angular frequency. It is found that the magnitudes of G' and G'' increase with frequency, suggesting the strong dependency of the viscoelasticity on frequency. In other words, the G' and G'' of S-HPAM and KYPAM6210 are closely related to the imposed angular frequency. Within the shear rate range examined, the intersection point of the elastic (G') and viscous (G'') modulus of S-HPAM is lower than that of KYPAM6210, indicating that the elasticity of S-HPAM is higher than that of KYPAM6210 resulting from the stretching of polymer chains under the dynamical shear field.

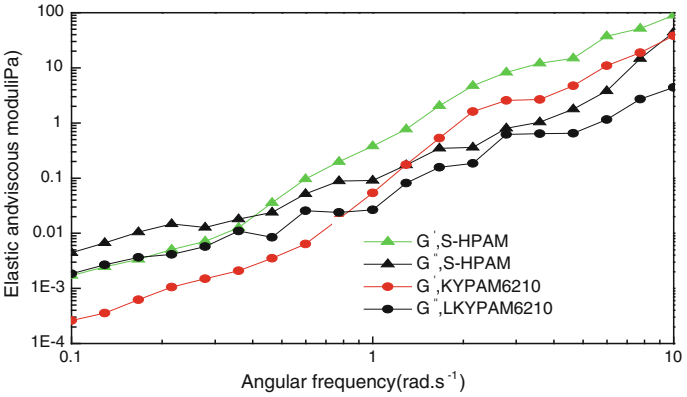

Fig. 6. Dynamic rheological curves of polymer solutions: Test conditions: 78 °C, concentration 800 mg/L, salinity 16,800 mg/L

3.2 Flow in Porous Media

Figure 7 shows the injection pressure response versus PVs for various concentrations of S-HPAM and KYPAN6210 polymer solutions flowing through approximate $130 \times 10^{-3}\mu m^2$ cores (10×2.5 cm). The injection pressure responses of the two polymer solution show a similar trend, i.e., the injection pressure gradient increased gently with the pore volume of injected polymer solution and then reached a steady stage after a peak value. Apparently, S-HPAM produced the higher value of injection pressure gradient followed by KYPAM6210. Table 3 lists the RF and RRF values. It can be also seen that S-HPAM produced the higher values of RF and RRF. In other words, thickness of the adsorbed polymer layer of S-HPAM on the surface of core is bigger than KYPAM6210. This result could be interpreted by bigger coiling molecular size of S-HPAM than KYPAM6210.

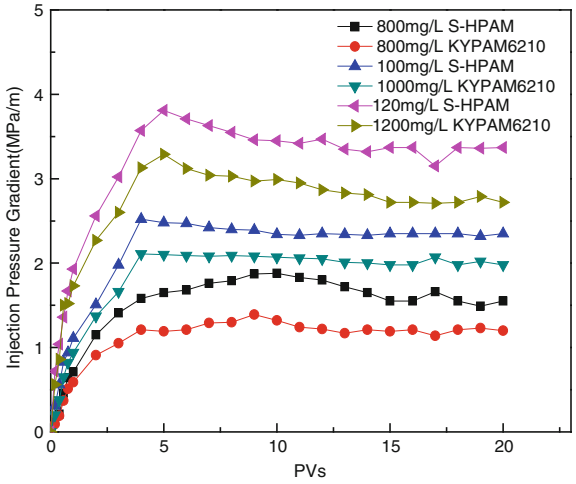

Fig. 7. Injection pressure gradient of polymer solutions versus PVs: Test conditions: 78 °C, salinity 16,800 mg/L

Table 3. The resistance coefficient and residual resistance coefficient of the polymer

Polymer	Concentration (mg/L)	Porosity (%)	Permeability to air ($\times 10^{-3}\mu m^2$)	*RF*	*RRF*
S-HPAM	800	19.7	129.8	10.33	7.06
	1000	21.0	127.7	16.79	10.5
	1200	19.6	126.8	24.07	13.5
KYPAM6210	800	20.3	134.0	8.46	6.85
	1000	20.9	133.2	16.50	9.33
	1200	19.2	130.4	20.15	12.00

3.3 Core Flooding Tests

The enhanced oil recovery experiments of S-HAPM and KYPAM6210 solutions were conducted on approximate 367 $\times$ $10^{-3}\mu m^2$ (permeability to air) artificial heterogeneous cores (4.5 $\times$ 4.5 $\times$ 30 cm) with a Dykstra–Parson coefficient of 0.946. The results of oil displacement experiments are listed and illustrated in Fig. 8. It is found that 22.8% EOR by S-HPAM flooding was obtained, whereas the EOR of KYPAM6210 was 18.7%. Thus, the enhanced oil recovery ability of S-HPAM is better than KYPAM due to its high mobility control represented by RF which can be generally attributed to three mechanisms: viscosity, elasticity [22, 23], and permeability reduction (or RRF) (Table 4).

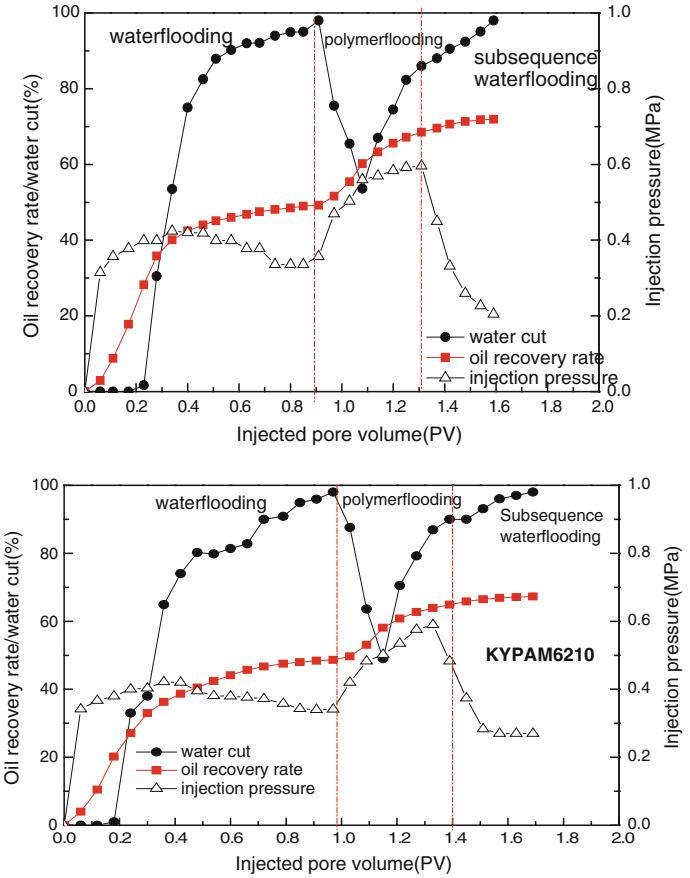

Fig. 8. Oil recovery rate, water cut, and injection pressure versus injected pore volume of polymer solutions: Test conditions: 78 °C, salinity 16,800 mg/L. Injected volume = 0.43PV, Injected rate = 0.31 mL/min

Table 4. Results of enhanced oil recovery of polymer flooding

Polymer	S_{oil} (%)	η_{app} (mPa s)	E_1 (%)	E_2 (%)	EOR (%)
S-HPAM	74.5	17.62	49.2	71.9	22.8
KYPAM6210	75.5	17.34	48.6	67.3	18.7

Remark η_{app}, the apparent viscosity of polymer solution; S_{oil}, the oil saturation in core; E_1, the oil recovery rate by water flooding; E_2, the total oil recovery rate by water flooding and polymer flooding; EOR = $E_2 - E_1$

4 Conclusions

In this work, we carried out comparative studies on the rheological properties, flow characteristics in porous media, and EOR performance for two types of temperature-tolerant and salt-resistant polymers, S-HPAM and KYPAM6210. The main collusions drawn from this study are as follows:

1. S-HPAM and KYPAM exhibit the similar shear-thinning property. However, the antiaging property of S-HPAM is more excellent than KYPAM6210. The behaviors of antiaging property can probably be explained by the introduction of sulfonic group into S-HPAM molecular structure, which results in improving hydrolysis resistance of polymer.
2. Under the same experimental conditions, the elasticity, viscosity, resistance coefficient (RF), and residual resistance coefficient (RRF) values of S-HPAM are higher than KYPAM6210. In other words, the mobility control of S-HPAM is higher than KYPAM6210, which has higher EOR ability.
3. Core flooding tests indicate that S-HPAM possesses favorable properties for EOR. Under the same experimental conditions, S-HPAM could enhance the oil recovery rate to 22.8%, while the oil recovery rate of KYPAM6210 is 18.7%. Therefore, S-HPAM shows excellent potential to enhance oil recovery from high-temperature and high mineralization reservoirs.

Acknowledgements. We acknowledge the financial support from Guangxi Colleges and Universities Key Laboratory of Beibu Gulf Oil and Natural Gas Resource Effective Utilization (2017KLOG17) and Jiangsu Oilfield Company of SINOPEC (JS16026). We also thank Beijing Research Institute of Chemical Industry and Jiangsu Oilfield Company for providing polymer and oil samples.

References

1. Thomas S (2008) Enhanced oil recovery: an overview. Oil Gas Sci Technol 63(1):9–19
2. Lake LW, Johns RT, Rossen WR et al (1986) Fundamentals of enhanced oil recovery. Society of Petroleum Engineers, USA
3. Wang D, Cheng J, Wu J et al (2005) Application of polymer flooding technology in Daqing Oilfield. Acta Petrol Sin 26(1):74–78. (in Chinese)
4. Sun H (2006) Practice and understanding on tertiary recovery in Shengli Oilfield. Pet Explor Dev 33(3):262–266 (in Chinese)
5. Seright RS, Campbell AR, Mozley PS et al (2010) Stability of partially hydrolyzed polyacrlamide at elevated temperatures in the absence of divalent cations. SPE J 15(2): 341–348
6. Wei B (2015) Flow characteristics of three enhanced oil recovery polymers in porous media. J Appl Polym Sci 132:415–418
7. Yi Z, Liu X, Fang Z et al (2015) Structure and properties of temperature-tolerant and salt-resistant polyacrylamide for tertiary oil recovery. Petrol Chem Technol 44(6):770–778 (in Chinese)

8. Yi Z, Huang F (2010) Research on the copolymer of AM and AMPS and its drying. Fine Spec Chem 18(8):25–28 (in Chinese)
9. Zhao F, Mao B, Yi Z et al (2012) Synthesis of AM/AMPS copolymer by adiabatic reaction and its performance. Fine Chem 29(12):1226–12310 (in Chinese)
10. Yi Z, Zhao F, Liu X et al (2014) Synthesis of and performance evaluation of temperature-tolerated and salt-resisted polymers for tertiary oil recovery. Sci Sin Chim 44(11):1–9 (in Chinese)
11. Cheng J, Luo J, Li Zh et al (2004) Application and study progress on salt-tolerant comb-shaped polymer. Fine Spec Chem 12(6):10–12 (in Chinese)
12. Li H, Zhao H, Chen H et al (2006) Field application of hydrophobically associating polymer based in situ crosslinking/gelling fluid for profile modification in Zhongyuan Oilfields. Oilfield Chem 23(1):54–58 (in Chinese)
13. Tang S, Luo P (2002) Advances in research of hydrophobically associating water-soluble polymer. Modern Chem Industry 22(3):10–15
14. Wang Z (2011) The recent advances in study of AMPS polymer in China. Fine Spec Chem 19(8):42–47 (in Chinese)
15. Tao L (2011) EOR pilot test using AMPS polymer flooding in high temperature reservoirs. J Oil Gas Technol 33(9):141–144 (in Chinese)
16. Hirasaki GJ, Pope GA (1974) Analysis of factors influencing mobility and adsorption in the flow of polymer solutions through porous media. SPE Reservoir Eng 3:337–350
17. Sarsenbekuly B, Kang Wanli, Yang Hongbin et al (2017) Evaluation of rheological properties of a novel thermo-viscosifying functional polymer for enhanced oil recovery. Colloids Surf A 532:405–410
18. De S, Koesen SP, Maitri RV et al (2017) Flow of viscoelastic surfactants through porous media. AIChE J
19. Gupta PK, Sridhar T (1985) Viscoelastic effects in Non-Newtonian flows through porous media. Rheol Acta 24:148–151
20. Zhong C, Luo P, Ye Z et al (2009) Characterization and solution properties of a novel water-soluble terpolymer for enhanced oil recovery. Polym Bull 62(1):79–89
21. Wang D, Wang G, Wu W et al (2008) Influence of the micro-force produced by viscoelastic displacement liquid on displacement efficiency. J Xi'an Shiyou University (Nat Sci Edition) 23(1):43–55. (in Chinese)
22. Xia H, Wang D, Liu Zh et al (2001) Study on mechanism of polymer solution with viscoelastic behavior increasing microscopic oil displacement efficiency. Acta Petrol Sin 22(4):60–65 (in Chinese)
23. Xia H, Wang D, Guan Q et al (2002) Experiment of viscoelasticity of polymer solution. J Daqing Inst 26(2):105–108 (in Chinese)
24. Xia H, Zhang J, Liu S (2011) Viscoelasticity and factors of polymer solution. J Daqing Inst 35(1):37–41 (in Chinese)
25. Li Daoshan, Kang Wanli, Zhu Hongjun (2003) Studies on viscoelasticity of aqueous hydrolyzed polyacrylamide solutions. Oilfield Chem 20(4):347–350 (in Chinese)
26. Wunderlich T, Stelter M, Tripahty T et al (2004) Flow-induced chain scission as physical route to narrowly distributed, high molar mass polymer. Polymer 45(4):1223–1234

Analysis and Study on Operating Trend of the Rotor System of Oil Pump Unit

Wencai Liu[1,2(✉)], Qihua Wang[1], and Qiyong Peng[1]

[1] CNPC Research Institute of Safety & Environment Technology, Beijing, China
{wencailiu, wangqihua, pengqiyong}@cnpc.com.cn
[2] HSE Key Laboratory of CNPC, Beijing, China

1 Introduction

The energy of vibration is a major harmful factor for machines. This is especially true for rotary machines like oil pump units, where the vibration of the rotor system plays the most important role in vibration of, or even damage to, the units. Moreover, the major symptoms of the most other failure modes are also in the form of vibration [1]. Focusing on vibration of the rotor system of oil pump unit, present work conducted operating trend analysis on metrics which can reflect the energy of rotor vibration.

2 Operating Trend Analysis of the Rotor System

In vibration of rotary machine, sub-synchronous frequency component is the dominant factor which affects the operational stability of the machine [2, 3]. When the machine runs at a stable condition, the centerline orbits at all the measuring point on rotor would show little jerk value, and the centerline orbits would be of small radii and well synchronized, and thus, the centerline orbits at the two shaft ends would have a small relative jerk value and small vibration energy; when there is instable factors, such as oil whirl, fluid-excited instability, etc., in the sliding bearing of the machine, a sub-synchronous frequency components would appear, worsening the coaxially of the centerline orbits, making the rotor sway more, and the radii of the centerline orbits increase; while in the case of misalignment/imbalance, the radii of centerline orbits increases, and the initial phase difference between the two measuring points changes as well. In short, when the rotor has a fault, the relative vibration between two shaft ends would increase; consequently, the energy of the said relative vibration would rise. The metric of energy, i.e., the RMS value, would increase accordingly. Therefore, the energy of the relative vibration between two shaft ends can be employed to diagnose the operating condition of a machine.

Based on relative vibration energy at two shaft ends of an oil pump unit, using a 3D rotor centerline orbit derived from multi-point, dual-channel acceleration signals, a metric reflecting the relative vibration energy at two ends was extracted, and an operating trend analysis is conducted on an oil pump unit. Qualitative analysis revealed

S. M. Shemwell and J. Lin (eds.), *Proceedings of the International Petroleum and Petrochemical Technology Conference 2018*,
https://doi.org/10.1007/978-981-13-2173-3_5

that the relationship between the operation condition of the oil pump unit rotation shaft and relative vibration energy at the two shaft ends basically follows a bathtub curve, except that there are extra inflection points on the curve. From multi-point dual-channel centerline orbit vibration signals, a 3D centerline orbit was created, and based on that, the relative jerk value of centerline orbits between two shaft end measuring points was extracted [4]. The relative jerk value combined the phase and centerline orbit radius data, and extracted a metric which can reflect the relative jerk energy at two shaft ends. The results of experimental study confirmed that metric is consistent with the operation condition curve of the machine and conclusion of qualitative analysis, and thus proved the feasibility of this approach in condition analysis and diagnosis of rotor systems.

2.1 Operating Trend Analysis of Rotor System Based on Relative Vibration Energy

Vibration energy is a key contributing factor to machine damage, and it is represented by the RMS value of vibration signal over a wide frequency band. This RMS value is independent of rotation speed, but can reflect the maximum destructive energy the machine subject to.

The relative vibration energy between the two shaft ends refers to the vector difference between the impact energies at two adjacent measuring points on rotor at the same time (the measuring points located at two shaft ends, with measuring plane normal to the axis); the vibration energies at the measuring points can be represented by *RMS* values; therefore, the relative vibration energy between two adjacent measuring points can be represented by the vector difference of *RMS* vibration of the two points at the same time.

(1) Running-In Period

During the running-in period, due to the influence of machining accuracy, abrasive dust, and other debris, the operation of the rotation shaft is relatively unstable, and the rotation shaft inflicts impact on the bearing seats. This impact is generally not very high. Under such condition, the centerline orbits are not regular, the relative vibration energy between the two shaft ends is higher than normal condition, but exhibits a decreasing trend. Indicators that represent energy (such as the *RMS* value) are also higher than normal, but they also gradually decrease with the wear. The inflection point A indicates the transition from this period to normal operation period.

(2) Normal Operation Period

Theoretically, in normal operation period, the relative vibration energy between two shaft ends is constant. In actual field operation, when the machine entered stable operation condition, centerline orbit at each measuring point on the rotor was close to circle or ellipse [5]. The relative jerk value was small, the radii of centerline orbits were very small and of approximately synchronized in phase; therefore, the impact of rotation shaft and rotor to the bearing seats was relatively low, and the relative jerk value of centerline orbits between the measuring points should be low too; the relative vibration energy between two shaft ends would fluctuate around a center value within a narrow range, and the RMS value as a metric for energy would also fluctuate in a

narrow range. The transition from this period, the early- and mid- failure period, is indicated by the inflection point B.

(3) Early- and Mid-Failure Period

When the machine enters the failure period, if their rotor has a problem, such as oil whirl in sliding bearing, or fluid-induced instability, a sub-synchronous frequency component would appear. Due to wearing of rolling bearing or other factors, the coaxial of centerline orbits would become worse, swaying of rotor would aggravate, and radii of centerline orbit would increase. In the case of misalignment/imbalance, the radii of centerline orbits would increase, and the initial phase difference between the two measuring points would change as well. In short, when the rotor has a fault, the relative vibration between two shaft ends would increase, and the impact on bearing seat would increase accordingly; consequently, vibration energy of the shaft would rise. The metric of the energy, i.e., the *RMS* value, would increases. The transition from this period to the late failure period is marked by inflection point C.

(4) Late Failure Period

When the machine enters late failure period, if the vibration is caused by wearing or misalignment, then as the wearing of bearing continues, the impact of rotor to the bearing seat would decrease a bit, and then goes up when the wearing becomes more serious. This causes an increase of swaying motion of rotation shaft in operation. Like the case of horizontal misalignment, the relative vibration energy between two shaft ends would rise again. The phenomenon is the relative vibration energy between two shaft ends which drops a bit first, and then increases.

According to above analysis, from the running-in stage of new machine to frequent failure period, the changing trend of relative jerk value and vibration energy between two shaft ends would be similar to a "bathtub curve," except that there would be an extra inflection point C in the late failure period, which indicates that the bearing enters a badly worn period. See Fig. 1.

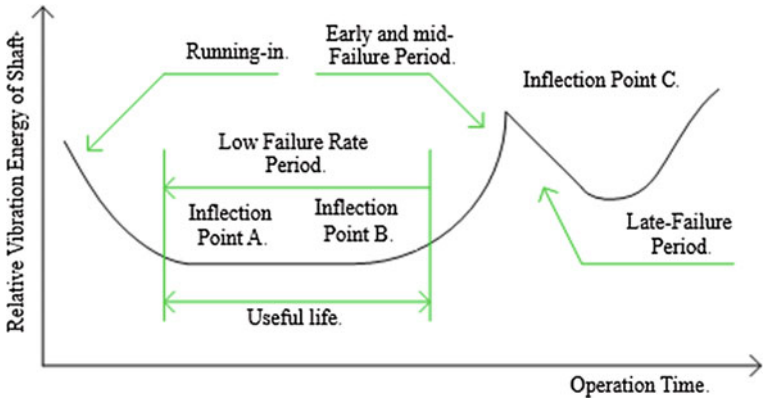

Fig. 1. Qualitative curve of the relative vibration energy between two shaft ends

2.2 Quantitative Extraction of the Relative Vibration Energy of Rotation Shaft Based on 3D Centerline Orbit

(1) Analysis and calculation of the relative jerk value between two shaft ends based on 3D centerline orbit

When the rotor runs, the movement of the centerline orbits at two measuring points is shown in Fig. 2. $A1A2$ is a line between two centerline orbits at the two measuring points, where $A1$ and $A2$ are two points on the two centerline orbits at circle i, respectively. Theoretically, the planes at the two measuring points should be parallel.

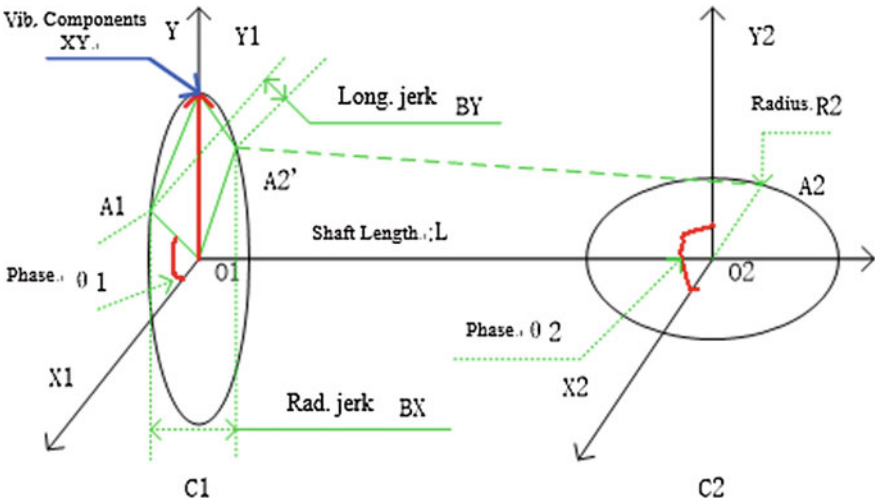

Fig. 2. Quantitative extraction of relative jerk value

Calculation of the relative jerk value between two centerline orbits at circle i:

(1) Project the point $A2$ to the plane $X1O1Y1$, get point $A2$. This eliminates the need for shaft length L in calculation.

(2) Radial jerk value:

$$\mathrm{BX}_i = |X_{A1} - X_{A2'}| = |R_1 \cos(\theta_1) - R_2 \cos(\theta_2)| \tag{1}$$

(3) Longitudinal jerk value:

$$\mathrm{BY}_i = |Y_{A1} - Y_{A2'}| = |R_1 \sin(\theta_1) - R_2 \sin(\theta_2)| \tag{2}$$

(4) Overall jerk value:

$$\mathrm{XY_i} = \sqrt{(\mathrm{BX}_i)^2 + (\mathrm{BY_i})^2} \tag{3}$$

(2) Selection and extraction of characteristic parameter for relative vibration energy at two shaft ends

As shown in Fig. 2, to describe relative jerk value between two shaft ends of rotor, three parameters, namely, radial jerk value, longitudinal jerk value, or overall jerk value (moduli of the radial, longitudinal vibration, and their vector sum), can be considered. The RMS value of the overall jerk value can be employed to represent the overall energy of relative jerk value, i.e., the relative vibration energy between two shaft ends.

$$\mathrm{XY}_{\mathrm{rmv}} = \sqrt{\frac{1}{\mathrm{num} * N - 1} \sum_{i=0}^{\mathrm{num}*N} (\mathrm{XY}_i)^2} \quad i = 0, 1, 2 \ldots \tag{4}$$

where N is the circle number, and XY_i is the overall jerk value of the point on number i orbit.

$\mathrm{XY}_{\mathrm{rmv}}$ is an absolute value which can quantitatively reflect the relative vibration energy between two shaft ends.

3 Field Test

To verify above assumption, a field test was conducted on the oil pump motor in a *CNPC* pipeline facility, wherein the centerline orbit signals at two shaft ends of a rotor were collected from the new machine running-in stage to the late failure prone period, and energy metrics were extracted. The data from 305# unit is listed in Table 1 and

Table 1. Relative vibration energy between two shaft ends

Metric	Number of days and corresponding metric					
Operation time (day)	0	32	34	36	38	40
Relative vibration energy between two shaft ends	31.65	30.44	24.26	24.51	42.11	9.93
Operation time (day)	130	131	132	133	242	243
Relative vibration energy between two shaft ends	4.23	3.73	4.72	1.83	2.66	1.5
Operation time (day)	335	425	471	563	564	565
Relative vibration energy between two shaft ends	3.65	10.78	42.82	60.9	45.26	77.07
Operation time (day)	566	567	568	570	571	572
Relative vibration energy between two shaft ends	28.22	16.91	28.06	17.21	42.59	31.32
Operation time (day)	573	574	575	576	577	578
Relative vibration energy between two shaft ends	44.88	58.01	61.22	74.08	28.45	48.85

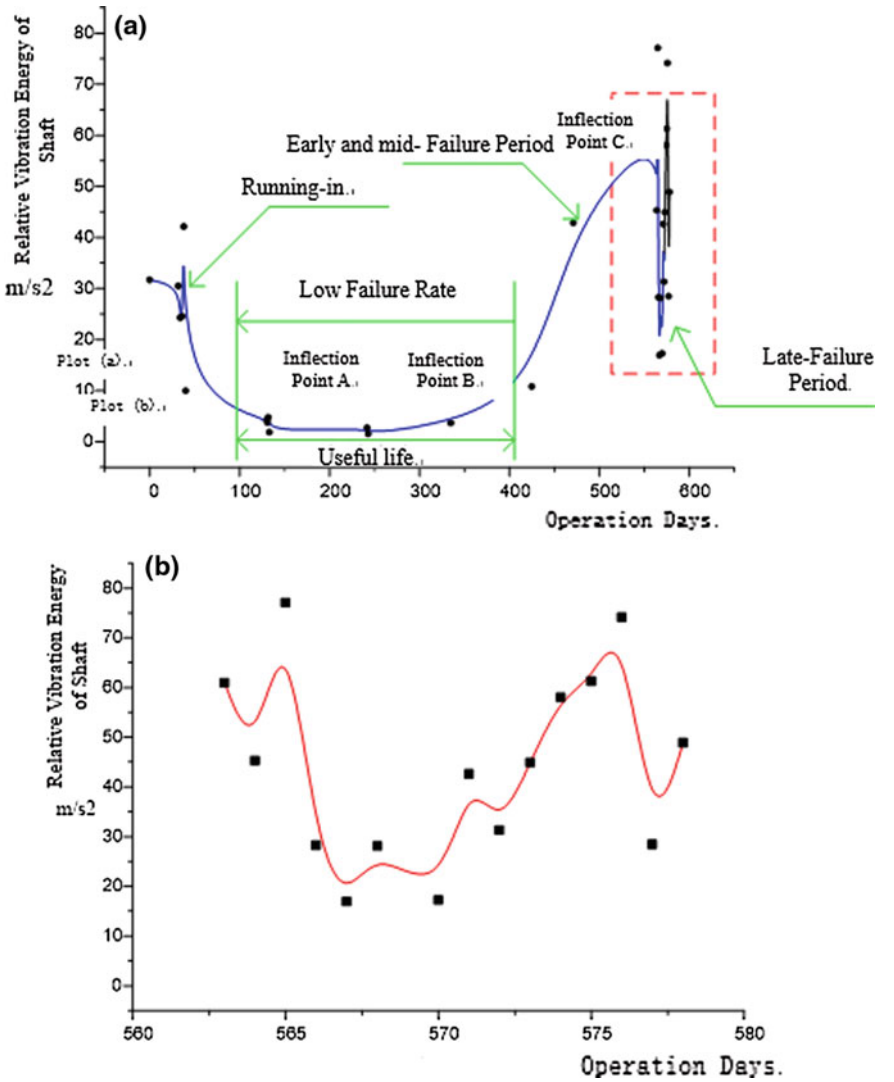

Fig. 3. Variation trend of relative vibration energy between two shaft-ends. (**a**) is qualitative curve of the relative vibration energy between two shaft-ends, (**b**) is local zoom-in of the line in the red dash-line box

plotted in Fig. 3. The speed of the machine was 2980 rpm. The sampling frequency of the data acquisition channels was 16,000 Hz, and the data length was 1024 *X60* points. The arrangement of the measuring points is shown in Fig. 3.

From the variation trend of relative vibration energy between two shaft ends in Fig. 3, it can be seen that, during running-in period of rotor system, the vibrations at two

shaft ends and the relative vibration were all high, due to factors like machining accuracy, debris, etc. The vector difference between *RMS* values of vibration and two shaft ends, i.e., the vibration energies of vibrations at two shaft ends and of the overall relative vibration were all high. In the low failure rate period, the relative vibration energy became significantly lower and the vibrations were well balanced, with the relative vibration energy fluctuated around a small stable value in a narrow range. In the early- and mid-failure period with higher failure rate, the relative vibration at two shaft ends increased and became less synchronized, due to wearing or looseness of parts, with the relative vibration energy began to increase. In the late failure period, due to serious wearing of rotor shaft, some relative vibration components caused by misalignment could be reduced, however, the swaying movement of rotor increased, causing further wearing of the bearings, therefore, and the relative vibration energy at two shaft ends exhibited a small decrease followed by an increase. By determining the inflection point C, we could decide whether the bearings had entered a badly worn period.

4 Conclusion

In the present work, we conducted a qualitative analysis on relationship between the relative jerk value between two shaft ends and the machines' operation condition, using a 3D centerline orbit derived from multiple measuring points, multichannel centerline orbit vibration signals, and carried out a quantitatively extraction of energy metric of the relative jerk value between two shaft ends, i.e., the vector difference between RMS measuring point vibration values. Field test shows that the change of relative vibration energy between two shaft ends follows a "bathtub curve," except that there is an additional inflection point C, which represent the rotor that had entered a badly worn period; the result of qualitative analysis is confirmed by the test results. Furthermore, the test proves that the relative vibration energy between two shaft ends can be used to analyze and diagnose the operation condition of rotor system, and provide a parameter for prediction of its operating trend.

Acknowledgements. This work is supported by the national key research and development program of China "Typical storage of dangerous chemicals safety warning and protection integration key technology research and application demonstration (2016YFC0801200)".

References

1. Shu Dawen X (1998) Application and research of equipment fault diagnosis technique in mining machinery in China. J Kunming Univ Sci Technol 23(2):68–71
2. Jardine AKS, Lin D, Banjevic D (2006) A review on machinery diagnostics and prognostics implementing condition-based maintenance. Mech Syst Signal Process 20:1483–1510
3. Wang L, Mehrabi MG (2002) Hidden Markov model-based tool wear monitoring in machining. ASME J Manufact Sci Eng 124:651–658

4. Lee JM, Kim SJ, Hwang Y et al (2004) Diagnosis of mechanical fault signals using continuous hidden Markov model. J Sound Vib 27(6):1065–1080
5. Scholkopf B, Smola A, Muller KR (1999) Kernel principal component analysis. Advances in Kernel methods-support vector learning. MIT Press, Cambridge M A, pp 327–352

Torsional Impact Tool Based on the Problem of Stick-Slip Vibration and Its Application

Xin Ling(✉) and Wei Li

School of Petroleum Engineering, Northeast Petroleum University, Daqing 163318, China
lingxinlll4@163.com, our.l26@126.com

1 Introduction

PDC bits have been widely used in geological exploration and development because of its high drilling speed, long life, good stability, and flexible bit design. However, when drilling in deep competent formation, especially in multi-interbedded formation, there are generally problems such as low drilling efficiency and premature failure of PDC bits [1]. Mechanical vibration is the main reason for the premature failure of the bottom hole assembly (BHA) and the drill string. There are three types of drill string vibration: torsional vibration (stick-slip) [2], axial vibration (bit bounce) [3], and lateral vibration (whirling motion) [4]. This paper focuses on the study of the stick-slip vibration of the drill pipe. The stick-slip effect means that the top of the drill string rotates at a constant speed, while the bit speed varies between zero and six times of rotation speed of the surface. The appearance of the stick-slip effect is due to friction between the different components of the drill string and the friction between the drill string and the wellbore [5].

The stick-slip instability of the drill string is traditionally attributed to the dry friction model at the bit rock interface [6] (Stribeck effect). However, in recent years, many scholars have established many models with very fixed friction coefficients, which also show stick-slip instability. Richard [7] established a model with a single degree of freedom. Abbassian [8] established a model with two degrees of freedom. Mihajlovic [9] combined the turntable system model with two degrees of freedom model. In 2007, Richard coupled the axial and torsional motions at the drill–rock interface to analyze the stick-slip vibration [10]. A two degree of freedom model with drag bit was established, which presents a stick-slip motion by time delay.

In field test, in order to reduce the stick-slip effect, many attempts have been made. In recent years, Ulterra and Halliburton have developed torsional impactor. In 2000, the Ulterra company proposed and developed a torsional impactor to assist the rock breaking of the PDC bit, which were widely used in major oil fields. TorkBuster developed by Ulterra can drive the turbine with high-velocity drilling fluid, and then drive the impactor to strike the transmission shaft, eventually transmitting the torsional impact energy evenly to the drill bits. Rotary impact device developed by Halliburton can also drive the turbine with high-velocity drilling fluid, making the impact block hit the base in the opposite direction yet to transmit energy. The Southwest Petroleum University has developed a torsional impact tool that works in a similar way to the

S. M. Shemwell and J. Lin (eds.), *Proceedings of the International Petroleum and Petrochemical Technology Conference 2018*,
https://doi.org/10.1007/978-981-13-2173-3_6

TorkBuster of Ulterra, which drives the impactor with the help of a screw. Therefore, the SLTIDT torsional impact tool developed by Shengli Oilfield uses the fluid pressure difference between drilling fluids to drive the internal impact hammer to circle the impact repeatedly. In 2014, Prof. Li [11] developed a near drill torsional impactor and applied it to Jilin Oilfield, Tarim Oilfield, and Daqing Oilfield, where the average speed increased to 39–145%. More important, the average lifespan of the tool was about 120 h, and the performance was stable and the effect of slanting was good. In addition, many major research institutions, such as Daqing Oilfield Drilling Engineering and Technology Research Institute, Beijing Drilling Engineering Technology Research Institute, have carried out researches on the torsion impact tools.

2 Mechanical Model of Stick-Slip Vibration System with PDC Bit

The basic structure of the rotary drilling system mainly consists of drilling rig, drill string, and drill bit. The main component of the drill string is a set of bottom hole assembly (BHA) made of heavy steel pipes and a drill pipe made of fine pipes. For the convenience of analysis, the following assumptions are set up as follows: (1) boundary conditions: a constant upward force H_0 and a constant angular velocity Ω_0 applied to the top of a drill string by a drill rig; (2) the wellbore is vertical; (3) no lateral motion of a bit; and (4) ignore the friction between the string and the wellbore and between the string and the drilling fluid.

Based on the above assumptions, a drilling system model with two degrees of freedom, including the axial and torsional vibrations of a drill string, is established, as shown in Fig. 1. $U(t)$ and $\Phi(t)$ represent the vertical position and angle position of the bit, respectively. Particle M and moment of inertia I represent bottom hole assembly (BHA). The torsional stiffness C of the spring represents the torsional stiffness of the drill string. The angle position of the vertex of the drill string is expressed in $\Omega_0 t$.

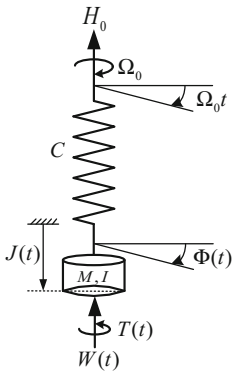

Fig. 1. Simplified model of drilling system

As shown in Fig. 1, when an upward pulling force H_0 and a constant angular velocity Ω_0 are applied to the upper end of the torsion spring, there is corresponding response that $p(t) = \{W(t), V(t), T(t), \Omega(t)\}$, which is usually a function of time t. There are two conjugated kinetic quantities and kinematic quantities: bit drill pressure W and rate of penetration $V = dU/dt$, moment of rotation T and bit rotate speed $\Omega = d\Phi/dt$.

As shown in Fig. 1, the motion equation of the bit in the torsional direction and the axial direction is

$$I\frac{d^2\Phi}{dt^2} + C(\Phi - \Omega_0 t) = T_0 - T(t) \tag{1}$$

$$M\frac{d^2U}{dt^2} = W_0 - W(t) \tag{2}$$

where T_0 is the driving torque provided by the drill rig and $W_0 = W_s - H_0$ (W_s is fluid column pressure).

$T(t)$ is the torque of bit, which consists of two parts: (1) T_c is used to overcome the shear strength of rock. (2) T_f is used to overcome the frictional force during drilling.

$$T(t) = T_c + T_f \tag{3}$$

When the stick-slip effect is produced, the boundary conditions of the model have discontinuous properties. For simplicity, we suppose that the bit does not rotate in reverse. The bit stops turning when $t = t_k$.

$$\frac{d\Phi}{dt} = 0 \tag{4}$$

Equation (1) is deformed into

$$C(\Phi_k - \Omega_0 t) = T_0 - T(t) \tag{5}$$

In the stage of stick, drill string continuous rotation. The torque applied to the bottom hole assembly by the drill string is

$$T(t) = T_0 - C(\Phi_k - \Omega_0 t) \tag{6}$$

As time increases, $T(t)$ begins to accumulate until its size reaches the torque needed to overcome the cutting rock:

$$T_c + T_f = T_0 - C\left(\Phi_k - \Omega_0 t_p\right) \tag{7}$$

3 Research and Development of Torsional Impact Tools

At present, the main methods to reduce and solve the stick-slip vibration are to optimize the parameters of drilling parameters, reduce the weight on bit (WOB), or improve the performance of drill fluid [1]. This paper mainly adopts the way of using the torsional impact tool and the optimization of the bit structure to reduce the vibration.

3.1 The Structure of Torsional Impact Tool

The main structure of the tool is shown in Fig. 2, where the current divider, the starter, and the hydraulic hammer are the core components of the tool,

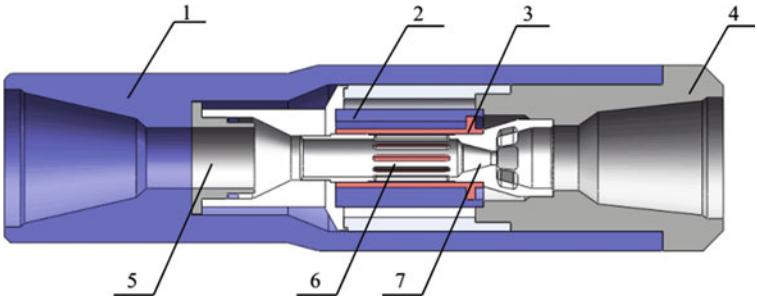

Fig. 2. Structure profile of torsional impact tool

where 1 is short shell, 2 is hydraulic hammer shell, 3 is hydraulic hammer, 4 is transmission joint, 5 is diversion device, 6 is starter, and 7 is current divider.

The torsional impact tool can convert the fluid energy of the drilling fluid into axial, circumferential, high-frequency, and stable mechanical shock energy, and transfer the mechanical energy to the bits, which can well restrain the stick-slip vibration and the axial bit bounce with the PDC bits.

The diversion device distributes the drilling fluid transmitted from the drill collar, where fluid containing large particles is discharged through the current divider. The drilling fluid that does not contain large particles is transported to the starter and the hydraulic hammer to avoid that tool was jammed shut during the working process. The fluid from the diversion device opens the starter, which let hydraulic hammer to realize periodic and repeated torsional shocks. The torsional impact force formed by the hydraulic hammer is transmitted to the bits through the transmission joint, thus overcoming the viscous and slippery vibration of the PDC bit.

3.2 The Transfer Efficiency of Torsional Impact Tool

Impact energy transmitted by high-frequency torsional impactor to PDC bits will affect the rock breaking effect and eliminate the stick-slip effect of the PDC bits. Without

considering loss of energy about heat, sound, and light during the impact process, energy transfer efficiency of impact system is defined as the ratio of the work done by the impact system to break the rock and initial kinetic energy of an impact system, which we shall denote by η.

$$\eta = \frac{W_1 + W_2}{W} \tag{8}$$

where W_1 is the part of the impact energy that is eventually used for rock breakage, J, W_2 is the energy lost in the impact process of the impact system, J, which is equivalent to the deformation energy of the impact system, and W is the initial energy of the impact system.

Considering the impact of shock wave resistance, the equation of energy transfer efficiency of the impact system is derived:

$$\eta = \frac{4\pi Er^2}{4\pi Er^2 + lk} \cdot Z \tag{9}$$

where E is the modulus of elasticity of a tool material, GPa; k is the compressive strength of rock, MPa; l is the distance from the impact to the working face of the rock, m; and Z is the wave resistance coefficient.

According to the characteristics of rock mechanics and tools in drilling strata, the relationship between the diameter and length of PDC bits and the energy transfer efficiency of impact system of high-frequency torsional impactor is analyzed, as shown in Figs. 3 and 4.

From Fig. 3, we can see that the cross-sectional area of PDC bits has a logarithmic relationship with transfer efficiency. With the increase of PDC bits area, the energy transfer efficiency of the system is higher, and the performance of high-frequency twist impactor is more stable than that of PDC bits.

As we can see from Fig. 4, the energy transfer efficiency is linearly decreasing with the increase of PDC bits length. That is, the longer the length of PDC bit is, the more energy loss will be. Therefore, when selecting the combination of PDC bit and high-frequency torsional impactor, we should choose ultrashort single drill bits as much as possible, which is helpful to improve the application efficiency of torsional impactor.

4 Laboratory Experiment

4.1 The Experimental Condition

The drilling company of Bohai drilling Tarim Oilfield has used the torsional impact tool since 2010. The tool is mounted on the PDC bit, and its performance parameters are shown in Table 1.

The torsional burst experiment of PDC bit was carried out in the laboratory using the simulation test system of rock breaking with torsional impact tool. The diameter of the drill bits was 50.0 mm, the cutting tooth diameter was 13.2 mm, and rotate speed

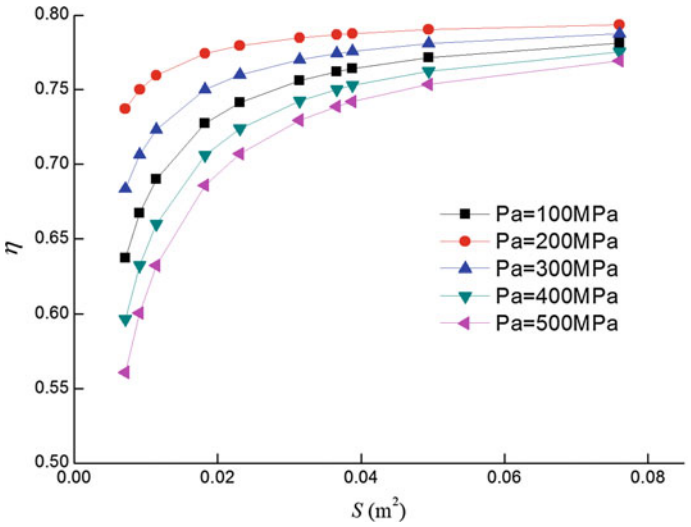

Fig. 3. Relation diagram of energy transfer efficiency η and bit area S

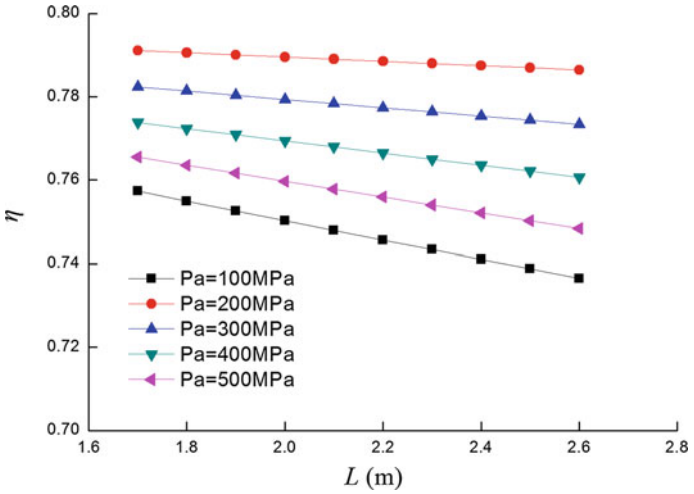

Fig. 4. Relationship between energy transfer efficiency η and bit length L

Table 1. The parameters of tool performance

Outer diameter (mm)	178
Delivery volume (L/s)	18–75
Pressure drop (MPa)	2.7–3.0
Working frequency (r/min)	750–1500
Impact force (N)	2000
Working temperature (°C)	350

was designed to be 200 r/min. Tap water is used as drilling fluid for carrying cuttings and cooling bits. In this experiment, the red sandstone is selected as the experimental rock sample. The PDC bit is double teeth, and the drilling pressure is 5 kN.

4.2 The Experimental Result

Rudat (2011) theoretically analyzes [12] that in conventional drilling process, because there is the stick-slip vibration impact, drill need to accumulate a certain torque energy to the broken rock. This torque curve of bit will produce a cyclical fluctuation, and this stick-slip vibration will affect the bit service life.

Figure 5 shows the curve of the relationship between the torque and the drilling time of the bit. During conventional drilling, the drill bit produces a distinct periodic viscous stick-slip vibration, which leads to a large periodic fluctuation about bit torque. When the bit torque is not sufficient, the sticky occurs, and the rotate speed is reduced. So, the energy is accumulated. When the accumulated energy reaches the energy of the broken rock, the bit is suddenly released, and slipping occurs. The more the torque is accumulated, the greater the fluctuation after the release. However, the technology of torsional rock breaking changed the rock breaking way of PDC bits, from continuous torque input to continuous torque and periodic high-energy impact superposition. By applying a certain frequency of torque, the torque fluctuation of the bit can be reduced obviously, so it can cut the rock steadily and avoid the damage to the drill string.

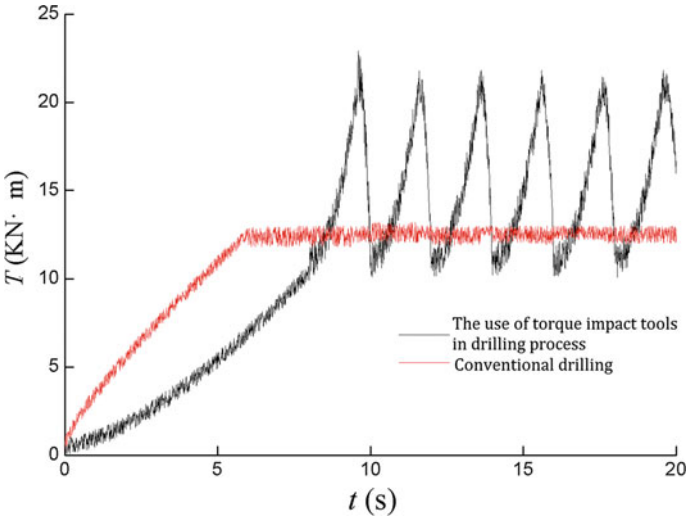

Fig. 5. The change curve of drill bit vibration with time

It is proved by laboratory experiments that the effect of torsional impact can obviously inhibit the stick-slip effect. In the process of drilling, when the high-energy drilling fluid flows through the tool, the torsional impact force (about 2kN) and the impact frequency (about 1500r/min) produced by the tool are transmitted directly to the

PDC bit, which makes the bit does not need to wait for storing enough torque energy to cutting formation. It can effectively avoid the stick-slip phenomenon of PDC bit, so as to improve the speed of mechanical drilling.

5 The Field Test

5.1 Application and Effect of Tools

The drilling tool combination used in the torsional impact tool test site of QG5 well is Φ215.9 mm drill bit + Φ180 mm torsional impact tool + Φ165 mm drill collar + Φ214 mm centralizer + 215.9 mm drilling string. The bit has five blades with five nozzles whose diameter is 15.8 mm and the PDC cutter whose diameter is 13 mm. The field drilling parameters are as follows: the drilling pressure is 80–140 kN, rotate speed is 50–80 r/min, and the delivery volume is 30–32 L/s. The lithology of the drilling strata is dominated by sandstone mudstone. The rate of penetration in this well is 4.29 m/h. The rate of penetration of the conventional drilling assembly in the adjacent well is 1.75–2.12 m/h. By comparison, the QG5 well uses the torsional impact tool, and the rate of penetration is greatly improved. The tool worked in well after it is tested at wellhead, when the tool worked for 128 h, pulling it out the well, it can be seen that the appearance of the torsion impact tool is good (Fig. 6) and the drilling bit wears slightly (Fig. 7).

Fig. 6. Resonator arrive wellhead

Fig. 7. Abrasion status of PDC bit

5.2 Influence of Drilling Parameters on the Speed Effect of the Tool

The lithology of the 4020–4185 m section is the same, all of which are gray sandstone. According to different drilling pressures and rotate speeds, the average value of drilling time is obtained and drawn in Fig. 8.

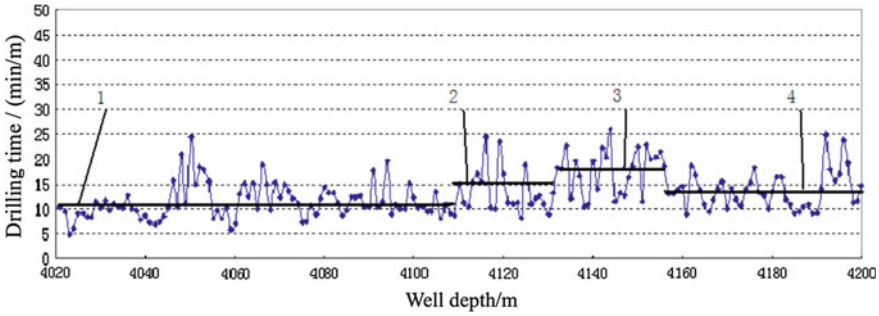

Fig. 8. Relationship between drilling time and well depth

1, 2, 3, and 4 represent four different drilling parameters of drilling processes, respectively. In the first stage, drilling pressure is 80 kN, rotate speed is 50 r/min, the average drilling time is about 11 min/m, and it is drilling into 4110 m. In the second stage, drilling pressure is 80 kN, rotate speed is increased to 80 r/min, the average

drilling time is about 15 min/m, and it is drilling into 4132 m. In the third stage, drilling pressure is decreased to 50 kN, rotate speed is 80 r/min, and the drilling time continues to increase with an average of about 17 min/m. In the third stage, it is drilling into 4156 m, where drilling pressure is increased to 80 kN and rotate speed is decreased to 50 r/min. At this time, the drilling time decreased significantly with an average of about 14 min/m. Through real drilling data, we can see that the best drilling parameters exist in the drilling process, that is to use high drilling pressure and low speed to maximize drilling speed.

6 Conclusion

1. A torsional impact tool, which produces 1500 Hz/min impact frequency, has been independently developed. The main structure of the tool is introduced, and the working state and speed increasing mechanism of the tool are analyzed.
2. Through the laboratory experiments, it is proved that the periodic torsional impact load can effectively restrain the stick-slip effect of the PDC bit.
3. The transfer efficiency model of torsional impact energy is given. The model analysis showed that the PDC bit length, energy decay faster, so torsional impact energy transfer efficiency is low. When the PDC bit section is large and the length is small, energy transfer efficiency of high-frequency torsional impacting tool is high.
4. The field application shows that when it adopts drilling parameters with high drilling pressure and low speed, torsional impactor and the optimized PDC bit can effectively eliminate the stick-slip vibration effect of PDC bit, and reduce the torsional vibration of drill string, then effectively protect the matching parts consisting of drill bits and drilling tools. Moreover, it can effectively reduce drilling costs.
5. The QG3 well experiment in Tarim Basin of Xinjiang shows that the drilling technology with the torsion impact tool and PDC bit increases the penetration rate more than 1 times compared with the conventional drilling tool and PDC bit

Acknowledgements. Funding: This work was supported by the Natural Science Foundation of China [grant numbers 51774093].

References

1. Warren TM, Oster JH (1998) Torional resonance of drilling with PDC bits in hard rock. SPE 49204
2. Jansen JD, van den Steen L (1995) Active damping of self-excited torsional vibrations in oil well drillstrings. J Sound Vib 179(4):647–668
3. Spanos PD, Sengupta AK, Cunningham RA, Paslay PR (1995) Modeling of roller cone bit lift-off dynamics in rotary drilling. ASME J Energy Resour Technol 117:197–207
4. Jansen JD (1991) Non-linear rotordynamics as applied to oilwell drillstring vibrations. J Sound Vib 147(1):115–135
5. Kyllingstad A, Halsey GW A study of slip/stick motion of the bit. SPE Drilling

6. Challamel N, Sellami H, Chenevez E (2000) A stick-slip analysis based on rock/bit interaction: theoretical and experimental contribution. In: Presented at the SPE/IADC Conference, New Orleans, Louisiana IADC/SPE 59230
7. Richard T (2001) Self-excited stick-slip oscillations of drag bits. Ph.D. thesis, University of Minnesota
8. Abbassian F, Dunayevsky VA (1998) Application of stability approach to torsional and lateral bit dynamics. SPE Drilling and Completion 13(2):99–107
9. Mihajlovic N, van Veggel AA, van de Wouw N, Nijmeijer H (2003) Analysis of friction-induced limit cycling in an experimental drill-string system. ASME J Dyn Syst Meas Contr
10. Richard T, Germay C, Detournay E (2007) A simplified model to explain the root cause of stick-slip vibrations in drilling systems with drag bits. J Sound Vib 305:432–456
11. Li W, Yan T, Zhang Z (1988) Rock response mechanism and rock breaking test analysis for impact of high frequency vibration drilling tool. Petrol Drill Tech 41(6):25–28
12. Rudat J, Dashevskiy D (2011) Development of an innovative model-based stick/slip control system. Soc Petrol Eng

Resin Application as Permanent Well Barrier for Wells with Sustainable Casing Pressure in Sichuan

Xin Zheng[1(✉)], Minh Vo[1], San Su[1], Xiao Chaohong[2], and Da Wang[3]

[1] Unocal East China Sea Ltd, UECSL, Beijing, China
{xzao, vomi, sxfa}@chevron.com
[2] Southwest Oil & Gas Field Company, CNPC, Beijing, China
nxia@chevron.com
[3] Halliburton Energy Service (China) Limited, Beijing, China
da.wang@halliburton.com

1 Introduction

Sichuan Basin is a well-known petroliferous sedimentary basin [1]. It is in Southwest China and surrounded by mountains on all sides.

The hydrocarbon exploration and development in Sichuan Basin started in middle 1950s. Since then several regional geological reconnaissances have been conducted, vintages of seismic data including 2D and 3D have been acquired, and multiple exploration and appraisal wells have been drilled to advance the exploration activities in this basin. Nearly, 30 large-to-mid-scale gas fields [2] and numerous small gas fields have been discovered to date, and tremendous development drilling activities have been carried out to deliver gas productions from the gas fields in this basin.

The sedimentary rocks in Sichuan Basin are composed of two distinctive successions, i.e., the lower section of carbonates rocks from Sinian to middle Triassic in age, and upper section of clastic rocks from late Triassic to present in age. From bottom to top, the recognized major gas-bearing formations in Sichuan Basin include Sinian, Carboniferous, Permian, and Triassic (Fig. 1). Most of the gas fields of large scale are found in Permian and Triassic formations. Specifically, the deep gas reservoirs in upper Permian and lower section of lower Triassic gas reservoirs contain high H_2S content, while the shallow gas reservoirs in upper section of lower Triassic to upper Triassic are mainly sweet gas.

The wells drilled in Sichuan Basin typically consist of five casing strings (Fig. 2), namely, 20″ conductor, 13-3/8″ surface casing, 9-5/8″ intermediate casing, 7″ production casing, and 5-1/2″ (pre-drilled) liner from outer to inner. The 20″ casing is usually set at about 20 m to separate the surface acquirer which provides drinking water. The 13-3/8″ surface casing is usually run from surface to several hundred meters to prevent the mud loss into the shallow porous rock units. The 9-5/8″ intermediate casing runs from surface to the bottom of a regional well-known major mud loss zone in the upper section of lower Triassic formation at ~2000 m. After this mud loss zone, the highly deviated well started to kick off and build up angels. The 7″ production

S. M. Shemwell and J. Lin (eds.), *Proceedings of the International Petroleum and Petrochemical Technology Conference 2018*,
https://doi.org/10.1007/978-981-13-2173-3_7

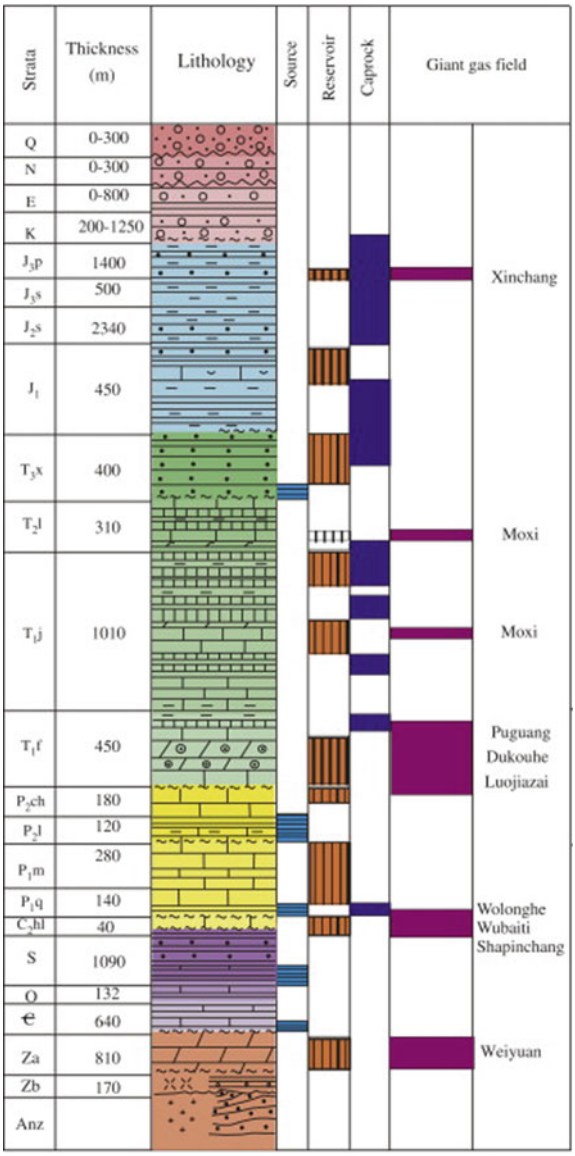

Fig. 1. Sichuan Basin gas sources [3]

casing is usually hung up on the 9-5/8″ casing with several hundred meters' overlap and the casing shoe is set above the major pay zone. Finally, the 5-1/2″ liner or pre-drilled liner is hang on the 7″ casing shoe, and the well can then be completed ready for the production phase (if selected as a development well).

Sustainable casing pressures SCP well are to describe the case that one of the well's annuli has pressure and after being bled off, the pressure can build up back to the level

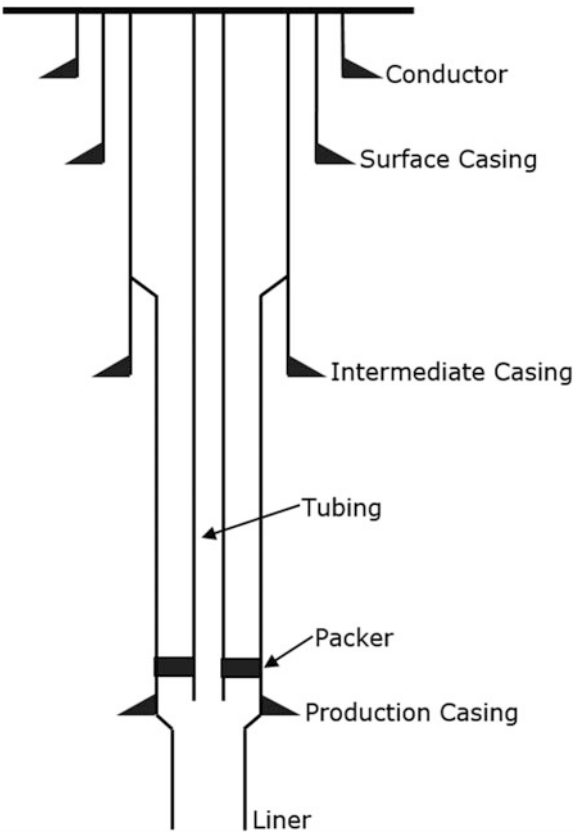

Fig. 2. Typical well in Sichuan Basin

prior to bleeding off. It is more serious when the casing pressure has gas at the high pressure. Unless there was a deformation of casing/tubing that gas could travel across the annuli, the most likely possibility is the gas migration from the deep sources to the surface in each specific annulus.

Sustainable casing pressures SCP have been reported from above 50% of gas wells in Sichuan Basin [4]. As mentioned, for the pressure in a specific casing, the gas should be sourced from the deeper gas zone(s). The topmost gas zones for surface, intermediate, and production casings are thought to be from the upper Triassic, upper section of lower Triassic, and lower section of lower Triassic formations, respectively.

2 Well Integrity Issue with SCP

A typical well design is to ensure that the well can support a safe and reliable production and development for a long time (i.e., 20 years). The cement job quality is very important to ensure that the well can be operated as designed during the field life. For

the safe operations, the well requires two independent well barriers at all time [5]. This is even more critical when working in the high H_2S environment, because any well control situation can lead to a large environmental impact, even fatality.

Due to a poor cement job quality and/or a material deterioration, several wells in the field development in Sichuan have severe sustainable casing pressures in more than one annuli, which put the well in the status of non-compliance with the safety rule mentioned above (i.e., two independent well barriers). The common solution for this situation is that a well intervention operation is needed to eliminate the gas migration path and if not successful, add an extra well barrier(s) to permanently secure the well in a safer and more reliable condition, normally called a plug and abandon activity.

According to API RP 57 and Oil & Gas UK "Guidelines for the suspension and abandonment of wells" [6], the well barrier shall need at least 100 ft cement and the Portland cement is the time proven and most recognized well barrier. This is because that cement is a reliable agent to establish high compressive strength barrier with excellent economical performances, but challenge emerges out from those compromised well integrity wells with sustained casing pressure (SCP) such as idle wells in Sichuan Basin. Those wells contained SCP either right after completion due to less-quality cement job or gradually seen pressure ramp up in multi-annuli due to deteriorated cement bond. The micro-crack among annuli (between cement and casing, cement and formation and/or inside cement sheath) allowing gas migrating from reservoirs to the surface throws curveballs for cement to be efficiently pumped and/or squeezed into micro-channels due to its significant solids friction.

Because of these challenges, the resin or resin-type sealant, with solid-free properties to enhance pumpability, appears to be one alternative to increase the probability of success in communicating through micro-fissuring, and with the below superior properties, resin bears enormous potential to serve as permanent well barrier sealant.

Compared with standard Portland G cement, resin owns the following advantages:

- High-pressure seal (1000 psi/ft),
- Chemical resistance (acid/CO_2),
- Contamination resistance (overcome inefficient mud displacement),
- Increased elasticity (up to 20%),
- Increased compressive strength (up to 15,000 psi),
- Solid-free (0 yield point as liquid), and
- Drillable (easy to drill via common drilling assembly).

However, despite those strengths, resin is not always adding value to every well intervention operation. Its excessive cost (approximately a few times of the cost of common Portland cement) and relatively hard to fix if inappropriate setting requires creative well solution prior to apply the resin technology to any well intervention resolution [7].

3 Practical Application of Resin in Oil Industry

Due to the abovementioned superior property over traditional cement slurry, resin has been utilized as one option of micro-channel squeezing remedial job to address SCP and restore well integrity. Halliburton has been working for different operators globally in attempt to seeking for an effective and efficient mean to kill SCP with resin application. China is one of the major areas in which resin product has been widely used.

More specifically, one operator in Sichuan had been suffering SCP issue, which needs to be solved by a successful plug and abandonment. Cement slurry squeezing methodology had been applied with unsatisfactory outcome. As a result, the resin application has been raised up in several trials to seal off SCP: the casing pressure had been totally ceased or dramatically reduced to a very small level after single or multiple resin plugs squeezed into micro-annulus with various volumes. All the wells with SCP had been successfully abandoned.

One of the key successful factors for resin application is to expose all the micro-channels. And different methodologies had been applied as a combination with resin squeeze, including DynoSlot gun perforation and section milling.

Case Study 1: One well in China Sichuan area was suffering around 500 psi in the A annulus pressure. DynoSlot gun perforation which is designed for 360° coverage was applied for roughly 10 m perforation interval. Injectivity test with water was performed, and results proved the leaking was very tight. The 0.8 m^3 resin with 6 h thickening time and 24 h waiting on resin time was pumped through coil tubing, and bullhead squeezing at high pressure is conducted. Around 90-l resin was estimated to be squeezed into micro-channel based on pressure drop data during squeezing. After waiting on resin, annulus bubbles were monitored for several days, and the annulus bubbles were dramatically reduced while still existed. A second DynoSlot perforation was applied followed with 1 cubic resin. To minimize the casing ballooning effect during bullhead squeezing which may potentially close some micro-channels during squeeze, squeezing pressure was staged down before resin built up viscosity. Around 70-l resin was estimated to be squeezed into micro-channel. After waiting on resin at low pressure, annulus bubbles were completely ceased (Fig. 3).

Case Study 2: One well in China Sichuan area was suffering around 400 psi A annulus pressure. Section milling methodology was applied to achieve a roughly 2 m window after which the cement was removed by a reamer run. Hydra-wash was then performed to thoroughly clean the window. The 1.4 cubic resin was then pumped through drill pipe with optimal pumping schedule to achieve best displacement efficiency at section milling window after which applying bullhead squeezing. Stage down squeeze was performed to mitigate casing ballooning effect. After waiting on resin, bubbles were largely reduced, and remaining bubbles were suspected from shallow formation. A second section milling operation together with reamer run and hydra-wash was performed at shallow depth to isolate the potential shallow gas. The 1 cubic resin was pumped, and stage down squeeze was performed to mitigate casing ballooning effect. After waiting on resin at low pressure, annulus bubbles were completely ceased.

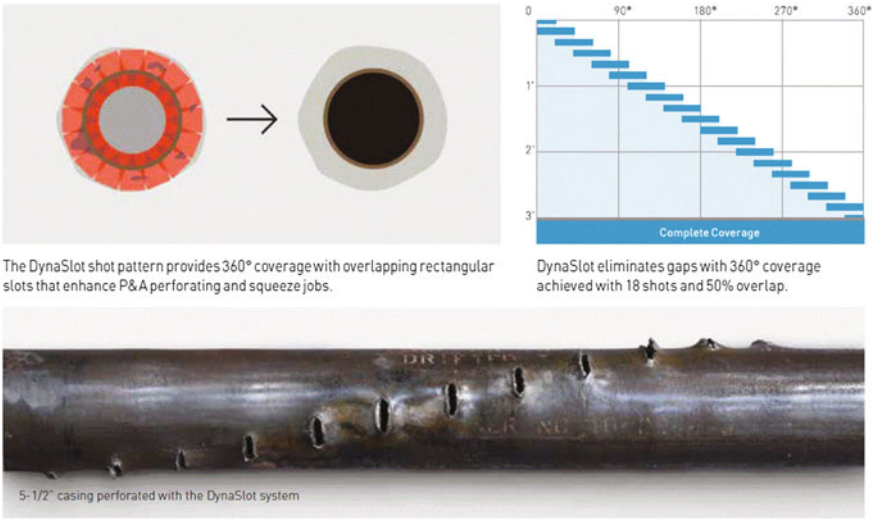

Fig. 3. Squeezing chart

4 Verification Test for Resin Application as Permanent Well Barrier for Sour Gas Wells

As stated previously, some idle wells in Sichuan Basin have sustainable casing pressure and thus have potential of H_2S exposure risk. Hence, any sealant if selected shall conduct specific test to meet the regional and company requirement for sour gas well permanent barrier.

Two Halliburton WellLock resin systems are selected in the verification test based on the anticipated bottom-hole static temperature (BHST) focusing on two vital areas: shrinkage and sour gas resistance [8].

5 Shrinkage Test

There are two sets of resin samples with different formulations immersed in two dilute sulfuric acid systems individually under pressure and temperature (high temp: 110 °F bottom-hole static temperature (BHST) and 95 °F bottom-hole circulating temperature (BHCT); low temp: 204 and 160 °F). Evaluation data was recorded in after 1, 5, and 30 days while replacing fluid each time. After 30 days testing timeframe, compression test is also performed while comparing the measurement of diameter, length, and weight. See shrinkage result in Table 1.

Note that under both low- and high-temperature conditions, the WellLock resin showed shrinkage (see specimen shrinkage per Fig. 4).

Table 1. Resin shrinkage results

Temp (°F)	Initial sample Vol (ml)	Final sample Vol (ml)	Shrinkage (%)
BHST: 110	201.7	191.21	5.20
BHCT: 95	201.26	190.86	5.17
BHST: 204	199.93	190.78	4.58
BHCT: 160	201.26	192.19	4.51

Fig. 4. Shrinkage after curing

The low temperature indicated an average 5.2% total shrinkage while the high temperature showed an average of 4.5% total shrinkage. However, the designed test failed to extinguish the shrinkage based on liquid or post set. Halliburton lab test quoted that 3–3.5% shrinkage in the liquid phase and 1–1.5% shrinkage after set. It was clear from Fig. 4 that top level of sample has been dropped while tight contact with well surface remained.

6 Sour Resistance Test

Due to the safety hazard concern of testing with H_2S, dilute sulfuric acid with varied sour density (5 and 25% mass fraction H_2SO_4) was utilized. This assumes that H_2S dissolved in either mud or water would form H_2SO_4 in wellbore condition. Result of 1-day testing showed that the low-temperature resin in both 5 and 25% mass fraction sulfuric acid had signs of surface blooming with additional 7.5% weight increment noticed in both. The high-temperature resin in 5% mass fraction shows surface blooming with color change and 4.5% weight increment (See Fig. 5), but the high-temperature resin in 25% mass fraction indicates no surface blooming or discoloration and minimal weight gain.

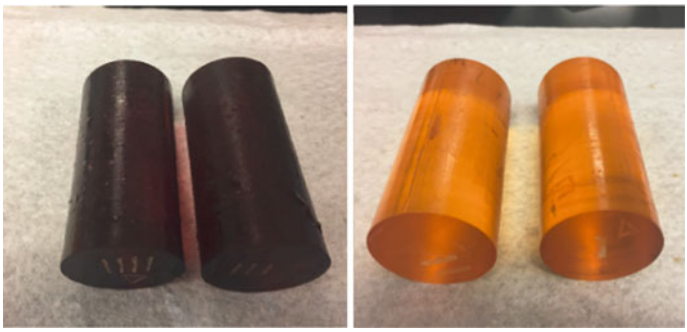

Fig. 5. Sour resistance test (Right: 25% H_2SO_4 2000 psi/204 °F; Left: 25% H_2SO_4 2000 psi/110 °F)

7 Resin as Well Barrier for SCP Wells

Prior to pump and/or squeeze sealant to seal off gas migrating path and kill sustained casing pressure, the vitalest step is to how to efficiently get all micro-fissuring fully exposed. There are over 20 wells in Sichuan Basin applying resin technology into P&A campaign by another operator with various methodologies attempting to establish micro-crack expose path: perforation and squeezing (DynoSlot gun perforation), abrasive sand jetting, and section milling. The detail methodologies are listed in Table 2 as follows:

Table 2. Resin application methodology

Methodology	Job quantity	POS
DynoSlot gun	5	50% or less
Abrasive jetting	3	50% or less
Section milling	17	90% or higher

7.1 DynoSlot Perf and Resin Squeeze

DynoSlot is enhanced perforating tools, which is designed to perforate with coil tubing while applying 360° perforation coverage (Fig. 6). There are 18 shots per 1.3 m for each 360° coverage interval. After perforation, a hydra-wash run is performed to clean out all perforation debris.

7.2 Abrasive Sand Jetting and Resin Squeeze

Like DynoSlot, the abrasive jetting tool is also deployed with coil tubing and supplies 360° jetting coverage (Fig. 7). High-speed sand jetting aims at penetrating through casing to wash out cement sheath behind and create enough cavities to spot and squeeze resin, which at the same time placing the potential issue that the clean gel and sand debris might remain in cavity without efficient cleaning out. The actual resin

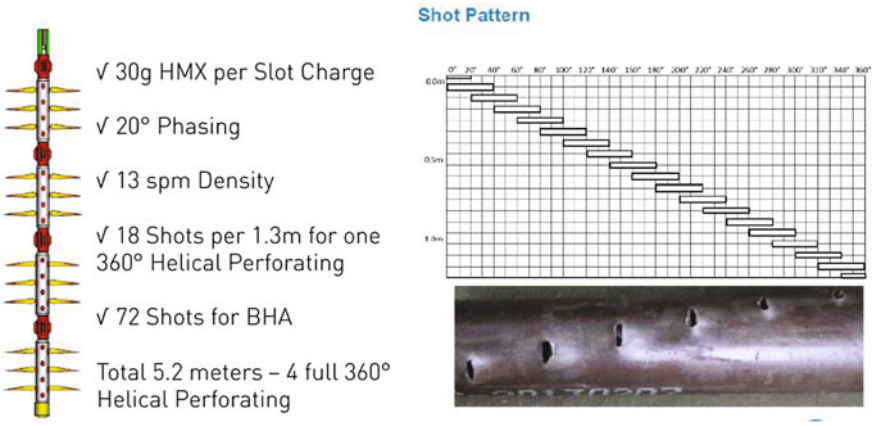

Fig. 6. DynoSlot perforation assembly

squeeze volume further proves the disadvantage: the squeezed volume is less than that of section milling trial.

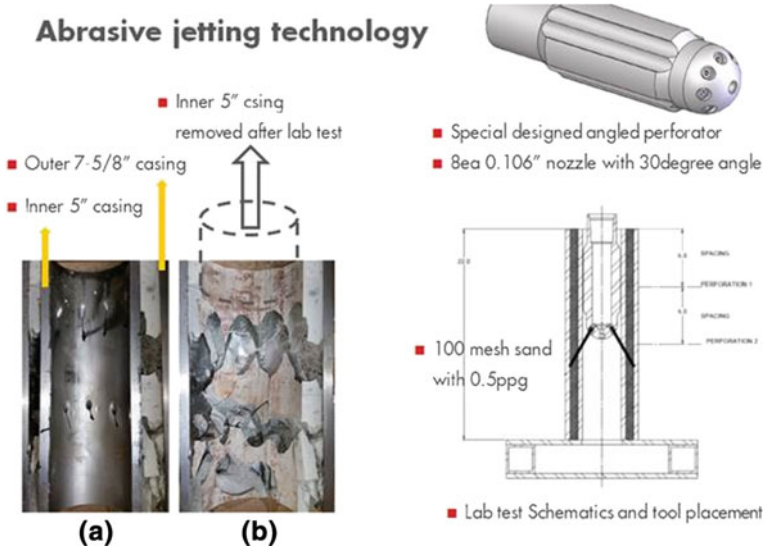

Fig. 7. Abrasive sand jetting

7.3 Section Milling and Resin Squeeze

This is the most effective but also the most costing mean compared with former two methodologies. Performed with snubbing unit and combined with reaming, hydra-wash, and surfactant soak, the entire 360° section milling window can fully be exposed and cleaned.

The first several runs with section milling assembly are to cut and mill out a certain depth of casing, followed by reamer run to ream out cement sheath behind casing or even further penetration to the formation (Rock to Rock reaming). Then, a hydra-wash run is performed to enhance the cleaning out process. At last, resin is squeezed into section milling window combined with cement plug spotted on top of resin plug.

The final field data analysis indicated around 50% or even less probability of success POS for DynoSlot perforation and abrasive sand jetting. At least two or three attempts have been conducted prior to seeing significant SCP decreasing while using the abovementioned methodologies. The main reason behind is the failure to get all micro-channels completely exposed. Gas still seeks for un-sealed cracks to communicate between gas layers and surface. The section milling methodology proves to have more than 90% POS for average 2 m section milling window achieved. The cost is also significant since section milling requires workover unit and is time-consuming to open the window (various from 0.2 m/day to 0.2 m/h highly depends on casing size, grade, thickness, and depth).

7.4 Planned Resin Application as Permanent Well Barrier to Sour Gas Wells with SCP

By synthesizing resin lab test as well as collecting lessons learned from the neighboring Operator's P&A operation, a combination of section milling and perforation methodology has been designed with resin application as sealant and cement as permanent well barriers.

Section milling is the dominant method to expose the entire annuli prior to cement/resin spotting and squeezing. Perforation and squeezing is performed below each planned section milling window as operational barrier to decrease the gas exposure volume (even perforate and squeeze indicates less than 50% probability of success POS in terms of kill annulus pressure, it is still proven way to decrease a certain amount of sustained casing pressure value to reduce the risk of encountering great amount of gas after opening the section milling window).

For a case study in this application, the well of interest has three gas layers required to be isolated. The deepest sour reservoir (A gas layer) is planned to be sealed by spotting 100 ft cement plug across entire annuli (normally via section milling) concerning uncertainty in long-term resin sour resistance. The shallower sweet gas zone B is also isolated by cement for conservative consideration. This barrier on top of the gas zone B serves as the primary isolation of sweet gas zone and secondary isolation insurance to seal off deeper sour gas zone.

For the shallowest gas zone C, a trial of resin plug is determined to seal off the gas migration path after getting two deeper zones fully secured. A 2 m section milling interval is decided to squeeze resin, which can save significant rig time and cost comparing to section milling. Another 100 ft cement plug is remained to be spotted at top of resin plug inside casing considering there is no longevity test to fully prove its performance in terms of permanent P&A (the longest test time frame for resin plug is less than 2 years so far).

The typical permanent well barrier design concept is listed in Fig. 8.

Conventional cement barriers are set accordingly to isolate the sour gas A and the sweet gas B. The 7 ft (2 m) section milling window squeezed by resin is established to isolate sweet gas zone C.

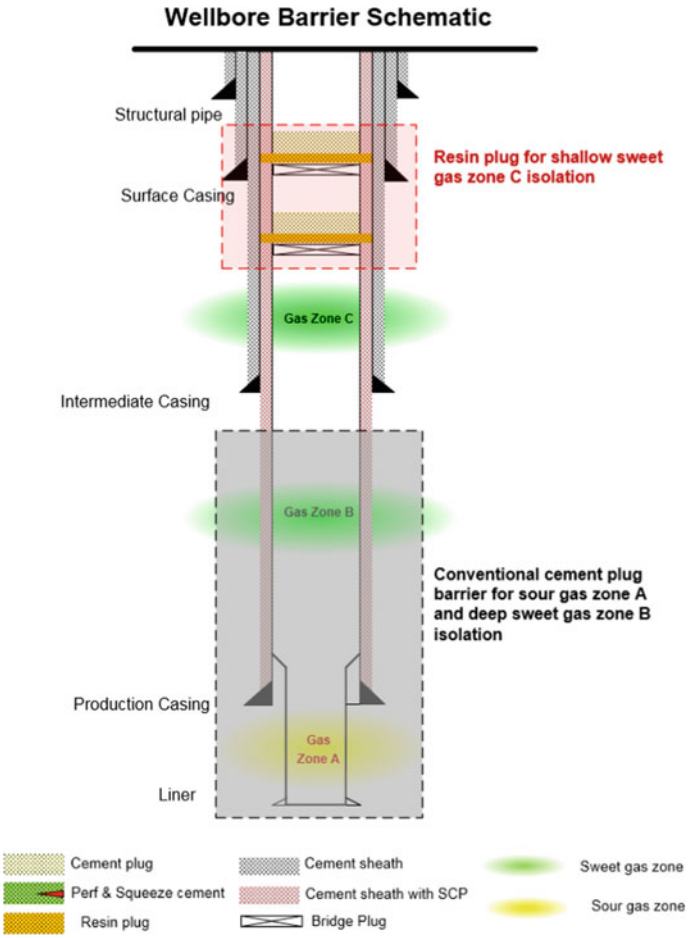

Fig. 8. Permanent well barrier using resin technology

8 Conclusion

Resin has been tested and used in the oil industry, proving to be an effective sealant to kill sustained casing pressure for the wells with poor cement jobs. Its superior mechanical property shed convincible evidence that it can withstand the harsh down-hole environment and remains its integrity as sealant. In combination with optimized annuli exposure methods such as section milling and perforation, resin application helps achieve rig time and cost saving, while successfully mitigate sustained casing pressure and add extra reliable well barrier for the wells with sustainable casing pressure.

Acknowledgements. The authors would like to thank management of UECSL, SWOG, and Halliburton for their permission to share the information in this paper. The authors also thank all the personnel, particularly field operators, who involved in the data collection at the field site and providing suggestions to the resin application as the permanent well barrier.

References

1. Ma X (2017) A golden era for natural gas development in the Sichuan Basin. Nat Gas Ind B 4 (2017):163–173
2. Ma Y, Cai X, Zhao P et al (2010) Distribution and further exploration of the large-medium sized gas fields in Sichuan Basin. Acta Petrolei Sinica 31(3):347–354 (in Chinese)
3. Ma Y, Zhang S, Guo T et al (2008) Petroleum geology of the Puguang sour gas field in the Sichuan Basin, SW China. Mar Pet Geol 25(4–5):357–370
4. Wu Q, Tang M, Luo W et al (2016) Diagnostic and evaluation method of annulus pressures and its application in high H_2S gas wells in Yuanba field. In: Drilling and production technology, Nov 2016 (in Chinese)
5. NORSOK Standard D-010 (2013) Well integrity in drilling and well operation
6. OP071 Oil & Gas UK (2012) Guidelines on qualification of materials for the suspension and abandonment of wells
7. Beharie C, Francis S, Ovestad KH Wellcem. Resin: an alternative barrier solution material. In: SPE Bergen one day seminar, Bergen, Norway, Apr 2015. SPE-173852-MS
8. Veigel J, Prescott R, Bevern J, Zheng X, Martin R ETC preliminary report of CDB P&A with resin project S170094 & S170095 (ETC-TS30) ASBU

Water Disposal Management in a Sour Gas Field Development in Sichuan

Yan Xue[1(✉)], Minh Vo[1], Yue Yu[1], Frank Singleton[1], and Junliang Zhang[2]

[1] Unocal East China Sea Ltd, UECSL, Beijing, China
{ynxu, vomi, yydf, sifr}@chevron.com
[2] Southwest Oil and Gas Company, CNPC, Beijing, China
kvdd@chevron.com

1 Introduction

This paper is to present a sour gas project development in Sichuan, China. The full field development schematics are shown in Fig. 1.

The project involves the development of gas resources in Triassic carbonate reservoirs, of which their structure is normally large. The reservoir fluid is dry gas, with high concentration of H_2S and CO_2.

For this paper, the disposal water and its treatment process will be key and described at a deeper detail.

2 Disposal Water Sources at the Gas Plant GP

There are two sources of water at the gas plant, which are treated before injection into the subsurface formation: (a) the produced water from the producing wells collected at gathering station and (b) the river water after usage in the sulfur plant and gas plant (GP). At the current stage of production, the produced water collected at the gathering station (GS) is stable and its volume is very small, approximately 1% of the river water (Fig. 2). As the water sources have different compositions and impurities, the water treatment for these water sources is different.

3 Produced Water and Its Treatment at GS

The produced water accumulated at GS is mainly the water from the subsurface gas formation, coming along with a small amount of overhaul water, as shown in Fig. 3.

The produced water from the producing wells have two phases in the surface facilities: (a) liquid phase and (b) vapor phase. The liquid phase can be firstly separated at the production separators at the GS. For the vapor phase, it comes along with the gas stream into the filter separators, and then, to the dehydration unit (TEG). The vapor

S. M. Shemwell and J. Lin (eds.), *Proceedings of the International Petroleum and Petrochemical Technology Conference 2018*,
https://doi.org/10.1007/978-981-13-2173-3_8

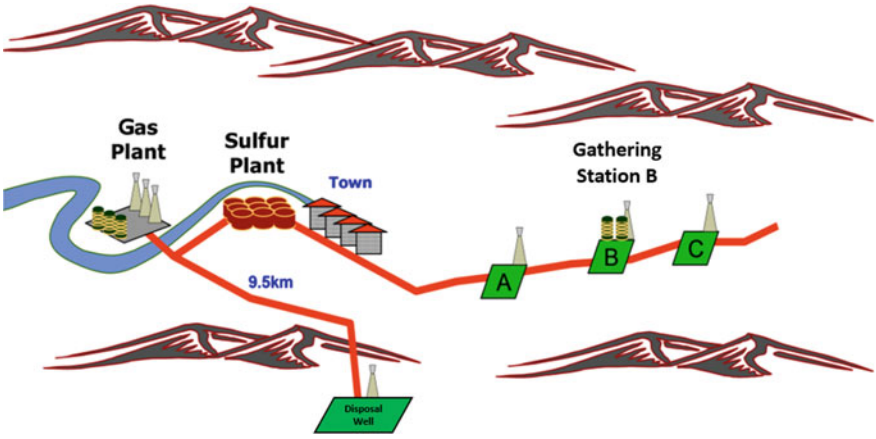

Fig. 1. Surface layout of sour gas project development

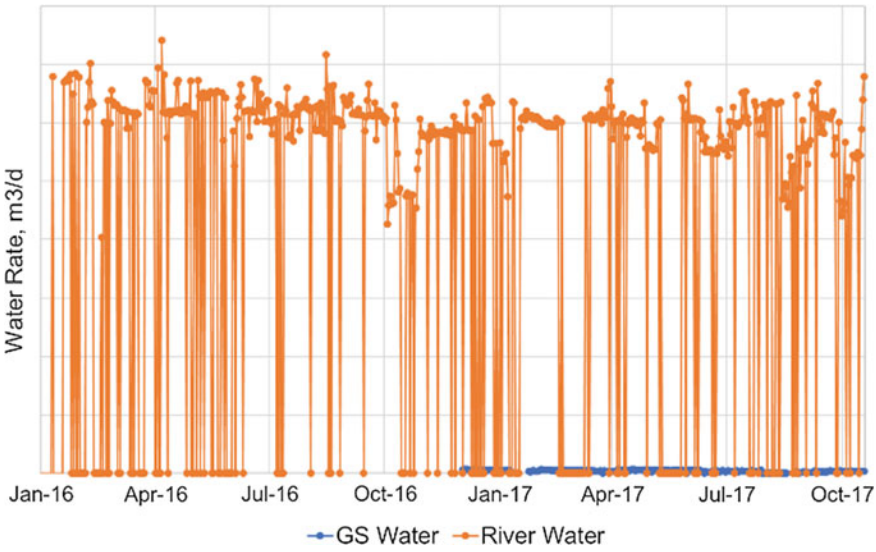

Fig. 2. Two water sources at the gas processing plant

water will thus be completely separated from the sour gas. All the water sources, including separated water, vapor water, and overhaul water, will flow into a flash drum to remove H_2S before it goes to the produced water tank from where it is trucked out.

For sour gas field development with high H_2S, the elemental sulfur precipitation occurs when the reservoir pressure declines. With multiple stages of filtration put in place to remove sulfur/solids at gathering station, elemental sulfur is accumulated at the filters of the surface facilities equipment (Fig. 4).

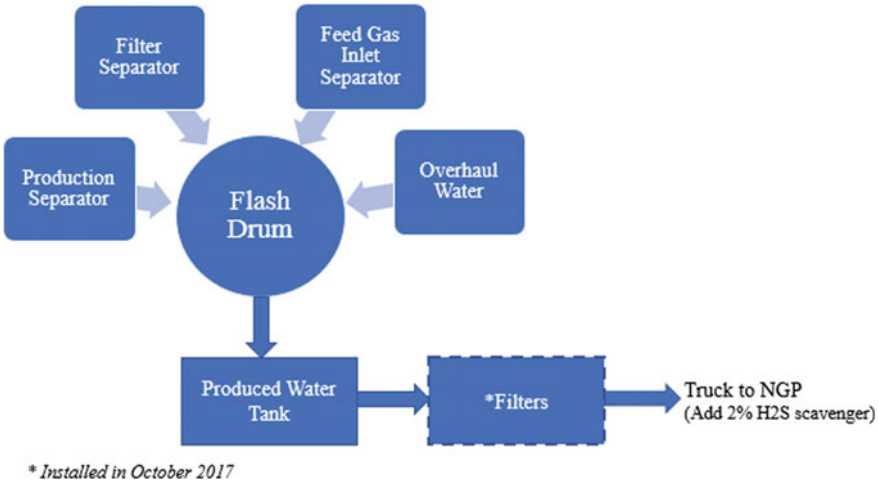

Fig. 3. Water process at gather station

Fig. 4. Solids (mainly sulfur) in separator filters

Some of the elemental sulfur is found as suspended solid particles in the produced water. Table 1 shows the pH, concentration of solids, and grease from the water samples of the flash drum. As the produced water volume is small, it is decided to treat the produced water at the GS before transporting the water by trucks to the gas processing plant.

An additional filter was added by operations at the downstream of the produced water tank. After the installation of this filter, the water quality has improved significantly (Table 1).

Table 1. Water quality at gathering station

Sample date	pH	TSS, mg/L	Grease and oil, mg/L	Sample location	Comment
9/28/2017	10.3	726	241	Bottom of produced water flash drum	With 2% H2S scavenger
9/28/2017	6.5	1204	374	Bottom of produced water flash drum	No scavenger
10/6/2017	10.6	333	40	Bottom of produced water flash drum	With 2% H2S scavenger
10/6/2017	5.7	122	99	Bottom of produced water flash drum	No scavenger
Installation of the temporary filter					
10/16/2017	10.4	187	184	Bottom of produced water flash drum	With 2% IKS scavenger
10/16/2017	5.7	58	90	Bottom of produced water flash drum	No scavenger
10/16/2017	10.6	95	89	After produced water filter	With 2% H2S scavenger
10/16/2017	5.9	25	32	After produced water filter	No scavenger
10/29/2017	10.4	93	100	Bottom of produced water flash drum	With 2% IKS scavenger
10/29/2017	5.8	126	138	Bottom of produced water flash drum	No scavenger
10/29/2017	9.9	99	107	After produced water filter	With 2% H2S scavenger
10/29/2017	5.8	17	65	After produced water filter	No scavenger
10/31/2017	8.6	60	57	Bottom of produced water flash drum	With 2% H2S scavenger
10/31/2017	5.6	34	36	Bottom of produced water flash drum	No scavenger
10/31/2017	6.0	84	47	After produced water filter	With 2% H2S scavenger
10/31/2017	5.6	26	19	After produced water filter	No scavenger

4 Water Treatment Process at GP

There are four sources of water at GP, including (a) field water (so-called the "produced" water described above, which is trucked in from GS), (b) water from reverse osmosis (RO) unit, (c) biochemical wastewater, and (d) overhaul wastewater. Each stream is treated differently and most of the water after treatment will go to the water disposal tank.

For the water flows into RO unit, it is from boilers and cooling systems. The RO unit will filter out the small solids when it goes through the multimedia filter and carbon filter. If the water quality is still poor, indicated by sampling analysis, it will

recycle to the balance tank and go through the filtration process again until it meets the required standards. After the RO unit, part of the water will be reclaimed and reused by the cooling system and the rest will flow to the injection tank (Fig. 5).

Fig. 5. RO unit water process

Biochemical wastewater is the human waste generated in the GP. Multistage of physical treatment equipment is in place to ensure the final treated water meets the standards (Fig. 6).

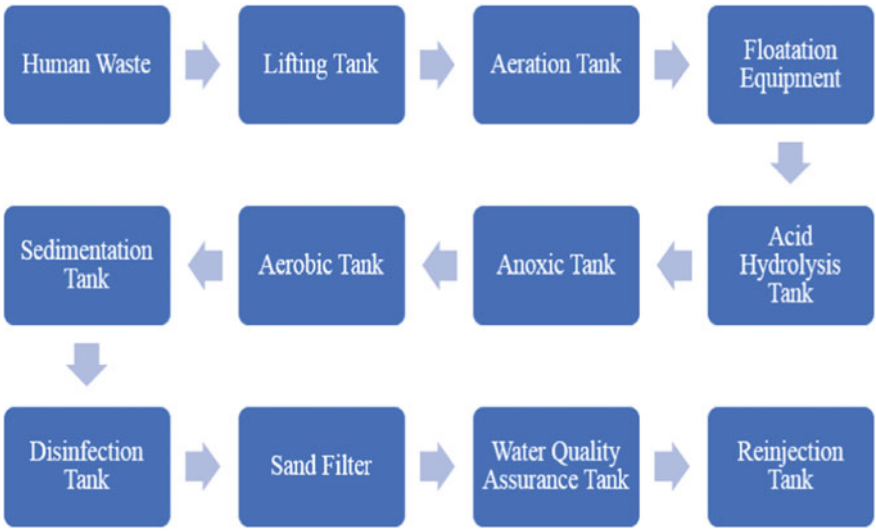

Fig. 6. Biochemical wastewater process system

Overhaul wastewater is generated during maintenance. The treatment process is mainly to eliminate oil, grease along with solids (Fig. 7).

Fig. 7. Overhaul wastewater process system

Note that after the field produced water is transported to GP, it is further treated by going through a flash drum and stripper (Fig. 8).

Fig. 8. Produced water process system at GP

5 Water Injection Objectives and Injection Formation

Based on the approved overall development plan, the operator is to inject all the produced water and water generated as a by-product of the purification plant into the subsurface formation. Produced water and the gas plant effluent injection are intended to meet the following objectives:

- The water will be treated before injection to remove most impurities. This will protect the injection system and tubulars from corrosion, and to assist with the dilution of impurities in the receiving aquifer to undetectable levels.
- Able to inject the water without disrupting gas production.
- Avoid injection into the current producing formation and into any other future prospective formations.
- Injection should be into a confined aquifer deep beneath the phreatic zone to reduce a chance of mixing with local groundwater as much as possible.
- The injection formation should have sufficient permeability to allow the anticipated water volumes to be injected at the planned rates and pressures.
- The injection pressure should be kept at a minimum, to assist in keeping the injectant away from the phreatic zone.
- Injection wells must be well cemented to avoid channeling of injection water to the phreatic zone or to the surface.

Selecting injection formation criteria include the following:

- The injection target needs to have good permeability to inject within the designed parameters.
- The injection target should have sufficient volume.
- The injection target must be sealed from surface to ensure the water will not have any negative impact to air, groundwater, and nearby wells.

6 Disposal Well Selection

After the injection formation is determined, all the available and appropriate wells in the field had been reviewed and evaluated. To select the best candidate for water disposal, several factors were taken into consideration, including lost circulation volume during drilling, well condition, and the distance of the candidate well to the GP.

Two wells were identified as the most appropriate candidate, one as the primary disposal well and the other as a backup disposal well. As the selected disposal wells had been suspended for several years, recompletion operation was designed to provide integrity, reliability, and safety at the maximum disposal rate. The well life was estimated at 20 years. The well design was comprised of the features described below.

- *Simplicity* with standard and proven equipment. Overall, the completion design was simple with a minimal number of completion accessories. Only a packer with flow profiles was run. The flow profiles were designed to receive tubing plugs and/or down-hole pressure gauges and/or a wire line insert injection check valve. All the equipment was standard and proven in the industry.
- *No dynamic seals*: The tubing was latched directly into the packer to eliminate movement of the seals between the tubing and the packer.
- *Packer*: Packer was set hydraulically on the injection tubing string. The packer was a one-trip, hydraulic set, permanent, and mill-able type.
- *Tubing*: The tubing string was corrosion resistance alloy (CRA) to ensure the disposal well completion reliability for over 20 years. This was due to disposal of water estimated to have high oxygen content.

Figure 9 illustrates the wellbore condition before and after recompletion of the disposal well.

However, during the workover operation, new information has been collected. Based on the latest risk assessment, only one disposal well is completed. The contingent plan is to lease several water disposal wells of an offset gas field if emergency occurs. In a long run, the plan is to drill a backup disposal well as needed.

7 Water Disposal Simulation Modeling

Geological data, including seismic, logging, and mudlogging data, were integrated and interpreted using industry's state-of-the-art technologies and methods. This allows defining boundaries of the water injection formation with a greater confidence (Fig. 10). As a result, the static model more accurately reflects the geological framework of the injection zone.

The injection simulation is then carried out with a dynamic simulation software, which is a multiphase, multicomponent fluid finite difference commercial simulation software widely applied to petroleum industry. The simulation model increases the ability to predict water quality and reservoir pressure at any point in the aquifer.

Based on injection simulation forecasting results, the following conclusions can be drawn:

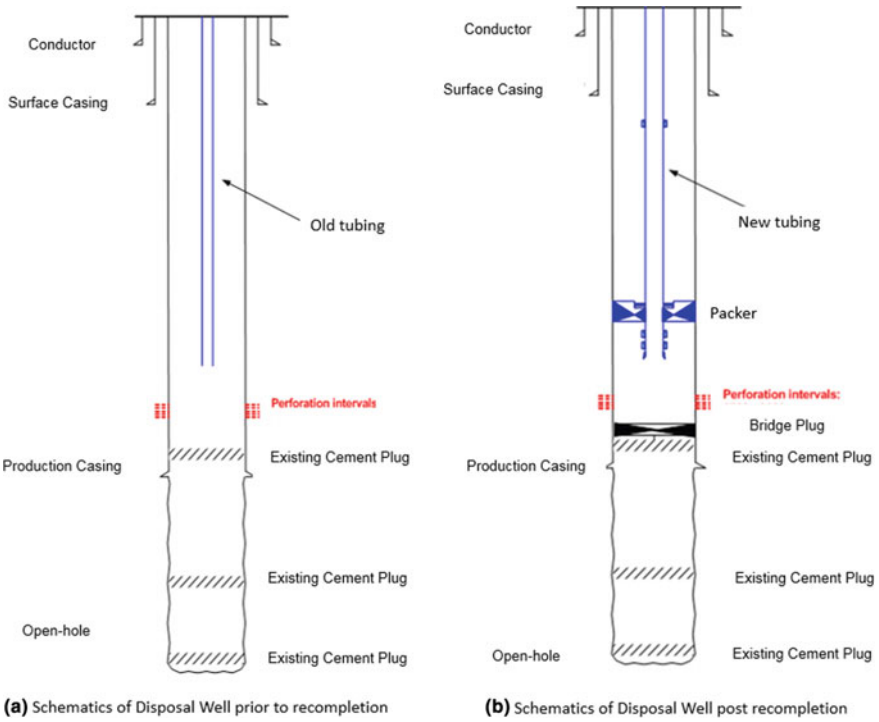

Fig. 9. Disposal well schematics

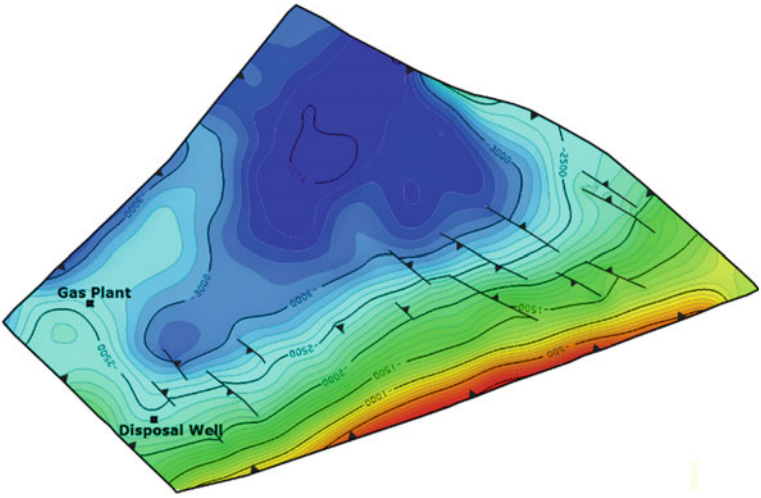

Fig. 10. Injection formation depth structure map

- The injection formation selected contains sufficient space to contain the disposal water volume that needs to be injected.
- Based on the maximum injection rate summation, the two mutually spare wells can meet the design requirement of 20-year steady injection at the maximum injection rate.
- The simulated result shows that the reservoir average pressure increase caused by injection does not lead to a fracture of upper cap formation; the diffusion range of disposal water in the injection formation is limited; the maximum diffusion range in 20 years does not exceed 2.5 km around the well hole, which will not exert bad influence on the upper part ground water aquifer.
- Suppose there is an ideal connectivity between the injection stratum and surface outcrop, based on 20-year injection at maximum injection rate, the simulation result shows that the maximum diffusion radius of injected disposal water in the injection formation in 10000 years does not exceed 6 km and it will not reach shallow aquifer or affect the shallow stratum environment.

An injectivity test was conducted on the selected disposal well during recompletion operation. The results indicated an excellent injectivity even without acid stimulation.

8 Performance Surveillance at Disposal Well

Surveillance plan is to support disposal performance forecasts for this well, to reduce uncertainty in the well injectivity.

The well injectivity model will be calibrated with a regularly acquired well head pressure (WHP) and disposal rate data. The measured injection WHP data will be converted to bottom-hole pressure (BHP) estimates. The well injectivity model is essentially used to detect changes in injectivity due to formation damage.

- An initial reservoir pressure measurement will be obtained with a static BHP measurement before water disposal begins.
- Disposal water composition will be regularly measured to assist in the design of remediating agents in stimulation treatments if necessary.
- Safeguarding the near-well environment, both deep and shallow, against possible leakage of disposal water is the objective of the testing and cement squeeze mitigation. Additionally, measures will be undertaken to quickly detect leaks in the event the cement fails.

9 Health Safety Environment HSE Surveillance

a. Detection of contamination of a deep formation above the injection reservoir, through a breach in the cement behind casing, is accomplished by monitoring of tubing injection pressure and flow rate.

- Significant increases in the injectivity of the well may be an indication that additional reservoir is open to injection. This performance change also may indicate hydraulic fracturing of the injection formation; however, such a fracturing event, common in the disposal well, is usually preceded with a period of injectivity decrease due to plugging.
- The estimated wellhead injection pressure that results in a BHP equal to the estimated injection formation fracture pressure, at various injection rates, is presented in Table 2. Caution will be taken when WHP approaches these values, and indications of fracturing, such as a sudden drop in WHP, will be closely monitored.

Table 2. Max WHP controlled at injection formation fracture pressure

Injection rate, BWPD	WHP maximum, psig
16500	2700
13000	3500
9000	3300
0	3200

After such an event, a decision will be made, depending on all available data, to run a noise log to detect flow behind the 9-5/8" casing. If such is detected, disposal will be ceased and cement squeeze attempted to stop the flow. Disposal will resume when the flow is stopped.

b. The next surveillance for HSE is the injection reservoir seal. It is monitored by reservoir pressure tracking not to exceed the fracture pressure at the weakest point of the reservoir anhydrite seal, located at the crest of the structure, at 1300 m TVD.

- A fracture of this type is more dangerous than a reservoir fracture at the well, as for the case of the latter, careful monitoring can detect such, and injection operations ceased before significant contamination occurs.
- However, a breach at the seal cannot be controlled at the well. Further, the contamination into formations above the seal would continue for as long as the injection reservoir is over-pressured.
- Fracture pressures of the disposal well were calculated using the Daines equation, which relates the fracture pressure to the estimated overburden pressure (as calculated from the density log), the estimated pore pressure, and the Poisson's ratio of the rock. The Poisson's ratio is assumed to be a property related to lithology, only, and is estimated from known anhydrite values, and measured P and S seismic velocities in the gas production reservoir.
- The fracture pressure model is calibrated to a known fracture pressure as determined by well leak off test data.
- The injection reservoir pressure at the crest is estimated to not exceed 85% of the anhydrite seal fracture pressure.

- Static reservoir pressure monitoring will be performed to ensure that the anhydrite seal pressure at the crest is not exceeded.

c. Detection of shallow contamination will be accomplished with three groundwater monitoring wells located near the surface location of the disposal well (Table 3).

Table 3. Groundwater monitoring wells

Well name	Depth (m)	Location (relative to disposal well wellhead)	Purpose
Well 1	61	360 m NW	Far downstream monitor
Well 2	70	100 m NW	Near downstream monitor
Well 3	62	355 m SE	Upstream monitor

- Disposed water composition and monitoring well water composition are both be measured regularly, to establish any correlation changes that may occur that will indicate groundwater contamination. Table 4 describes the composition measurements that will be taken and the measurement frequency.

Table 4. HSE surveillance

Type	Element monitored	Frequency
Disposed water composition	Suspended solid content oil content pH	Daily
Monitoring well water composition	Water temperature, COD, pH, oil, total hardness, ammonia nitrogen, nitrate nitrogen, sulfate, fluoride, permanganate index, sulfide, total soluble solid	Pre-disposal base line, then annual low, normal, and high water periods

Currently, there is only one injection well to take all the disposal water. Therefore, it is vital to maintain the injectivity and prevent the formation from being plugged by solids. Besides, it is required by regulation that the reinjected water of gas field shall meet certain standards as indicated in Table 5.

Table 5. Injection water requirements

Index	Range
Total suspended solids, mg/L	<25
Mid-value of suspended particle diameter, Um	<10
Oil and grease, mg/L	<30
pH	6–9

Daily water sample of the injection water is taken and analyzed at a local lab. Analyzed parameters include pH, oil content, and total suspended solids, Fig. 11. The water samples are also sent to an external lab regularly to conduct the analysis on the mid-value of suspended particle diameter. Actions are taken accordingly when abnormal water quality is observed. Overall, the injection water quality is in good condition and solids are well controlled which means the water process system is efficient and reliable.

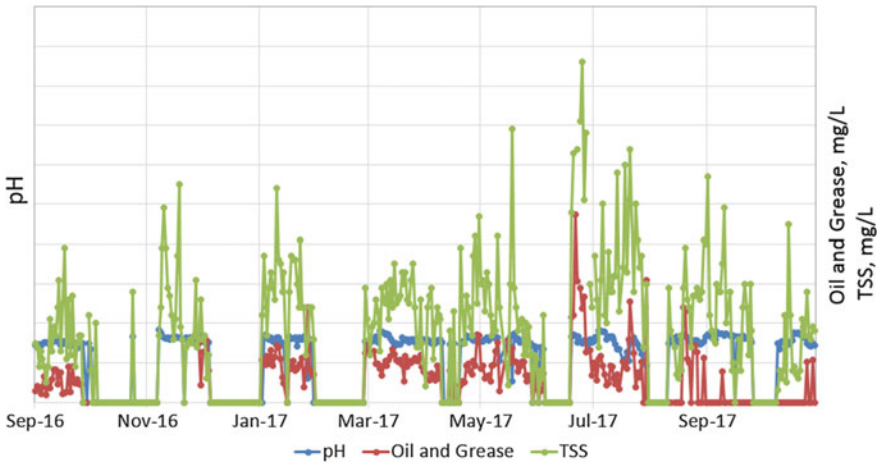

Fig. 11. Injection water quality monitoring

10 Injection Well Performance Monitoring

The injection well is monitored by SCADA, including injection pressure, injection rate, and pump status. Real-time data is available to operators in the field and engineers in the office.

Due to the excellent injectivity of this disposal well, there is no sign of injectivity contamination so far (Fig. 12).

11 Chemical Program for Water Treatment

Chemical plays an important role in keeping the water safe for transportation and clean for injection. Different chemicals are applied to achieve this goal.

At the gathering station, the water is treated with 1% H_2S scavenger before trucking out to GP. This is for the safety sake of the personnel who are involved in the water transportation and the safety of the community.

At the GP, chemicals are used at several locations to keep the water meet specifications. Coagulant is added to the upstream of the de-oiler and the fiber filter of the

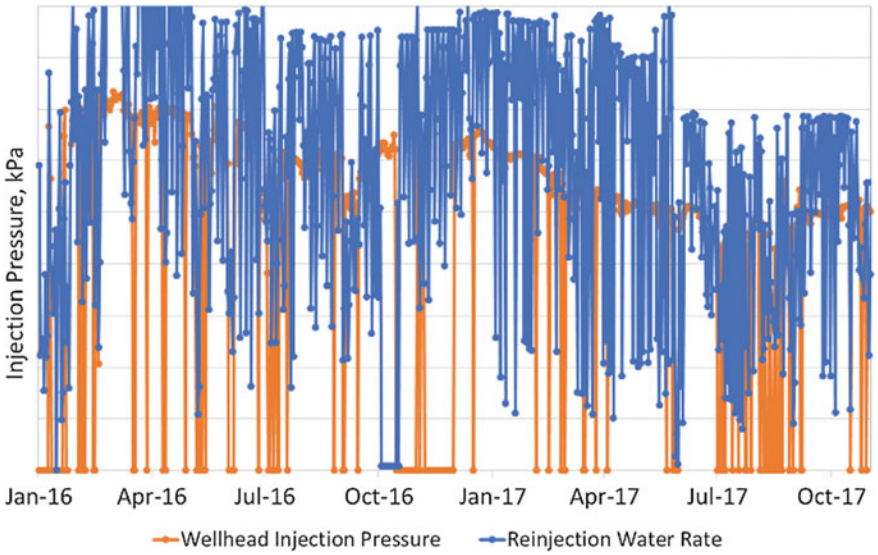

Fig. 12. Injection well wellhead monitoring history

overhaul water stream. The objective is to increase particulate size and improve the efficiency of solids removal through the fiber filter.

After the water is mixed at the injection tank, oxygen scavenger and biocide are injected into the water at the tank outlet. The oxygen scavenger is to keep the water oxygen-free, which helps minimize bacterial growth. If testing indicates bacterial growth in the water, a blend of non-oxidizing biocides can be added to kill the bacteria.

12 Conclusions

With the clear understanding of the water disposal treatment system, the visible monitoring system in place has proved that the work can be optimized in the real time.

- There are four water sources at the gas plant: field water trucked from gathering station, wastewater from RO unit, biochemical wastewater, and overhaul wastewater.
- Real-time surveillance data provides the possibility to monitor the water quality at different locations, and hence mitigation actions can be taken timely and injection requirements are met.
- Several chemicals are added to the water streams to keep the water compliant with injection requirements and safe for transportation and injection.
- Currently, there is one disposal well taking wastewater and the injection formation has excellent injectivity and can last for over 10 years before a backup disposal is available.

13 Challenges

The biggest concern for the injection water is that blending several different streams together could cause scale formation in the tank because of the different water compositions. Produced water with elemental sulfur precipitation can be very high in total dissolved solids (TDS) and includes species such as barium and strontium that form sulfate scales that are very difficult to treat. The reverse osmosis wastewater ("thick water") will also be high in TDS, so there is a possibility of an incompatibility between these two waters leading to additional scale formation, which could

- Increase TSS and particulates, resulting in the injection water no longer meeting specifications;
- The scale could potentially plug the reservoir, causing a loss of well injectivity.

Another challenge is the inevitable sulfur precipitation at gathering station. Even though several filters are installed, water is sometimes still contaminated by sulfur. To reduce exposure to H_2S and maintain production, the filters are not changed frequently. They are only replaced when pressure difference of the filter separators reaches the design limit.

Chemical treatment program needs to be optimized timely so that the treatment is effective, efficient, and economical. Particularly, H_2S scavenger, coagulant, and scale inhibitor are the most critical chemicals in the water treatment process.

Acknowledgements. The authors would like to acknowledge the management of UECSL and SWOG for their permission to publish this paper. The authors also thank all the personnel, who assisted in the publication of this paper.

Reference

1. Recommended Practice for Produced Water Reinjection in Gas Field, SY/T 6596-2004

Ultrasonic Flow Metering Device and Field Trial Success at Sour Gas Field Development

Yue Yu[1(✉)], Minh Vo[1], Sihe Zheng[1], and Junliang Zhang[2]

[1] Unocal East China Sea, Ltd, UECSL, Chengdu, China
{yue.yu, minh.vo, sihe}@chevron.com
[2] Southwest Oil & Gas Field Company, SWOG, Chengdu, China
kvdd@chevron.com

1 Introduction

This joint venture sour gas field development project is in Sichuan, China. The reservoir fluid is dry gas, with a high concentration of H_2S and CO_2. The gas flow measurement devices, located after the wellhead and before dehydration facilities, are the combination of the target flow meters and the orifice flow meter.

Meter accuracy is important for daily production measurement, well performance surveillance, and future development optimization. For a cost-effective solution, if a flow meter, e.g., target flow meter, could provide the reading error within ±10%, it is acceptable. Currently, there are two types of meters have been used in the field.

- Orifice flow meter is very reliable and normally located after the well pad separator, which provides an accurate measurement due to its device structure and dry gas rate measured. However, due to cost and operations requirement, there is only one orifice meter at each well pad so only one well can be measured at a time.
- Target flow meter is cost competitive, mainly used for the individual well's sour gas rate measurement but due to high H_2S and condensed water phase in gas (multiple-phase measurement), the accuracy is questionable.

With the practical results, the target flow meters have been replaced frequently due to the failure of providing the reliable measurement (or the target flow meters have a reading error larger than ±10% after some time put in operations). To improve the measurement accuracy and reliable operations, the target flow meter performance/failure has been investigated and several different kinds of flow meters have been reviewed, investigated, and tested.

S. M. Shemwell and J. Lin (eds.), *Proceedings of the International Petroleum and Petrochemical Technology Conference 2018*,
https://doi.org/10.1007/978-981-13-2173-3_9

2 Issues of Target Flow Meters at Sour Gas Field Development

Target meter is installed after first choke to measure gas flow rate coming directly from wellhead. Within the meter, a physical target is located directly in the fluid flow as shown in Fig. 1. The deflection and the force bar on the target are measured and then are converted to fluid velocity.

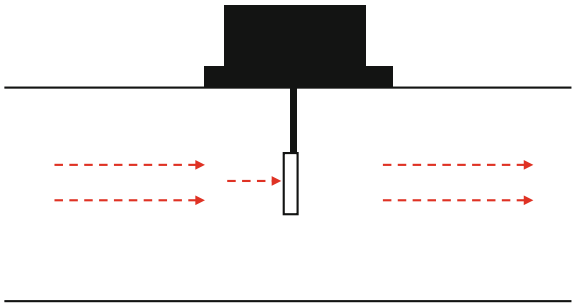

Fig. 1. How a conventional target flow meter works?

It is cost competitive and can be used for any type of liquid or gas. Therefore, the target flow meter selected to be the primary flow meter source for this joint venture gas field development. Frequent calibration is expected for verifying the measurement results.

However, the practical results showed a far low performance for the target flow meters. Investigation has been conducted whenever a target flow meter was failed. It has been learned that, for the sour gas field development, in addition to solid and condensed water produced from subsurface, chemicals are also injected for hydrate and corrosion inhibition. As a result, these target flow meters are exposed to different "debris" such as sulfur, MEG, corrosion inhibitor, solids, water, etc. These elements affect target meter operations and make it frequently failed.

More specifically, since first gas, the target meters installed in this project have shown very unreliable measurement. Figure 2 shows the reading error of several producers, of which some of them were more than 50%. This led to frequent replacement of target meters. When gas demand is high, the replacement work had to be delayed, thus the wrong reading might last for long time.

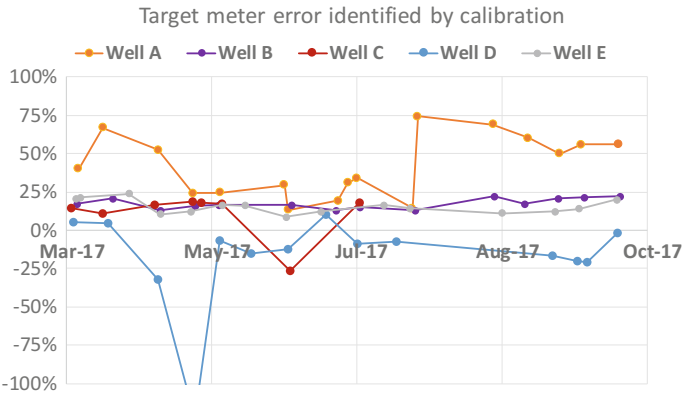

Fig. 2. Target flow meter error record

For a typical target flow meter failure, the target was open and after collecting the materials at the target, it is found that elemental sulfur was covered outside the target as shown in Fig. 3. As a result, the sensor resistance increased to about 10.10 KΩ, which is more than the maximum acceptable value. These two (sulfur around the target and sensor resistance) have been identified as the typical failure in our target flow meters.

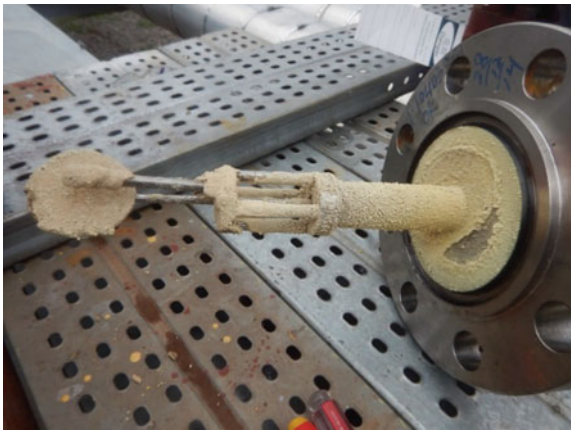

Fig. 3. Target flow meter covered by solids, most sulfur

To solve this issue and improve the data accuracy for daily well production measurement, a search for another device that can be more appropriate to this sour gas field development, associated with a certain level of condensed water and chemicals mixed in the flow, is needed.

3 How Ultrasonic Flow Meter Works?

Ultrasonic flow meter technology has been widely used in the conventional oil and gas field development [1]. When the ultrasonic flow meter is working, an acoustic signal is transmitted between upstream and downstream transducers (Fig. 4). Due to the gas flowing difference, time taken from downstream to upstream is different from the opposite direction. This difference is used to calculate gas flow rate [2].

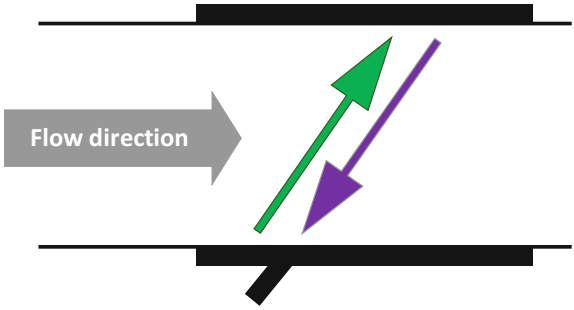

Fig. 4. Acoustic signal transmitted in two directions

Based on the pipe geometry data, gas composition, pressure, and temperature information, Reynolds number can be calculated. It varies with various flow profiles when flow rate is changing. This Reynolds number is then used to adjusted the velocity calculation (Fig. 5).

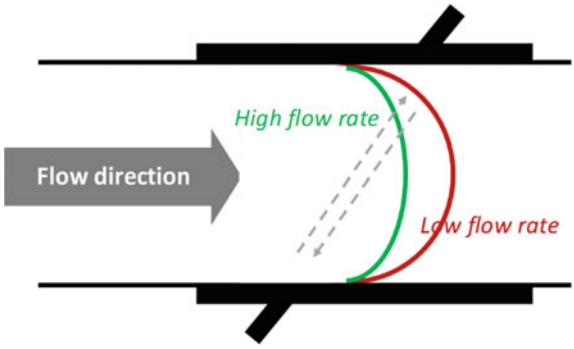

Fig. 5. Reynolds number varies with different flow rates

From delta t (time difference), geometric size, and Reynolds number, the real-time gas flow rate can be estimated. However, the ultrasonic flow meter has a challenge with the signal noise. Figure 6 shows the short circuit noise along the pipe wall. Normally, the larger and thinner the pipes are, the less short circuit noise there will be.

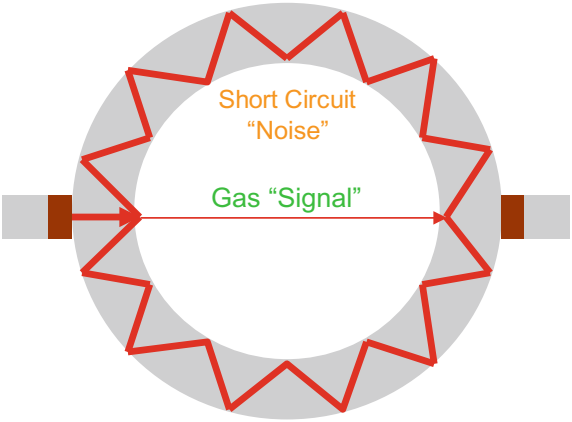

Fig. 6. Signal noise is key to impact accuracy

In the practical field application, with a nonstandard condition, the flow velocity can be calibrated by pressure and temperature acquired in the real time. Gas composition and specific gravity are also the necessary inputs for calibrating gas from ideal to nonideal [3]. The whole workflow can be explained by Fig. 7.

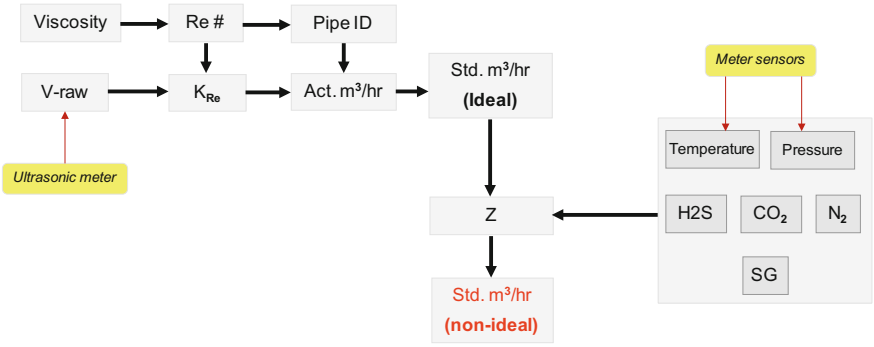

Fig. 7. Workflow of calculating flow rate from ultrasonic flow meter measurement

4 Pilot Test Deployment

To minimize the measuring error/signal noise, it is important to install the ultrasonic flow meter at appropriate pipeline locations. The criteria below should be met for any good measurement [4].

- Straight segment pipes before and after the ultrasonic flow meter location: 10–20 times and 5–10 times of pipe diameter.

- Remove loose paint and rust, particularly no insulation material, welding seam, or vibration or other interference nearby.
- Measure pipe thickness at various points along the axis of the pipe. Variation allowable depends on different manufacturers.

In the pilot tests, two types of the ultrasonic flow meters were installed based on the above standards. One was installed on vertical segment of pipe and the other was on horizontal segment, as shown in Figs. 8 and 9.

Fig. 8. Type I ultrasonic flow meter with vertical segment of pipe

Tests were conducted for each type of flow meter, assuming a constant pressure (8.8 mPa) and a constant temperature (20 °C). Real-time pressure and temperature during the six hours were slightly varied, in the range of 8.71–8.83 mPa and 22.4–22.9 °C.

Two different locations were tested: one is after the wellhead (i.e., wet gas, multiple phases); the other is after the separator (i.e., dry gas, single phase).

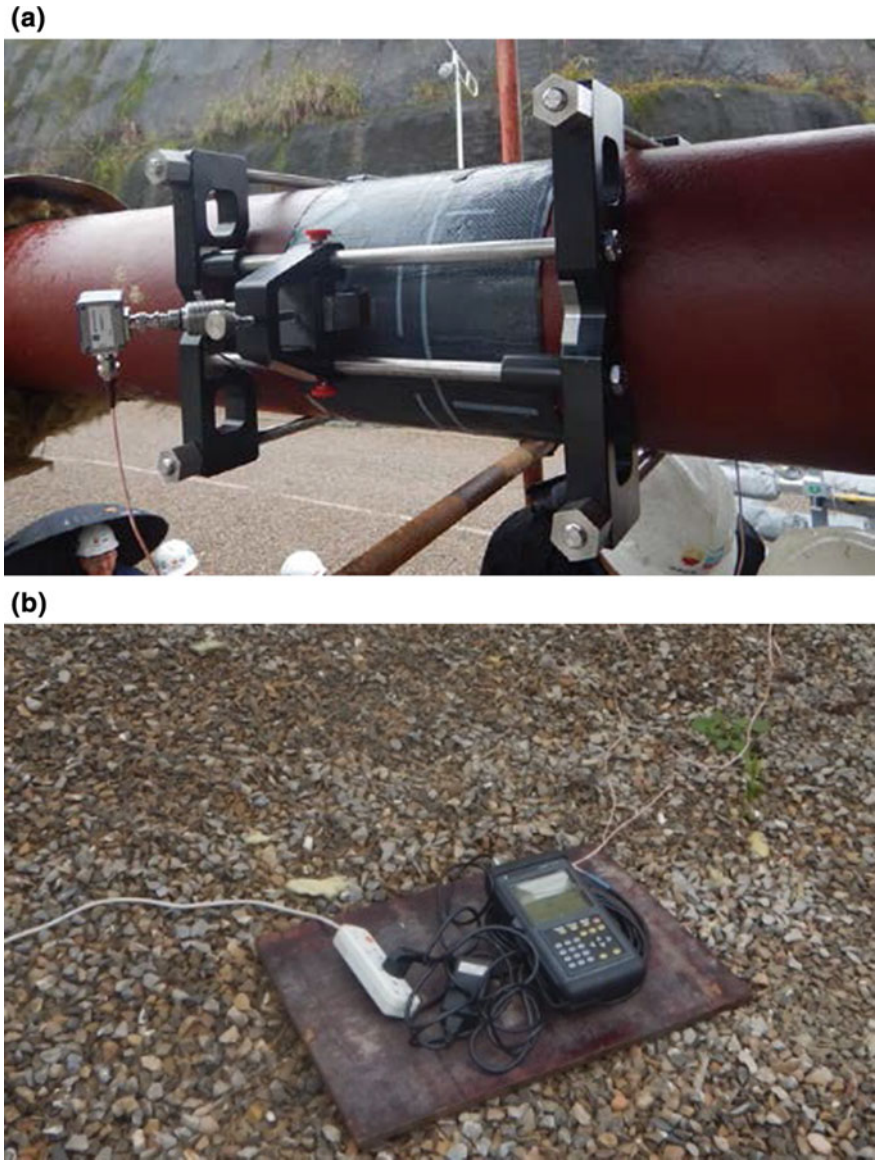

Fig. 9. **a** Type II ultrasonic flow meter with horizontal segment of pipe. **b** Type II ultrasonic flow meter's digital measurement

Like most of other gas projects, orifice meter is used. It is a flow rate measuring device works with reducing pressure at restricting flow. A relationship between the pressure and the velocity of the fluid can be built based on Bernoulli's principle. It has very good accuracy for dry gas flow measurement, so orifice meters are installed after the separator. And thus, there is no negative impact from condensed water or chemical injection. However, due to the room limit and design, only fluid from one well can be separated at one time. This is just for test purpose and after dry gas measured by orifice meter, it would mix together with separated liquid and be sent to fathering station for dehydration. This is also the reason why this process is normally called as "test separation." Even though only one well at a time, flow velocity measured from it can be used as benchmark when evaluating the accuracy of the tested ultrasonic flow meter.

To compare different types of meter and the impact of different installation locations, below pilot tests were designed and conducted. Tested meter was either installed after wellhead or after test separation as summarized in Table 1. Based on instruction of meter vendors, meters were installed either vertically or horizontally. To ensure getting representative results, each test lasted for $\sim$24 h with constant first choke opening. The second choke is controlled by wellhead pressure, thus also steady during whole test.

Table 1. Pilot tests design

Tests	Tested meter	Installation location	Installation direction
1	Type I	After separator	Vertically
2	Type I	After wellhead	Vertically
3	Type II	After separator	Horizontally
4	Type II	After wellhead	Horizontally

Figure 10a–d shows the measurement of the flow rate of both tested ultrasonic flow meter and the orifice flow meter as benchmark. It can be found that both meters worked very well after the separator when most of the water liquid phase has been removed. However, the measuring error is significantly larger when the flow meters were installed before the separator. In general, Type II ultrasonic flow meter (i.e., horizontal pipe segment) has better accuracy no matter where it was installed, compared with Type I (i.e., vertical pipe segment).

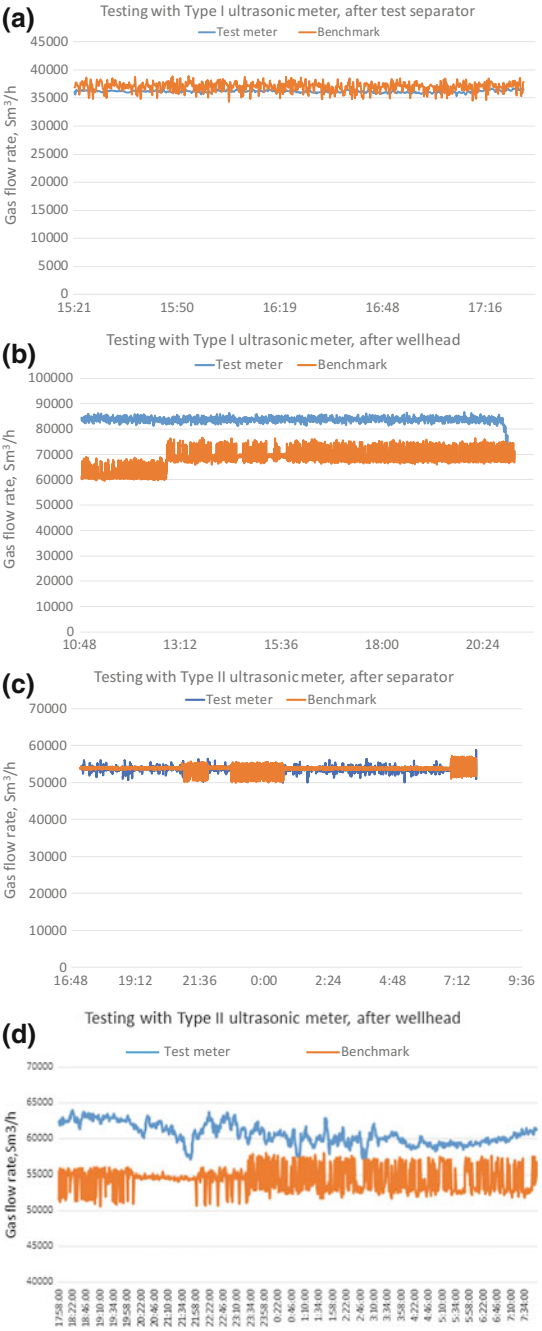

Fig. 10. **a** Flow rate with Type I ultrasonic flow meter versus orifice flow meter after separator. **b** Flow rate measurement with Type I ultrasonic flow meter after wellhead versus orifice meter after separator. **c** Flow rate measurement with Type II ultrasonic flow meter versus orifice meter both after separator. **d** Flow rate measurement w/Type II ultrasonic flow meter after wellhead versus orifice meter after separator

Detailed results are summarized in Tables 2 and 3. In these tables, the error percentage measures the gap between two average flow rates while totalizer percentage measures the gap between two total flow rates.

What we got from the pilot tests are as follows:

- Compared with the device installed on the horizontal pipe segment, installing the ultrasonic flow meter installed on vertical pipe provides better data quality.
- Condensed water in the gas stream interfered with the flow measurement. The measurement accuracy can be up to 99% when water is removed.
- When condensed water and chemicals are mixed with gas, Type II error grew to 10%. However, it can be found that the error is stable during the whole test. It provides the chance of further calibration to narrow the gap.

Each well has slightly different wellhead pressures. Ambient temperature also varies time by time. Real-time pressure and temperature information can be acquired and used for further flow rate calibration.

Table 2. Test results of Type I ultrasonic flow meter

Type I vertical pipe segment ultrasonic flow meter				
Installed location	Average flow (m^3/h)		% Error	Totalizer % Error
	Tested meter	Benchmark		
After separator	36,152	36,977	2.3	2.0
After wellhead	83,471	67,845	23.4	N/A

Table 3. Test results of Type II ultrasonic flow meter

Type II horizontal pipe segment ultrasonic meter				
Installed location	Average flow (m^3/hr)		% Error	Totalizer % Error
	Tested meter	Benchmark		
After separator	53,632	53,880	0.4	0.85
After wellhead	60,603	54,394	10.2	N/A

In fact, the above pilot tests were done with a steady production and a constant choke opening. To verify its accuracy when well production is changing [4], a test with flow rate suddenly and gradually change was conducted. In Fig. 11, the ultrasonic flow meter has a higher sensitivity than orifice meter when a flow rate is changing, especially in a short period of time.

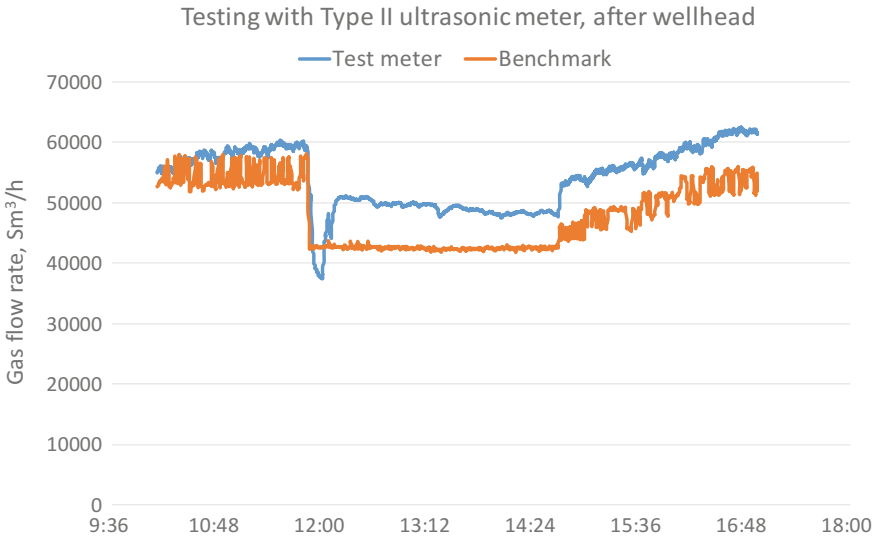

Fig. 11. Flow rate measurement w/Type II ultrasonic flow meter after wellhead versus orifice meter after separator, with changing production rate

5 Measurement Calibration

Since the main components (CH_4, H_2S, and CO_2) are very stable from all wells, it is fair to say gas composition has little or no impact on measuring accuracy.

Figure 12 shows that in the whole year water–gas ratio is also stable (maximum difference is within 0.05 MMScf/d). This is consistent with our reservoir interpretation that only condensed water in produced so its volume is easily predicted and can be maintained stable within years.

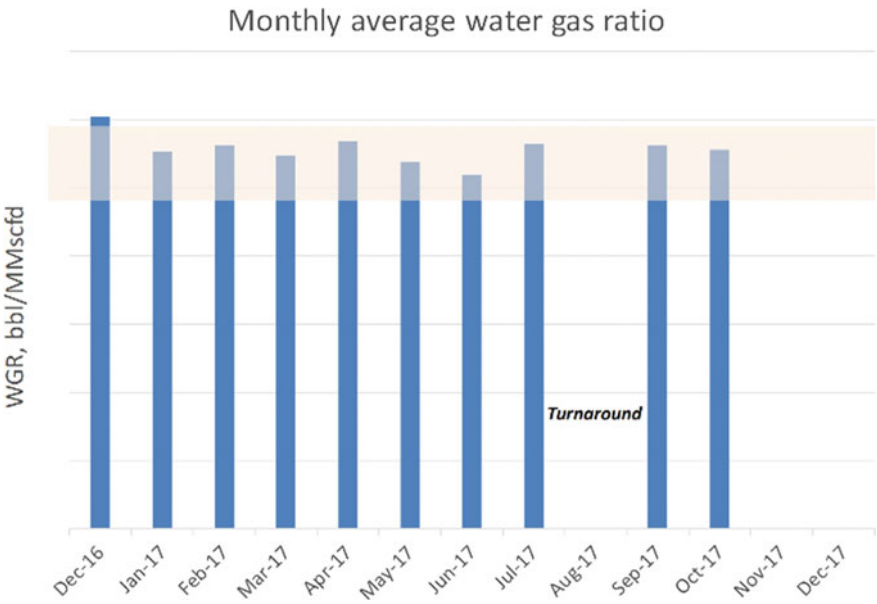

Fig. 12. Stable WGR from all wells

Since condensed water is the biggest reason of measuring error and the error is quite constant within test duration (12 h), the orifice meter flow rate can be applied to calibrate the reading [5].

Every month gas from each well is separated and measured by the orifice meter for twice, each time with at least six hours. Comparing the value with the ultrasonic flow meter measurement values, a correction factor can be determined and used to calibrate the whole month flow rate from the ultrasonic flow meter. The correction factor will change accordingly with more water produced in later life when reservoir depletion is more.

Chart below (Fig. 13) is an example that when the correction factor is used, even though production changes sharply, the overall accuracy of wet gas measurement can still be quite good, compared with orifice meter.

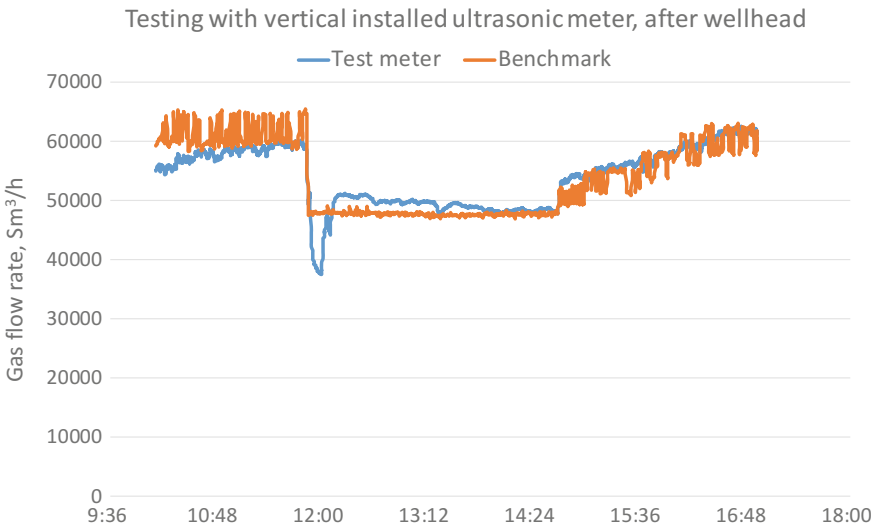

Fig. 13. Calibrated flow rate measured by ultrasonic flow meter matching well with orifice flow meter

6 Conclusion

The successful pilot test has been conducted in a sour gas project development. It has proved that after a proper deployment and calibration, the accuracy of the new type of flow meter can be achieved, as high as 99%.

- In any sour gas project development, safety is always the priority. By deploying the ultrasonic flow meters, the operational risk can be eliminated since the meter body has no direct exposure with sour gas stream and so, routine pipeline isolation and purge activities are not needed during operation, as the practical work required for the target flow meters.
- It is also cost saving that routine maintenance of the ultrasonic flow meter, such as replacing couplant and sampling material, is much simpler than conventional target flow meter and the orifice meter.
- If produced gas composition is stable and dry, or only condensed water exists, the error between real and measured will be stable and thus, a correction factor can be applied to calibrate the gap. When reservoir depletion, WGR will change, and correction factor update is needed to improve its reliability.
- Ultrasonic meter is more sensitive than orifice meter when changing operation condition such as production rate. It may overestimate or underestimate the change when production is not stable. Real-time pressure compensation and appropriate calibration can reduce the measuring error.
- There are some alternatives available in industry to accurately measure gas flow with water, such as Venturi meter [1] and sonar meter. However, considering the constraint of sour gas operational risk and well tests data available, ultrasonic meter can be one of the most safe, reliable, and cost-saving ways for gas measurement.

Acknowledgements. The authors thank UECSL and CNPC for their permission to publish this paper. The authors also thank all the personnel, particularly field operators, who involved in the data collection at the field site and providing suggestions to the design of the real-time visualization system.

References

1. Ward ER (2006, January) New class of meter solves old problem impacting well test accuracy. Soc Petrol Eng. https://doi.org/10.2118/100893-ms
2. Funck B, Baldwin P (2011, January) Wet gas ultrasonic clamp-on flow measurement. In: Offshore Mediterranean Conference
3. McKee RJ (1991, January) Transient considerations for flow measurement at gas production facilities. Soc Petrol Eng. https://doi.org/10.2118/21678-ms
4. Hatton GJ (1997, January) Multiphase flow meters and application trends. In: Offshore Technology Conference. https://doi.org/10.4043/8547-ms
5. Nederveen N, Washington GV, Batstra FH (1989, January) Wet gas flow measurement. Soc Petrol Eng. https://doi.org/10.2118/19077-ms

Effect of Additives on Viscosity of Sulfonate Gemini Surfactant Solution

Yahui Zheng[2], Shanfa Tang[1,2(✉)], Mingzheng Pu[2], Jiaxin Wang[2], and Tianyuan Zhou[2]

[1] Hubei Cooperative Innovation Center of Unconventional Oil and Gas, Yangtze University, Wuhan 430100, China
18627874020, tangsf2005@126.com
[2] School of Petroleum Engineering, Yangtze University, Wuhan 430100, China

1 Introduction

With the development of unconventional reservoirs, the limitations of polymer cross-linked fracturing fluid in the field applications appear constantly [1, 2]. Compared with the traditional polymers cross-linked fracturing fluid, clean fracturing fluid is composed of viscoelastic surfactant and the corresponding salt solution, and it has the characteristics of high rate of flowback, simple site preparation, easy injection process, and less damage to the formation [3], however, the conventional single-chain surfactant has poor stability at high temperature (>80 °C), resulting in high dosage of the agents. Gemini surfactants contain two hydrophobic chains and two hydrophilic groups with unique molecular structure and a variety of special properties that have lower Krafft point, oil–water interface tension, critical micelle concentration (CMC), and higher viscosity than ordinary single-chain surfactants [4–6], so it has a wide application prospects in the construction of temperature-resistant clean fracturing fluid system. Currently, the research on the application of Gemini surfactant in cleaning fracturing fluid is more focused on cationic Gemini surfactant. Hua and Zhu et al. [7] mixed the concentration of 2–2.5% cationic Gemini surfactant with 4% NaCl or 15% hydrochloric acid, respectively, to form a clean fracturing fluid, and found that their temperature resistance reached 95 and 80 °C, respectively. Moreover, Yang et al. [8] found that the cationic Gemini surfactant with lower concentrations (1%) can still maintain a higher viscosity (50 mPa s) at high temperature (120 °C) and high shear rate (100 s^{-1}). However, due to the positive charge-carrying properties of cationic Gemini surfactant, it is easily adsorbed on the surface of oil-bearing rocks and results in a wettability alteration of the oil–gas seepage channels, leading to about 14% permeability damage to the reservoir [9]. Based on the fact that anionic Gemini surfactant has lower adsorption loss and reservoir damage than cationic Gemini surfactant, domestic and foreign scholars have conducted research on anionic Gemini surfactant viscoelastic fracturing fluid in recent years. Tang et al. [10, 11] studied the viscosity behavior of

S. M. Shemwell and J. Lin (eds.), *Proceedings of the International Petroleum and Petrochemical Technology Conference 2018*,
https://doi.org/10.1007/978-981-13-2173-3_10

sulfate Gemini surfactant solution and found that increasing the length of the hydrophobic carbon chain and the spacer group and the additives concentration favored the increase of solution viscosity. In particular, adding the same amount of sodium dodecyl benzene sulfonate, the solution viscosity can be increased ten times [12]. Zhao et al. [13] constructed a carboxylate Gemini surfactant cleansing fracturing fluid (3% DC16-4-16 + 0.04% ZnO) and they found that this kind of carboxylate Gemini surfactant system had good shear stability at high temperature(100 °C), carrying proppant stability (<5 cm min^{-1}) and fast automatic breaking performance (20 min, <5 mPa s). However, there is little systematic research on the effect of additives on the viscosity behavior of anionic Gemini surfactant solution at high temperature ($\geq$ 90 °C), especially sulfonate Gemini surfactant. In this paper, the viscosity behavior of laboratory preferred sulfonate Gemini surfactant (DS18-3-18) solution at high temperature and the effect of different types of additives (NaCl, SDBS, dodecanal, nano-MgO) on the viscosity of DS18-3-18 solution was studied by viscosity measurement, and their micellar microstructures were observed by SEM to study its thickening mechanism. Accordingly, this study will provide an experimental basis for the application of DS18-3-18 in building temperature-resistant clean fracturing fluid system and theoretical basis for the study of microscopic viscosity-increasing mechanism.

2 Experimental

2.1 Materials

The sulfonate Gemini surfactant (DS18-3-18) was supplied by the School of Petroleum Engineering, Yangtze University and purified with ethyl alcohol by rotary evaporation, then dried to constant weight. The additives of NaCl, SDBS, and dodecanal were provided by Tianjin Beilian Chemicals Co., Ltd (Tianjin, China). The nanoparticles of MgO were provided by HT.NANO (Nanjing, China).

2.2 Solution Preparation

6% solution of each surfactant was prepared by weighing accurately 3 g of each and dissolving with distilled water to make 50 mL of the solution. For preparation of 1, 2, 3, 4, and 5% solution of each surfactant, same protocols were applied; however, 0.5, 1, 1.5, 2, and 2.5 g were used instead of 3 g.

2.3 Solution Viscosity Measurement

Viscosity test of sulfonate Gemini surfactant solution is performed by a Physica MCR-301 rheometer. The temperature of the viscosity test is 90 °C and shear rate is fixed with 170 s^{-1}. The viscosity test error is 1 mPa s $\pm$ 0.005 mPa s.

2.4 Microstructure Measurement

The micellar structure of sulfonate Gemini surfactant solution was measured by using an S4800 field emission scanning electron microscopy. The test solution was placed in a liquid nitrogen tank for quick freezing. After freezing, the sample was quickly placed in a freeze dryer for drying for 24 h. The samples were coated with a conductive adhesive on a scanning electron microscope and the platinum was sprayed with an ionic sputtering apparatus. Finally, the samples were observed by S4800 field emission scanning electron microscopy.

3 Results and Discussion

3.1 Effect of Concentration

The viscosity of DS-18-3-18 solution was investigated through changing the concentration at 90 °C and 170 s^{-1}. As can be seen from Fig. 1, the viscosity of the DS-18-3-18 solution increases with the increase in the concentration, and there is a sharp increase when the concentration increases from 3 to 4%. Then the viscosity tends to increase slowly as the concentration of the solution becomes more than 4%, and the tackifying ability becomes weaker. The reason is that the micelle structure of sulfonate Gemini surfactant changes in solution with the increase in the concentration, and the micelles change from spherical micelle into rod micelle, and even intertwine to form stable network structure which exhibits better viscosification [14]. However, the micellar structure self-curls up to a steady state as the concentration continues to increase, leading to the viscosity changing little. Thus, 4% DS-18-3-18 solution is selected for the next research of additives effect.

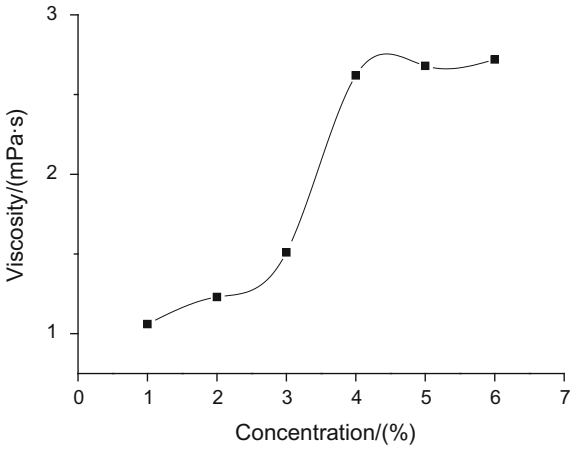

Fig. 1. Effect of concentration on the solution viscosity of DS18-3-18

3.2 Effect of Additive on Viscosity of Sulfonate Gemini Surfactant Solution

3.2.1 Effect of NaCl

The effect of concentration of NaCl on the viscosity of 4% DS18-3-18 solution was investigated at 90 °C and 170 s^{-1}. It can be clearly seen from Fig. 2 that the 4% DS18-3-18 solution viscosity decreases with the concentration of NaCl increasing, and the solution viscosity decreases from 3.08 to 0.53 mPa s. These phenomena may attribute to the strong repulsion between the Na+ and the head group of the DS18-3-18, such repulsion will reduce the solubility of the surfactant in water and will not be conducive to the formation of micelles in the solution, then resulting in a decrease in viscosity [15]. Therefore, NaCl does not exhibit viscosification for DS-18-3-18 solution.

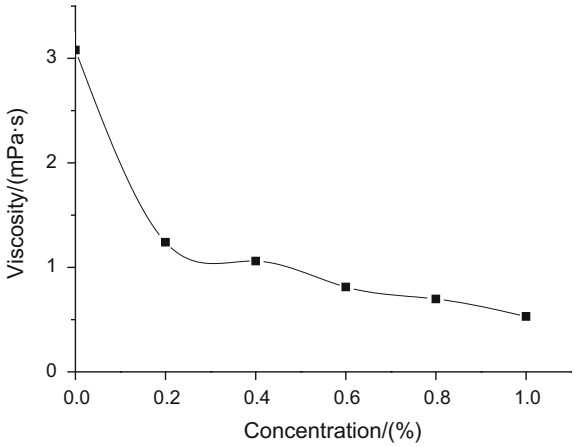

Fig. 2. Effect of concentration of NaCl on the viscosity of 4% DS18-3-18 solution

3.2.2 Effect of SDBS

The effect of different concentration of SDBS on the viscosity of 4% DS-18-3-18 solution was investigated at 90 °Cand 170 s^{-1}. As is shown in Fig. 3, the viscosity of DS18-3-18 solution shows an increasing trend with the increases in the concentration of SDBS, and reaches its maximum of 6.13 mPa s at the concentration of 3%. The possible reason is that the surfactant of SDBS with single-chain has a synergistic effect on DS18-318, resulting in the formation of a network structure in the solution, which leads to an increase in solution viscosity [11]. Thus, the addition of SDBS is beneficial to the temperature resistance and viscosity increasing of the 4% DS-18-3-18 solution.

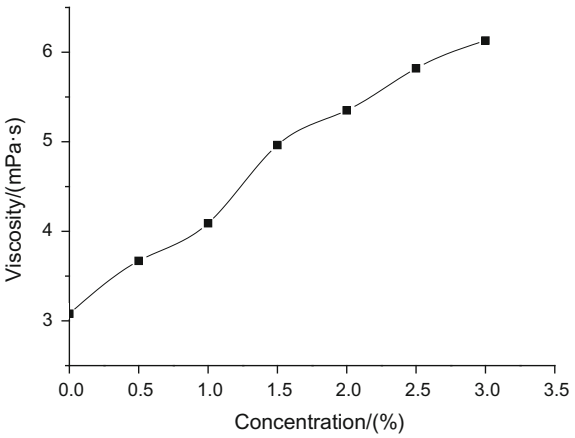

Fig. 3. Effect of concentration of SDBS on the viscosity of 4% DS18-3-18 solution

3.2.3 Effect of Dodecanal

The effect of different concentration of dodecanal on the viscosity of 4% DS-18-3-18 solution was investigated at 90 °C and 170 s^{-1}. As can be seen from Fig. 4, the viscosity of the 4% DS-18-3-18 solution increases with the concentration of dodecanol increasing. Especially, the viscosity of the solution increases from 3.08 to 32.75 mPa s when the concentration of dodecanol is 3%, which satisfies the viscosity(25 mPa s) requirement for the effective fracturing fluid to carry proppant at high temperature. This is due to the fact that the water-insoluble dodecanol can effectively reduce the critical micelle concentration of DS18-3-18, and its long carbon chain and alcoholic hydroxyl structure make it easier for surfactant to form rod-like micelles, which is beneficial to the increase of the viscosity of the system [16]. Therefore, the addition of dodecanol is significant to increase the temperature-resistant viscosity of the solution.

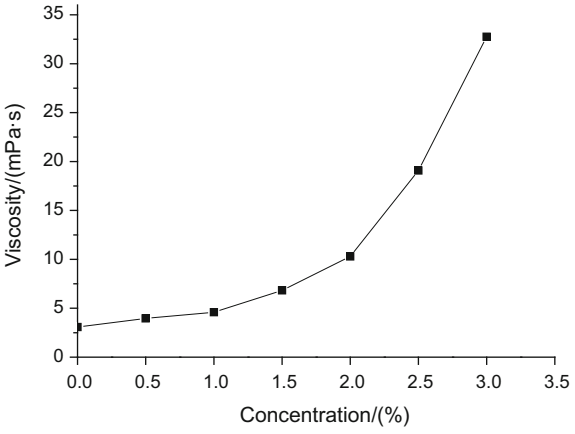

Fig. 4. Effect of concentration of dodecanal on the viscosity of 4% DS-18-3-18 solution

3.2.4 Effect of Nano-MgO

The effect of different concentration of nano-MgO on the viscosity of 4% DS-18-3-18 solution was investigated at 90 °C and 170 s^{-1}. Figure 5 shows that the viscosity of the 4% DS18-3-18 solution increases first and then decreases with the increase in nano-MgO concentration. And the temperature-resistant viscosity performance of the solution is the best at the nano-MgO concentration being 0.020%, which means the viscosity of 4%DS18-3-18 + 0.02%MgO increasing to 17.2 mPa·s and being 6.4 times than that of 4%DS18-3-18. Consequently, the addition of nano-MgO plays an important role in the thickening effect of 4% DS18-3-18 solution. The possible reason for this phenomenon is that nano-MgO under a certain concentration acts as a connecting factor in the space nodes where the micelles are intertwined by themselves to promote the cross-linking of the micelles and obviously increase the viscosity of the solution and the stability of the network structure [17]. The nanoparticles will adsorb each other in solution with the further increase in the amount of nanoparticles, then affecting the micellar structure in solution, and making the solution viscosity decreased.

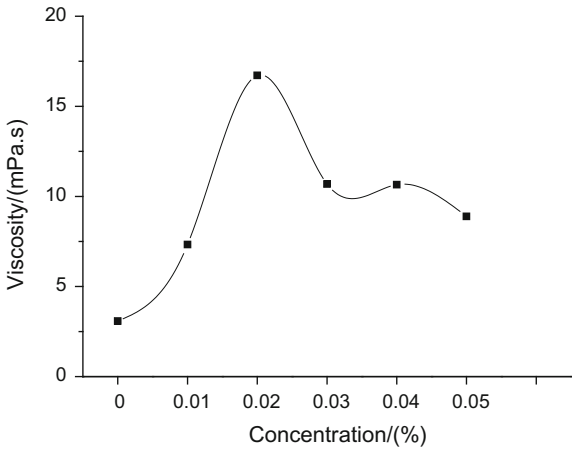

Fig. 5. Effect of concentration of MgO on the viscosity of 4% DS-18-3-18 solution

3.3 Thickening Mechanism

As can be seen from Sect. 3.2, the viscosity of the NaCl-added compound solution decreases, and the viscosity of the compound solution added with SDBS or dodecanal all increases. Therefore, the micellar structure of the compound solution of 4% DS18-3-18 and its additive was investigated by SEM to study the effect of additives on solution microstructure and illustrate the mechanism of viscosity increase. It can be easily observed from Fig. 6 that DS18-3-18 with no additive self-assembled in solution to form a large number of sheet micelles over the entire space and the structure is complete (Fig. 6a); DS18-3-18 with 1% NaCl self-assembled in solution to form the sheet micelles but the number of sheet micelles is significantly less than 4% DS18-3-18 solution, leading to the decreased viscosity in solution (Fig. 6b); micelles formed by

self-assembly of DS18-3-18 with 3% SDBS in solution turn into worm-like from the previous sheet, and the diameter of worm-like micelles is about 1 μm, and these worm-like micelles entangle with each other to form a network structure, leading to the increased viscosity in solution (Fig. 6c); and DS18-3-18 with 3% dodecanol self-assembled in solution to also form the sheet micelles and the number of sheet-like micelles increases significantly compared with 4% DS18-3-18, and the micelles arranged more closely to form the obvious layered shape, resulting in a significant increase in viscosity of the solution (Fig. 6d). Thus, the sheet micelle with the close structure may be the reason that the solution with 4% DS18-3-18 and dodecanol has better resistance to temperature. However, the microscopic thickening mechanism of nano-MgO on DS18-3-18 solution is under study and will be described in another paper.

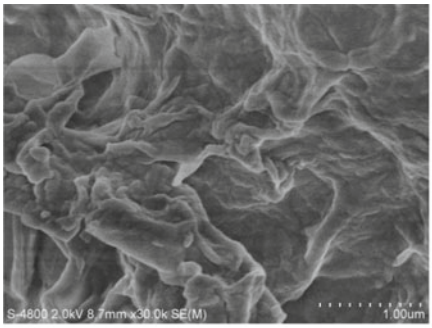

(a) micellar structure of 4% DS18-3-18 solution

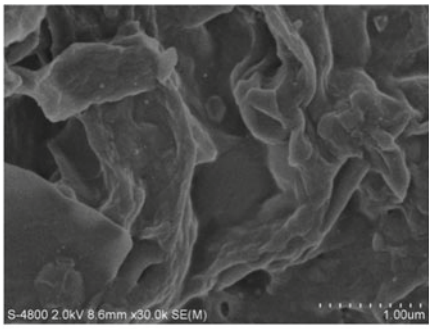

(b) micellar structure of 4%DS18-3-18+1% NaCl

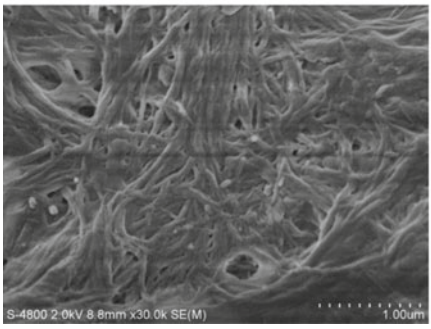

(c) micellar structure of 4%DS18-3-18+3% SDBS

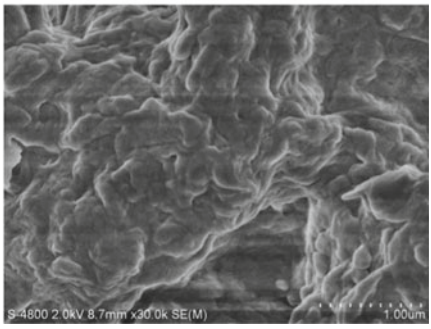

(d) micellar structure of 4%DS18-3-18+3% dodecanal

Fig. 6. Effect of additives on the microstructure of sulfonate anionic Gemini surfactant solution

4 Conclusion

(1) The viscosity of the DS-18-3-18 solution increases with the increase in the concentration and the increase tends to be gentle when the concentration is more than 4%, and the optimal concentration of the solution is 4%.
(2) The NaCl additive cannot increase the viscosity of the 4% DS-18-3-18 solution, and the additives of SDBS, dodecanal, and nano-MgO can be a significant increase in the viscosity of their complex solution.
(3) The viscosity of the compounding solution with 4% DS18-3-18 and 3% dodecanol can reach 32.75 mPa s at 90 °C, which meets the required viscosity of the fracturing fluid.
(4) The additives can change the micellar structure of the anionic Gemini surfactant solution, affecting the viscosity of the solution; furthermore sheet micelles with close arranged structure are more conducive to the solution viscosity.

Acknowledgements. This work is supported by the National Natural Science Foundation of China (51474035): The fundament study of high-temperature clean fracturing fluid constructed by anionic Gemini surfactant and nanoparticle and Innovation Fund Project of Hubei Cooperative Innovation Center of Unconventional Oil and Gas (HBUOG-2014-2): Adsorption desorption characteristics of shale gas and optimization of clean fracturing fluid.

References

1. Beckwith R (2012) Depending on Guar for shale oil and gas development. J Pet Technol, pp 44–55
2. Li L, Nasr-El-Din H, Cawiezel K (2010) Rheological.:'Properties of a New Class of Viscoelastic Surfactant'. SPE Prod Oper 25(3):355–366
3. Yan Z, Dai C, Zhao M et al (2015) Research and application of clean fracturing fluid. Oilfield Chem 32(1):141–145
4. Xu L (2010) The synthesis and evaluation of gemini. Daqing Petroleum Institute
5. Zhou P (2016) Synthesis and solution viscoelasticies of novel trimeric anionic surfactants. Jiangnan University
6. Li G, Zhao L, Wang P et al (2016) Synthesis of quaternary ammonium gemini surfactants N, N′-bis (dodecyl tetramethyldimethyl)-1,4-p-xylylene chloride and performance. Fine Chem 33(5):519–523
7. Hongjun Zhu, Hua Niu, Pingjun Lou et al (2011) Synthesis and properties of acid cleansing fracturing fluid containing gemini surfactant. Adv Fine Petrochemicals 12(10):5–8
8. Yang J, Guan B, Lu Y et al (2013) Viscoelastic evaluation of gemini surfactant gel for hydraulic fracturing. SPE165177
9. Liu Y, Guo L, Bi K et al (2011) Synthesis of cationic gemini surfactants and their application in water locking damage. Fine and Specialty Chem 19(8):8–10
10. Tang S, Liu Z, Liu S et al (2011) Research on rheological behavior of anion gemini surfactant solution. Adv Mater Res, pp 146–147
11. Pi Y, Zhang L, Liu Z et al (2011) Study on the rheological properties of sulfate gemini surfactants. J Oil and Gas 33(6):135–138

12. Ye Z, Han L, Chen H (2009) Effect of sodium salicylate on the properties of gemini surfactant solutions. J Surf Deterg 80(3):324–327
13. Tang S, Zhao C, Tian L et al (2016) Temperature-resistance clean fracturing fluid with carboxylate gemini surfactant: a case study of tight sandstone gas reservoirs in the Tarim Basin. Nat Gas Ind 36(6):45–51
14. Han L, Chen H, Luo P (2004) Visual behavior of gemini surfactants. Acta Phys Chim Sin 20 (7):763–766
15. Zheng Y, Huang Q, Mei P et al (2009) Influence of inorganic salts on the properties of gemini surfactants and its synergistic effect. J Oil and Gas Technol 31(6):145–149
16. Ji Y (2008) Rheological properties of anionic surfactant wormlike micelles and tertiary oil displacement agent application. Shandong University
17. Tang S, Cui Y, Xiong X et al (2014) Study on the viscosity of anionic gemini surfactant (GA-16) solution and its influencing factors. J Oil and Gas 36(8):146–149

Detection and Assessment of Natural Gas Pipeline Slip

Ke Cai(✉), Zhixin Chen, Fengping Yang, and Jiangang Lai

CNPC Tubular Goods Research Institute, Xi'an, Shaanxi, China
{caike, chenzhix001, yangfengping, laijiangang}
@cnpc.com.cn

1 Introduction

A natural gas pipeline foundation pit collapsed due to the inappropriate measures of a nearby underground garage residential construction somewhere in Guangdong on November 11, 2011, and the underground silt layer flow leads to the pipe slip deformation. The pipe specifications are φ660 × 12.5 mm spiral welded, made of L450MB, and manufacturing standards are GB/T9711.2-1999-oil and natural gas industries—Steel pipe delivery technology standard conditions. The design pressure of the pipe is 7.8 MPa, the normal operating pressure is 6.0 MPa, and the current operating pressure is 5.5 MPa. The slip length was 65 m; significant deformation length was 35 m, and 0.7 m on the horizontal deformation. The vertical fall is not obvious as shown in Figs. 1 and 2.

In order to prevent further deformation of the pipe, the stress relieving was implemented on the deforming part, and also the evaluation of the security situation.

2 Test

Following items were tested in the field: pipe wall thickness, deformation testing and nondestructive testing, and nondestructive testing including magnetic particle testing, ultrasonic testing, radiographic and magnetic memory testing.

Pipe wall thickness and deformation The pipe wall thickness was measured, according to the manufacturing requirements for Φ660 pipe, wall thickness should between +15% and −10%, and the pipe wall thickness should meet the requirements.

The deformation of the pipe is shown in Figs. 3 and 4. The slip length was 65 m, the actual excavation length was 51.8 m, and the main deforming part was about 35 m. After the pipeline accident, 14 points were monitored on slip section of the pipeline, found that the pipe horizontal position slipped after the accident, and then gradually rebound, the rebound volume size is shown in Table 1. The maximum amount of spring back is at 13# monitoring points, the maximum resilience value was 0.38 m, the actual displacement was 0.7 m, lied 0.8 m to the south of 4# girth weld, the deformation was symmetrical, and vertical sinking was obvious. There was no significant excessive deformation, local buckling, surface scratches, and other mechanical damage.

S. M. Shemwell and J. Lin (eds.), *Proceedings of the International Petroleum and Petrochemical Technology Conference 2018*,
https://doi.org/10.1007/978-981-13-2173-3_11

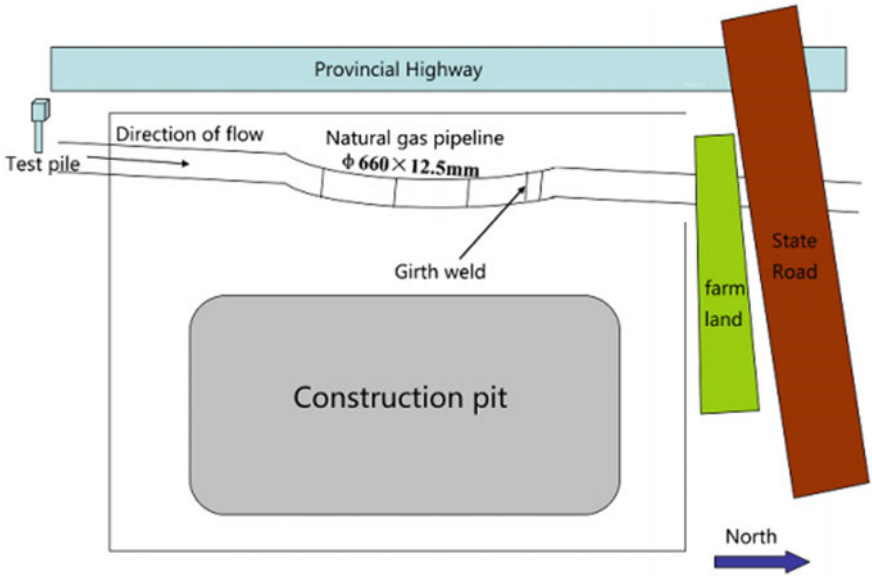

Fig. 1. Diagram of slip pipe

Fig. 2. Excavation picture of slip pipe

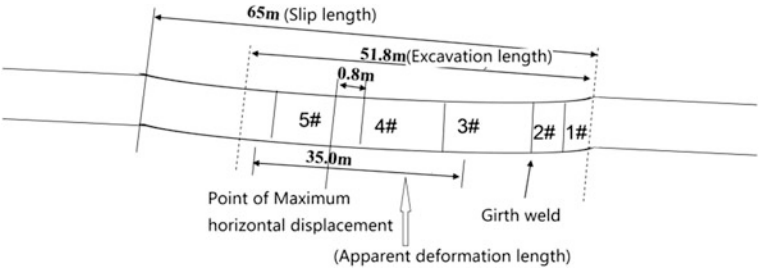

Fig. 3. Deformation of pipe

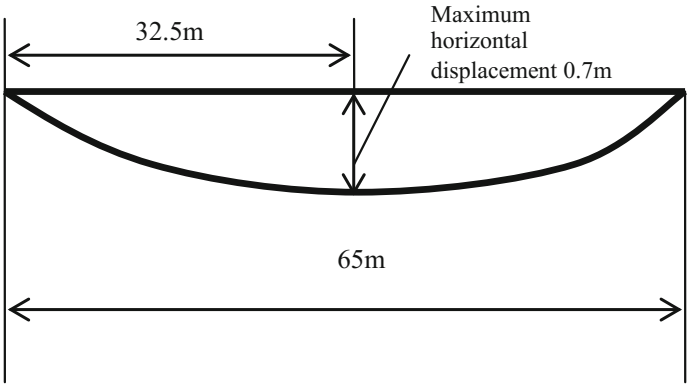

Fig. 4. Diagram of the pipe deformation

Table 1. Results of the resilience

Points	Max (m)
1	0.03
2	0.11
3	0.11
4	0.13
5	0.19
6	0.15
7	0.16
8	0.17
9	0.19
10	0.22

Nondestructive testing including magnetic memory testing, magnetic particle inspection, ultrasonic testing, and radiographic detection was conducted. Stress detection is to check if there exists stress concentration in the tube and welding;

magnetic particle testing is to check the weld surface defects; ray inspection and ultrasonic testing of welds are mainly to check whether there are internal bulk-type or area type defects.

The 100% magnetic memory stress testing, magnetic particle testing, radiographic testing, and ultrasonic testing were conducted on the girth weld 1#–5#. In addition, spot check was carried on spiral weld on a larger deformation part between the girth weld 4# and 5#.

Results showed that there were defects in girth weld 1#, 2#, 3#, and there were no defects in 4#, 5# girth weld and spiral weld, while stress concentration was obviously on the outside part of large deformation part.

3 Stress Analysis, Finite Element Method, and Safety Assessment

Local slippage causes pipe bending and the additional axial stress. The pipe may yield and failure if the axial stress is too great [1]. Therefore, stress distribution of the pipe should be calculated and the maximum stress should be assessed to see whether it meets the design requirements according to status in quo [2]. The pipe stress can be calculated theoretically and numerically. The former one is calculated according to the theoretical equation in design specifications, the latter is considered more realistic conditions, using the finite element method, in order to examine if there is overstressing when there is excessive slippage, and to determine whether the pipeline can operate safely [3].

The following is an analysis of pipe slip from theory calculating, finite element method, and safety assessment.

Theoretical calculation of pipe stress before slip should be done when pipe stress analysis is considered, pipe stress is divided into the main circumference stress, axial and radial stresses. The combined effect of stress can be measured by equivalent stress. The radial stress of the thin-walled tube can be considered zero, and not considered in the safety assessment. The following are calculations of steel circumference stress, axial stress, and equivalent stress.

3.1 Circumference Stress

The formula of circumference stress σ_h is:

$$\sigma_h = pD/(2\delta) \tag{1}$$

where σ_h is the circumference stress generated in the pipe under pressure, MPa; p is the pressure in the pipe, MPa; D is the outer diameter of the pipe, mm; δ is the pipe wall thickness, mm. Take the normal operating pressure p 6 MPa, according to pipe size, the result is

$$\sigma_h = 6 \times 660/(2 \times 12.5) = 158.4\,\text{MPa} \tag{2}$$

These should immediately follow the title. For multiple-authored articles, list the names of all the authors, followed by the full postal and email addresses, using identifiers to link an author with an address where necessary.

3.2 Axial Stress

Pipeline pressure, temperature difference, elastic laying, etc. will cause axial stress. The pipeline is a straight pipe, there is no elastic laying before slipping, and gas temperature change is small because pipelines are buried, there is no need to consider the effects of temperature and elastic laying. The main consideration is the axial stress caused by pressure.

Because axial deformation of the buried pipeline is not free, pipe axial stress σ_a is calculated as Eq. 3:

$$\sigma_a = \mu\sigma_h = \mu pD/(2\delta) \tag{3}$$

where σ is axial stress produced by internal pressure, MPa; μ is Poisson's ratio for the steel, taken as 0.3. The normal operating pressure is given as 6 MPa, then the axial stress is calculated in Eq. 4:

$$\sigma_a = 0.3 \times 6 \times 660/(2 \times 12.5) = 47.5\,\text{MPa} \tag{4}$$

3.3 Equivalent Stress

According to GB 50251-2003, σ_e is calculated by maximum shear stress theory as Eq. 5:

$$\sigma_e = \max(\sigma_h, \sigma_a, \sigma_r) - \min(\sigma_h, \sigma_a, \sigma_r) \tag{5}$$

where σ_e is equivalent stress, σ_h is axial stress, σ_r is radial stress. From the above calculation can be known that σ_h is 158.4 MPa, σ_a is 47.5 MPa, σ_r is around 0 before slip, then

$$\sigma_e = \sigma_h - \sigma_r = 158.4\,\text{MPa} \tag{6}$$

Pipe stress calculated after slip The slip mainly affects the axial stress and can be considered has no effect on the hoop stress and radial stress. In the stress analysis, based on flexible pipe laying formula in GB 50423-2007, steel pipe slip can be viewed as some degree of bending under loads, resulting in bending stresses in the pipe, which produce pipe axial tensile stress on the outside of neutral layer and the axial compressive stress in the inner neutral layer. Therefore, in the theoretical calculations, the slip pipe can be seen as pure bends deformed by external force.

Curvature of the pipe may be measured by R_b after slip. The results show that the pipe slip 0.7 m within 65 m, and according to Pythagoras, the radius of curvature R may be 754.8 m.

The equation of axial stress caused by slip and axial stress due to bending steel is

$$\sigma_{\mathrm{Am}} = Ey/(R_b) \tag{7}$$

where σ_{Am} is axial stress caused by bend, MPa; y is the distance of some dot to neutral layer, mm; R_b is curvature radius, mm; E is Elastic Modulus, MPa. When y is outside the neutral layer, y is positive, when in the inside, y is negative, thus in the outside of neutral layer there is axial tensile stress, and in the neutral layer is axial compressive stress. According to the geometry of the pipe, the value of max y is $D/2$, and the axial stress is the maximum, its value is:

$$\sigma_{\mathrm{Am}} = \pm ED/(2\mathrm{Rb}) \tag{8}$$

For this part of pipe, E is 2×105 MPa; D is 660 mm, R_b is 754800 mm (about $1143.6D$), and the axial stress is:

$$\sigma_{\mathrm{Am}} = \pm 87.4\,\mathrm{MPa} \tag{9}$$

When σ_{Am} taking as positive, there is axial tensile stress in the convex of the pipe, and as negative, there is axial compressive stress in the concave side of the pipe.

The axial stress is the sum of the axial stress σ_a produced by the gas pressure and the axial stress σ_{Am} of the bending stress after sliding. According to formula (4) and (9), the maximum axial tensile stress after superposition is:

$$\sigma_{\mathrm{AT}} = \sigma_a + \sigma_{\mathrm{Am}} = 47.5 + 87.4 = 134.9\,\mathrm{MPa} \tag{10}$$

The maximum tensile stress is located on the wall of the convex side of the pipe. And the maximum axial compressive stress is

$$\sigma_{\mathrm{AC}} = \sigma_a - \sigma_{\mathrm{Am}} = 47.5 - 87.4 = -39.9\,\mathrm{MPa} \tag{11}$$

The maximum compressive stress is located on the concave side of the pipe.

Equivalent stress calculation after slip Equivalent stress calculation is still the formula (5). For the convex side of the pipe wall (tension), because the axial stress after sliding is 134.9 MPa, still less than the ring stress 158.4 MPa, and the equivalent stress remains unchanged, $\sigma_{\mathrm{epull}} = \sigma_h = 158.4$ MPa. For the concave side of the wall (pressure), the ring stress is 158.4 MPa, radial stress is zero, and axial stress is −39.9 MPa, so the equivalent stress $\sigma_{\mathrm{epull}} = 158.4-(-39.9) = 198.3$ MPa.

Finite element calculation of the slip pipe stress The theoretical calculation of slip simplified the actual pipe stress situation, and using finite element method to calculate the forces after pipeline slip can get a more realistic pipeline axial stress. First, establish the finite element model of the steel pipe, then fixed the pipe in the circumferential direction, so that the pipe can axially stretching (elongation of the pipe may be subject to transverse load) and the load is applied on one side (simulated soil driving force), make the pipe deformed just the same with actual happened, and check the value of the axial stress.

According to the specifications of the pipeline, establish the geometry of the pipe section. Taking pipe length 80 m, as shown in Fig. 5a, fix the pipe in circumferential direction at two ends of the pipe within 7.5 m, no axial constraint, as shown in Fig. 5b. The pipe is divided by four node shell elements, the entire segment is divided into 16,000 units, and the shell thickness is 12.5 mm. Pipe material properties are as follows: elastic modulus 200 GPa, Poisson's ratio 0.3, yield strength is taken as 480 MPa according to the data provided, and tensile strength and elongation are set to 535 MPa and 0.18 according to the standard used. The pipe ends are fixed and normal pressure of 6 MPa is applied inside it, then lateral load is applied on one side of the pipe to make it slip. The pipe loading and restraint are shown in Figs. 6 and 7.

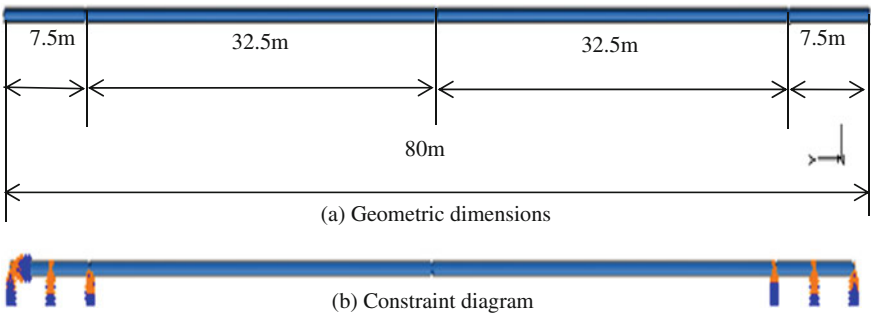

Fig. 5. Diagram of steel pipe geometric dimensions and constraint

Fig. 6. Diagram of pipe internal pressure

According to the above conditions, the load of transverse slip is increased until the horizontal midpoint displacement of 0.7 m occurs, the diagram of the deformation, the axial stress and the equivalent stress (according to the third strength theory) in the worst sliding part shown in Figs. 8, 9, and 10. The maximum hoop stress of convex side is 154.1 MPa, axial tensile stress is 198.1 MPa, and the maximum equivalent stress is 198.1 MPa. For the concave side, the hoop stress is 153.9 MPa, axial compressive stress is −199.3 MPa, and the maximum equivalent stress is 353.2 MPa.

It can be seen, the values of finite element calculation pipe axial stress and the theoretical stress are different, due to the following two aspects: first, in the theoretical calculation, the axial stress generated by the internal pressure is 0.3 (Poisson Ratio)

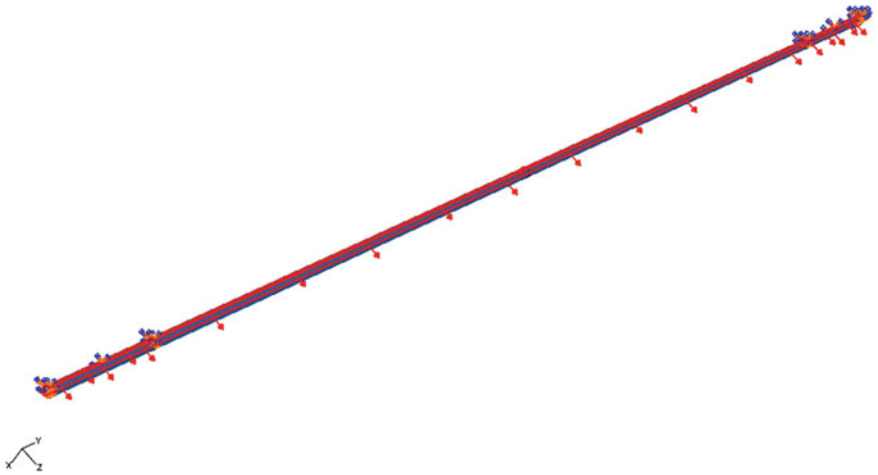

Fig. 7. Diagram of pipe subject to transverse load

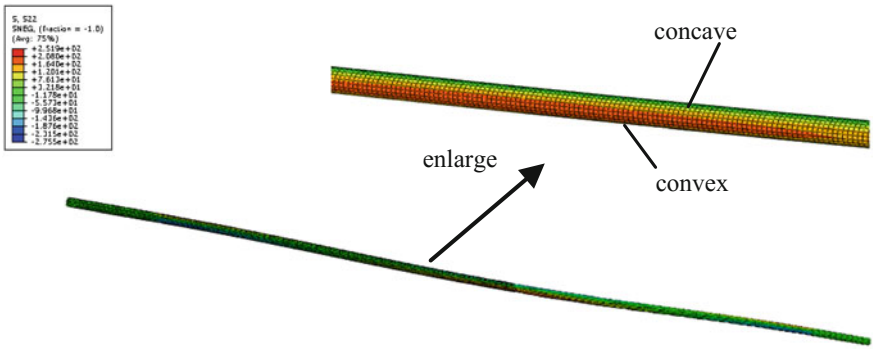

Fig. 8. Deformation diagram of pipe after sliding load

times of the hoop stress, that means the pipe is axially inextensible, but in the actual model, the pipe is axially extensible (soil can flow, the pipe is not a strong constraint); second, actually the slip pipe is subject to one side lateral load forces, not pure bending. There are some differences between the theoretical models. Therefore, the finite element calculation is commonly used in the pipeline safety assessment.

Safety assessment of slip pipe This section is to inspect whether the pipeline meeting with the strength design requirements after slip according to theoretical calculations, finite element results, and relevant standards.

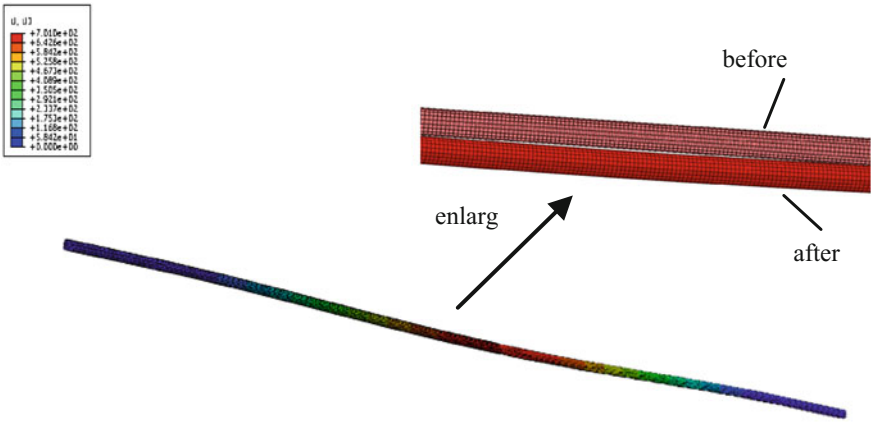

Fig. 9. Axial stress nephogram of pipe subjected to sliding load

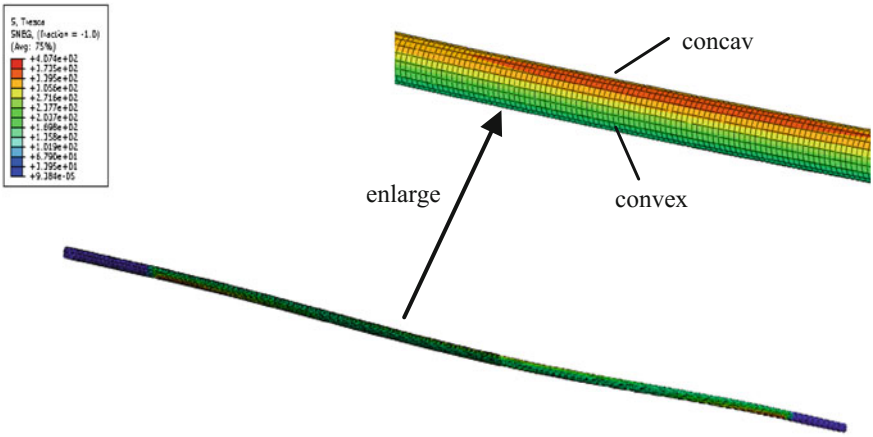

Fig. 10. Equivalent stress nephogram of pipe subjected to slip load

According to GB 50251-2003, its radius of curvature and equivalent stress should meet certain conditions after pipe bending. Below are the results of checking.

(a) The Radius of Curvature

According to the information above, take the pipe slip as bending under load, and the radius of curvature R_b is 754.8 m, compared with the outer diameter of the pipe D = 660 mm, R_b = 1143.6D. It is set in GB 50251-2003 that when laying pipelines, its radius of curvature should be no less than 1000D. From the results we can know, the radius of curvature after slip meet the criterion of GB 50251-2003.

(b) The Equivalent Stress

According to GB 50251-2003 Part V: the equivalent stress of combination of the axial stress and hoop stress of buried straight pipe stress should be less than 90% of the minimum yield strength of the pipes. The pipe material is L450MB, and the required minimum yield strength is SMYS 450 MPa, 0.9SMYS is 405 MPa.

In this pipe, the maximum equivalent stress of the convex side (extension side) is 198.1 MPa; the maximum equivalent stress of concave side (compression side) is 353.2 MPa, less than 0.9SMYS. All results meet the requirements of GB50251-2003.

According to SY/T 0330-2004, the allowable bending stress calculation expression for axial is

$$\mathrm{SA} = \mathrm{FDSMYS} - \mathrm{SE} - \mathrm{SS} \tag{12}$$

And there is

$$\mathrm{SA} + \mathrm{SE} + \mathrm{SS} = \mathrm{ST} = \mathrm{FDSMYS} \tag{13}$$

where SA is the allowable axial bending stress; SE is the original axial stress, 47.5 MPa; SS is the axial tensile stress caused by stretching in pipe moving, here the SS is zero; ST is allowable axial stress after the slip; FD is the coefficient of pipe strength design, the pipe area scale factor is 4, which corresponds to the coefficient is 0.4; SMYS is minimum required yield strength of the pipe, 450 MPa. According to the calculation, the allowable axial stress ST is 180 MPa after slip.

We can know from the theoretical calculation that under the normal pressure of 6 MPa, the maximum axial stress after slip is 134.9 MPa. In finite element analysis, the maximum tensile stress σ_{Aten} is 198.1 MPa and the maximum axial compressive stress σ_{Acom} is −199.3 MPa. According to the analysis above, finite element calculation is taken as a basis for checking the stress.

The above analysis shows that the actual total axial stress $\sigma_A$is

$$\sigma_A = \max(198.1, \mathrm{abs}(-199.3)) = 199.3 > \mathrm{ST} = 180 \tag{14}$$

Therefore, the actual axial stress σ_A is slightly larger than the allowable axial stress after the slip ST. Therefore, there is a certain risk in the pipeline if checked by allowable axial stress.

4 Conclusions and Recommendations

The range of line pipe wall thickness specification requirements is between 12.13 and 13.00 mm, the test results meet the requirements of the technical specifications.

There is no significant excess deformation, local buckling, and surface damage found on slip pipe. The total length of slip pipe is 65 m, and the main deformation length is about 35 m, after the release of the load, pipeline rebound significantly. The actual horizontal displacement is 0.7 m, no obvious vertical pipe sinking is observed.

Nondestructive testing was carried out on five girth welds and some spiral welds. It was found that 1#, 2#, 3# girth weld had defects, 4#, 5# girth weld and spiral weld seam had no defects, while stress concentration was more obvious on the outer part of greatly deformed pipe.

In accordance with the requirements of GB50251-2003 "gas pipeline project design", the radius of curvature of the pipe and the maximum equivalent stress after slip meet the design specifications. The maximum axial stress according to SY/T0330-2004 "Recommended practices for nonstop of transporting pipelines" is 180 MPa, but the actual stress is 199.3 MPa, beyond the requirements of the specification, and pipeline safety decreases.

Maximum axial stress is greater than the allowable stress in areas which slip pipe is located; it becomes less safe, the suggestion is to release pipeline external stress and to continue serve after it rebound. It is recommended that pile foundation being constructed on both sides of the pipe (pile foundation should be constructed down to bearing stratum), and the pipe being placed in ways of cement culvert with cover, and cement culvert being fixed through piles.

References

1. Feng Q, Zhao L (2001) Buckling analysis of buried pipes subjected to fault movements. Earthq Eng Eng Vibr 21(4):80–87
2. Shang E, Yu Y (2009) Effect of starting pressure gradient on the production performance of fractured well. J Xi'an Shiyou Univ (Natural Science Edition) 24(4):46–48
3. Yi L, Ding K, Qian C (2011) Ersearch on calculation method of long-distance pipeline's deformation based on strain. Chin J Solid Mech 32(S):310–313

Experimental Study on Wall Sticking Occurrence Temperatures of High Water Cut Crude Oil Gathered and Transported at Normal Temperatures

Xiong-yi Hu[1(✉)], Xue-ling Zhao[2], Chun-Yan Ma[2], Zai-xing Wang[2], Yi-chi Liu[1], Jie Liu[1], Jin Cao[2], Tao Zou[2], and Jiao Li[3]

[1] Hebei Huabei Petroleum Ganghua Survey Planning and Design Company Limited, Renqiu, China
gh_hxy@petrochina.com.cn
[2] Petrochina Huabei Oilfield Company, Renqiu, China
[3] China University of Petroleum (East China), Qingdao, China

1 Introduction

At present, most crude oil produced by the Chinese oilfield is high waxy, high gel point, high viscous crude oil, and in order to make it have better flowability, the heating process is usually used to ensure that the oil–gas gathering and transportation process carries on normally. However, the high energy consumption, the narrow variation ranges of allowable throughput, and the risk of oil gelling during the pipeline shutdown can cause potential issues when the pipeline is heated for the transportation of crude oil. With the development of crude oil gathering and transportation technology, water drive technology and the gathering and transportation technology at normal temperatures have been widely used. Along with the continuous development of oil fields, many oil fields have entered the stage of high water cut. During the high water cut stage, the pattern of multiphase flow in the pipeline is extremely different from the initial development of the low water cut [1, 2], and there is the phase transition point. When the water content is higher than the point, multiphase flow is changed from W/O emulsion into O/W emulsion with the rapid decline in liquid viscosity [3]. Research has shown that crude oil with high water cut has the capacity to move at or even below the gelling temperature [4]. Based on this conclusion, high water cut crude oil was often transported by the gathering and transportation technology at normal temperatures to reduce energy consumption and the cost of production.

Liu [5–7] carried out a long-term experimental study about the gathering and transportation at normal temperatures in Daqing Oilfield. The research found that: during the high water cut period, the gathering and transportation at normal temperatures could be used for crude oil gathering, and the temperature limit of the gathering was about 2 °C blow gel point of the crude oil. When the temperature is below the temperature limit, there will be the phenomenon of crude oil wall sticking. The reason for the phenomenon of sticking wall is that with the decrease of the gathering and transportation temperature, the viscosity of the dispersed oil emulsion in the water

S. M. Shemwell and J. Lin (eds.), *Proceedings of the International Petroleum and Petrochemical Technology Conference 2018*,
https://doi.org/10.1007/978-981-13-2173-3_12

increases, and the droplets will coalesce slowly. When the shear stress of water is less than the adhesion of emulsion on the inner wall of the pipeline, emulsion droplets of crude oil will stick wall in the gathering pipeline. With the increase of viscous wall crude oil, the inner diameter of the gathering pipeline decreases gradually, which also leads to the increase in wellhead back pressure [8]. The experimental study of Tian Dong'en showed that in addition to the temperature, there is a certain relationship between the wall sticking of crude oil and the water content and the velocity of multiphase flow [9]. At present, the research on the wall sticking of crude oil is still in the initial stage, and sticking wall of crude oil has great influence on the gathering and transportation of crude oil at normal temperatures. How to avoid the wall sticking of crude oil is the key to the success of the gathering and transportation at normal temperatures. The heating gathering and transportation technology of high energy consumption are currently used to transport high water cut the crude oil in the Xiliu station of North China Oilfield. And the gathering and transportation at normal temperatures is the main measure to reduce the energy consumption of the Xiliu station. Therefore, a series of experiments have been conducted in the Xiliu Station of North China Oilfield to observe the wall sticking rules of high water cut crude oil, which is of great significance to realize the gathering and transportation at normal temperatures of some high water cut oil wells in Xiliu station of North China Oilfield.

2 Experiment

2.1 Materials

Oil samples used in this study were collected from two different oil wells in Xiliu station. The basic properties of two different oil wells, density–temperature curves and viscosity–temperature curves under different shear rates of two oil samples are listed in Table 1, Figs. 1 and 2, respectively.

Table 1. Basic properties of experimental oil wells

Oil well number	Current yield (t/d)	Water cut (%)	Gel point (°C)
10-47	7.78	85.6	32
10-7	5.50	93.0	32

2.2 Experimental Apparatus

In order to study the wall sticking characteristics of oil–water two-phase flow under oilfield conditions, a set of experimental device was designed. Experimental apparatus consisted of valves, experimental steel pipes, pressure gauges, transparent observation tube, pressure sensor, temperature sensor, filter, mass flow meter, and other equipment, as shown in Fig. 3.

The experimental apparatus was connected to the oil collection line of an oil well to form a bypass line for experimental testing in the oilfield. The ball valve and the gate

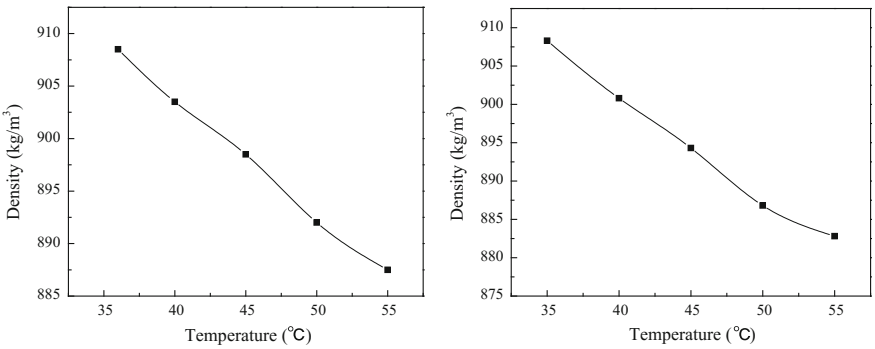

Fig. 1. Density–temperature curves of oil samples

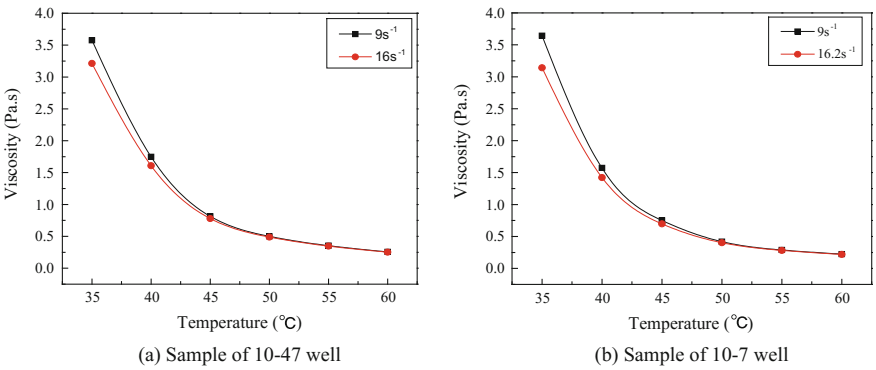

Fig. 2. Viscosity–temperature curves of oil samples

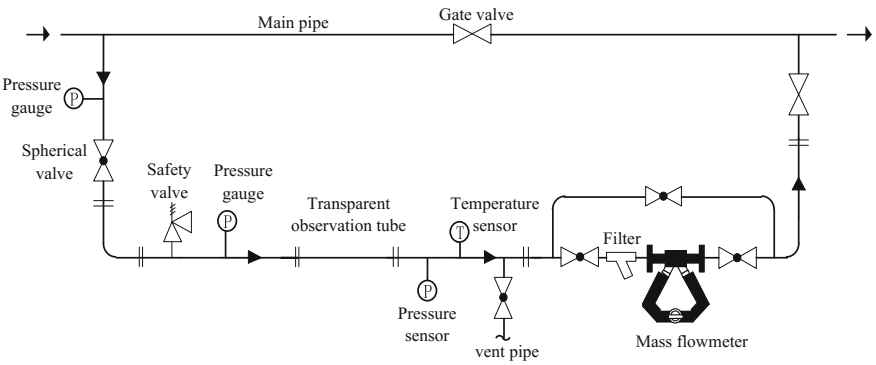

Fig. 3. The schematic diagram of field experiment apparatus

valve were used as the inlet valve and the outlet valve of the experimental pipeline to control the flow rate of the liquid, and steel pipes connected two pressure gauges, a safety valve, a transparent observation tube, a pressure sensor, a temperature sensor, a filter, a mass flow meter, and other equipment as the experimental main pipeline. Meanwhile, a GoPro camera was set at the transparent observation tube to photograph the flow pattern and flow state of oil–water two-phase flow. In order to be supported theoretically, the experimental apparatus must also rely on the other processes and facilities between wellhead and measuring space, such as wellhead pressure gauges and thermometers of measuring space, which were connected by the main pipe in Fig. 3.

The data provided by them and the experimental data measured by the experimental apparatus were used to theoretically analyze experimental results theoretically, which made the experimental results more reliable.

2.3 Experimental Procedures

Experimental oil–water two-phase flow came from two wells, 10-47 well and 10-7 well in Xiliu station, and both of them used three-pipe heat-tracing gathering and transportation technology. The experiment was carried out by heating or cooling. During the cooling experiments, first the hot water of two wells was stopped. When the liquid whose temperatures kept dropping flowed into the experimental device, the flow state of the oil flow was observed and photographed under different flow parameters. Meanwhile, the pressure, temperature, flow and other parameters measured by the experimental apparatus were recorded. After the experiment, the pressure drop from the wellhead to the pressure sensor of the experimental device was calculated. In addition, the relationship between the temperature measured by the temperature sensor and the pressure drop was analyzed. During the heating experiments, the hot water of the oil gathering pipeline was opened, which is the reason that the temperature of the oil–water two-phase flow entering the experimental device kept increasing. The next experimental steps were the same as the steps of the cooling experiments.

3 Results and Discussion

3.1 Definition of Wall Sticking Occurrence Temperature

In the Zheng Haimin's flow loop experiment, the wall sticking occurrence temperature (WSOT) was identified by decreasing the temperature at small increments under a fixed flow velocity, which was determined by pressure drop trend versus the temperature [10]. It was defined as the intersection point of two tangents, which meant that the growth rate of the pressure drop appeared to increase rapidly below the dew point temperature. It can be seen from Fig. 4, and T_0 was confirmed to be the WSOT.

However, the Zheng Haimin's flow loop experiments were carried out indoors, and its results could not be applied to the field experiments of Xiliu station because of the complexity of oilfield production. So a series of field experiments were carried out in order to obtain the wall sticking rules of high water content crude oil under actual

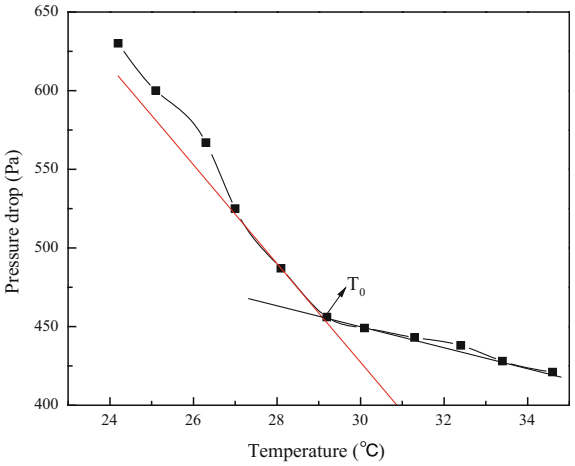

Fig. 4. Determination of WSOT

production conditions, and then the WSOT was a major concern in order to describe the rules better.

3.2 The Experiments Results of the 10-47 Well

During the 10-47 well cooling experiments, the flow rate was always maintained at about 0.047 m/s. As the liquid temperature decreased, the flow state of the oil–water two-phase flow was observed and photographed, and meanwhile, temperature, pressure, and other data were recorded. When the oil–water flow was found to be difficult to flow or even stopped, the temperature that sensor showed at this time was the WSOT of the high water cut crude oil. After the experiments, the pipeline pressure drops at different temperatures were calculated to plot the pressure drop–temperature curves. Several experiments have indicated that the temperature, at which the wall sticking of crude oil was observed, was the same as the temperature, at which the highest point of the first pressure drop mutation appeared in the pressure drop–temperature curves. The pressure drop–temperature curve of 10-47 well can be seen as Fig. 5, and T_1 was confirmed to be the WSOT equaling to 31.7 °C.

3.3 The Experiments Results of the 10-7 Well

In order to increase the reliability of the experiments, the experiments that were same as the experiments of 10-47 well were carried out for 10-7 well, the basic physical properties of which were similar to 10-47 wells. The results of the repeated experiments indicated that when the temperature of the high water cut crude oil dropped to the point at which the highest point of the pressure drop mutation first appeared in the pressure drop–temperature curves, the wall sticking began to appear. So, as shown in Fig. 6, T_2 was confirmed to be the WSOT, and T_2 equaled to 29.7 °C.

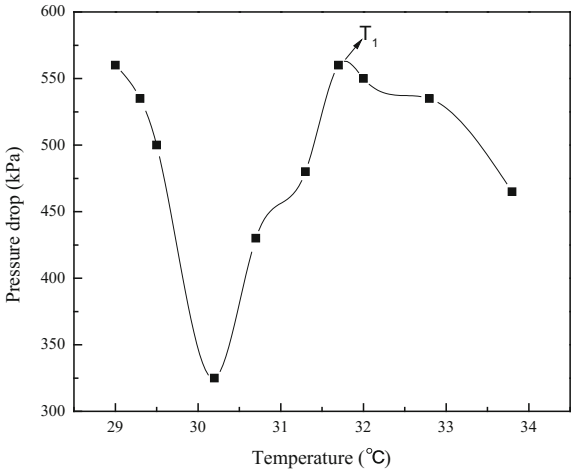

Fig. 5. Pressure drop–temperature curve of 10-47

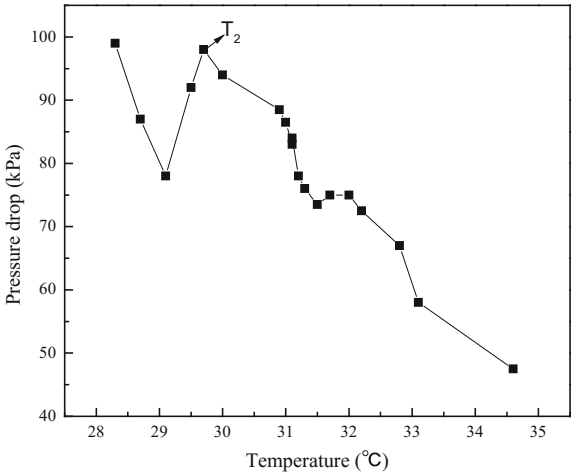

Fig. 6. Pressure drop–temperature curve of 10-7

By comparing the experimental results of the two wells, it can be seen that the change rules of pressure drop were same along with the change of temperature, and the wall sticking appeared when the highest point of the pressure drop mutation occurred first.

3.4 Discussion of the Experiments Results

Through Figs. 5 and 6, it can be observed that there was the highest point of the pressure drop in the curves, the temperature corresponding to the highest point was the

WSOT of the crude oil, and the WSOT of 10-7 well was lower than the WSOT of 10-47 because of the higher water cut of 10-7 well. The results of the curve analysis could be obtained by combining the phenomena observed by the transparent observation tube in the experiments as follows, when the fluid temperature was higher than the WSOT, the viscosity of the crude oil increased with temperature decreasing, which led to the increase of pressure drop. When the temperature was lower than the WSOT, the crude oil gradually adhered to the tube wall resulting in the decrease of the flow area and the pressure drop decreased gradually. When the temperature continued to decrease, more and more dead oil adhered to the pipe wall and even the case of pipeline congestion appeared, and at this time, the resistance of the fluid in the experimental pipes increased sharply, and then the pressure drop rose.

4 Conclusions

Wall sticking experiments with high water cut crude oil were conducted in a field experimental apparatus. Experimental results indicated that the transportation of the high water cut crude oil without heating was feasible at below the gel point, but wall sticking could still occur on the pipe wall. The temperature at which the wall sticking occurred was the WSOT. The temperatures point corresponding to the WSOT could be found by plotting the pressure drop–temperature curves. The WSOT was lower under the higher water cut conditions, and the wall sticking occurrence temperatures of two experimental oil wells were lower than their gel points. When the inlet temperature of oil–water two-phase flow was higher than the WSOT, the gathering and transportation at normal temperatures could be realized. The research on the wall sticking of crude oil in Xiliu station was of great use for the technical guidance of the gathering and transportation at normal temperatures.

References

1. Liu X, Liu L, Zhang Y et al (2008) The testing and analyses for oil-gas-water flow pattern with super-high water-cut in horizontal gathering-transportation pipeline. J EngThermophys 29(7):1167–1170
2. Qian Y, Yang L (2009) Research advances in oil-water two-phase flow. Chem Ind Eng Prog 28(4):566–573
3. Lv Y, He L, Wang A et al (2011) Study on the inverse characteristics of oil-water two-phase dispersed flow in horizontal tubes. J Petrochemical Univ 24(6):79–83
4. Chen Y, Tang L, Wang X (2007) Study on ultimate temperature in low temperature transportation of water cut oil. Offshore Oil 27(4):60–63
5. Liu X, Mao Q, Liu L et al (2013) Testing research for oil-gas-water flow pattern in Daqing oilfield. American Institute of Physics, pp 492–495
6. Liu X, Liu L et al (2009) Study on safe mixed temperature limits of Daqing periphery oilfield. Sci Technol Eng 9(20):6163–6166

7. Liu X (2005) The limit confirming and hydraulic/thermodynamic calculation method research for oil-gas-water mixing transportation safe in pipeline during oil producing with supper high water cut. Northeast Petroleum University, Daqing
8. Guo JH (2005) Temperature limit for oil-gas-water mixed transportation in safety during oil production with special high water-cut. Northeast Petroleum University, Daqing
9. Dong'en Tian (2015) Study on wall sticking rules of crude oil at high water cut stage in West Oilfield. Sci Technol Eng 15(9):176–179
10. Zheng H, Huang Q, Wang C et al (2015) Wall sticking of high water-cut, highly viscous and high gel-point crude oil transported at low temperatures. China Petrol Process Petrochem Technol 17(4):20–29

Numerical Analysis for Water Annulus Transportation of High-Viscosity Oil Under the Opening Ball Valve

Fan Jiang(✉), Sijie Li, Yongcheng Xu, and Jiangdong Chen

School of Mechanical and Electrical Engineering, Guangzhou University, Guangzhou, China
jiangfan2008@126.com, 598387302@qq.com

1 Introduction

The heavy oil reserves in the world are rich, but it easily leads to the problem of transport because of its higher viscosity and poor fluidity [1]. At present, there exists a new technique for heavy oil pipeline transport, called low-viscosity liquid annulus methods, which has been concerned by many scholars. This method would take the oil phase as the core flow, the water is used as a good lubricant to isolate the oil flow and pipe wall, and finally the flow pattern that core oil phase wrapped by water layer has been achieved, which is also known as the oil–water annular flow method [2, 3]. During the water annulus transportation, the vortex, severe water hammer, and other complicated three-dimensional flow phenomena could easily arise inside the tube due to the impact of pipeline auxiliary components such as the valve, annular nozzle. Especially the moment a ball valve opens rapidly, it easily induced dramatic changes in flow rate and pressure, as well as the core-annular flow will be seriously affected. Therefore, it is necessary to discuss the flow field characteristics of oil and water core-annular flow under a ball valve. Many scholars at home and abroad mainly study the change rules of the flow field inside the valve through theoretical analysis, numerical simulation, and experimental verification. Moujaes [4] used 3D CFD technique, analyzing the relation function of discharge coefficient, pressure loss coefficient and the valve opening based on different Reynolds number, and the simulation results are in good agreement with the experimental data published recently. Lee [5] developed an approximate method for predicting the flow resistance coefficient in the valve design. Valdes [6] simulated the cavitation flow in the check ball valve, which has been verified by test. Kerh [7] studied the fluid–structure interaction analysis of viscous incompressible fluid and control valve with finite element method and Newmark method, and the influence of the cell motion at the valve boundary on flow resistance is revealed. The flow characteristics inside the valve of a PFA lined ball valve under different valve opening are studied by Jeon [8]. Wan [9] developed an equivalent discharge coefficient for complex systems based on the hydraulic characteristics of a pressurized pipeline, and the results show that the maximum transient pressure is directly related to the discharge coefficient. Qu [10] discussed the influence of the different valve opening and the size of the valve cavity on the flow field characteristics

S. M. Shemwell and J. Lin (eds.), *Proceedings of the International Petroleum and Petrochemical Technology Conference 2018*,
https://doi.org/10.1007/978-981-13-2173-3_13

by using CFD. The flow field in All-welded ball valve under the compressible and incompressible medium is studied by Zhang [11]. Gong [12] discussed the flow state and the resistance coefficient of the ball valve at different opening and flow velocity. Zhou [13] explored the water hammer pressure characteristics of irrigation pipeline convex parts when the PVC ball valve was closed quickly. The above research focused on the study of the static characteristics of the pure liquid in ball valve, which normally using the CFD analysis method. Comparatively, little investigation has been made on the study of dynamic characteristics of multiphase flow in ball valve. Therefore, dynamic numerical simulation of oil and water core-annular flow when the valve is from the closed to fully opened is made, in order to discuss the flow field characteristics of multiphase flow in the valve pipeline system. Moreover, the result would promote the further research especially for core-annular flow in unsteady flow.

2 Mathematical Model

2.1 Two-Phase Model

Generally, *VOF* model or *Eulerian* model is used in the simulation of multiphase flow, nevertheless the *VOF* model could economize more computer resources compared to the *Eulerian* model, especially which has its unique advantages in dealing with the fusion and fragmentation of phase interface, thus *VOF* model is the best choice to simulate interfacial waves of the oil–water in calculation. In this paper, the oil phase and water phase are assumed as incompressible fluid and there is no mass transfer between the two phases, the partial differential equations for mass and momentum conservation are as follows:

Continuity Equation

$$\nabla \cdot \left(\overrightarrow{U}\right) = S_m \tag{1}$$

where $\overrightarrow{U}$, S_m are velocity field and the mass source term. This paper assumes the source term is 0.

The secondary phase in the computational cell is calculated by tracking the state density function for this phase. If the phase density is constant, it is equivalent to solving the nondimensional equation for the single phase:

$$\frac{\partial \rho_q \alpha_q}{\partial t} + \cdot \nabla\left(\rho_q \alpha_q \overrightarrow{U}\right) = 0 \tag{2}$$

In this case, mixture density has to be specified based on oil–water phase model. The density state equation is introduced, and the sum of the volume fraction of the oil phases and water phase is 1 for each computational cell. It is assumed that the change

of density is only related to the volume fraction of the oil and water, hence the mixture density can be expressed as

$$\rho = \alpha_w \rho_w + \alpha_o \rho_o \tag{3}$$

where ρ_o, ρ_w are density of water (kg/m^3) and oil (kg/m^3), respectively. α_o, α_w are volume fraction of water and oil.

Momentum Conservation

The external forces such as the jet force due to the opening valve, will be added to the conservation equation in the form of the source term.

$$\frac{\partial}{\partial t}\left(\rho \overrightarrow{U}\right) + \nabla\left(\rho \overrightarrow{U}\,\overrightarrow{U}\right) = -\nabla p + \nabla \cdot \left[\mu\left(\nabla \overrightarrow{U} + \nabla \overrightarrow{U}^T\right)\right] + \rho \overrightarrow{g} + \overrightarrow{F} \tag{4}$$

where p is flow pressure (Pa), $\vec{g}$ is gravity acceleration (m/s^2), $\vec{F}$ is external volume force (N); μ is mixture fluid viscosity (Pa·s), which based on the volume fraction a_q of oil and water, hence the mixture viscosity can be expressed as

$$\mu = a_w \mu_w + a_o \mu_o \tag{5}$$

The surface tension has little effect on each phase in high-speed flow, but in this case, the complex flow such as micro jet and vortex would easily arise inside the valve and pipeline, thereby the surface tension has become a physical parameter that cannot be ignored. The continuous surface force model (CSF) that established by Brackbill is used, which is assumed as the pressure jump across the surface. Obviously, the surface tension is the external volume force, which can be expressed as

$$F_{\text{vol}} = 2\sigma \frac{\alpha_o \rho_o K \nabla \sigma_w + \alpha_w \rho_w K \nabla \alpha_o}{\rho_o + \rho_w} \tag{6}$$

where σ is the tension coefficient of the oil–water interface. The surface curvature k can be obtained by calculating the normal gradient of the oil–water interface:

$$K = \nabla \cdot \hat{n}$$

where $\hat{n} = \frac{n}{|n|}, n = \nabla \alpha_q$

2.2 Turbulence Model

The standard $k - \varepsilon$ double equation turbulence model is commonly used in engineering application. Besides the basic N-S equations in the time-averaged flow, by using two transport partial differential equations, which are turbulent kinetic energy and turbulence dissipation rate, the closed turbulent equations is established for simulation [14, 15]. This turbulent model especially goes for the simulation of the annular flow, channel flow, and free jet flow. In this paper, the standard $k - \varepsilon$ turbulence equation is used and simplified as follow due to the incompressible flow.

The definition of the eddy viscosity coefficient:

$$\mu_t = \rho C_\mu \frac{k^2}{\varepsilon} \tag{7}$$

Turbulent kinetic energy k and turbulent dissipation rate ε equation are as follows:

$$\rho \frac{\partial k}{\partial t} + \rho \frac{\partial (k\vec{U})}{\partial x_i} = \frac{\partial}{\partial x_j}\left[\left(\mu + \frac{\mu_t}{\sigma_k}\right)\right] + G_k - \rho\varepsilon \tag{8}$$

$$\rho \frac{\partial \varepsilon}{\partial t} + \rho \frac{\partial (\varepsilon\vec{U})}{\partial x_i} = \frac{\partial}{\partial x_j}\left[\left(\mu + \frac{\mu_t}{\sigma_\varepsilon}\right)\frac{\partial \varepsilon}{\partial x_i}\right] + C_{1\varepsilon}\frac{\varepsilon}{k}G_k - C_{2\varepsilon}\rho\frac{\varepsilon^2}{k} \tag{9}$$

where a term G_k for the turbulent kinetic energy caused by an average velocity gradient is

$$G_k = \mu_t\left(\frac{\partial u_i}{\partial x_j} + \frac{\partial u_j}{\partial x_i}\right)\frac{\partial u_i}{\partial x_j}$$

The constant term in the equation is taken as empirical value:
$C_{1\varepsilon} = 1.44$, $C_{2\varepsilon} = 1.92$, $C_\mu = 0.09$, $\sigma_k = 1.0$, $\sigma_\varepsilon = 1.3$.

3 Numerical Calculation and Experimental Method

3.1 Computational Geometry

Figure 1 shows how the oil and water flow through the opening ball valve. The diameter D of ball valve and pipe are all 20 mm, with upstream pipeline diameters of $5D$ and downstream pipe diameters of $10D$ for this model. The oil phase is injected from the center of pipe, which wrapped by the water layer formed by annulus flow nozzle, flowing through an opening ball valve, two-phase flow gradually develops from the mixing emulsification to the core-annular flow pattern until the valve fully opened. In order to discuss the effect of the uniform opening speed of ball valve and the thickness of the water annulus on the core-annular flow, five kinds of ball valve opening time are selected: 1, 3, 6, 9, 12 s. Different thicknesses a of water annulus are 1.0, 1.5, 2.0, 2.5, and 3.0 mm, respectively. In view of the feasibility of the numerical simulation, the geometric model is reasonably simplified [12], which is shown in Fig. 2. The computational domain was meshed by ANSYS MESHING software based on hexahedron elements, and the used mesh can meet the accuracy requirement that to verify if numerical simulation can be a great tool for analyzing the core-annular flow through the ball valve, which is shown in Fig. 3, Eventually, the computational domain of oil and water CAF is analyzed with ANSYS FLUENT 17.

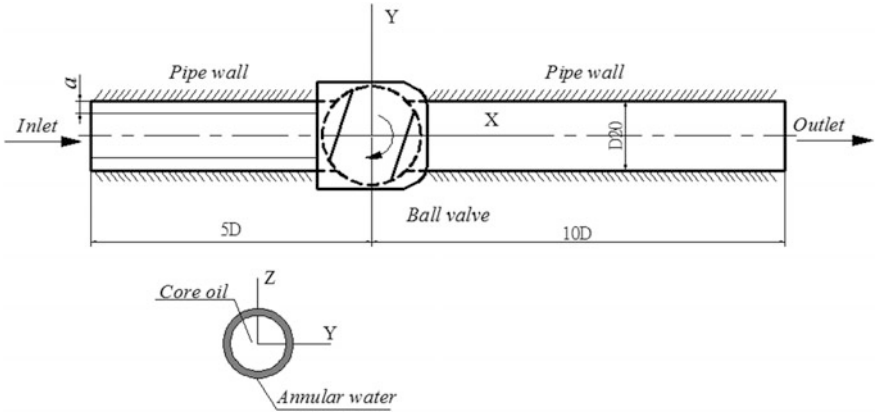

Fig. 1. Schematic description of CAF under a ball valve

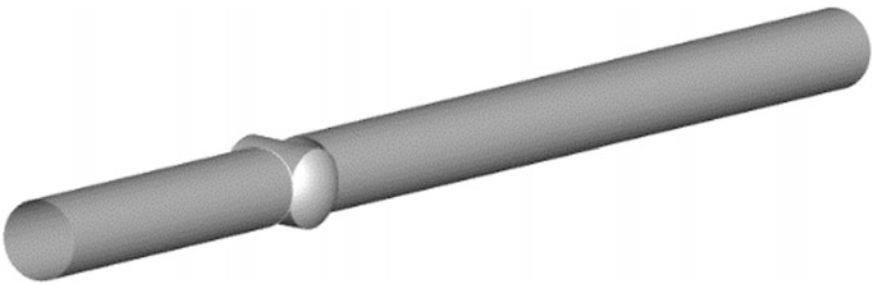

Fig. 2. Geometry model

Fig. 3. Mesh model

3.2 Initial and Boundary Condition

The governing equations are discretized using the finite volume method. The *Geo-Reconstruct* method is adopted for the volume fraction equation and interface reconstruction [15]. In order to obtain high definition oil–water interface, the second-order upwind scheme is used for discretization of each equation, the *SIMPLE* algorithm is used for pressure–velocity coupling. In this paper, the annular flow is taken as the

primary phase, and viscous oil is taken as secondary phase. The inlet and outlet boundary conditions are set as velocity inlet and pressure outlet, respectively. The time step of 5 × 104 and the maximum iteration times of 40 is selected to get the exact solution.

3.3 Performance Experiment

The experimental test section is depicted in Fig. 4. The experimental setup is mainly composed of several organic glass pipes, PVC ball valves, and pressure sensor. To promote the onset of core-annular flow, a ball valve is fully closed, the oil and water are injected through an annulus flow nozzle, the valve's opening speed is controlled, using the sensor for measuring the pressure between the valve front and back. Eventually, the experimental results are compared with simulation data, two-phase pressure drop of valve is plotted in Fig. 5. It shows that the experimental results and the simulated results have been declining. When the valve opening range is from 10 to 30%, the simulation values of pressure drop are higher than the experimental values. This is because, in the case of small valve opening, the complex unsteady flow could easily arise inside the valve, the frequency response as well as accuracy of sensing device cannot meet the requirements for such complex phenomena, so that causes measurement error. When the valve opening range is from 50 to 100%, two phase evenly flow and turn into CAF inch by inch, basically, there is no significant distinction of pressure drop at different valve opening speeds. Meanwhile, the opening speed of the ball valve has little effect on the pressure drop between the valve front and back.

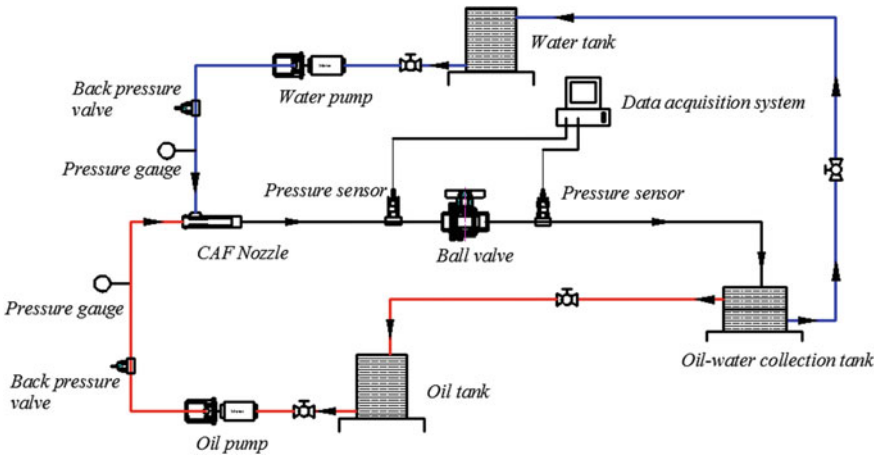

Fig. 4. Schematic description of CAF test system

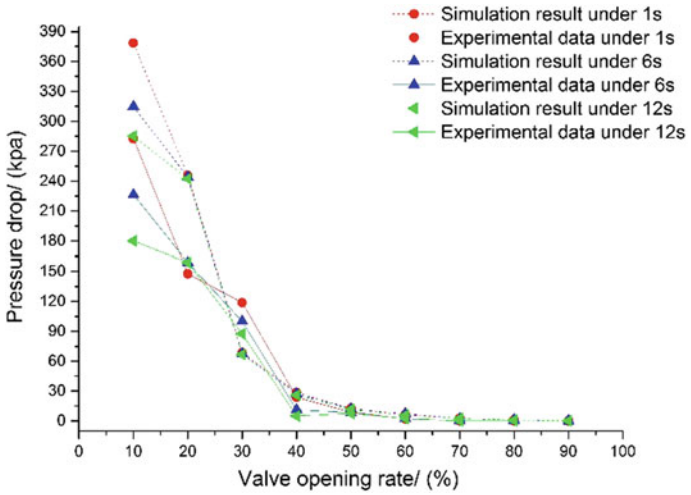

Fig. 5. Schematic description of CAF test system

4 Simulation Results and Analysis

4.1 Oil and Water Two-Phase Flow

Figure 6 shows the development of the core oil phase through ball valve at different time steps. Red color indicates the oil regions and blue color indicates the water regions. In order to reduce the phenomena that oil adheres to inner wall of tube, computational domain is initially filled with water. It is observed from Fig. 6, oil–water phase flow through ball valve is divided into three stages according to the flow pattern, namely the breakage of annular flow, the development of annular flow, and the stabilization of annular flow. In the early stage of simulation, the oil–water two-phase is injected into domain, forming a stable CAF in the upstream pipe. As the fluid through the ball valve, the smaller flow-path section makes water annulus separating and breakup, two phase have been mixed up together, worst of all, the complex vortex in the downstream pipeline and valve has been generated in form of oil phase and water phase. The whole breakage of annular flow should be avoided in experiment, which would aggravate the pressure drop of the two-phase flow, the efficiency, and quality in transport is seriously decreased. After time t = 2.5 s, the oil–water two phase came to the development of annular flow, annular flow is formed gradually with the increasing of valve flow-path section. It is obvious that core oil phase is strongly located off-center, a core oil flow along the upper wall of downstream pipe, which waves significantly. However, the oil phase has become the continuous and homogeneous fluid, there exists a small amount of oil–water mixed phase, and turbulence diminished, gradually two-phase flow changes into CAF. It is found that at the time higher than 4.5 s, the oil phase is completely wrapped by water layer, which forms perfect core-annular flow (PCAF), obviously, the change of flow-path section has almost no effect on the CAF.

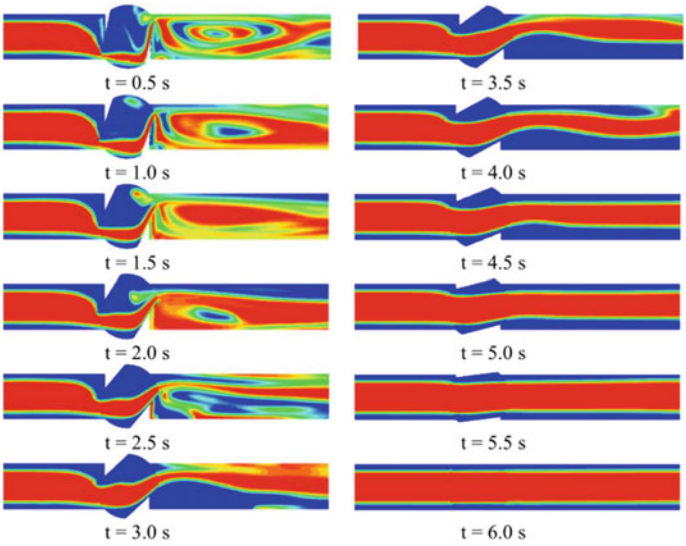

Fig. 6. Development of CAF with time for t_V = 6 s, a = 6 mm

4.2 Analysis of Flow Field at Different Opening Speed for the Same Water Annulus Thickness

The oil volume fraction of the downstream pipe with valve opening is plotted in Fig. 7. It is found that the volume fraction of oil phase grow with the valve opening before valve opening is 50%, and the oil volume fraction tends to a higher value at slower opening speed. This may be because the decrease of opening speed could lead to prolong the time that two phase through the valve at each valve opening, more oil phase is hoarded up in the downstream pipeline. After the valve opening is 50%, the volume fraction curve of the oil phase changes little, which tends to a stable value of 0.5.

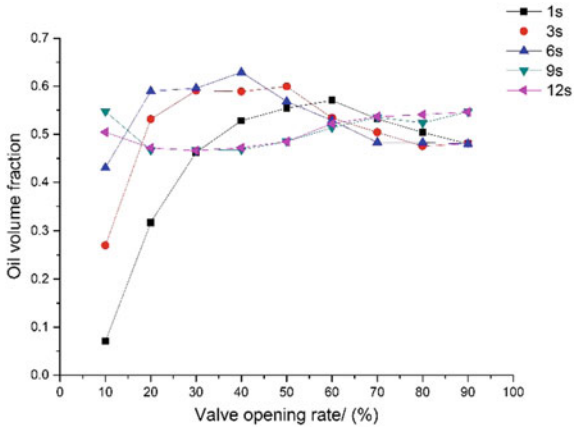

Fig. 7. The volume fraction of core oil as a function of opening speed

Figure 8 depicts the velocity contour at three kinds of valve opening which are 25, 50, and 75%, respectively. It is observed from Figs. 6 and 8, small flow-path section of inlet and outlet causes a throttle forming, generating a high-speed jet from that throttle area. Axial velocity of the jet core domain would be higher than surrounding velocity, which reached the maximum speed of 11.9 m/s. The greater the valve opening, the smaller the axial velocity of the jet place, meanwhile the pressure would rise up. The appearance of pressure inflection point is observed at valve opening of 50–60%, which shown in Fig. 9. The fluid from the valve outlet did not turn into high-pressure jet after inflection point, but expanded to all place, so the velocity profile gradients become smaller, the oil and water are to flow evenly, so the pressure is declined slowly and beginning to reach the environmental value. As it is evident from Fig. 8a, the location of negative axial velocity is after valve, which means the fluid has a reversal of flow. This is a result of transverse pulsation of turbulence from jet boundary and serious velocity bias. At the same time, the smaller throttle brings more fluid hoarded up in the downstream pipeline and gradually evolved a strong vortex. Comparing with different valve opening speed, the vortex core is farther away from valve as the opening speed increases. This may be because of the large entrainment effect for turbulent jets under the rapid opening, further driving the vortex core along the outlet of the pipeline. Moreover, the streamline density of valve opening of 25% is greater than that of 50% opening, which illustrates that the strength of vortex is larger in the early stage, as well the turbulence is more severe. Little by little, the vortex moves along the Y direction and then disappears with increasing of the valve flow-path section.

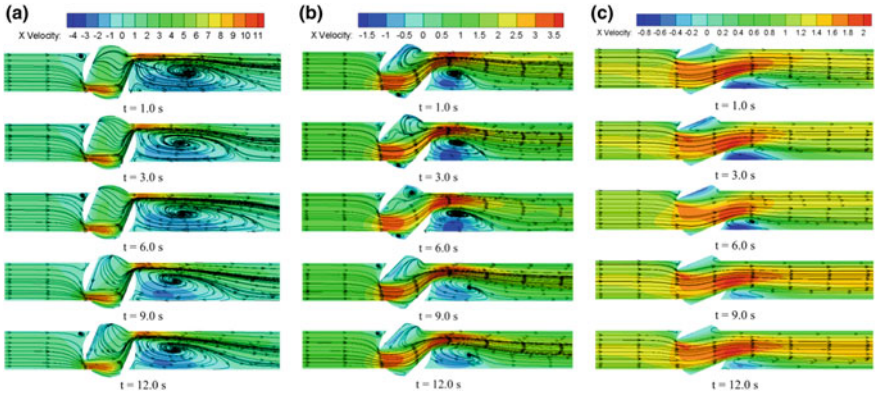

Fig. 8. The velocity contours at a function of opening speed, **a** valve opening of 25%, **b** valve opening of 50% and **c** valve opening of 75%

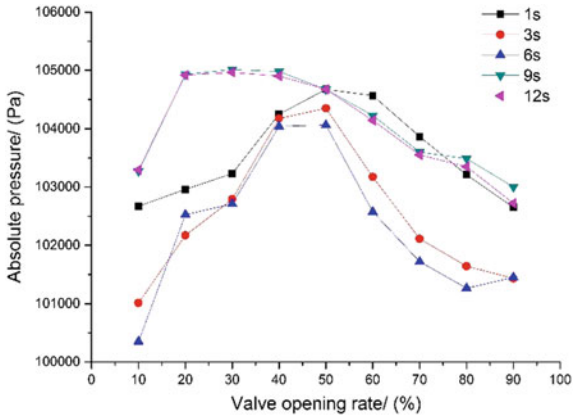

Fig. 9. The average pressure of valve outlet at a function of opening speed

4.3 Analysis of Flow Field at Different Water Annulus Thickness for the Same Opening Speed

Figure 10 indicates the volume fraction contours at valve opening of 40 and 50%. It is found that the turbulent mixing of oil phase and water phase after valve is increased with the decrease of annulus thickness, so the time for two fluid turn into the stable CAF will be delayed, which concluded that the variation of water annulus thickness has become a major condition to the rapid formation of oil–water core-annular flow during a ball valve opening. It is observed from Fig. 11 that the turbulent kinetic energy is larger at water annulus thickness of 1.0 and 1.5 mm, which further concluded that turbulent in downstream pipeline is more severe with the transport by narrow water annulus, which is bad for evolving to the PCAF either. During the water annulus transport, the flow shear stress is applied on the water annulus, which can effectively

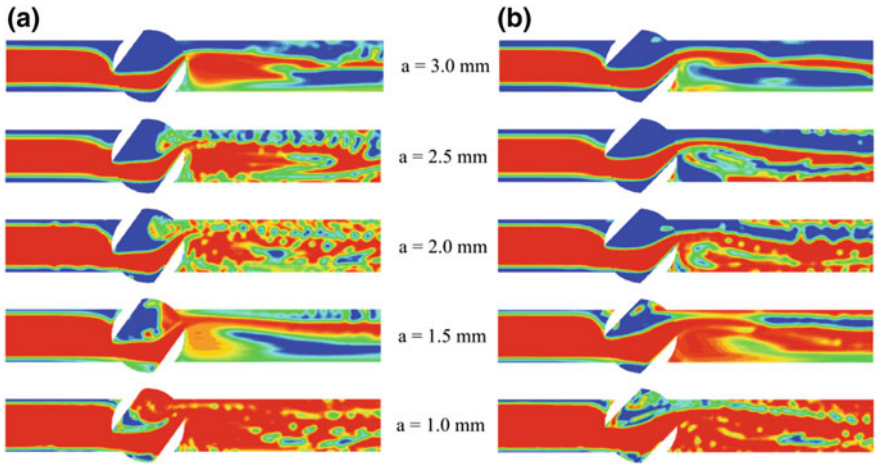

Fig. 10. The volume fraction of core oil of **a** valve opening of 40% and **b** valve opening of 50%

reduce the flow friction and speed up the evenly flow of oil–water two phase, thereby the turbulence kinetic energy decreases with the increase of the thickness. However, too large water annulus is not conducive to increasing the throughput of viscous oil. In addition, the valve opens more slowly, that leads to minimize resultant surge and shock, so the turbulent kinetic energy is decreased.

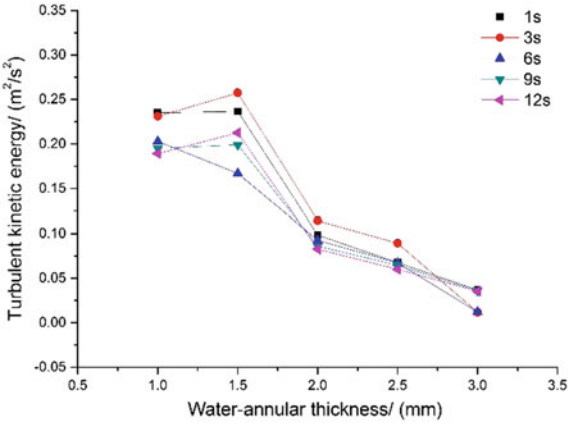

Fig. 11. Turbulent kinetic energy in downstream pipe with annulus thickness

Oil phase adheres to the wall and flow along the pipeline after the breakup of water annulus, the frictional resistance in the process of pipeline transport is greatly increased, this stick phenomenon is regarded as an important indicator for breakup of the oil–water annular flow completely, hence the stick distance is discussed necessarily, which is from where the oil first adheres to the wall to the valve center, that could be more intuitive to study the instability mechanism of CAF. The stick distance curve with valve opening is plotted in Fig. 12. It is illustrated that the stick distance has a similar varied trend with the increase of valve opening at different water annulus. Under the condition of low valve opening, there is oil phase on a collision course with the pipe wall by the effect of the throttle, which caused the oil adhesion rapidly. The oil adhesion indicates that core-annular flow pattern of oil and water has been significantly damaged. The stick distance rises up with the valve opening, which concludes that the core oil flow is gradually wrapped by the water layer and flows along the center of the pipeline, eventually turn into the PCAF. However, the stick phenomenon is more severe when the thickness range is from 1.0 to 2.0 mm, in large part, it is because of serious turbulent mixing of oil phase and water phase at the initial time, and the oil on the wall is difficultly washed away by thin water layer. The volume fraction of computational domain at valve opening of 100% is depicted in Fig. 13. It is found that only the stick phenomena are completely disappearing at the water annulus thickness of 3.0 mm. Due to the effect of velocity fluctuation, a small amount of oil phase still

adheres to the wall of downstream pipeline with droplet shape under the water annulus transport for rest of the thickness. At the same time, the oil–water interface waves are the result of fluid shear and interfacial surface tension, so wavy core-annular flow (WCAF) [16, 17] is easily generated.

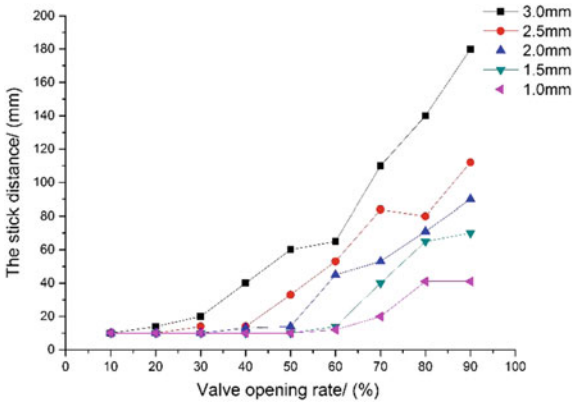

Fig. 12. The stick distance with valve opening at different water annulus

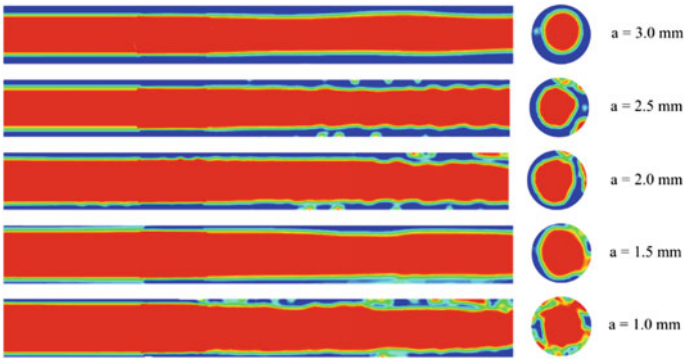

Fig. 13. The volume friction at valve opening of 100%

4.4 The Flow Resistance Characteristics of Ball Valve

The discharge coefficient of the ball valve could reflect the pressure loss of the fluid medium that through the ball valve, which could be estimated by using (10). The discharge coefficient of ball valve as a function of valve opening speed under transient simulation is plotted in Fig. 14.

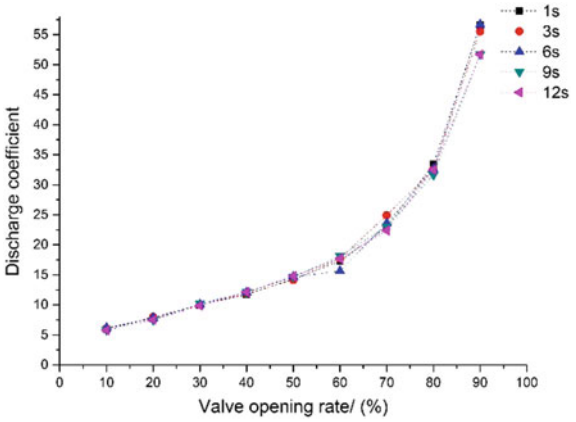

Fig. 14. The discharge coefficient at different opening speed

$$K_q = \frac{1}{A_v} Q_V \sqrt{\frac{\rho_L}{2\Delta p}} \tag{10}$$

where A_v is flow-path section of the ball valve (m^2), Q_V is the flow rate of the valve (m^3/s), ρ_L is density of the fluid, and Δp is pressure drop between the valve front and back.

As expected, discharge coefficient of ball valve rises up with the valve opening. When the valve opening is less than 50%, the complex vortex could easily arise in downstream place, there is flow blocking phenomena and the pressure loss becomes larger, thereby the discharge coefficient changes a little, which is not conducive to developing CAF. After the valve opening of 50%, the increase of the discharge coefficient is significant. This is because the turbulence gradually disappeared with the increase of the flow-path section, the oil and water evenly flow has appeared.

In addition, the opening speed of the ball valve has little influence on the discharge coefficient, all of which show a rising trend, and the discharge coefficient at same valve opening did not change significantly.

A mathematical model for the resistance coefficient of a ball valve can be expressed as:

$$\lambda = \frac{2\Delta p}{\rho_L u_v^2} \tag{11}$$

where Δp is pressure drop between the valve front and back, ρ_L is density of the fluid, and u_v is velocity of ball valve (m/s).

Figure 15 indicates the resistance coefficient as a function of valve opening speed. The resistance coefficient decreases with the increase of valve opening. The resistance coefficient drops sharply before the valve opening is 30%. The drop rate of resistance coefficient is slowed down while the valve is opening from 30 to 60%. After the valve opening of 60%, the resistance coefficient is relatively low, the ball valve has a better

flowing performance at this time, which is helpful to the formation of PCAF. The downward curve in the resistance coefficient is seen at different opening speed, and the resistance coefficient reaches the minimum at the opening time of 1 s, The inflection point of each curve is where the valve opening is about 50%, the resistance coefficient is basically consistent after the inflection point.

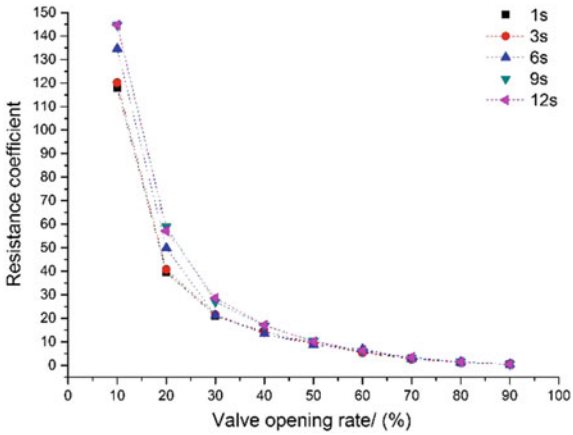

Fig. 15. The resistance coefficient at different opening speed

5 Conclusion

According to the visualization study of oil and water CAF transport under the opening ball valve, It is concluded that oil–water phase through ball valve, which could be divided into three stages based on flow pattern, namely the breakage of annular flow, the development of annular flow, and the stabilization of annular flow. The formation and turbulence of high-speed jet are the main reasons for the formation of a complex vortex in the downstream pipeline at the smaller valve opening. With the increase of the flow-path section of the valve, the oil and water two-phase flow gradually develops from the mixing emulsification to the CAF, and finally, the water annulus transport for high-viscous oil is made.

Different water annulus thickness formed by the annular flow nozzle has a great effect on evolvement of core-annular flow pattern. The turbulent kinetic energy of downstream pipe is larger at thickness of 1 and 1.5 mm. Droplet sticking to the wall in the downstream pipeline would aggravate the core oil wave, oil–water two-phase flow tends to be WCAF. Only by the thicker water annulus can accelerate the evolvement of the oil–water two phase from the breakup to the CAF. In addition, the lower valve opening speed would lead to minimize turbulence in downstream pipeline, which is conducive to the formation of CAF.

Based on the flow resistance simulation of the valve in two-phase flow, the flow resistance and discharge coefficient have a similar varied trend with the increase of

valve opening at different opening speed. The discharge coefficient varies a little and the resistance coefficient is great at the valve opening less than 50%, which shows the poor flowing performance. When the valve opening exceeds 50%, the growth rate of discharge coefficient increases while the resistance coefficient is at a low value, which illustrated that the better flowing performance would be conducive to the evenly flow for two phase, reduce the breakup to the core-annular flow of oil–water, as well efficiency in high-viscosity oil transport is improved.

Acknowledgements. This project is supported by Guangdong Provincial Natural Science Foundation of China (Grant No. 2016A030313653), and the Science and Technology Plan of Guangzhou City (Grant No. 201607010291).

References

1. Yaghi BM, Al-Bemani A (2002) Heavy crude oil viscosity reduction for pipeline transportation. Energy Sources 24(2):93–102
2. Jiang F, Yun L, Wang YJ, Liu ZZ, Chen CG (2016) Numerical simulation of non-Newtonian core annular flow through rectangle return bends. J Appl Fluid Mech 9(1):431–441
3. Jiang F, Wang YJ, Ou JJ, Chen CG (2014) Numerical simulation of oil–water core annular flow in a U-bend based on the Eulerian model. Chem Eng Technol 37(4):659–666
4. Moujaes SF, Jagan R (2008) 3D CFD predictions and experimental comparisons of pressure drop in a ball valve at different partial openings in turbulent flow. J Eng—Asce 134 (1):24–28
5. Lee JH, Lee KH (2010) Prediction of the resistance coefficient in segment ball valve. J Mech Sci Technol 24(1):439–442
6. Valdes JR, Rodriguez JM (2014) Numerical simulation and experimental validation of the cavitating flow through a ball check valve. Energy Convers Manag 78(12):776–786
7. Kerh T, Lee JJ, Wellford LC (2014) Transient fluid-structure interaction in a control valve. J Fluids Eng 42(11):199–204
8. Jeon HP, Kim DY, Lee JC (2014) CFD analysis on the flow characteristics with discharge coefficient in a PFA lined ball valve for different opening degrees. KSFM J Fluids Mach 17(4):76–78
9. Wan WY, Lian JJ, Li YZ (2005) Influence of valve system discharge coefficient on hydraulic transients. J Tsinghua Univ (Sci & Tech) 45(9):1198–1201
10. Qu D, Lou JJ, Zhang ZH et al (2017) Numerical simulation of dynamic flow field of ball valve based on dynamic mesh. J Naval Univ Eng 29(4):26–30
11. Zhang XH, Wang T, Jiao YR et al (2017) Simulation and analysis of flow field based on FLUENT software in all-welded Ball valve under different media. J Xihua Univ (Natural Science) 36(2):6–10
12. Gong Y, Gui L (2010) Numerical simulation and flow field analysis of resistance coefficient of ball valve. Water Resour Electr Power 36(3):20–24
13. Zhou JJ, Lv HX, Shi X et al (2014) Effect of PVC exhaust valves on water hammer protection of mountain irrigation pipes. J Northwest A&F Univ (Nat Sci Ed) 42(11):199–204
14. Cazarez-Candiaa O, Piedra-Gonzálezb S (2017) Modeling of heavy oil–water core-annular upward flow in vertical pipes using the two-fluid model. J Petrol Sci Eng 150:146–153

15. Kaushika VVR, Ghosha S, Das G, Das PK (2012) CFD simulation of core annular flow through sudden contraction and expansion. J Petrol Sci Eng 86:153–164
16. Ameri M, Tirandaz N (2017) Two phase flow in a wavy core-annular configuration through a vertical pipe: analytical model for pressure drop in upward flow. Int J Mech Sci 126:151–160
17. Tripathi S, Bhattacharya A, Singh R, Tabor RF (2015) Lubricated transport of highly viscous non-Newtonian fluid as core-annular flow: a CFD study. Procedia IUTAM 15:278–285

Study of the Method Laying Fiber Optic Cable in the Same Trench with Pipeline in Permafrost Region

Guizhi Liu(✉)

Telecommunication Department, China Petroleum Pipeline Engineering, Co., Ltd. (Engineering), Langfang, China
cppe_liugz@cnpc.com.cn

1 Introduction

Based on the consideration of land expropriation, project cost, easy to maintain, and many other factors, FOC is to be laid in the same trench with pipeline (hereinafter referred to as LIST) in the pipeline project of China. The technology of laying FOC in the same trench with the pipeline has more than twenty years of experience in China, but most pipeline routes are located in non-permafrost regions. But if it is in permafrost, for the pipelines, especially the crude oil pipeline, it should have a thaw collapse effect on permafrost because the temperature of the pipeline transport medium is more higher than that of the permafrost environment [1]. The thaw collapse effect will result in extra force on the cable, which will affect the operation safety of the FOC and make it more difficult to guarantee the quality of the cable laid in the same trench with the pipeline. In this paper, it will discuss that force analysis of the FOC laying in the same trench with the pipeline, so as to study the cable laying method and protection measures in permafrost region.

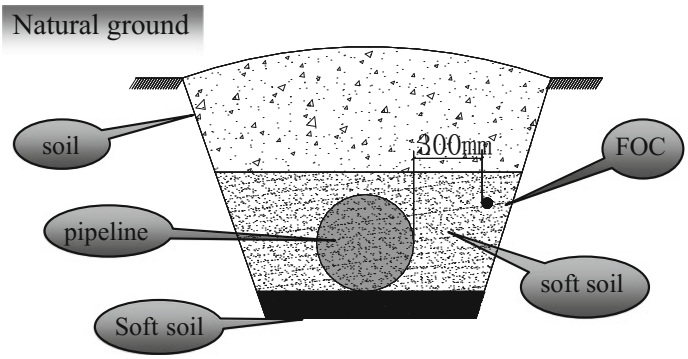

Fig. 1. Typical drawing for FOC LIST

S. M. Shemwell and J. Lin (eds.), *Proceedings of the International Petroleum and Petrochemical Technology Conference 2018*,
https://doi.org/10.1007/978-981-13-2173-3_14

2 FOC LIST in Normal Area

In normal area, the FOC is usually laid on the horizontal side of the top of the pipeline or lower position. The FOC can also be laid on the bottom of the trench while the pipeline's diameter is smaller. Normally, the space between FOC and pipeline is no less than 300 mm according to the code SY/T 4108-2012. The typical drawing of FOC LIST is shown in Fig. 1[2–4].

The FOC can be laid in two ways: direct burial laying and laying in cable ducts. To avoid the impact damage on the cable while trench backfill, the way of direct burial laying is often used in flat terrain and simple regions such as desert, plains, etc. But the way of laying in cable ducts is generally adopted in areas with poor geological conditions, such as mountainous regions, washy regions, stony regions, and other varied topography regions. The duct is often HDPE with silicon core. The Installation of FOC is blowing air method. The horizontal space between the duct and the pipeline is usually no less than 300 mm [2–4].

3 FOC Laying Method in Independent Ditch in Permafrost Area

In northwest and northeast China, there are many successful cases of FOC have been laid in the Permafrost area. According to Chinese design standard, operating temperature of normal FOC is between −40 and +60 °C [5], So the FOC installation can adopt the way of laying in cable ducts or direct burial laying or aerial installation. In order to avoid the damage from plough, cultivation and flood washed, buried depth of the FOC or the duct shall be deeper than 800 mm. The FOC line is often to be buried in the frozen soil in permafrost region in order to avoid disturbing frozen soil and protect the natural environment. The FOC line often is asked to buried under the frozen soil layer to guarantee its safety while in seasonally frozen region.

4 The Study for FOC LIST in Permafrost Region

Because of the temperature difference between the oil/gas and frozen soil, the transmitting pipeline will influence the frozen soil temperature. Normally, the crude oil pipeline's temperature is more than 0 °C, and the temperature of the pipeline is the equivalent of a heat source that continuously heats the frozen soil around the pipeline, causing the ice rich frozen soil to gradually melt and consolidation deformation, and also the ground began to sink. The water melted by ice is gathered in the trench. The water in the trench can accelerate the further melting and settlement of the frozen soil surrounding pipes. According to research, within three years, the thawing depth of the pipeline to the surrounding frozen soil can reach 1–1.5 m for different thickness of insulating layer of the pipeline correspondingly. And as the run time progresses, the depth of thawing settlement will be further increased [1, 6]. Figure 2 shows the site of

one buried crude oil pipeline. The picture was taken in spring time after one-year construction, and also was in thaw season. The picture shows the changes in ground surface caused by thawing settlement.

Fig. 2. Picture of surface change because of thaw settlement

It is going to make a differential degree of thaw collapse because the thermal effect of the pipeline is inconsistent with the different soil (mainly ice content). That means some soil areas are seriously sinking and some of them are less serious [1, 7]. In such different soil areas, the FOC LIST will be stressed as shown in Fig. 3 [1, 7–9].

Suppose that the FOC is to be laid in permafrost region and goes through three areas in a row, namely rock section, a section of soil that contains more water and rock section. Because of the lower water content in the rock area, the melting effect is weak, while in the water-rich soil area, the melting of ice will cause shrinking of the soil and then the soil will sink under the action of gravity. And the length of the downward extension of the FOC line on both sides of the soil section is to be limited because of the gripping force of the soil. In this situation, no upward support force from the soil to support the FOC line in B section, as a result, a situation of aerial cable in a watery rich B section is formed. And the optical cable line is subjected to downward pressure from the overlying soil, therefore, three bending points are formed at the interface of A and B and in the middle of the optical cable line. By means of finite element method, due to the downward deformation of the cable line, it will produce tensile force Fg1x, Fg2x1, Fg2x2, and Fg3x in the axial direction of the optical cable line, The larger the aerial section L, the greater the downward pressure, and the radius of curvature of the bending point is more smaller [8, 9].

According to relevant specifications, after FOC laying, the radius of curvature of FOC at bending point shall not be smaller than the 10–15 times (depend on the type of FOC) of the outer diameter of the FOC [3]. The curvature radius of the HDPE silicon core tube shall not be less than 15 times of the diameter of the tube. The radius of curvature at the bending point in Figs. 3 and 4 will increase with the increase in differential thawing settlement between A and B section. When the radius of curvature of the bending point exceeds the allowable radius of curvature, macro-bending loss will appear in the optical fiber. As the thawing settlement further, the attenuation of optical

fiber gradually deteriorated. When suffered force in optical fiber line exceeds a certain value, it will lead to optical fiber break, or even FOC break [10].

On analysis, the largest axial tensile force of the fiber optic cable is at the interface between area B and area A, that is, the location that FOC is the most likely to break fiber or cable.

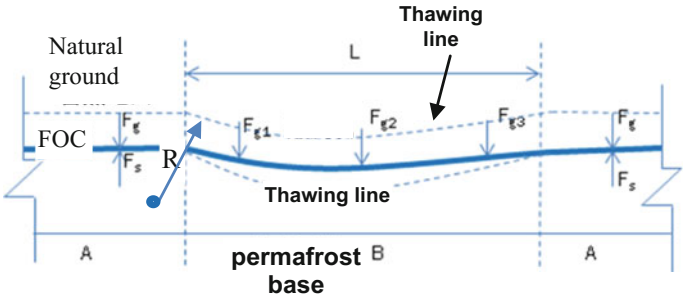

Fig. 3. The force analysis diagram under the state of thawing settlement

The tensile force at the ends of the FOC line is $F = 1/2$ (G* cosα), G = optical cable gravity + fiber earth gravity, details are shown in Fig. 4. The "α" is the angle between the cable and the gravity direction, When "α" = 0°, the force is the maximum. When "α" = 90°, the force is zero.

Table 1 shows several typical FOC and HDPE tube's mechanical performances. The total effective bearing area "S" of HDPE silicon core tube with ¢40/33 mm (remove the hollow part of the outer wall between the ring area) is 1692.46 mm^2: experiment pulling force is S*18 = 30464 N, the index is about 3 times of the cable GTXOPY33 what is often used in special region in the current project. The experiment pulling force can be considered as the allowed pulling force of tube.

Table 2 shows the calculation results of "L" of typical FOC and HDPE tube. "L" will decrease with the increase of buried depth [8, 9]. The FOC and HDPE tube operation tensile force shall be no more than the long-term allowable tension of FOC and HDPE tube. In different buried depths, the maximum allowable suspension length "L" is different.

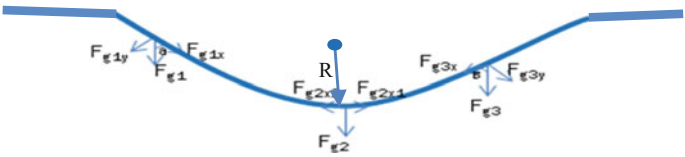

Fig. 4. Stress analysis drawing of FOC or duct under thawing settlement

Table 1. Comparison table of main mechanical performance of FOC and duct

Type	Diameter (mm)	Allowable long-term resistance (N/100 mm)	Allowable long-term tension (N)
GYTA53-24B1	13.1	1000	1000
GYTA33-24B1	14.5	3000	4000
GTXOPY33-24B1	13	10,000	10,000
HDPE with silicon core duct (¢40/33 mm)	40	Ring stiffness $\geq$ 50 kN/m^2	Unlimited, experimental tension $\geq$ 18 MPa, Also: 18 N/mm^2, Elongation at break $\geq$ 380%

Table 2. Calculation results of "L" of typical type FOC and silicon core HDPE duct under typical buried depth

FOC type	Buried depth: 1.2 m (m)	Buried depth: 2 m (m)
$GYTA_{53}$	6	4
$GYTA_{33}$	26	14
$GTXOPY_{33}$	72	44
Silicon core HDPE duct (¢40 mm)	219	134

5 Comparison and Analysis of Different Laying Methods

Buried: There are two ways to lay FOC LIST, direct burial and laying in cable ducts. When adopting the way of direct buried, the external force acts directly on the FOC, uneven force will cause the FOC bending when the uneven thawing settlement length exceeds the value shown in Table 2, and macro-bending loss will happen and attenuation of the optical fiber will be increased [10]. When the cable bears the pulling force beyond its permissible range for a long time, the fiber and FOC will gradually be broken [11, 12].

Laying in Cable Duct: When the cable laying in cable duct, the external forces in Figs. 3 and 4 act on the protection tube. When the overburden soil pressure is within the allowed pressure range of the protection tube, the FOC will not bear any external pressure. When the pressure exceeds the capacity of the protection tube, the tube will extend under downward pressure. The HDPE silicon core duct may be broken only in the case of the vertical depth of the settlement beyond the 180% of the horizontal length of the sinking section (assuming that the gripping force of soil at both ends is large enough, there is no extension of the silicon core on the two sides of the sinking section). That is, in a 10 m thawing settlement section, the broken HDPE silicon core duct will happen only in the case that a downward subsidence of 18 m duct occurs. Therefore, the fracture of HDPE silicon core duct due to the pressure of the thawing settlement section is almost impossible. Of course, when the silicon core extends downward, theoretically, the cable will also be subjected to a downward force, resulting in a certain amount of tension. But normally, the cable has a certain coiled

length (usually coiled FOC is not less than 12 m for each hand hole) on both sides of the hand hole [3], when the duct is pulled downward the cable will also be pulled downward but the coiled cable in the hand hole will be pulled into the duct in the time. It will counteract off some of the downward pulling force, so the pulling force on the FOC laid in the duct is very small compared to the pulling force suffered in the directly buried FOC.

Another advantage of laying FOC LIST with the duct in permafrost areas is that the laying time of FOC can be staggered with the construction time of oil/gas pipelines. In some ice-rich area of permafrost region, the construction time of oil and gas pipelines are often chosen in period of freezing in winter. But according to the specifications of FOC, the laying temperature should not be lower than −15 °C. When the weather temperature is too low to lay the cable, the HDPE tube can be laid first with the oil or gas pipeline in the same period. When the temperature rising the FOC then can be blown into the tube. It will reduce the damage of FOC in this way.

Because of the temperature raising the ground surface ice will thaw. So taking account of maintenance, another one required to be fully considered is that method of setting up and location of hand hole especially in ice-rich area. It must be determined that the way of installation of hand hole is in the conventional way buried or special way to install above the ground. The location of each hand-hole shall be considered fully not only the length of blowing cable but also the ease of entry to the site based on the actual conditions of the site.

6 Conclusion

The laying method of FOC LIST shall be determined according to the specific circumstances of the area. Natural geological conditions such as soil characteristics, groundwater level and depth of frozen soil along the route should be taken into account, along with external factors such as temperature, climate, and cultural environment. Because the FOC LIST with tube can bear more external mechanical force, the method of FOC laying with tube is more safe and reliable in the case of serious thawing settlement. But the construction temperature of HDPE pipe is also cannot be too low (normally is no lower than −20 °C), so the tube type shall be required specially or adopt steel tube suitable for FOC laying with blowing way in the case of the construction temperature is lower than −20 °C. And FOC blowing is recommended after the ambient temperature is higher than −15 °C in order to avoid damage to the FOC during the FOC laying.

References

1. Zhang X, Feng SG, Chen PC (2013) Thawing settlement risk of running pipeline in permafrost regions. Oil Gas Storage Transp, 365–369
2. Wu XY (2011) Technical application of laying in one ditch for fiber cable and oil or gas pipeline. Oil Gas Storage Transp, 547–549

3. Wang G, Gao JZ, Li GC et al (2012) Design and construction code of optical fiber cable (high-density polyethylene silicore duct) laying in the same trench with oil(gas) pipeline. SY/T 4108-2012, National Energy Administration, 3–4
4. Wei X (2015) Study of technical key point of fiber optical cable construction in optical fiber communication engineering. Inf Commun, 178–179
5. Wang Z, Shibing, Shuai M et al (2009) Stranded loose tube optical fiber cables for outdoor application for telecommunication. YD/T 901-2009, Ministry of industry and information technology of the People's Republic of China, 14–16
6. Wang HJ (2014) The common fault and maintenance of communication fiber optical cable line. China New Telecommun, 17
7. Tan JD, Zheng J, Ma YB (2012) Displacement monitoring of Mohe-Daqing oil pipeline in the permafrost frozen area. Oil Gas Storage Transp, 737–739
8. Zhao L (2012) Analysis of tension load in overhead transmission line. Electr Power Constr, 42–45
9. Zhang J, Qin ZQ (2013) Calculation and analysis of ice non-balance tension in overhead transmission line. Mech Electr Inf, 45–47
10. Peng XL, Zhang H, Li YL (2014) Simulation study on influencing factors of macro bending loss of optical fiber. Laser Infrared, 1132–1136
11. Gao P (2010) Construction technical study of communication buried optical cable in plateau permafrost area of QingHai-Tibet railway. Railway Signal Commun, March, 52–53
12. Zhang T (2005) Study of influence on optical cable from perennial frozen soil. Railway Signal Commun, 49–50

Lessons Learnt in Annuli Cure of Gas Storage Well

Lunjie Chang[1(✉)], Shouwu Qiao[2], Yong Liu[1], Yongbin Shan[3], and Xiaohu Jin[3]

[1] Development Department of Tarim, PetroChina, Beijing, China
clj-tlm@petrochina.com.cn, 2315828984@qq.com
[2] No 4. Production Plant of ChangQing Oil Company of PetroChina, Beijing, China
qsw_cq@petrochina.com.cn
[3] EverGreen Energy Service, LLC, Beijing, China
{shanyb, jinxh}@ever-greenservice.com

1 Introduction

S6H well is a gas production well. Well is completed with 5″ tubing for the gas injection and production, 7″ production casing, 9 5/8″ technical casing, 13 3/8″ surface casing, and 20″ conductor pipes. See Fig. 1.

In April 2014, well began to inject gas into the depleted gas formation. Multiple cycles of gas injection and production as shown in Fig. 2.

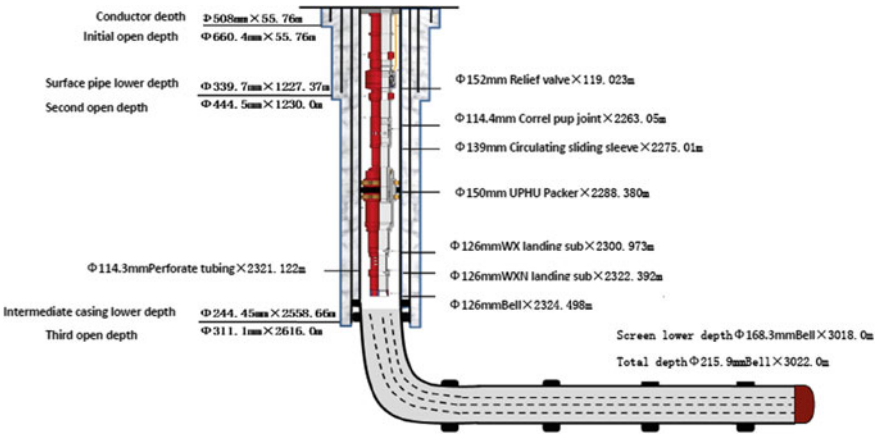

Fig. 1. Well schematic

S. M. Shemwell and J. Lin (eds.), *Proceedings of the International Petroleum and Petrochemical Technology Conference 2018*,
https://doi.org/10.1007/978-981-13-2173-3_15

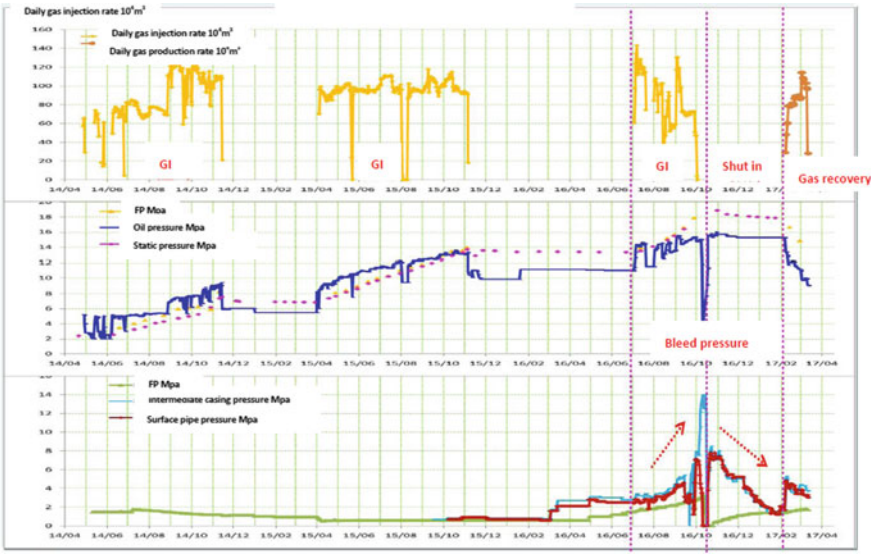

Fig. 2. Gas injection and production

Two cycles of gas injection were ended in Oct 2015. Tubing pressure increased up to 16 MPa. At the end of the second cycle of gas injection, pressure built up in Annuli B and C. Before the third gas injection in July 2016, the pressure in annulus A/B/C is about 1.7/2.8/2.6 MPa. With the onset of 3rd gas injection, the pressure in annulus A/B/C kept increasing and reached up to 3.5/14/7 MPa at the end of 3rd gas injection. Tubing pressure was bled off and well was shut in for almost 4 months. Pressures in A/B/C dropped down to 1.8 MPa. When gas production started in Feb 2017, pressures in A/B/C increased up to 5 MPa at the start of production and reduced down to 3 MPa simultaneously at the end of production.

Multiple tests of pressure bleed off and build up were made to observe the communication between A/B/C.

When pressure bled off in annulus A, there was no significant pressure change in annuli B and C. When pressure bled off in annulus C, the pressure in annulus B dropped in same trend. When both pressures in annuli B and C dropped to the bottom, they built up pressure simultaneously.

Conclusion of annuli pressure build-up:

A. Annulus A has no communication with Annuli B and C.
B. Annulus B built up pressure due to the gas migration from the gas formation.
C. Neck seal and pack-off seal were both failed in annulus B.
D. Gas migration is up to wellhead within annulus B. It is a combination of micro-channeling alongside the casing cement and cement formation interface as well as contamination and channeling within the cement. Gas migrated from the gas storage zone and up through those channels to top of cement. Gas penetrated through the fluid atop of TOC up to surface wellhead. It went through neck seal and pack-off seal and communicated with annulus C.

2 Job Performance

Since annulus B is the main cause for pressure build up, job purpose to cure gas migration in annulus B. It is understood that pressure in annulus C will diminish when the pressure in annulus B is eliminated.

From the original VDL data, top of cement in annulus B was indicated at 85 m.

Job target is to cure the gas migration in Annuli B.

Material, tools, and hands were mobilized to well site. The pressure in annulus B was bled off. Cleaning agent was pumped into annulus B to fill up the annulus and locate how much fluid to be displaced. Data showed that there was only 3.5 m fluid space atop of TOC left in the annulus. A hose was placed and went into 3 m and stopped. This implied that TOC is almost up to surface and the space for dumping sealant will be only about 3 m.

Since the space to pour sealant is so limited, pressure on wellhead must exert to overcome the pressure below. However, neck seals and pack-off seals in the void of technical casing spool were failed. Any pressure applied to annulus B will be bled through annulus C. In addition, due to lower surface temperature at 7–18 °C, the sealant will crosslink very slow.

After discussion with client, a modified operation procedure was made as below,

A. Client squeezed grease into the void to temporarily shut off the void leak during pressure applied for crosslink
B. Wait for one week when the weather becomes a bit warmer. Sealant will be pumped and crosslinked during the temperature ranges from 15 to 20 °C. Crosslink time will be 4 days.
C. A total of 1.5 m sealant will be pumped into the annulus. If the pressure was not cured, there would be still min. 1.5 m space left for further operation.

Grease was injected and void was temporarily shut off. A peak pressure of 15 MPa was tested ok. Annuli B pressure was bled off down to zero while the pressure in annulus C went down to zero too. Sealant was pumped into the annulus and fell down to supposed TOC at 3 m below.

Valve was closed and pumping pressure increased to 15 MPa. It dropped down to 7 MPa and built up to 13 MPa. Multiple cycles of pressure up maintained the wellhead pressure in annuli B at steady 7 MPa. About 30 min later, the pressure in annulus B started to increase slowly. Day one pressure went up to 10 MPa. Day two pressure went up to 12.8 MPa. Day three pressure went up 13.8 MPa. Day four pressure kept stable in the morning but sharply went down to zero at 2 pm afternoon. The sharp down was because the void sealing failed and pressure communicated with annulus C. Once communicated, the pressure in annulus B dropped down to zero and slowly built up.

6 h later, the pressure in annulus B started to build up. In 24 h, pressure grew up to 7 MPa. This indicated that the cure of annulus B gas migration failed.

3 Lesson Learnt

Due to low surface temperature, void sealing failure and uncertainty of annuli conditions, the job was finally suspended. From this job, curing of annuli pressure build-up depends highly on the following understanding

A. Accurate TOC—Top of cement is vital to decide the correct temperature and pressure value at curing point.
B. Fluid condition—To assure a safe gravity fall of sealant, annuli fluid atop of TOC must be fully understood.
C. Sealant—Sealant must have the strong bond strength to casing, no permeability itself after crosslink, reliable crosslink time and fully cure time, no reaction to annuli fluid, gas and other material, etc.
D. Recipe selection—Precisely selection of recipe based on accurate temperature and pressure data is also key to success.
E. Integrity—If pressure has to apply on surface to overcome gas migration pressure during crosslink, fully annuli integrity atop of TOC must be secured.

3.1 Understanding Gas Migration

Understanding the mechanisms of gas migration is complicated by the evolution of annular cement column with time. The slurry begins as a dense, granular suspension that fully transmits the hydrostatic pressure [6]. As slurry gels, a two-phase material comprises of a solid network with pore fluid forms. Finally, the setting process reaches a point that the cement is for all intents and purposes an impermeable solid. After slurry placement, gas may enter through different mechanisms according to the cement states as below [1].

State 1—Dense Granular Fluid: When the pump stops, the slurry in the annulus is a dense, granular fluid that fully transmits the hydrostatic pressure. If pore pressure is not greater than hydrostatic pressure, gas cannot invade into cement.

State 2—Gelation Process: Almost immediately after the pump stops, the annulus pressure drops due to the combination of gelation, fluid loss, and shrinkage. When the pressure within the annulus falls down below the pore pressure, the gas invasion will happen. Even with the existence of mud filter cake, a 1 psi formation differential pressure will force gas to invade.

State 3—A two-phase material: Once a cement column becomes fully self-supporting, it is a matrix of interconnected solid particles containing a fluid phase. Continuous hydration reduces the volume and causes shrinkage. Shrinkage gives space for gas to invade. Gas invades and extends gas bubbles into rising plume.

State 4—An elastic solid: When hydration completes and cement becomes elastic and brittle material, gas fingering may stop but invasion continues to migrate along the microchannel of cement casing and casing formation interface.

Figure 3 illustrates the gas migration within annulus during above states.

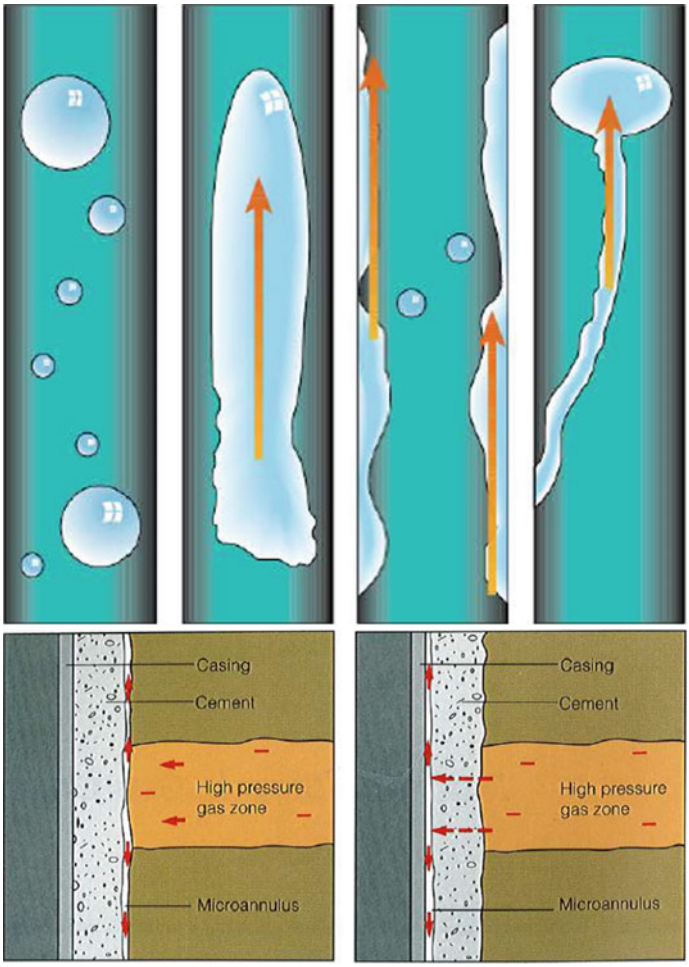

Fig. 3. Gas migration in annulus

3.2 Understanding TOC

Top of cement can often be determined by CBL/VDL log data. However, it is not always true that a correct TOC can be precisely determined by VDL log. First, the log is often done when the casing is completed. Well might be produced by a number of years and migration may blow out particles that accumulate atop of TOC. With continuous gas migration over time, such an accumulation may add on TOC over several meters to dozens of meters. Second, due to gas migration, there will be extensively channels and micro-channels along the cement column. The accumulated volumn of those channels and micro-channels may reach up to a few liters to dozens of liters. Third, due to the technology limit in the early days, some VDL log data may not be accurate so the TOC is difficult to locate and may be incorrect.

See Fig. 4 to illustrate the TOC conditions in the annulus.

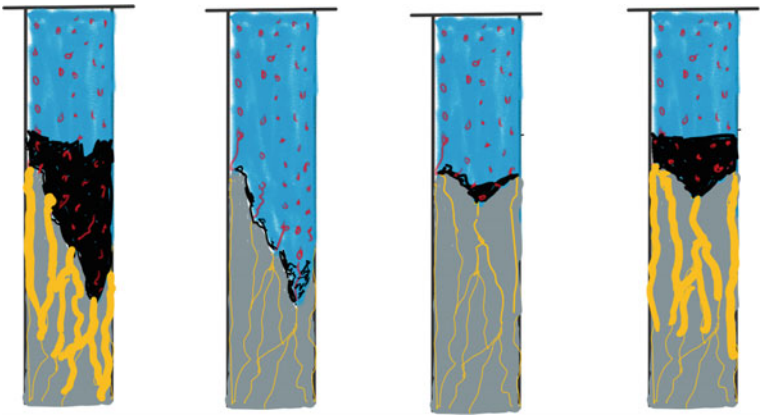

Fig. 4. TOC conditions

When the sealant is pumped and gravity fall on top of TOC, surface pressure or hydrostatic pressure will overcome the gas migration pressure.

The designed sealant plug length may be partially or totally lost when

(a) Slope TOC will absorb partial sealant volumn.
(b) Large channel will take more sealant volumn.
(c) High positive differential pressure atop of sealant will force more sealant into channels.

If major volumn of sealant is lost due to the above reasons, the sealant plug after crosslink may disappear or too short to take necessary gas migration pressure.

Multiple pumps of sealants can eventually set up a reliable sealant plug length.

If TOC depth is not accurate, designed crosslink time will be wrong. Resin sealant is thermoset and highly relies on the temperature at curing point for an exact crosslink time. If TOC depth is wrong, the sealant may take much longer or shorter time to crosslink. In the worst case, it will never crosslink or start to gel during the gravity fall.

Unfortunately, in most jobs, the TOC depth is not accurate and sometimes even uncertain. In this scenario, the recipe must be carefully designed to avoid gelling during gravity fall process. And time to wait on crosslink may take longer than the designed crosslink time in case that TOC depth is shallow than the designed TOC depth.

Designing a higher temperature and longer crosslink time than the known TOC depth will be a safer operation.

3.3 Understanding Annulus Fluid

Not always the fluid atop of TOC is pure liquid or fresh water. You will never know if or not any grease, debris, rusty particles are floating up and down within the fluid. The

annulus may be treated before and some kinds of material might be pumped into it and can never be circulated out of the annulus, see Fig. 5.

Fig. 5. Highly suspected grease circulated out of B annulus of S6H

Figure 5 illustrates the fluid circulated out of annulus. Suspected grease was floating within the fluid. Those greases are high viscosity and will certainly delay or stop the gravity fall of the sealant. A few steps must be done before the pumping of sealant into annulus:

(a) Try to circulate the fluid within the annulus as much as possible and take any samples of the debris or muddy to lab.
(b) Mix the debris and muddy with sealant and test in lab to verify if they react to each other.
(c) Make a column of fluid containing those debris and muddy, Sealant falls by gravity to make sure that sealant has no problem to gravity fall. If not, adjust sealant density to make a heavier sealant to verify a proper gravity fall.
(d) If those debris or muddy severely exist within the annulus, a chemical agent may be pumped into annulus to dissolve or get rid of them before pumping sealant.

Fluid density is also of concern. Sealant must be heavier than annulus fluid to secure a proper gravity fall. If the fluid density is near to sealant density, gravity fall will take much longer time. In this case, the sealant must be weighed to increase the density. Heavier sealant yields faster gravity fall but more difficult to penetrate the channels. So compromisation must be considered to assure a properly gravity fall and strong penetration into channel to shut off gas migration.

Annulus fluid must be sampled and tested at lab to avoid any reaction between debris/mud/rusty/grease and sealant. And sufficient gravity fall speed must be evaluated for a proper sealant density to secure a timely gravity fall and strong channel penetration.

3.4 Gas Frozen

Migrated gas may contain moisture or water. When surface temperature is below the gas frost point, gas will hydrate to form a cap on wellhead. Such an ice-like cap may have no or little permeability that any sealant can not be pumped into it. When second operation was deployed for SH6, surface temperature went down to 10 °C. Gas migrated did not contain moisture. But, gas came up through a water column above TOC and brought water and moisture up to wellhead. When this mixture came up to low temperature at wellhead, it frosted and formed a hard cap. Any fluid trying to circulate the annulus could not be pumped into it. Therefore, the job must be suspended and deployed until the frost melts with warmer weather.

When a gas frozen is met, pump glycol to pull down the frozen point. Gas frozen will melt to allow a sealant to pump in. Or job has to be suspended until weather gets warmer.

3.5 Understanding Annulus Geometry

Annulus geometry will be dependent with gravity fall speed, crosslink time, bond strength, adhesion to wall as well as sealant plug length. Remember annulus is between two casings. Inner casing consists of pipe and casing collar. Collar is bigger than pipe. Therefore, at each of the collar, there will be a restriction. Falling speed at this point will be faster and adhesion to pipe wall will be more than other points [2]. Smaller annulus yields slower crosslink time because crosslink reaction is proportional to the surface area of the sealant [3]. Smaller annulus also requests slow pump rate to avoid the sealant instantly flow back from the other swing valve.

Of course, accurate annulus geometry will guarantee an accurate annulus volumn, which is very important in calculating sealant volumn. The smaller the annulus is, the more adhesion of sealant to wall will be. Adhesion volumn is related to annulus size, height of gravity fall, fluid status and must be predicted before the sealant pump.

Always make sure of annulus volume, min. restriction, approx. fall rate of sealant crosslink time for smaller annulus, sufficient consideration of adhesion volumn.

3.6 Understanding Pressure and Temperature System Within the Annulus

Pressure system within the annulus is the key to a success for gas migration cure. Theoretically, pressure atop of sealant at curing point must be greater than the max. gas migration pressure upwards in order to avoid any gas invasion into the sealant [1] during sealant pure fluid state, a two-phase state, and solid state. Simply speaking, the hydrostatic pressure atop of the sealant at curing point must exceed the max. gas migration pressure. When gas migration meets the downward pressure, the potential pressure and energy from the gas zone will quickly bounce up. Thus, the process of pressure build-up is much faster.

If the hydrostatic pressure atop of sealant is not enough to overcome the migrated gas pressure, a surface pump pressure must be exerted to increase the pressure applied

to sealant. In this case, annulus and wellhead integrity above the curing point is crucial to maintain a continuous additional downward pressure on sealant.

Since sealant is thermoset, it is very important that the temperature at curing point shall be as accurate as possible. Sealant can cure the gas migration only when it is fully hard. If the temperature is not accurate, time to fully hard will be difficult to predict. A failure may happen if disturbance to pressure happens before the sealant is fully hard. Once the gas invades into sealant, the sealant will no longer be able to shut off gas migration regardless if or not it is fully hard later.

If temperature or pressure cannot be accurate or even uncertain at curing point, be sure to select a recipe designing for higher temperature and longer crosslink time for a safer and high success job.

3.7 Understanding Sealant

Sealant is the key to success. A sealant must possess the following feature in order to cure the gas migration

(a) Thermoset predictable.
(b) High bonding strength to pipe wall. Min. 1200 psi/ft bonding strength [4].
(c) No shrinkage during and after crosslink [3].
(d) No reaction with water, acid, akalkalilai, H_2S, CO/CO_2, cement, metal, gas, etc. [5].
(e) No permeability after crosslink [4].
(f) Elastically when pressure is applied [3].
(g) No hydration [4].
(h) Wide range of temperature.
(i) Multiple recipes selectable.

To meet the above criteria, only the proprietary epoxy resin can be considered. Most polymer sealants are too weak to shut off gas migration and cannot be taken into consideration. Normal epoxy resins are mostly a bit shrunk during crosslink [4] and therefore cannot be taken into account too. Right angel resin shall be cautious to use since it is fast crosslink and more glassy than slower crosslink resin [5]. Unfortunately, those sealants are proprietary chemicals and will not be disclosed to public. Company has to rely on its expertise to select the right sealant for the job.

Recipes selection

Recipe gives time to fall, gel, pump, hard and fully hard at specific temperature and space. Accurate time and space secure accurate recipe. A number of lab tests must be performed to determine the appropriate recipe for a job. In some case, the field test is necessary to verify the sealant recipe before it is pumped into the annulus. Unfortunately, those recipes are proprietary information and will not be disclosed to public. Company has to rely on its expertise to select the right service.

Select right resin and experienced service team is the key to success.

4 Conclusion

S6H annulus gas migration cure job gains many deep understanding of annulus gas migration cure. A number of criteria for understanding annulus TOC, fluid, gas hydration, annulus geometry and temperature and pressure system exhibit how to make a successful gas migration cure. Sealant property and recipe selection are also introduced.

Those criteria and material selection are key to a successful annulus gas migration cure and help colleagues in this field to better understand the annulus gas migration, select the right service companies or design a better plan.

Acknowledgements. We thank for the work and data from SH6 annulus gas migration cure service team and contribution from sealant designer and engineers.

References

1. Bearden WG, Spurlock JW, Howard GC (1965) Control and prevention of inter-zonal flow, JPT, 579–84. (Trans., AIME, 234)
2. Dusek K (1985) Epoxy resins and composites I, advances in polymer science 72. Springer, Berlin
3. Dusek K (1986) Epoxy resins and composites II, advances in polymer science 75. Springer, Berlin
4. Dusek K (1986) Epoxy resins and composites III, advances in polymer science 78. Springer, Berlin
5. Stewart RB, Schouten F (1988) Gas invasion and migration in cemented annuli: causes and cures. SPE Drilling Eng
6. Sutton DL, Sabins F, Faul R (1984) Annular gas flow theory and prevention methods described. Oil & Gas J, 84–92, 10 Dec 1984

Research on the Design Concept and Key Technology of a New Topology Gas Station

Mingjun Du[1,2(✉)], Jiaqiang Jing[1], Xinqiang Xiong[2], Zhigui Zhang[2], and Cheng Wu[1]

[1] Southwest Petroleum University, College of Petroleum Engineering, 610500 Chengdu, China
0086+13833770803dmj260750009@163.com
[2] China Petroleum Engineering & Construction Corp North Company, 062552 Renqiu, China

1 Introduction

With the sustained and rapid development of national economy, the populace's essential demand for vehicle purchasing is increasing vigorously, which raises higher requirements for the construction of urban gas stations. As primary infrastructure for urban development and residents' daily life, the layout rationality, safety and scientific management of gas stations have absorbed widespread attention [1]. Affected by market opening and regional competition, the number of urban gas stations has grown greatly. Redundant gas stations not only take up city resources and reduce their own utilization but also bring a huge risk to urban safety. Furthermore, there is a higher standard for safety and environment protection of gas stations in recent years with the extreme deterioration of the urban environment [2]. What oil sales enterprises and urban development need to solve urgently in the future is integrating resources, saving land, changing decentralization to centralization, reducing oil vapor discharge, and oil gas loss [3].

In China, with constant development of digital cities, urban resources sharing and informatization process are both greatly promoted in 2016. Digital cities must bring unprecedented opportunities for social development in future under the guidance of innovation-driven national strategy and new urbanization construction. As infrastructure of city service, the gas station will be transformed and upgraded to meet the demand of urban development.

The author analyzes requirements of urban gas stations' development in future and demonstrates the design concept of topological gas stations from multiple perspectives, such as forward-looking, feasibility, safety and convenience, which lays a solid foundation for the sustained development of hazardous industries in city.

S. M. Shemwell and J. Lin (eds.), *Proceedings of the International Petroleum and Petrochemical Technology Conference 2018*,
https://doi.org/10.1007/978-981-13-2173-3_16

2 Design Concept of Topological Gas Station

The design concept of topological gas stations is to replace original gas stations with oiling machines as new sale terminals [4]. According to spatial geography information of radiation areas, storage terminals are set up (Level One Station and Level Two Station) in a proper location, and can also rely on the existent oil depots around the city. Oil products are mostly stored in storage and transportation terminal and delivered directly to the oiling machines by pipelines, which has realized remote self-refueling service. The great advantages of this concept are resource conservation, improvement in the utilization rate of refueling sites and reduction of hidden danger and loss (See Fig. 1).

Fig. 1. Pipeline system layout of topology gas station

Pipelines can be designed into circular structure or tree-like structure due to the requirements of geographical features and radius of the radiation areas in topologic refueling concept.

Considering spatial limitations of oil utilization, diesel is mostly used for public transport (large vehicles and trucks which are not allowed in urban areas) while gasoline is mostly used for small vehicles and private cars. Taking distributing demand of oil type into account, diesel oiling machines can be set around storage terminals or transport companies, where it will be needed massively. Whereas, gas–oil oiling machines can be arranged around densely populated residential areas, commercial areas, office areas, and traffic arteries. The idea above avoids various disadvantages of original refueling method and saves lots of manpower. The layout of refueling sites in topology gas station is shown in Fig. 2.

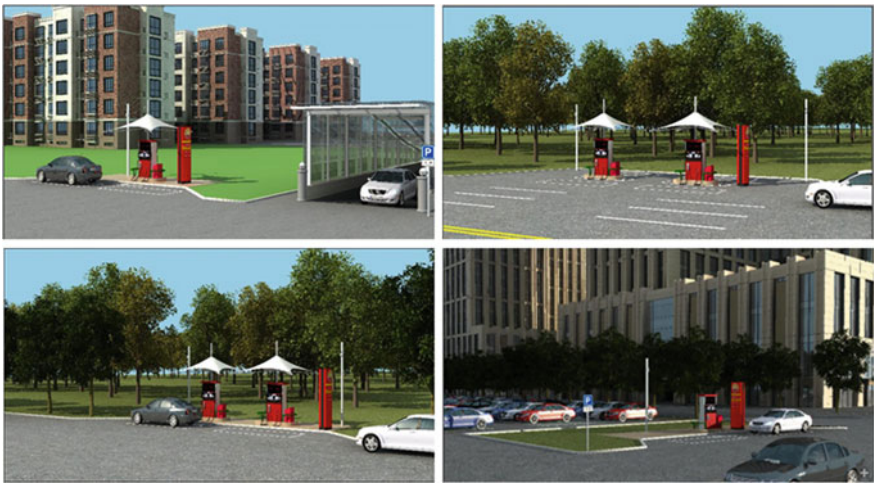

Fig. 2. Layout of refueling sites in topologic gas stations

Oiling machines have their own electronic screen, integrated surveillance, and intercom system. The safety facilities as bumping posts, fences, and fire extinguishers are arranged around the oiling machines. In addition, the management department should arrange personnel to inspect refueling sites regularly.

3 Key Technology of Topological Gas Station

3.1 Control Principle

The key technology of topological gas station design is transportation. To solve the problems brought about by differences in delivery distance to storage station, delivery quantity, and altitude among oiling machines, the author makes a systematic study on control of topology gas station technology based on the idea of urban constant pressure water supply.

Through computational simulation by SPS, for both circular and tree-like topology gas stations, it is feasible to use pressure stabilizing technology. Namely, the pressure of main pipelines is kept in a certain range. At the end of each branch line, a pressure regulator valve is arranged in front of the refueling site, which will ensure pressure behind valves to be stable and meanwhile avoid equipment overpressure. The pump station is set in the storage terminal and adopts the operation mode of different displacement pumps (frequency conversion) connected in parallel. By this means, vehicle refueling can be achieved in the whole radiation area [5]. For the coefficient of each refueling site is not balanced, there may be only a few refueling vehicles in some points, especially at night. Then a small displacement pump can meet refueling needs. Pipeline pressure will decrease with refueling vehicles increasing. At the same time, control system will output a pump-running signal when the pipeline pressure drops to a

certain value, which shows the small displacement pump is unable to meet refueling needs. To maintain the pressure and volume, some large displacement pumps start to operate sequentially. On the contrary, the pipeline pressure will rise with refueling vehicles decreasing. Pump-quit signal will be outputted by control system when the pressure is higher than a certain limit. Large displacement pumps should be consistent with the order "start last and stop first" to keep the pipeline pressure in a certain range and ensure the stability of oil transfer system.

3.2 Determination of the Number of Refueling Guns in Radiation Radius

According to the design concept of new topological gasoline station, objective constraints of urban construction are combined. For topological refueling system relying on oil depot, because storage and transportation terminal is the oil depot itself, there is no need for tank truck distribution. Refueling points and the number of oil gun in its radiation radius in principle are not limited with only a few conditions, mostly depending on the first and second class gas stations within urban areas as storage and transportation terminals. Therefore, effective delivery quantity and consumption of oil in a single day are the main factors that restrict the number of refueling guns in radiation radius.

For example, taking an urban secondary station as the terminal of storage and transportation, the maximum number of refueling guns of single oil (such as 92# gasoline) is analyzed in its radiation radius. The peak valley curve of refueling volume and service vehicles in the gasoline station is shown in Fig. 3.

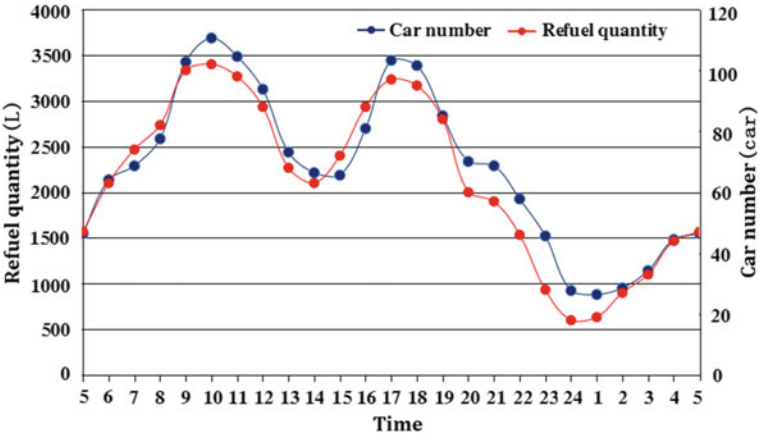

Fig. 3. Valley peak curve of a gasoline station

Analysis of Fig. 3 shows that there are two peaks of oil refueling during the day of the station, which is 9:00–12:00 a.m. and 16:00–19:00 p.m. The trough period is mainly from 23:00 to 5: 00 next morning. According to statistics of storage tank volume of the secondary station (Table 1) and the refueling vehicles, oil tanker distribution is not needed in trough period, and the oil storage quantity of the station can meet night refueling requirement.

Table 1. Table of storage tank configuration of secondary topological gasoline station

Gasoline station level	Capacity of single tank	Number of tanks of 92#	Number of tanks of 95#	Number of DIESEL TANKS of 0#
Secondary	30 m^3	2	2	2

For the secondary topological gasoline stations in urban areas, although the amount of refueling could greatly increase compared with that in traditional secondary stations, the daily oil peak valley curve will not fluctuate significantly. Therefore, topological gasoline stations do not take into account the distribution of road tanker (poor night delivery security) from 11: 00 p.m. to 5: 00 a.m. next day. The road tanker of topological service station allows delivery time to be 17 h from 5: 00 a.m. to 11: 00 p.m.

Since the road tanker is gravity dump truck, unloading time (including auxiliary time) is about 1 h, and the tank needs about 30 min after unloading. Suppose there are spare tanks available that can unload the oil tanker when the tanker comes into the station. The number of delivery vehicles of single oil is at most about 11 in one day. The probability of this working condition in actual operation is small (Except for the type and quantity of refueling points in the radiation area, the imbalance coefficient of time consumption is large. The peak and valley curves of different refueling points are superimposed during the day, which is also the best design concept of topological gasoline station.) Because of disequilibrium of refueling quantity in each period and the limit of tank capacity in the station, distribution of the oil tanker also has corresponding peak and valley curve. Because there are no oil tanker distribution statistics, on the basis of analysis of urban station refueling in peak curve, we thought that for urban secondary topology station, the number of road oil tankers of every product should not be more than 8 every day. The delivery time is shown in Table 2.

Table 2. Single oil tanker delivery schedule of the secondary topological gasoline station

Delivery time	The number of road tankers	Remark
5:00–9:00	1	
9:00–16:00	3	Consider the peak hours of the morning and the relative low point of midday
16:00–20:00	2	Meet peak consumption in the afternoon
20:00–23:00	2	In addition to this period of consumption, the consumption will be maintained between 23:00 and 5:00 next morning

The effective volume of a road tanker is 27 m^3; the total delivery volume of a kind of oil product (e.g., 92# gasoline) is 216 m^3 in one day. Assuming that the product can be consumed in one day, according to the formula of standard sales of the tanker, it is determined that the maximum number of refueling guns for single oil in the secondary topological gasoline station is 108. If a certain oil (such as 92# gasoline) sets two guns at each refueling point, you can supply 54 refueling points; if refueling volume per

vehicle is 30 L, 7200 vehicles can be served per day and the average number is 133 vehicles in each Refuel point.

As can be seen from the above data, the topological gasoline station maximizes the utilization rate (Turnover times) of the storage tank in the station, which has the obvious advantages compared with the traditional gasoline station.

3.3 Delivery Radius and Diameter Determination

Determination of the distribution radius of topological gasoline station is mainly limited by the design pressure of pipeline. Due to the lack of relevant regulations to define the allowable operating pressure of pipeline in urban areas, design pressure of the process system can only be defined from the perspective of security. Under different operating pressures, explosion danger area of oil and gas diffusion after gas pipe leakage was analyzed by simulation software PHAST, and combined with the present domestic conventional gas station design pressure (0.6 MPa). We think topological gasoline station pipeline design pressure should be no more than 1.0 MPa.

After confirming the design pressure of pipeline, we can use SPS software to set up calculation model according to space layout and corresponding number of refueling gun of the proposed the refueling points, and to determine the radius of dry branch pipe diameter and distribution distance.

4 Equipment Selection of the Topological Gasoline Station

For the new type of topological gas stations, the key equipment is the tank, pump unit, and intelligent self-service refueling machine. The same oil tanks of topological gasoline stations will use the pipe to link the bottom of tanks and the valves to control import and export of oil. In principle, the number of tanks for each type of oil is not less than 2, and one of them is used for oil export and the other for import [6]. The storage and transportation terminals shall set up one, two or three stages of oil and gas recovery process to ensure meeting the discharge standards.

Intelligent self-service tanker is the most critical equipment of topological gasoline stations. Its functions include self-help, voice prompt, WeChat payment, credit card payment, cash payment, invoice printing, etc. The operation panel mainly includes flexible and fast man–machine interface, which can be applicable to all ages. The security aspects mainly include anti-theft, anti-damage alarm system, and low-intensity impact tanker automatic shutdown (pipeline inlet valve automatic shutdown) system, Automatic closing system of fuel tanker for surrounding fire conditions and HD video monitoring system. Oil and gas recovery of refueling process can be integrated into the tanker, using the process of condensation or membrane separation to realize oil and gas recovery.

Because the buried pipeline is used from storage terminal to refueling point, considering from the perspective of security and environment, the pipeline, in addition to anticorrosion system, should also set up the leak detection system and double pipe can be used if conditions allow.

5 Technical Advantages of New Topological Gas Station

5.1 New Technology Can Improve the Security of Oil Distribution

Refined oil product, especially gasoline, is inflammable, explosive and volatile, which is prone to cause fire and explosion accidents in the process of highway loading, unloading, and transportation. Although a variety of precautions have been taken by relevant departments, such kind of fire and explosion accidents still occur occasionally. Furthermore, with the rapid increase in the transportation of raw materials, safety problems brought by road tanker transport are becoming more and more prominent. Compared with tanker transport mode, pipeline transport has distinctive characteristics such as "carrier static, cargo closed". The oil products move forward under the action of pressure difference. The pipeline transport mode can fundamentally improve the safety status of raw material transportation.

5.2 The New Technology Can Improve the Quality of Oil Products

Tanker transport can reduce the mass of oil products, resulting in decline of quality. There are three main reasons as follows. (1) In the process of loading, unloading, and transportation, light components lose and the mass of oil products reduces because of the big breathing loss and small breathing loss phenomena. (2) In tanker long-distance transportation, small breathing loss phenomenon gets severe under the influence of both diurnal and regional temperature difference, which leads to lots of moisture adsorbed into oil products and reduced quality. (3) In the process of tanker transportation, the entry of dust grains will affect the quality of oil products, especially when it is going through areas with serious wind and sand. However, the leak proofness of pipeline can effectively avoid the loss of light components and the pollution caused by impurities and moisture so that the safety in the use of oil consumption machinery can be ensured.

5.3 The New Technology Can Alleviate the Transportation Pressure of Urban Road

At present, the gas station in our country adopts tanker for distribution. With the continuous development of future urban construction and incessant improvement of refined oil product requirements, the number of delivery tank trucks will increase year by year. Since highway capacity has been oversaturated, especially for the old city, it is necessary to invest in the expansion or construction of new roads to meet the requirements of various material transportation. The increasing pressure of highway transportation and the contradiction between supply and demand of the tanker put forward the objective requirement for the pipeline construction.

5.4 The New Technology Can Effectively Save Land and Improve the Efficiency of Refueling

Covered area of new topological gas station is only about 5% of the area of traditional gas stations, and the location selection of the former is not so limited. At present, the number of private cars is increasing rapidly, and urban traffic is becoming increasingly congested. The fuel stations will be set up in all neighborhoods, centralized office areas and main arterial roads, which will maximize the satisfaction of customers' efficient refueling demand.

5.5 The New Technology Can Effectively Reduce the Transportation Cost of the Enterprises

As is known to all, the buried pipeline has the advantages of few topographical restrictions, good safety and closeness, low oil wastage, and little pollution to the environment. In addition, its economical efficiency is also noteworthy. The related calculation shows that pipeline transportation is the lowest cost method to transport oil on land and it costs only one-seventh of the cost of highway transportation.

5.6 The New Technology Can Reduce the Pollution to the Environment of the Traditional Refueling Process

The traditional gas station is equipped with buried horizontal tanks and fire-resistant breathing values. Although the gas station has considered one, two, even three times of oil and gas recovery, they still do not realize fully closed gas emission. The new refueling process employs pipeline transportation. Therefore, the operation temperature of oil products is stable and the volatilization rate is low. Meanwhile, the research and development of new refueling tanker can ensure the new technology to achieve airtight refueling and zero or micro emission, which is far less than the requirements of national emission standards.

5.7 The New Technology Can Adapt to Requirements of Future Urban Development

At present, urban heat supply, water supply, and other public facilities are managed by specialized companies. Based on this concept and combined with continuous development of digital city, we can boldly predict that in the future, all infrastructure at the service of city, gas station included, will be uniformly projected, constructed and managed by the government, which avoids repetitive construction and malignant competition among petroleum, petrochemical and other social enterprises, and develops urban construction from the perspective of safe and inhabitable city for real to achieve social harmony and convenience to our people and country.

6 Conclusion

As a new design concept, topological gas stations are an important guarantee to adapt to the planning and development of urban green health in the future, and have great market potential. New technology has broken the traditional design concept, which requires to revise current design specification for gas station and to exploit key equipment and facilities in order to fit in with the demand of new refueling system. It is expected that the new type of topological gas station can be applied and play an important role in the planning of the Xiong'an New Area and the new urban districts.

References

1. Shen L (2010) Study on spatial optimization of urban gas station. M.A. thesis, Ocean University of China
2. Shi Z (2016) Study on the method of gas station operation safety evaluation and its application. M.A. thesis, Chinese Marine University
3. Wang B, Liang Y, Zhang H (2018) Research progress on two distribution of refined oil. Oil Gas Storage Transp 37(2):121–125
4. China Petroleum Group Engineering Design Co., Ltd. NC Company (2017) A topologically remote refueling system. China Patent ZL201720311410.7
5. China Petroleum Group Engineering Design Co., Ltd. NC Company (2017) A gas station for topologic refueling systems. China Patent ZL201720310945.2
6. China Petroleum Group Engineering Design Co., Ltd. NC Company (2017) An oil storage device for topologic refueling system. China Patent ZL201720328881.9

Defoaming Characteristics of Crude Oil Foams Containing CO_2

Xiaokai Xing(✉), Heng Zhou, and Xuhui Guo

National Engineering Laboratory for Pipeline Safety, Beijing Key Laboratory of Urban Oil and Gas Distribution Technology, China University of Petroleum, 102249 Beijing, China
xingxiaokai@vip.sina.com

1 Introduction

The collapse characteristics of crude oil foams and the influence of defoaming net on it are acquired by experiment. It is recommended to increase the mesh number and layer number of defoaming net appropriately while installing it at a certain distance from the inlet of the separator to function on foam with less liquid in order to get better defoaming effect.

After entering the separator, the CO_2 flooding produced fluid will release CO_2 due to depressurization, which may cause foaming problems for high foaminess crude oil. Crude oil foam will occupy the gas phase space in separators, deteriorate separation effect and cause oil overs in serious cases. It is necessary to study the collapse characteristics of crude oil foam to effectively eliminate the foam in separators in order to improve production efficiency. Recently, there are researchers [1, 2] who produce crude oil foam by depressurizing saturated live crude oil to study the properties of foam and evaluate defoamers. Rooke et al. [3] claimed that installing proper internals is a relatively cost-effective way in dealing with foaming problems, while at present the design and installation of defoaming internals are mostly based on experience. Little research has been done on defoaming internals and most of them are based on the numerical simulation method [4, 5]. For orifice and mesh structure are commonly used in defoaming [6], the effect of this kind of structure on the collapse characteristics of crude oil foam is studied in this paper based on defoaming net(mesh), hoping to provide reference for the design of defoaming internals.

2 Experimental Principle and Method

In order to simulate the crude oil foams in separators, crude oil foams are produced by depressurizing live crude oil, which is saturated under the certain pressure of CO_2. The experimental setup is shown in Fig. 1. The oil sample was produced in Hei-59 block of CO_2 flooding pilot zone in Jilin Oilfield, whose physical properties are shown in Table 1. Put 1 L oil sample in the pressure piston vessel, leaving about 2.4 L gas place, then inject CO_2 to drive away the air, and then pressurize to 0.66 MPa. The

S. M. Shemwell and J. Lin (eds.), *Proceedings of the International Petroleum and Petrochemical Technology Conference 2018*,
https://doi.org/10.1007/978-981-13-2173-3_17

temperature of pressure piston vessel is kept at 50 °C. It means the crude oil is saturated when the pressure is stable, which is about 0.5 MPa. The next step is to produce foams and observe. Place the graduated cylinder in 50 °C water bath and spray the live crude oil (about 220 mL) in it through a tube, then observe the collapse of foam. When studying the effect of defoaming net, the process of crude oil flowing through the defoaming net is simulated by moving the defoaming net through the foam at a certain speed with an electromotor device. The speed is determined by the ratio of the produced fluid flow rate to the cross-sectional area of liquid phase in separator, which is about 2 mm/s according to the field data.

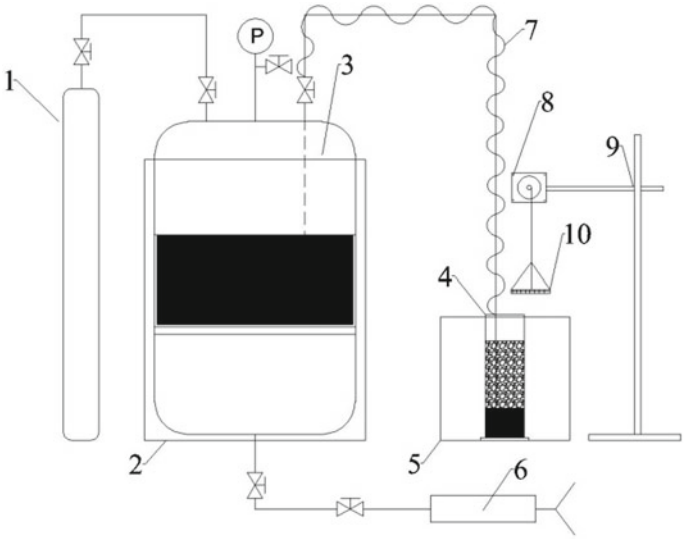

1−CO_2 cylinder 2−Heater band and insulation layer
3−Pressure piston vessel 4−Graduated cylinder
5−Water bath 6−Manual pump
7−Thermal insulation belt 8−Electric machinery
9−Iron stand 10−Defoaming net

Fig. 1. Schematic diagram of experimental device

3 Analysis of Foam Collapse Characteristics in Natural State

Typical crude oil foam made in the experiment is shown in Fig. 2. In the process of foam collapse, there will be a foam–air interface and a foam–liquid interface. Take liquid volume as V_l, foam volume as V_f and the total volume $V_t = V_l + V_f$. Define the

Table 1. Physical properties of crude oil in Hei 59 block

Wax content (%)	Gel point (°C)	Density (20 °C) (kg/m^3)	Viscosity (50 °C) (mPa s)
23.6	33	850	28.6

end of spraying as zero time and the collapse process can be described by the total specific volume V_t/V_{t0}, liquid specific volume V_l/V_{t0}, foam specific volume V_f/V_{t0}. The change of the above three parameters with time is shown in Fig. 3. In the experiment, we observe that $V_{t0} = V_{f0}$, indicating that there is no free liquid at the end of spraying, the mixture is completely made up of foam.

As seen in Fig. 3, the process of foam collapse in natural state includes three stages. In the first stage, the height of foam–air interface is stable, and the height of foam–liquid interface keeps increasing. There are lots of small bubbles rising up inside the foam system independently, namely without coalescence, while bubbles on the surface grow up with coalescence and collapsing. In the second stage, the height of foam–air interface reduces approximate linearly, the height of foam–liquid interface increases with lower speed. The bubbles inside the system are coalescing and the bubbles on the surface have various sizes (seen in Fig. 2), coalescing and collapsing violently. In the third stage, the height of foam–air interface decreases, and the height of foam–liquid interface keeps stable. The bubbles keep coalescing and collapsing, the size of which is smaller than that in the second stage, and tends to be uniform. The speed of foam collapse is slower in the third stage. It takes 144 s for the foam to collapse completely.

According to the above phenomena, gravity drainage plays a dominant role in the first stage, the desorbed CO_2 bubbles rise due to buoyancy and the crude oil flows down to the bottom of the cylinder. For the drainage process just starts, there is still much crude oil between the bubbles, which hinders the coalescence of bubbles. As the drainage process going on, the liquid film between bubbles gets thinner and the gas diffusion and coalescence effect get stronger. As the liquid content in foam decreases, because of the capillary force, the drainage rate slows down and the increase rate of liquid volume decreases, so both gravity drainage and coalescence are important in the second stage. In the third stage, coalescence is the dominant effect with drier foam, which has a low drainage rate, the homogenization of bubble size reduces the coalescence and gas diffusion effect [7], so the collapse rate in the third stage is relatively low.

4 The Foam Collapse Characteristics Under Defoaming Net Effect

Due to many factors to concern, such as location, number, material quality, and so on, the design of defoaming mechanical device is a test for the creativity of designer [8]. The influence of various factors on defoaming effect is studied, like function time of net, number of layers, mesh number, and material quality, compared with foam collapse characteristics in natural state.

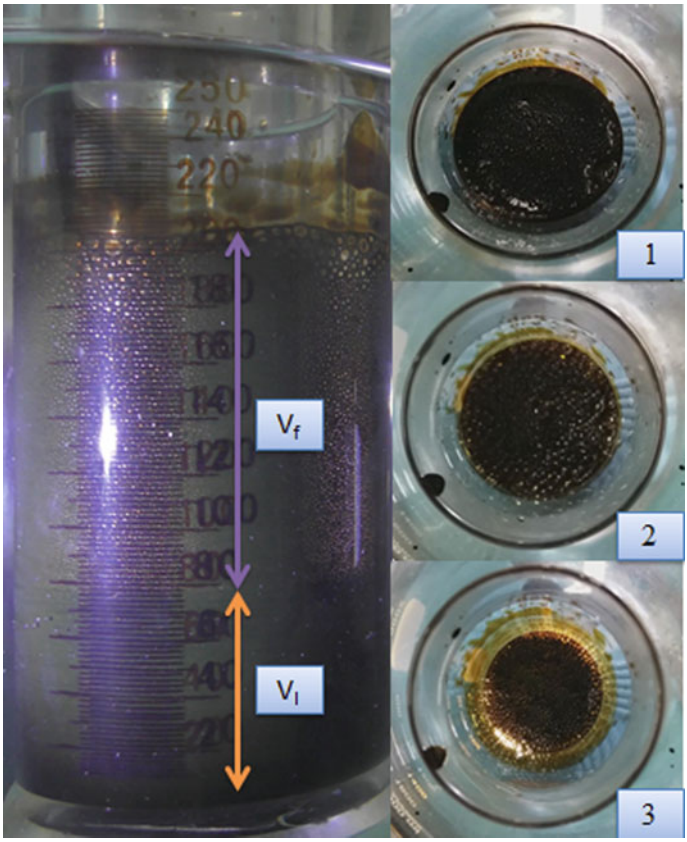

Fig. 2. Crude oil foam (side view and top view)

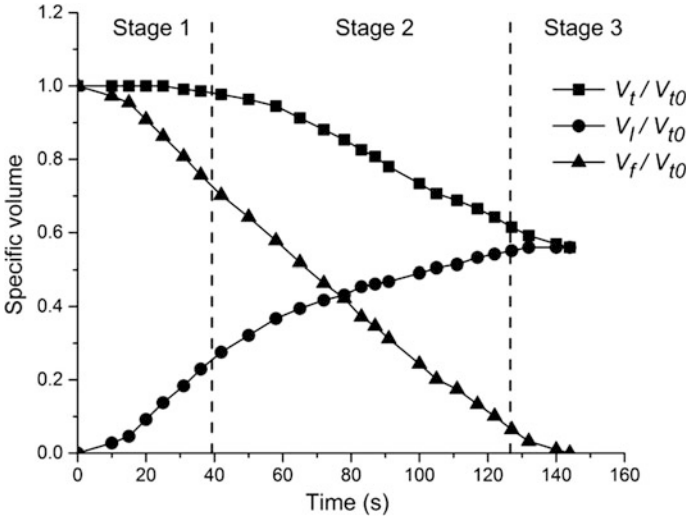

Fig. 3. Specific volume changes with time

4.1 The Effect of Function Time of Net on Foam Collapse

The function time of defoaming net indicates the location of defoaming net in separators. Defoaming net with single layer, 0.5 mm thread diameter and 14 mesh number is used at certain time after spraying. When the function time of net is 13, 31, 51 and 69 s, the time for foam to collapse completely is 140, 135, 132 and 139 s, shortened by 2.8, 6.3, 8.3 and 3.5%, respectively compared with that of natural state. The change of foam specific volume with time is shown in Fig. 4.

It can be noticed that both the early function time (at the beginning of foam forming) and the late function time (at the end of foam collapse) are not effective for defoaming. Meanwhile, the effect of defoaming net with single layer is not obvious, defoaming time is shortened by only 8.3% at most.

4.2 The Effect of Layers of Net on Foam Collapse

For single layer of defoaming net has no obvious effect, the defoaming net with 14 mesh number and 0.5 mm thread diameter is arranged in 1, 2, 3, and 4 layers (1 cm apart) to function at 51 s after the end of spraying. It takes 132, 130, 127, and 123 s for

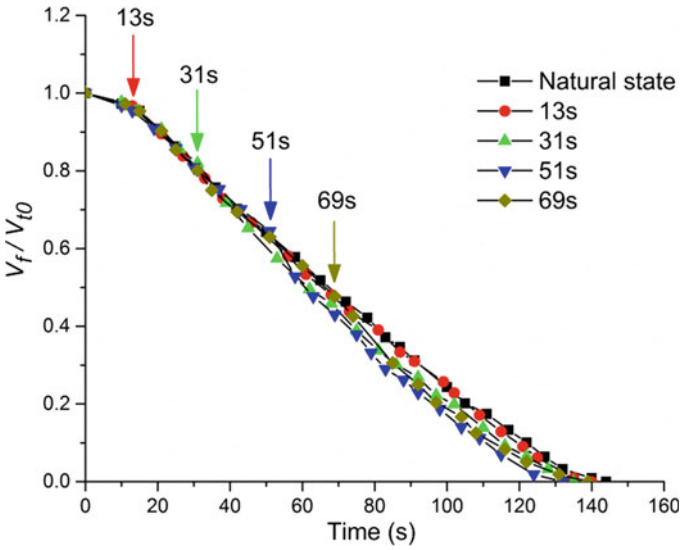

Fig. 4. Foam specific volume changes with time with different function time

the foam to collapse completely, shortened by 2.8, 6.3, 8.3 and 3.5% respectively compared with that of natural state. The change of foam specific volume with time is shown in Fig. 5.

It can be seen from the Fig. 5 that when using more layers of net, the defoaming effect is better. At 61 s after spraying, the foam affected by four layers of net has an obviously less foam specific volume than the others. With more layers of defoaming

net, the defoaming effect is better, which is good for eliminating foam accumulation during gas–liquid separation. Compared with collapse in natural state, the collapse rate in the later period (100 s after spraying) is lower. It can be observed clearly that the volume of remaining bubble becomes larger and the film gets thinner after the function of defoaming net.

4.3 The Effect of Mesh Number on Foam Collapse

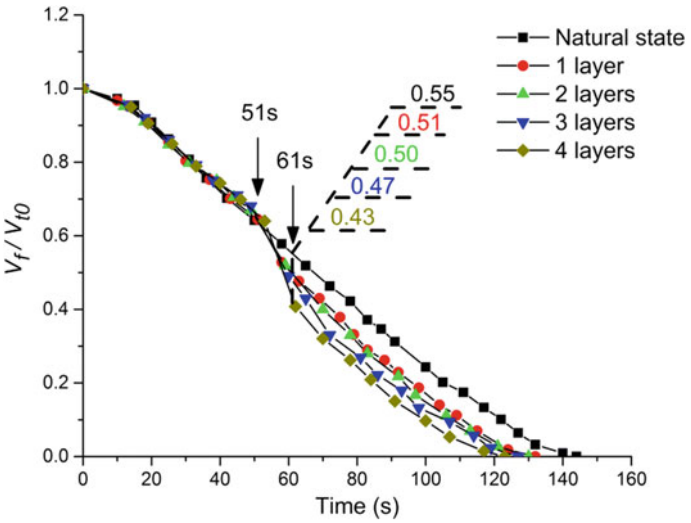

Fig. 5. Foam specific volume changes with time with different layers of net

The mesh number is a significance parameter of defoaming net, representing the number and size of defoaming mesh. Defoaming nets with three layers, 0.5 mm thread diameter and different mesh number are used at 51 s after spraying at the speed of 2 mm/s. When the mesh number of net is 5, 14 and 24, the time for foam to collapse completely is 137, 127, and 114 s, shortened by 4.9, 11.8, and 20.8%, respectively compared with that of natural state. The change of foam specific volume with time is shown in Fig. 6.

According to Fig. 6, defoaming is more effective with the increasing of mesh number. Foam specific volume is about 0.28 with 24 mesh number of net at 61 s after spraying, while with other mesh number of net, the foam specific volume is about 0.5. In other words, the high mesh number defoaming net can reduce the foam accumulation effectively during gas–liquid separation.

4.4 The Effect of Other Factors on Foam Collapse

In order to study the effect of material quality of defoaming net on foam collapse, stainless steel net and nylon net with three layers, 0.5 mm thread diameter and 14 mesh number are used at 51 s after spraying. The time for foam to collapse completely is 127

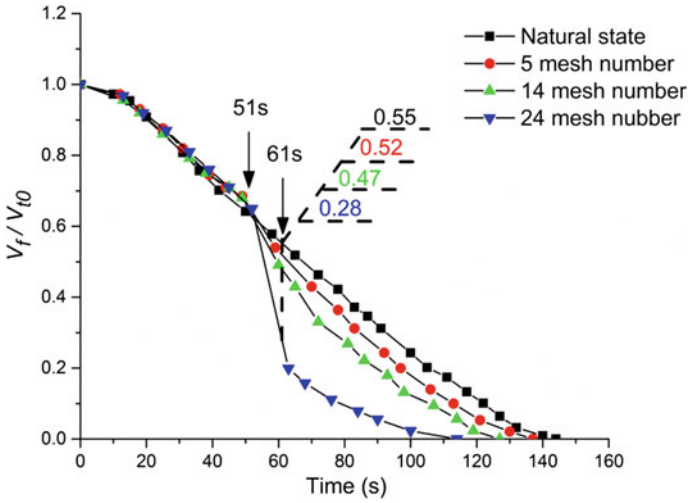

Fig. 6. Foam specific volume changes with time with different mesh number of net

and 137 s, shortened by 11.8 and 4.9% respectively compared with that of natural state. Therefore, we can know that the defoaming effect of stainless steel net is better than nylon net.

In the condition of 14 mesh number, 0.5 mm thread diameter, three layers and 51 s function time, the defoaming net is moved at the speed of 2, 5 and 11 mm/s, respectively. The time for foam to collapse completely is 127, 124, and 126, with few differences. In the condition of 14 mesh number, three layers, 51 s function time while moving at the speed of 2 mm/s, the time for foam to collapse completely with defoaming net of 0.1 and 0.5 mm thread diameter is 131 and 127 s. The effect of 0.5 mm thread diameter is slightly better.

Taking research of sieve plate defoaming device for reference, we assume that the defoaming mechanism for defoaming net is the shear and deformation effect on foam film. When the bubbles enter the mesh, the bubbles get deformed due to the decrease of the flow area. As the upper surface of the bubble overflows from the mesh, the bubble will expand due to the pressure drop through the defoaming net, and tends to collapse or coalesce for the film becomes thinner. When the bubble diameter is smaller than the mesh size, only some of the bubbles will change shape [9]. If the function time of net is too early, defoaming effect will be worse for the foam contains much liquid and the volume of bubble is small, so it is not recommended to install the defoaming net right after the inlet of separators. The foam will be acted on for several times when using the multilayer net, and the collapse and coalescence of bubbles are promoted more effectively. After the function of defoaming net, the liquid content of foam decreases, leading to lower drainage rate as well as some film stabilization effect such as Marangoni effect [10], so the collapse rate gets lower than that in the natural state. As the mesh number increases, there will be more meshes in a certain area and the mesh size will be smaller, which means more bubbles will be influenced and the film will deform more, leading to a better defoaming effect. However, when the mesh size is too small, it

tends to be clogged by impurities and cause local accumulation of foam, which is unfavorable to gas–liquid separation. So the mesh number should not be too large and the defoaming net should be installed on the upper part of separators to prevent clogging. Defoaming effect of stainless steel net is better than that of nylon net, it is speculated that the greater strength of stainless steel mesh causes stronger foam shearing effect. The net speed has little effect on the bubble collapse, presumably due to the rupture time of bubble is far less than the operation time of net. At different speeds, the net has a similar effect on the foam. The effect of 0.5 mm thread diameter defoaming net is better than that of 0.1 mm. The reason is that the shear effect is greater when the thread diameter is bigger, and the mesh size of 0.5 mm thread diameter net is smaller than that of 0.1 mm.

5 Conclusion

The collapse process of CO_2 flooding crude oil foams is composed of three stages: foam drainage, foam drainage with coalescence of bubbles, coalescence of bubbles. As defoaming net has a better effect on the foam with less liquid, it is recommended to be installed at a certain distance from the inlet of the separator. The more layers and mesh number of defoaming net, the more effective the defoaming net is. However, when the mesh size is too small, it tends to be clogged by impurities. So the mesh number should be appropriate and the defoaming net should be installed on the upper part of separators with few impurities. With greater strength and bigger thread diameter, the defoaming net is more effective. Considering cost issues, defoaming net with greater strength and bigger thread diameter can be chosen for separators.

References

1. Blázquez C, Dalmazzone C, Emond E et al (2016) Crude oil foams. Part 1—a novel methodology for studying non-aqueous foams formed by depressurization. Fuel 171:224–237
2. Fraga AK, Santos RF, Mansur CRE (2012) Evaluation of the efficiency of silicone polyether additives as antifoams in crude oil. J Appl Polym Sci 124(5):4149–4156
3. Rooker Mitohel, Weihua Zhang (1985) The foaming problems of crude oil in separator. Foreign Oilfield Eng 01:10–18
4. Kharoua N, Khezzar L, Saadawi HNH (2012) Using CFD to model the performance of retrofit production separators in Abu Dhabi
5. Zhian Deng, Dandan Liu (2017) Numerical simulation on separation characteristics of internal components of separator used for CO_2 flooding produced fluid. Oil Gas Storage Transp 06:722–727
6. Garrett PR (2015) Defoaming: antifoams and mechanical methods. Curr Opin Colloid Interface Sci 20(2):81–91
7. Blázquez C, Dalmazzone C, Emond E et al (2016) Crude oil foams testing and ranking of antifoams with the depressurization test. Energy and Fuels 31(2):1285–1294

8. Laurence Lawton L, Wang S (1985) The foaming crude oil needs special separation technique. Energy Conserv Petrol Petro Chem Ind 1985(1):11–14
9. Liu Y, Wu Z, Zhao B et al (2013) Enhancing defoaming using the foam breaker with perforated plates for promoting the application of foam fractionation. Sep Purif Technol 120 (6):12–19
10. Wang J, Nguyen AV, Farrokhpay S (2015) A critical review of the growth, drainage and collapse of foams. Adv Coll Interface Sci 228:55–70

Analysis on the Cause of the Defects of the Weld Seam in a Butt Welded Flange Ring

Xiang Zhang(✉), Ke Cai, and Tingting Qu

Tubular Goods Research Center of CNPC, 710065 Xi'an, China
zhangxiang003@cnpc.com.cn

1 Introduction

As one of the commonly used pipe fittings, welding neck flange is widely used in natural gas pipeline network due to its excellent dimensional stability and good sealing. Natural gas station as the main line of the pipeline network, its efficient and safe operation is the guarantee of stable transmission. There are complex processes in the station and an amount of flange connection with different manufacture specifications and quality standards are applied [1–4]. Therefore, in order to ensure the safe operation of the pipeline, the inspection, evaluation, and defect analysis of the pipe flange are important for preventing accidents.

A compressor station carried out safety assessment of service flanges, phased array ultrasonic testing found that the weld seam of welding neck flange connected to filter separator was defective, the defect position was in the direction of 12 point—460 mm (Airflow direction to clockwise +), the defect depth was 15 mm. As shown in Fig. 1, the pressure classification of the flange was the CLASS 900 (PN150), the material was the 16MnD, the production inspection standard was the ASME B16.5-2009 [5], and the midline of elbow was at an angle of 90° to the ground. The inspected period is 2 years as the SY/T 6477-2000 [6] recommended. Therefore, the flange was replaced after the usage of 2 years used. In order to reduce the generation of similar defective parts and ensure the safety of pipeline operation, there is a need to analyze the cause of the defect.

S. M. Shemwell and J. Lin (eds.), *Proceedings of the International Petroleum and Petrochemical Technology Conference 2018*,
https://doi.org/10.1007/978-981-13-2173-3_18

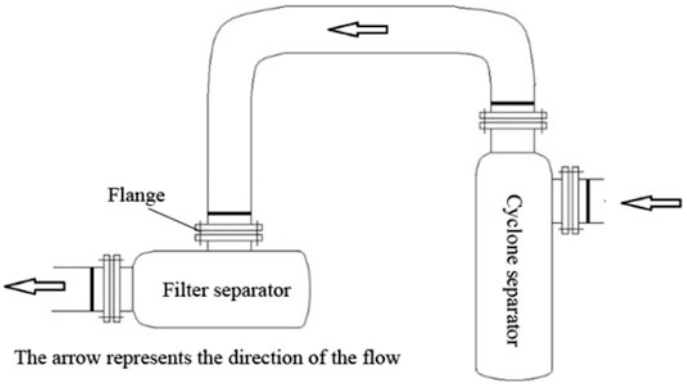

Fig. 1. The position of flange

2 Research Process and Experiment

2.1 Macro Observation

The macro photo of flange, elbow and weld seam was shown in Fig. 2. As shown in Fig. 3, the defect area was detected by phased array testing was in the direction of 12 point—460 mm to 12 point—563 mm, the defect length was 103 mm. The surface of sample was smooth, there were no signs of forging scars, cracks, and other defects.

Fig. 2. Macro-morphology of flange

Fig. 3. The defect found by phased array detection

2.2 Ultrasonic Detection

The MS380 type ultrasonic detector with sensitivity of Φ2—14 dB was used to detect the weld seam. The scan mode of detector was selected as zigzag. Detection found that the marking defect was stripe shape with 45 mm in length. The sampling position was shown in Fig. 4, samples of weld seam were intercepted and marked with 2-1$^{\#}$ ~ 2-11$^{\#}$, where 2-8$^{\#}$, 2-9$^{\#}$, 2-10$^{\#}$ were samples of the area marked in Fig. 3, 2-10$^{\#}$ was closest to 12 point position of the elbow. It could be observed that the adjacent profiles of 2-9$^{\#}$ and 2-8$^{\#}$, 2-9$^{\#}$ and 2-10$^{\#}$ were defective and had the same position, the direction of the defects was perpendicular to the profiles. But these defects were observed on the other side of sections of 2-8$^{\#}$ and 2-10$^{\#}$. As the length of three samples was about 37 mm, it was indicated that the length of the continuous defect was between 37.72 and 111 (i.e., 3 × 37) mm, which was consistent with the result of phased array ultrasonic testing, as shown in Figs. 5, 6 and 7.

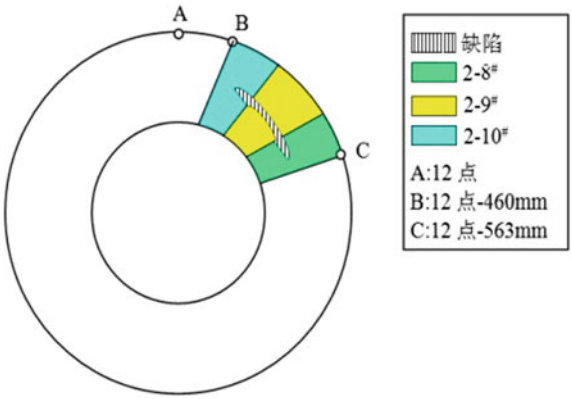

Fig. 4. Girth weld sample diagram

Fig. 5. Defect in 2-8# and 2-9#

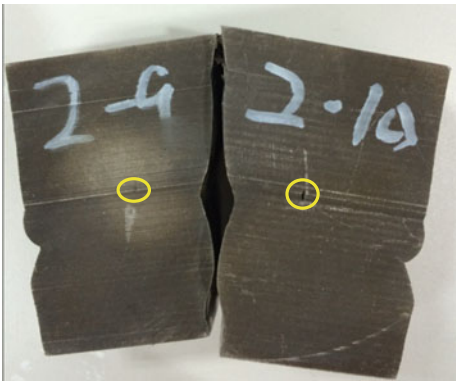

Fig. 6. Defect in 2-9# and 2-10#

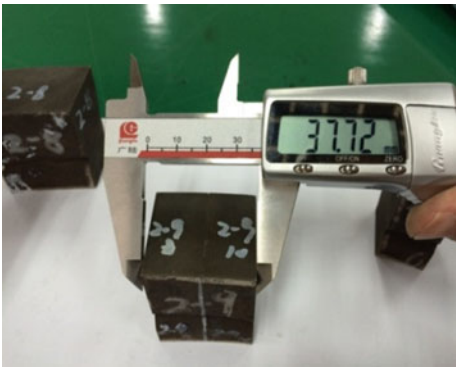

Fig. 7. Defect length of 2-9#

2.3 Chemical Composition Analysis

According to the standard of the ASTM A751-2014 [7], the chemical composition of the flange was analyzed by ARL 4460 direct- reading spectrometer, the result was shown in Table 1.

Table 1. Chemical composition analysis result of the flange (Wt $\times$ 10^{-2})

Elements	C	Si	Mn	P	S	Cu	Cr	Ni	Nb	Al
content	0.17	0.34	1.02	0.018	0.012	0.017	0.02	0.013	<0.0001	0.022
standard requirements	≤0.35	0.10 ~ 0.35	0.60–1.05	≤0.035	≤0.040	≤0.40	≤0.30	≤0.40	≤0.02	/

From the analysis of Table 1, it was shown that the chemical composition of the flange was in line with the requirement of the ASME B16.5-2009 [5] cited from the standard of the ASTM A105 [8].

2.4 Metallographic Analysis

The defective sample was analyzed by the MEF4 M metallographic microscope and image analysis system. As shown in Figs. 8 and 9, the matrix microstructure of flange was ferrite + pearlite, the girth welding structure was intragranular acicular ferrite + granular bainite + polygonal ferrite + pearlite, and pearlite + ferrite was layer by layer distribution. As shown in Fig. 10, there were cracks between the root welding consumables of 2-8# and 2-10# and the base metal, and the crack of 2-10# was wider than 2-8#. The edges of the crack are smooth, which indicated that the crack generated from 2-10# and extended to 2-8#, the microstructure near the crack was the same as the weld seam, the gray nonmetallic substance existed in the gap. As shown in Fig. 11, the lack of inter-run fusion was presented in the weld seam of 2-10#.

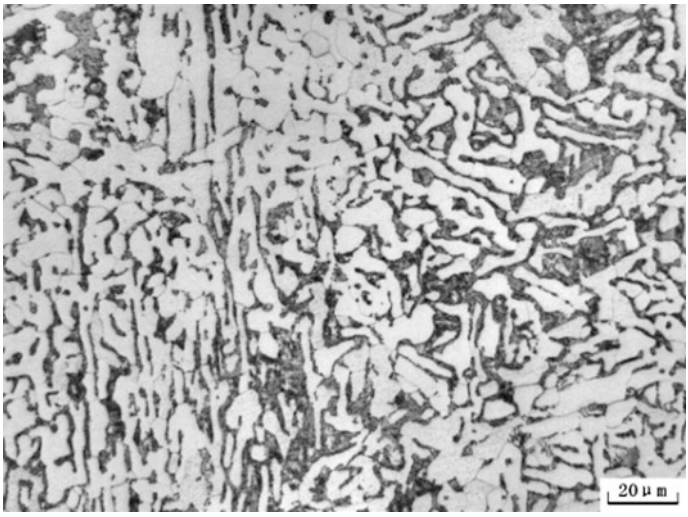

Fig. 8. Microstructure of flange

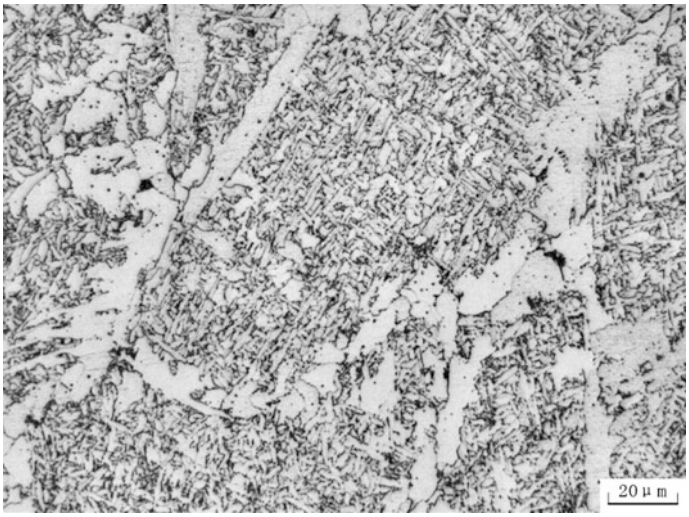

Fig. 9. Microstructure of circumferential weld

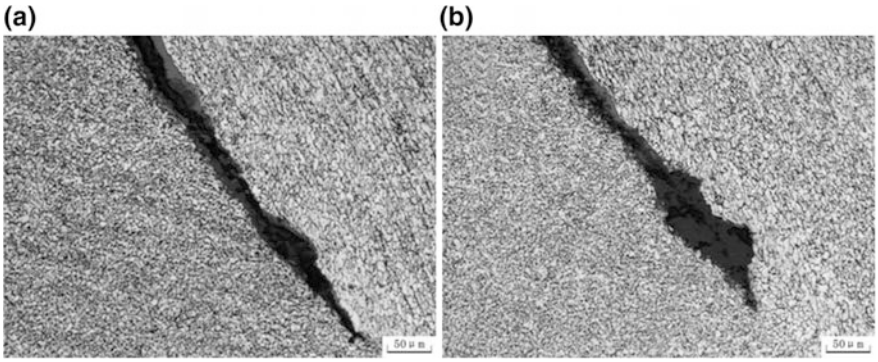

Fig. 10. Cracking morphology. **a** 2-8#, **b** 2-10#

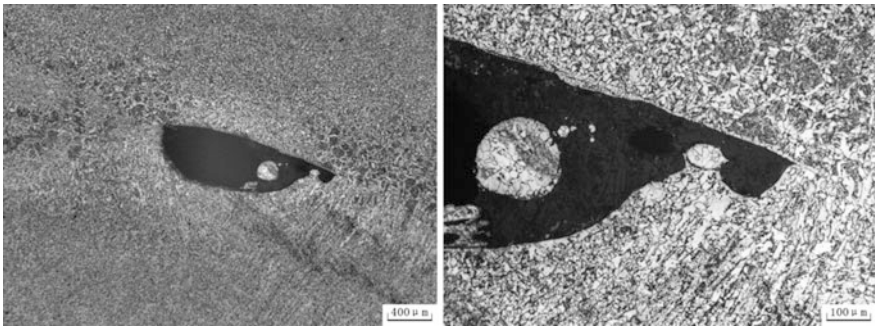

Fig. 11. Lack of fusion in 2-10#

2.5 Energy Spectrum Analysis

The gray porous structure was analyzed using X-ray spectrum, and the results were shown in Fig. 12. It shows that the main constituent elements of the gray porous structure were Ca, Si, O, Fe, Mn, Ti, C, K, and so on. In order to find out the source of the gray porous structure, the composition of the electrode coating used for girth welding was analyzed. The result showed that the main elements were O, Si, Mn, Ca, Ti, and so on. The gray porous structure in the crack was similar to the composition of the coating, and it could be judged that the gray porous structure came from the residual coating during welding.

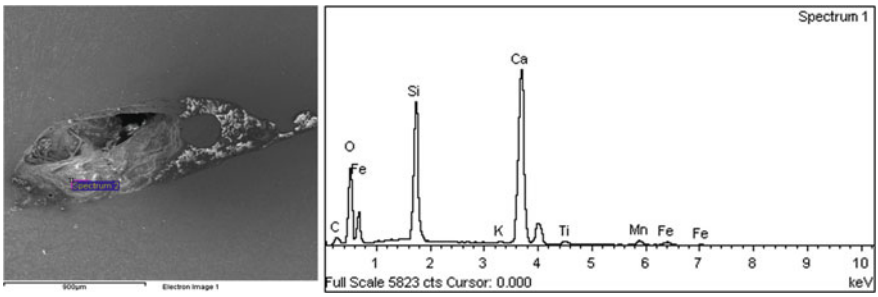

Fig. 12. The morphology and energy spectrum of gray porous material in the cracking

3 Result Analysis

Through the above analyses, it could be seen the following.

(1) The cracks generated between the root welding consumables and the base metal, both ends were more smooth and extended along the circumferential direction of the girth welding.
(2) The residual coating of the slag in the weld seam and the defect of the lack of inter-run fusion were the internal causes of the generation of the cracks [9–11].

The cracks in the weld seam generate from the lack of inter-run fusion containing the gray slag. According to the state of non-fusion, the lack of inter-run fusion belonged to black non-fusion [12, 13]. The main reason for the formation of black non-fusion can be analyzed as the following. First, the influence of welding parameters: the welding current is small and the speed is fast, resulting in the base material was covered by liquid iron before melting. It was easy to cause non-fusion. The welding speed was too low, resulting in the molten metal flowed to the bottom of the arc, and the arc could not reach the groove. It also occurred the non-fusion and the slag defect. Second, the impact of the welding process: the slag removal was not complete or method was not proper after backing welding, resulting in impurities which could not be melted or spilled in time in the case of fast welding. When welding a portion of arc heat was used to melt impurities and the remaining heat was not enough to melt the metal in bead, resulting in the formation of black fusion [14, 15]. Third, the impact of the external

stress: The temperature in the pipeline changed, which caused a certain tensile stress. The defect area was justly located near the direction of 12 point of the maximum tensile stress acting on the pipe, while the non-fusion affected the continuity of the weld material, this caused the stress to be concentrated here. Therefore, under the action of external force, the crack was easily formed around the defect and extended in a certain direction to form a potentially dangerous defect.

4 Conclusion and Suggestion

Through above analyses could draw the following conclusions:

(1) The manufacture of the flange complied with requirements of the ASME B16.5-2009.
(2) The root cause of the formation of the girth weld defect was that welding parameters were not set correctly, the operation of the welding process was not standardized, the interlayer was not fused in welding, and there were remaining slag coatings in the non-fusion defect.
(3) The external cause of the formation of the girth weld defect was that the non-fusion occurred near the direction of 12 point of the maximum tensile stress acting on the pipe, causing the stress to be concentrated in the defect and extending in a certain direction.

The following actions were recommended in order to avoid the same problems with flange welding, to strengthen quality control, and to further prevent leakage accidents:

(1) Welding parameters needed to be determined by the welding procedure qualification, to choose the appropriate welding speed, to be clear and strictly enforce the welding process of welding, and to monitor the quality of the field welding construction.
(2) In order to prevent the formation of the slag in welding, the slag removal should be timely after backing welding, the reflow method should be used to arc extinguish in arc stopping.
(3) After welding the workpiece should be immediately done nondestructive testing to ensure the quality of welding,the defective workpiece should be promptly done repairing welding or take other treatments.

References

1. Ke C, Xiao-fang MA, Jin-feng LI et al (2015) Failure analysis of cracked flange welding of venting valve. Pipeline Tech Equip 5:23–26
2. Liu Y, Wang P, Wang G (2013) Cracking analysis of circumferential weld for steel pipe and flange butt joint. Pipeline Tech Equip 3:30–35
3. Liang F (2003) The study on the intensity computation and the finite element analysis for the national standard pipe flange. Hefei University of Technology, Hefei, pp 1–4

4. Chen Z, Zhang H, Xiao P (2014) Numerical simulation and analysis of the temperature field of welding neck flange's quenching process. Mech Res Appl 27(2):120–150
5. ASME B16.5-2009, Pipe flanges and flanged fittings
6. SY/T 6477-2000, The evaluation method of remaining strength of the oil & gas transmission pipeline with the flaw part 1: The volumetric type flaw
7. ASTM A751-2014, Standard test methods, practices, and terminology for chemical analysis of steel products
8. ASTM A105/A105M-10, Standard specification for carbon steel forgings for piping applications
9. Qi L, Liu X, Liu R et al (2013) Cracking reason analysis on circumferential welded joints of spiral submerged arc welded pipe. Welded Pipe Tube 36(1):54–59
10. Qi L, Liu X, Liu Y et al (2012) Cracking reason analysis on circumferential welded joints of X80 SAWH pipe. Welded Pipe Tube 35(6):16–21
11. Niu Y, Li T, Zheng C (2012) Failure analysis and treatment of nozzle flange weld of centrifugal pump. Petro-Chem Equip Technol 33(4):58–60
12. Hong-yan LI (2015) Cause analysis and quality control of lack of fusion in submerged arc welding. Mech Electri Inf 27:94–95
13. Ke XU, Lei-hua PU, Hong-hong DUAN et al (2011) Identification of incomplete penetration and lack of fusion in weld nondestructive testing. Welded Pipe Tube 34(6):51–53
14. Zhang C (2013) V-shaped welds unfused defect solution. Weld Technol 42(1):62–63
15. Li-xia ZHU, Jin-feng LI, Cai-hong LU et al (2016) Leakage failure reason analysis of butt circumferential weld for a natural gas pipeline. Welded Pipe Tube 39(3):55–60

Relationship Between Microstructure and Mechanical Properties of X90 Pipeline Steel

Xiang Zhang(✉) and Fang Yang

Tubular Goods Research Center of CNPC, Xi'an 710065, China
zhangxiang003@cnpc.com.cn

1 Introduction

With the increasing consumption of petroleum and natural gas, pipeline pressure and diameter will continue to improve to increase the transmission efficiency. In order to ensure the stability, safety, and economy of the pipeline structure, it put forward higher requirements on the performance of pipeline steel. By reducing the thickness of steel pipe, decreasing steel pipe weight, it would significantly drop the amount of steel and cut down the construction and maintenance cost. Analysis of the Statistics Canada shows that it can reduce 7% of the construction cost [1], for every increase of one grade of steel. Now, X90, X100 super high strength pipeline steel instead of X70 and X80 pipeline steel is an inevitable trend as the construction and development petroleum and gas transportation pipe.

However, the microstructure and mechanical properties are not stable now because the X90 pipeline steel is still in trial production phase. This paper is intended to analyze the microstructure and mechanical properties of the X90 pipeline steel manufactured by different enterprises. Moreover, a reference for the development and application of domestic high-grade pipeline steel was provided.

2 Material and Experiment Conditions

The material was selected from the X90 spiral submerged arc welded pipe of Ø1219 mm × 16.3 mm, it has been on the specimens respectively for chemical detection, tensile test, and Charpy impact test. The tensile specimen, which was the round bar specimen intercepted from the pipe body, the gauge inner diameter was 8.9 mm and the gauge length was 35 mm, has done an experiment on the MTS810-15 material testing machine (25t). According to API SPEC 5L-Specification for line pipe [2], the yield strength was $R_{t0.5}$. The size of the Charpy impact (V-notch) specimen was 10 mm × 10 mm × 55 mm, and the temperature was 20, 0, −10, −20, −40, −60 °C. The methods of tensile test and Charpy impact have carried out by ASTM A370—The mechanical properties of steel products standard test methods and definitions. The chemical compositions of two test pipeline steel are shown in Table 1.

S. M. Shemwell and J. Lin (eds.), *Proceedings of the International Petroleum and Petrochemical Technology Conference 2018*,
https://doi.org/10.1007/978-981-13-2173-3_19

Table 1. Chemical composition of grade X90 pipeline steel (wt%)

Element	C	Si	Mn	P	S	Cr	Mo	Ni	Nb	V	Ti	Cu	Fe
1#	0.046	0.30	1.86	0.0066	0.002	0.30	0.31	0.29	0.086	0.041	0.014	0.25	Surplus
2#	0.052	0.21	2.00	0.0088	0.0014	0.37	0.3.0	0.39	0.095	0.019	0.012	0.26	Surplus

3 Results and Discussion

3.1 Microstructure Characteristics

The microstructure pictures of pipeline steel are shown in Figs. 1 and Fig. 2. As known from the Fig. 1, the microstructure of 1# mainly consists of granular bainite, polygonal ferrite, and M/A island, and the grain size is 11.6 grade. The microstructure of 2# mainly consists of granular bainite and M/A island, and the grain size is 12 grade. It shows that the steel fabricated by TMCP process acquires tiny austenite grains by increasing the rolling depth at recrystallization temperature. And primary rolling is at low temperature, which is beneficial to acquire a large number of granular bainite grains and flaky M/A islands. Because of the high temperature of the finish rolling and fasten rate of the cooling, a small number of fine martensitic grains was acquired to improve the strength and the hardness of steel [3]. In addition, the Nb content in 2# is higher than that in 1#. The pinning effect on grain boundary and subgrain boundary resulting from SDLE (solute drag-like effect) of Nb atoms and strain strengthening can significantly prevent or delay the recrystallization of γ phase during the TMCP process [4–6]. Obviously, it is beneficial to the grain refinement of the steel.

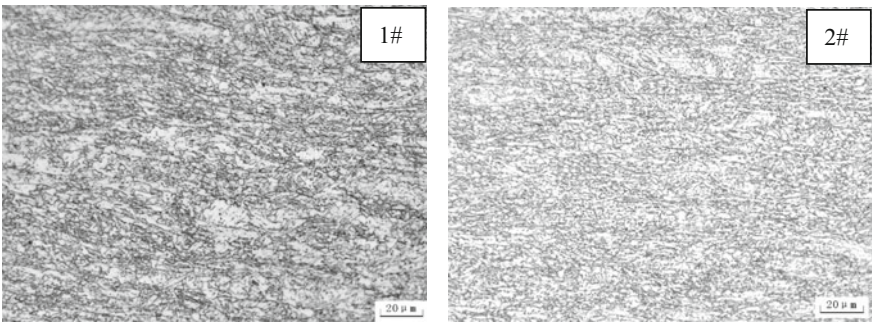

Fig. 1. Microstructure on the surface of grade X90 pipeline steel

3.2 Tensile Results

Figure 3 is the tensile curve of two kinds of X90 grade pipeline steel. It indicates that the yield strength and tensile strength of 1# are lower than that of 2#. It is because that PF exists in 1#, which is equilibrium phases and has low dislocation density. Generally, the dislocation density of PF is 1×10^7 to 1×10^8 cm^{-2}, and the effect of dislocations strengthening is not obvious [7]. The microstructure of the 2# is composed of granular bainite and M/A island. The ferrite grains in the bainite are tiny and dislocation density is high, both of these increase the resistance of dislocation motion, limiting the slip of dislocation. Meanwhile, the grain size of 2# is smaller than that of 1#, so more tiny grains and more grain boundaries can block the initiation and propagation of cracks [4].

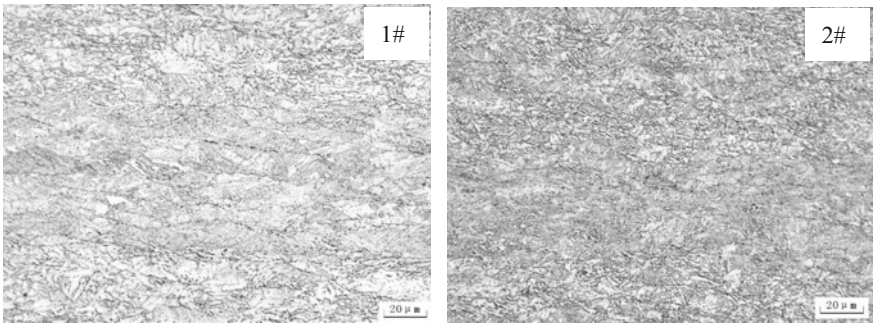

Fig. 2. Microstructure in wall thickness center of X90 pipeline steel

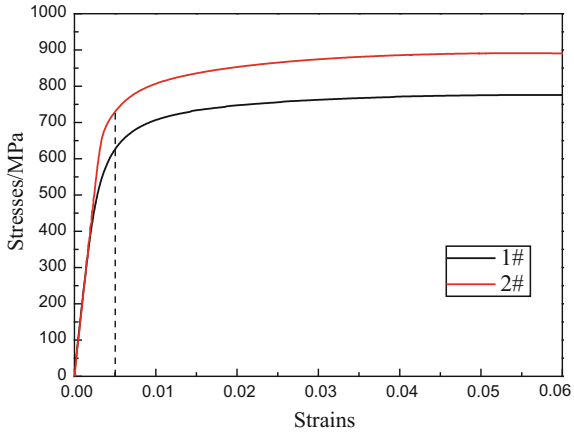

Fig. 3. Stress-strain curves of X90 pipeline steel

3.3 Charpy V-notch Impact Results

Figure 4 is Charpy V-notch toughness curves of X90 pipeline steel. It can be seen that two specimens have the same impact energy level between the 20 °C and −20 °C. When the temperature is −40 °C, the impact energy of both specimens decreases slightly. However, the impact energy of 1# decreases sharply at −60 °C. It shows that ductile-brittle transition temperature of 1# is between −40 °C and −60 °C. And the ductile-brittle transition temperature of 2# is below −60 °C.

Figure 5 shows the SEM pictures of fracture at 20 °C. It shows that both 1# and 2# have dimple fracture morphology. Some M/A islands acted as the hard grain are pulled out by impacted forces, and form pore in the dimples. Figure 6 shows the SEM pictures of fracture. It can be seen that fracture morphology of the 2# is a dimple pattern with features of plastic fracture at −60 °C. However, the fracture morphology of 1# is smooth like the fluvial pattern with features of brittle fracture (Fig. 6). This is because the content of S in 1#, which directly affects the plasticity and toughness of pipeline, is higher than that in 2#. After the formation of MnS in the steel, especially in the low-

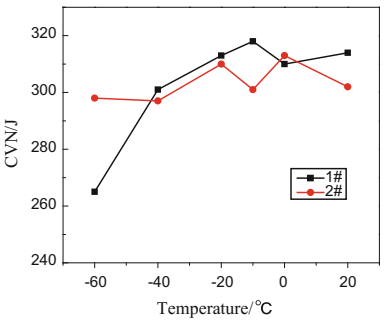

Fig. 4. Charpy V-notch toughness curves of X90 pipeline steel

temperature rolling, it stretches along the rolling direction because of its plasticity. This can increase anisotropy of steel which tends to hurt transverse performance.

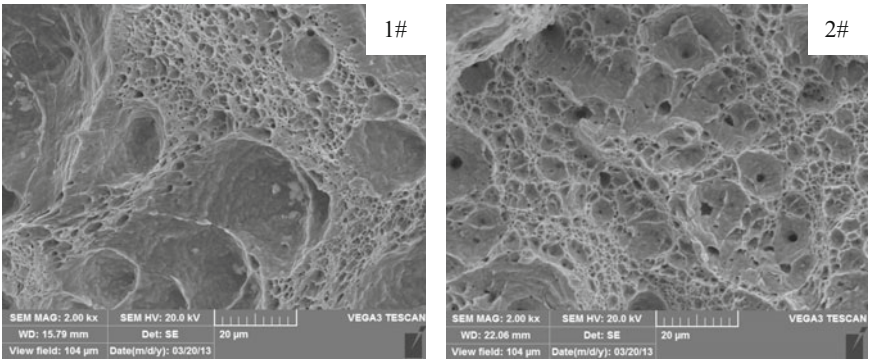

Fig. 5. Morphology of Charpy impact at 20 °C

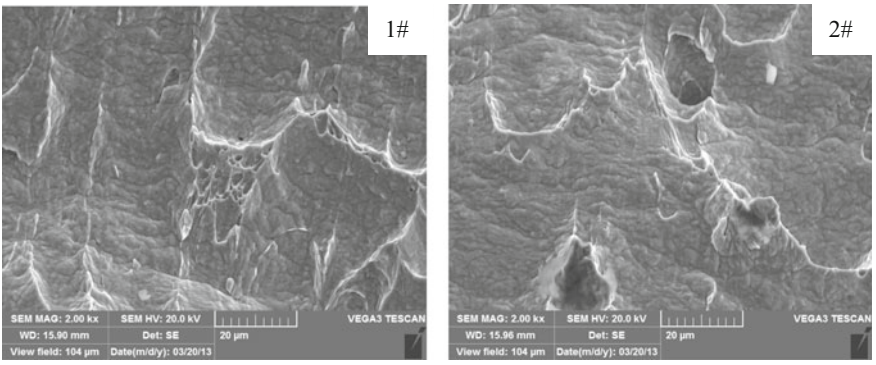

Fig. 6. Morphology of Charpy impact at −60 °C

4 Conclusion

1. The microstructure of X90 pipeline steel is mainly granular bainite and M/A island. When the PF exists because of its low dislocation density, the yield strength and tensile strength are decreased.
2. In the process of production, it should as far as possible to reduce the content of the S element, in order to improve the low-temperature flexibility of pipeline.

References

1. Huo C (2005) Research on the key technology of high pressure natural gas of high strength pipeline steel. Xian Jiao Tong University, Xian
2. American Petroleum Institute (2012) API SPECIFICATION 5L-2012 specification for line pipe [S]. Washington DC: API Publishing Services
3. Qi L, Yang L et al (2011) Relationship between microstructure and mechanical properties of X100 grade pipeline steel. Heat Process 40:15–19
4. Gao H (1995) Microstructure, performance and welding behavior of pipeline steel. Shaanxi science and Technology Publishing Company, pp 15–17, 163–170
5. Qi J, Huang Y, Zhang Y (2006) Microalloyed steel. Metallurgical Industry Publishing Company, Beijing, pp 45–88
6. Xue C, Wang X, Xin Y (2003) Nb microalloyed steel strengthening and toughening mechanism. Metal Heat Treat 28(5):15–18
7. Peng T, Gao H (2010) The basic characteristics of microstructure of pipeline steel. Pipe Weld 33(7):5–10

Determination of Titanium, Chromium, Magnesium, and Aluminum in Chromium-Based Polyethylene Catalysts by Inductively Coupled Plasma Atomic Emission Spectrometry (ICP-AES) with Microwave Digestion

Li-li Rong[1(✉)], Li-na Zhu[1], Tie-kai Zhao[1], Yan Liu[2], and Yan Zhang[1]

[1] Petrochemical Research Institute, Daqing Petrochemical Research Center, PetroChina, Daqing 163714, Heilongjiang, China
rll459@petrochina.com.cn
[2] Department of English, Qinhuangdao Vocational and Technical College, Qinhuangdao 066100, China

1 Introduction

The chromium-based polyethylene catalyst is one kind of catalyzer which is made by chromium compounds soaked with aluminosilica gel or silica gel carrier (i.e., Phillips chromium oxide catalyst). This catalyst was initially used for polyethylene production engineering of Univation Inc. and Phillips Inc. At present, the chromium catalyst has been developed from the traditional chromium oxide catalyst to organic chromium, reduced chromium, and other types. Because chromium catalyst has the features of high activity and simple preparation process, in addition, the polymer products contain long chain component and a small amount ultra high molecular weight polyethylene, it attracted more and more attention. In the process of synthesizing high-density polyethylene production (HDPE), there are nearly half of the products were made by supported catalyst system, the most common catalyst carriers used include silica gel (SiO_2), alumina (Al_2O_3), aluminum phosphate ($AlPO_4$), and its mixture [1–3]. In the synthesis process of the chromium-based polyethylene catalyst, the different ratio of chromic salts, metallic oxide, and cocatalyst influence the activity of the catalyst directly, so the effective analysis of chromium metal content in chromium-based polyethylene catalyst can help us to fully investigate the performance of the catalyst, and provide technical support for the subsequent production of various kinds of products. This is essential for the development of new products of synthetic polyethylene.

Dissolving samples is an indispensable important link in spectrum analysis, dissolving samples actually refers to samples decomposition, and it refers to producing the object for instrumental analysis and test into solution suitable for next step operation through the appropriate chemical treatment, in most cases, samples were manufactured into the form of aqueous solution. At present, there are less analysis methods and

S. M. Shemwell and J. Lin (eds.), *Proceedings of the International Petroleum and Petrochemical Technology Conference 2018*,
https://doi.org/10.1007/978-981-13-2173-3_20

document reports about metal elements in chromium-based polyethylene catalyst. According to the domestic report, the content of Cr(VI) in water can be measured chemical analysis, ammonium ferrous sulfate method or iodometric method.

Catalani et al. [4] put forward "the application of a metal free high performance liquid chromatography with inductively coupled plasma mass spectrometry (HPLC-ICP-MS) for the determination of chromium species in drinking and tap water"; Wang et al. [5] ever adopted microwave digestion technique to treat the samples, and measured by inductively coupled plasma mass spectrometry (ICP-MS); Pereira et al. [6] put forward "determination of elemental impurities in poly (vinyl chloride) by inductively coupled plasma optical emission spectrometry (ICP-OES). Samples were digested by microwave-induced combustion(MIC)." About the decomposition method of chromium-based polyethylene catalyst, we can adopt ways of microwave digestion and wet digestion. As early as in 1975, Abu-Samra et al. [7] utilized microwave heating for sample treatment for the first time. Under the closed heating environment, microwave heating make the heating rate of the material increases rapidly. With the increase in the pressure, the boiling point of the solvent is increased, the sample is completely digested, the time is saved, the energy is conserved, the amount of the chemical reagent is comparatively less, and the environmental pollution is also light. In contrast, using the wet digestion method has many shortcomings, such as the samples must be treated in normal pressure for a long time, and it is highly corrosive with large pollution [7, 8], so we use microwave digestion method to deal with samples.

In the choice of instrument detection, we can use inductively coupled plasma atomic emission spectrometry (ICP-AES), inductively coupled plasma mass spectrometry (ICP-MS), and atomic absorption spectrometry (AAS). ICP-AES has the characteristics of fast analysis speed, wide linear range, low detection limit, high accuracy, multielement simultaneous determination, and so on. As for AAS, the corresponding light source must be replaced when we determine different elements, determination of multielements cannot be completed simultaneously; linear range of standard working curve was narrow; it is difficult to eliminate chemical interference of matrix in the analysis of complex matrix samples [9–11]. In addition, ICP-MS was not suitable for the determination of high content samples, the sample content was too high to pollute the sample environment, and the instrument operation conditions were harsh, the sample determination cost was comparatively high. Therefore, we adopted ICP-AES to determine the samples. The method also researched interference of chromium matrix on the determination of other elements. Internal standard method was used for eliminating chemical interference caused by the chromium matrix, and the precision test and accuracy experiment were in progress, and the results were satisfactory and the method was accurate and reliable, which is worthy to be promoted.

2 Experimental

2.1 Instrument and Parameters

The measurements were performed on a 5300DV ICP-AES (PE, American company) and a MARS microwave oven (CEM, American company). The conditions of instrumental ICP-AES analysis are presented in Table 1, and the microwave digestion procedure is shown in Table 2. The registered wavelengths of the elements are Ti 334.940 nm, Mg 285.213 nm, Al 396.153 nm, and Cr 267.716 nm.

Table 1. ICP-AES instrument parameters

Instrument parameters	
Power of generator/W	1150
Frequency/MHz	27.12
Carrier gas pressure/MPa	0.221
Integration time/s	10
Cooling gas rate/(L min^{-1})	15
Auxiliary gas rate/(L min^{-1})	0.5
Lifting gas/(L min^{-1})	1.6

Table 2. Microwave digestion procedure

Step	Power/W	Ramp time/min	Working temp/°C	Remaining time/min
1	400	5	120	5
2	800	5	150	10
3	800	5	180	20

2.2 Reagents and Standards

Standards of Cr, Ti, Mg and Al at 1000 mg L^{-1} produced by National Standard Material Research Center were diluted to 50.00 mg L^{-1} to prepare mixed standard solution. A mixed standard solution of Li, Sc, In, Rh, Tb, Bi, Ge, and Lu, produced by Agilent(American company), was used as internal standard (100 mg L^{-1}). Diluted to 2.00 mg L^{-1} before used. The concentration was 70% for HNO_3, 36% for hydrochloric acid (HCl), and 30% for hydrogen peroxide (H_2O_2), all of which were in excellent purity.

All samples and working solutions were prepared with deionized water. The purity of argon was 99.9%.

2.3 Procedure

2.3.1 Samples Digestion

Weighed the chromium-based polyethylene catalyst sample 0.4000 g in the digestion vessel accurately, and then added 5 ml of HNO_3, 5 ml of HCl and 2 ml of H_2O_2 to the vessel. Shacked the lid slowly to make sure the solvent was homogeneously mixed. Put the digestion vessel on the shelf, keeping the samples symmetrical when there were multiple samples. Digested the sample according to the microwave digestion program mentioned in Sect. 2.1. The samples were cooled to room temperature when the digestion procedure was over. The disinfectant in the vessel was transferred to a 50 ml beaker with deionized water and then heated on a hot plate at 180 °C to remove excess acid and condensed into a small amount. After cooling, the solution was transferred to a 50 ml volumetric flask with deionized water. Added 5 ml of the mixed internal standard solution mentioned in Sect. 2.2 (2.00 mg L^{-1}) to the flask. Final volumes were made up to 50.0 mL with deionized water. The blank sample was prepared in the same manner and the above procedure was repeated. As the sample in the high Cr content, it was necessary to dilute the standard sample solution concentration to the certain range for further measure.

2.3.2 Preparation of Standard Series Solutions

Standards of 5.0, 10.0, 15.0, 20.0 ml of Cr, Ti, Al at 50.0 mg L^{-1} were respectively transferred to a 50 ml volumetric flask, made concentrations of 5.0, 10.0, 15.0, and 20.0 mg L^{-1} series of Cr, Ti, Al mixed standards for later use. Standards of 5.0, 10.0, 15.0, and 20.0 ml of Mg at 50.0 mg L^{-1} were respectively transferred to a 50 ml volumetric flask, made concentrations of 0.1, 0.2, 0.5 and 1.0 mg L^{-1} series of Mg standards for later use.

3 Results and Discussion

3.1 Discussion on Microwave Digestion Conditions

Combined with the characteristics of the closed high-pressure digestion and the rapid digestion, microwave digestion has become a popular sample preparation technology in recent years. This method has advantages of less acid consumption and high efficiency. The samples were treated in a closed environment to void the loss of volatile elements and possible pollution.

The common digestion methods mainly adopted include: using HNO_3, HCl, HF, H_2O_2, $HClO_4$, H_2SO_4, etc., acids combination to decompose samples. HNO_3 and HCl were strong oxidizing acids, they could be used to dissolve most of the metal and alloy. Generally speaking, H_2SO_4 has high viscosity. If H_2SO_4 was heated too quickly, the solution was easy to turn black. H_2O_2 could react directly with organic matter. The reaction is more severe at high temperature. It could be dissolved with HF if the sample contained insoluble aluminum silicate. Perchloric acid ($HClO_4$) could remove organic components of the sample, but there have hidden dangers of explosion when it was heated. Accordingly, there were considering the characteristic of chromium-based

polyethylene, HNO_3, HCl, and H_2O_2 can be used in combination. The amount of acid was determined by the dissolution of the sample, as shown in Table 3. The experimental result indicated that the effect of digestion sample was better when HNO_3, HCl, and H_2O_2 were used as 5, 5, and 2 ml, respectively.

Table 3. Investigation of the acids dosage

Acids system	Effects of digestion
2 ml HNO_3 + 2 ml HCl + 1 ml H_2O_2	Cannot be completely digested, solution showed turbidity
3 ml HNO_3 + 3 ml HCl + 1 ml H_2O_2	Cannot be completely digested, solution showed turbidity
5 ml HNO_3 + 5 ml HCl + 1 ml H_2O_2	Cannot be completely digested, solution showed turbidity slightly
5 ml HNO_3 + 5 ml HCl + 2 ml H_2O_2	Complete solution, solution showed clarification
5 ml HNO_3 + 5 ml HCl + 3 ml H_2O_2	Complete solution, solution showed clarification
6 ml HNO_3 + 6 ml HCl + 3 ml H_2O_2	Complete solution, solution showed clarification

The temperature and pressure sensing device are used in the microwave digestion system. By setting the temperature, time, and the power to control the dissolution process, according to the recommendation of microwave digestion instrument manufacturers, microwave procedures for CEM microwave digestion systems typically include two stages of rapid heating and constant temperature in a certain power. In this work, microwave power and digestion temperature should not be too high, and digestion time should not be too long. In order to avoid the process of reaction violence and the pressure suddenly increased, the sectional heating mode was used. The digestion procedure is shown in Table 2 of Sect. 2.1. The first step is heating to 120 °C under 400 W, keep 5 min; the second step is heating to 150 °C under 800 W, keep 10 min; the third step is heating to 180 °C under 800 W, keep 20 min. The power of digestion is automatic frequency conversion in the process of instrument resolution.

3.2 Select the Analysis Line

In the ICP-AES analysis, spectral interference will inevitably occur because of the multiple lines from various elements. Choose the spectral line that with no spectrum of interference or less interference as analysis line, according to the composition of the sample under test and the element contents. Under the working conditions in Sect. 2.1, the common lines of the elements in mixed standard solution in Sect. 2.3.2 were scanned. Calibrated the standard solution reversely to obtain the optimal line, according to the spectral line of elements, background contour, intensity of peak, and the corresponding linear fitting value of standard curve. The optimal lines adopted were Cr 267.716 nm, Ti 334.940 nm, Mg 285.213, and Al 396.153 nm.

3.3 Matrix Effect

The matrix effect refers to the elements interference phenomenon caused by the high concentration of matrix in the sample. In ICP spectral analysis, matrix interference was, on one hand, due to the existence of the matrix in which the substrate atoms, electrons and the measured density of particles were all changed. The change of the excitation state caused the emission intensity to be enhanced or reduced. On the other hand, the presence of the matrix changed the physical properties of the solution such as viscosity and surface tension and reduced the transfer rate, thereby reducing the strength of the analytical signal. In the case of large matrix analysis, the internal standard method can offset the fluctuation of spectral intensity caused by the fluctuation of the analysis condition, and improve the accuracy of the analysis. Usually, the high concentration of the matrix will produce a continuous background spectrum, so the analysis of the wavelength and the inner mark of the wavelength should be as close as possible to reduce the impact of background changes [12–15].

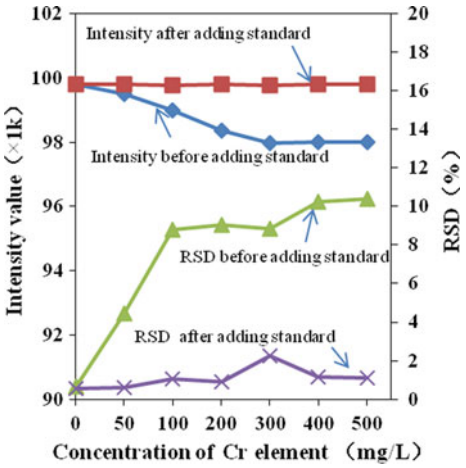

Fig. 1. Influence of matrix effect on Ti

The content of Cr in the sample was determined to be 1.05% by semiquantitative method, and the existence of Cr element might disturb other elements. In order to investigate the interference of Cr matrix to other elements, different concentrations of Cr (0–500 mg L^{-1}) were prepared. Ti, Mg and Al were added, respectively. The concentration of Ti was 10 mg L^{-1}, Mg was 2 mg L^{-1}, two copies, one of which was added 2 mg L^{-1} mixed internal standard solution. Under the condition of Sect. 2.1, the emission intensity and the concentration of the solution before and after adding the internal standard were determined according to the standard curves of Ti, Mg and Al mixed solution. The concentrations of Ti, Mg, and Al were, respectively, 2, 5, and 10 mg L^{-1}. Then, the relative standard deviation (RSD, %) was calculated. It can be seen from Figs. 1, 2 and 3 that the emission intensity of Ti element is decreasing and the emission intensity of Mg and Al increases with the change of Cr concentration in

the solution, and the RSD value of each element is obviously increased. After the addition of the internal standard elements, the emission intensity value of each element tends to be stable in the range of 0–500 mg L^{-1} Cr concentration, and the RSD values were also obviously reduced to less than 2%. The precision was improved significantly, and the matrix interference was basically eliminated.

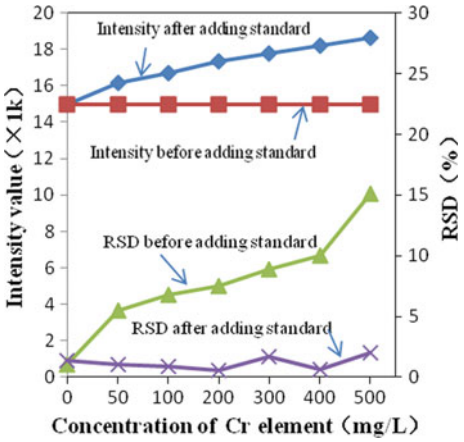

Fig. 2. Influence of matrix effect on Mg

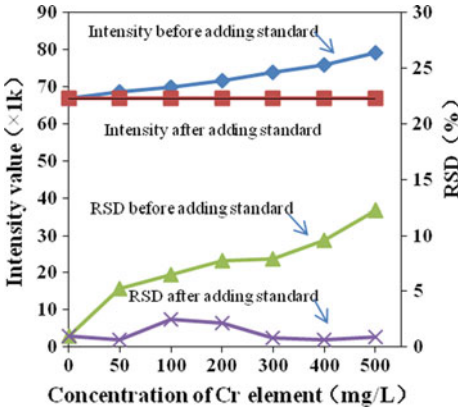

Fig. 3. Influence of matrix effect on AI

3.4 Calibration Curve and the Method Detection Limit Determination

Instrument detection limit reflects the instrument signal-to-noise ratio and the concentration threshold of the phase difference between signal and noise. But not as the starting point for quantitative and measurement. Method detection limit refers to a given analysis method. Elements of the minimum concentration were determined

through the reliable and reasonable confidence level, expressed in C_L. Method detection limits how to direct the measurement and calculation, and there is no unified regulation. With reference to International Union of Pure and Applied Chemistry (IUPAC) published the rules of 《the analysis term outline》 in 1998 [16], detection limit can be obtained by Bessel formula method. In general, the detection limit of the calculation is based on the blank sample of determination results with 9–12 times. It is the standard deviation of the blank sample solution corresponds to the concentration or content by k times (k is 2 or 3), using the simplified formula (1) calculation [17].

$$C_L = K \times S_C \tag{1}$$

Type: K is constant related to the degree of confidence. The proposed K is three as the standard detection limit calculation (the corresponding confidence level is 99.6% when K take three). Sc is expressed as the standard deviation of the blank solution concentration.

Under the optimum measure conditions, the standard series solution of Cr, Ti, Mg, Al were separately determined. The results show that the good linear relationship of Cr, Ti, Mg, and Al were showed within the scope of their respective concentration. The calibration curve and correlation coefficient are shown in Table 4. At the same time, the mixed standard solution of Cr, Ti, Mg, Al with 0.100 mg L^{-1} are given. Under the condition of the same determination, parallel to the determination of the blank solution density 11 times. As shown in Table 4, this method's detection limits of Cr, Ti, Mg, and Al were determined, respectively, with 0.00105, 0.00135, 0.00066, and 0.00234 mg L^{-1}.

Table 4. Determination of calibration curves and detection limits (n = 11)

Element	Linear range/ (mg L^{-1})	Calibration curve	Correlation coefficient	Standard deviation of blank solution/ (mg L^{-1})	DL/ (mg L^{-1})
Cr	0–20.00	y = 511.728 × +37.0155	0.99962	0.00035	0.00105
Ti	0–20.00	y = 16289.316 × −118051.6127	0.99992	0.00045	0.00135
Mg	0–1.00	y = 7873.3334 × −82.6671	0.99994	0.00022	0.00066
Al	0–20.00	y = 6508.6518 × −190.0518	0.99994	0.00078	0.00234

3.5 Accuracy Test

To test and verify the accuracy of this method, the same chromium-based polyethylene catalyst was weighed 4 samples and treated with the method of Sect. 2.3.1. In 3 of them, the standard solutions of Cr, Ti, Mg, and Al were spiked with different concentration value. (Dilution of Cr in the sample solution, then the standard recovery experiment was carried out). Generally, adding standard matter amount cannot be too large in the standard recovery experiment. It is advisable to determine and the content of 0.5–2.0 times. According to the method of 2.3, After treated of the sample was

constant volume in 50 ml PTFE volumetric flask. The content of each element was measured under the measurement conditions of Sect. 2.1, and the recovery results are shown in Table 5. It was possible to observe in Table 5, and the recoveries of Cr, Ti, Mg, and Al were between 97.5 and 104.0%.

Table 5. Results of recovery test

Element	Determination before adding standard/(mg L^{-1})	The adding standard matter amount/(mg L^{-1})	Determination after adding standard/ (mg L^{-1})	Recovery/ %
Ti	10.05	2.000	12.07	101.0
	10.05	5.000	14.99	98.80
	10.05	10.00	19.87	98.20
Cr	9.143	2.000	11.20	102.9
	9.143	5.000	14.02	97.54
	9.143	10.00	19.47	103.3
Mg	0.231	0.200	0.435	102.0
	0.231	0.500	0.724	98.60
	0.231	1.000	1.224	99.30
Al	5.782	2.000	7.742	98.00
	5.782	5.000	10.72	98.76
	5.782	10.000	16.18	104.0

3.6 Precision Test

Samples of the same chromium-based polyethylene catalyst were treated according to the method of Sect. 2.3.1. The sample of aqueous solution was prepared. If the concentration of Cr in the sample is higher, the sample needs to be diluted. Diluted to the standard curve can be linear range (the concentration of the standard curve of chromium is 5–20 mg L^{-1}). When those elements of Ti, Al, and Mg were measured, the internal standard method was used. Six parallel experiments were, respectively, carried out under the working conditions of Sect. 2.1. The precision of the measurement results was shown in Table 6. It was possible to observe in Table 6 that the relative standard deviation was 0.51–4.45% (RSD, $n = 6$).

Table 6. Precision test date ($n = 6$)

Element	Measured data/(mg L^{-1})			Average value/ (mg L^{-1})	Standard deviation/%	RSD/ %
Ti	10.03	10.12	9.98	10.02	9.95	0.99
	10.11	10.05	9.85			
Cr	9.121	9.202	9.110	9.147	4.70	0.51
	9.097	9.143	9.206			
Mg	0.228	0.231	0.224	0.226	1.00	4.45
	0.242	0.219	0.213			
Al	5.783	5.689	5.692	5.730	4.89	0.85
	5.712	5.704	5.801			

4 Conclusions

In this research, the sample of chromium-based polyethylene preparation methods was established with microwave digestion technique and further Cr, Ti, Mg, and Al determination by ICP-AES. This method has easy operation, low cost of equipment selection, low energy consumption, small elements, loss and high recovery of the results with microwave digestion technique. The determination result was accurate with reliable precision by ICP-ASE. It was necessary to use concentrated acids and longer digestion time (up to 60 min including the cooling step). In addition, reducing the laboratory waste generation and possible interferences in the determination step. This method is to develop new products, to speed up new technology and new achievements application provides important technical support. For service parts production at the same time, as well as the auxiliary research and development of scientific research project are of great significance.

Acknowledgements. We wish to thank the authors and peer reviewers for their timely contributions to this article. We would also like to thank Zhang Yan senior engineer and our colleagues, for their support.

References

1. Xu G, Cui N, Liu D et al (2012) Research progress of organosilyl chromate catalyst for ethylene polymerization. Synth Resin Plast Chin 29:70–74
2. The current situation analysis of China polyethylene and polypropylene and polyolefin production, vol 5. Rubber Plastics Machinery Times, Chinese, pp 32–33 (2016)
3. Liu Y, Fang Y, Zhu J et al (2002) Chromium-based catalyst for ethylene oligomerization and polymerization. Chin Polym Bull 29–36
4. Catalani S, Fostinelli J, Gilberti ME et al (2015) Application of a metal free high performance liquid chromatography with inductively coupled plasma mass spectrometry (HPLC-ICP-MS) for the determination of chromium species in drinking and tap water. Int J Mass 31–37
5. Wang Y, Shi Y, Zhang H (2008) Determination of lead, cadmium, mercury, chromium and arsenic in acrylonitrile-butadiene-styrene copolymer using microwave, digestion of ICP-M S. Spectrosc Spectral Anal Chin 28:31–37
6. Pereira LSF, Pedrotti MF, Miceli TM et al (2016) Determination of elemental impurities in poly(vinyl chloride)by inductively coupled plasma optical emission spectrometry. Talanta 152:371–377
7. Abu-Sarma A, Steven MJ, Kdrtyohann SR (1975) Anal Chem 1475–1477
8. Xu C, Liu X, Fu M et al (2012) Comparison of determination methods of six chromium content in chromium based polyethylene catalyst. Anal Instrum 6:54–56
9. Zang M, Liu L (2003) Analysis of Li-Si alloy for its major constituent lithium and for Fe, Ni and Cr present as impurities. PTCA (Part B: Chem Anal) 39:704–706
10. Tang S (2001) Determination of chromium in metal cluster compounds by atomic absorption spectrometry. Chin J Spectroscopy Lab 18:101–102
11. Chen Z (2016) Simultaneous determination of trace elements in waste SCR denitrification catalyst by inductively coupled plasma atom ic emission spectrometry (ICP-OES). Modern Chem Ind 36:183–186

12. Zhang Y, Shi L, Wu Y (2017) Determination of seven elements in manganese brass by inductively coupled plasma atomic emission spectrometry. Metall Anal 37:40–44
13. Zhou T et al (2006) Atomic spectrum sample processing technology. Chemical Industry Press, Beijing, pp 41–45
14. Zhou X, Wang J, Liu D et al (2017) Progress in application of coupled plasma atomic emission spectrometry in analysis of metal materials. Metallurgical Analysis 37:39–46
15. Fan G, Tang Y, Han P et al (2016) Determination of Co, Mo and Ni contents in hydrogenation catalyst by ICP-AES internal standardization method. Contemp Chem Ind 45:213–215
16. Renxuan X (2005) Plasma emission spectrum analysis. Chemical Industry Press Beijing, pp 152–153, 212–213
17. Xu W (1993) The detection limits of instrument and analytical method. Geol Lab 9:244–247

Investigation on Heat Transfer Characteristics of Hot Water Thermal Tracing with Thermal Cement

Yuqin Zhu(✉), Yaqian Guan, and Feng Xu

Xi'an Shiyou University, Xi'an 710065, China
1050226319@qq.com

1 Introduction

During the delivery of petrochemical materials, the heat loss of pipeline will cause the temperature drop and the increase of fluid viscosity, difficulties of material transport, even solidification of materials, and so on; the thermal process is usually used to solve the above problems. Steam tracing, electric tracing, and other forms of tracing [1, 2] have been widely applied in the industry. Compared with the jacket and electric heating, the heat tracing with heating pipe has the advantages on small investment and convenient to use, so it still plays a dominant role in the petrochemical industry [3]. However, because of the construction quality restriction, it is difficult to ensure the full contact between the process pipe and the heating pipe, resulting in the separation of the heating pipe from the process pipe. So there is a layer of air between the heat pipe and the process pipe, which will greatly reduce the heat transfer rate from the heat pipe to the process tube.

In order to improve the heating effect of tracing pipe, the air layer between the heat pipe and process tube may be replaced by the thermal cement with good thermal conductivity, as shown in Figs. 1 and 2. The thermal cement will keep the heat pipe in good contact with process tube, which not only greatly increases the heat transfer area but also changes the heat transfer type among heat pipe and process pipe, achieving the purpose of improving the heat transfer effect of the heat piping [4, 5]. The thermal cement is composed of a high-grade graphite-based materials and a variety of other materials, its main feature is to improve the effect of heat conduction with graphite, which has the advantages on high heat transfer efficiency, excellent heat transfer stability, and heating uniformity. Therefore, the application of thermal cement can not only improve the safe operation of chemical production equipment, but also obtain high economic and social benefits [6]. While because of the lack of theory and production data about heat tracing with thermal cement, it has not been applied popularly in the heat tracing at home.

The heat transfer mechanism and tracing characteristics of hot water heating system with thermal cement were studied and analyzed with computational fluid dynamics (CFD) simulation software in this paper, and energy-saving potential was researched as well based on energy quality and energy level matching, in order to provide a theoretical basis for the engineering application of thermal cement in low-temperature hot water heat tracing.

S. M. Shemwell and J. Lin (eds.), *Proceedings of the International Petroleum and Petrochemical Technology Conference 2018*,
https://doi.org/10.1007/978-981-13-2173-3_21

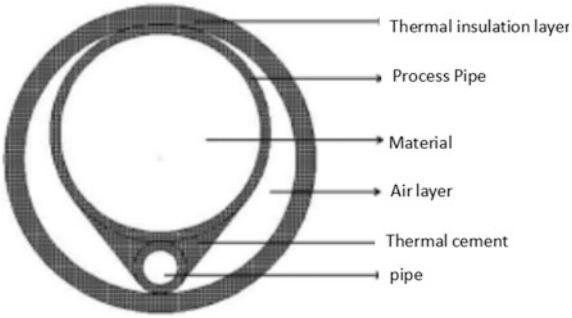

Fig. 1. Heat tracing system with thermal cement and heating pipe

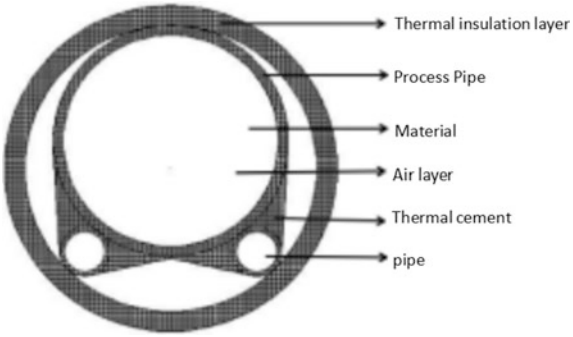

Fig. 2. Heat tracing system with thermal cement and two heating pipes

2 Control Equations and Calculation Instructions

The mass conservation equation, momentum conservation equations, energy conservation equation, and the k-ε equation of standard turbulence model [7] are used to simulate the heat transfer characteristics of heat tracing system with single shown in Fig. 1 and with two heat pipes shown in Fig. 2 respectively.

Mass conservation equation:

$$\frac{\partial \rho}{\partial t} + \frac{\partial(\rho u)}{\partial x} + \frac{\partial(\rho \upsilon)}{\partial y} + \frac{\partial(\rho w)}{\partial z} = 0 \tag{1}$$

Momentum conservation equations:

$$\frac{\partial(\rho u)}{\partial t} + \mathrm{div}(\rho u \overrightarrow{u}) = \mathrm{div}(\mu \mathrm{grad} u) - \frac{\partial p}{\partial x} + S_u \tag{2}$$

$$\frac{\partial(\rho v)}{\partial t} + \mathrm{div}(\rho v \overrightarrow{u}) = \mathrm{div}(\mu \mathrm{gard} v) - \frac{\partial p}{\partial y} + S_V \tag{3}$$

$$\frac{\partial(\rho w)}{\partial t} + \mathrm{div}(\rho w \overrightarrow{u}) = \mathrm{div}(\mu \mathrm{grad} w) - \frac{\partial p}{\partial z} + S_W \tag{4}$$

Energy conservation equation:

$$\frac{\partial(\rho T)}{\partial t} + \mathrm{div}(\rho \overrightarrow{uT}) = \mathrm{div}\left(\frac{k}{c_p}\mathrm{grad}T\right) + S_T \tag{5}$$

where ρ—fluid density, kg/m^3; t—time, s; u, v, w—velocity components in x, y and z directions, m/s. p—pressure, Pa; $\overrightarrow{u}$—velocity vector, m/s; μ—kinematic viscosity, Pa s; S_u, S_v, S_w—generalized source terms of momentum conservation; c_p—specific heat, kJ/(kg °C); T—thermodynamics temperature, K; k—heat transfer coefficient, W/(m^2 °C); S_T—viscous dissipation.

The radiation heat transfer could not be considered in the simulation model because of its surface uncertainty. There is natural convection in the air layer due to the existence of the temperature gradient, and the calculation results showed that it was the laminar natural convection heat transfer in the air layer. The convective heat transfer coefficients of the inner wall of heat pipe and of the inner wall of the process tube are calculated by the formulas of forced convection heat transfer in the pipe, and the convective heat transfer coefficient of the outer wall of the insulation layer is determined by formula (6).

$$\alpha_1 = 1.163 \times (10 + 6\sqrt{v_w}) \tag{6}$$

where, α_1—convective heat transfer coefficient of the outer surface of insulation layer, W/(m^2 °C); v_w—wind speed around the heat tracing system, m/s.

Since the structures of heat pipe heating system and air layer are complex, the unstructured grid is adopted [8]. There are only the triangular grids in the grid area and the grid spacing is 1 mm. The grids of the intersection of the narrow enclosed area in the air layer are divided into blocks and the boundary divisions are encrypted, the Boussinesq model is used to speed up the convergence rate of simulating calculation.

3 Verification of Simulating Model and the Analysis on Calculation Results

3.1 Simulation Conditions and Verification of Simulating Model

First of all, the heat transfer characteristics were simulated for the traditional hot water heat tracing system with a nominal diameter of 15 mm heat pipe without thermal cement under the condition of environmental temperature of 11.4 °C. The calculation

results are consistent with the design criteria of petrochemical pipelines, as shown in Table 1 [9], which verify the correctness and the reliability of the calculation models in this paper.

The design parameters of the petrochemical pipe in Table 1 [9] were used as the simulation conditions for one heat pipe with thermal cement and for two heat pipes of hot water heating system (Figs. 1 and 2), the stainless steel pipe and carbon steel pipe were used for the heat pipe and the process pipe, and calcium carbonate used as the insulation material. The convective heat transfer coefficient of hot water is 4500 W/(m^2 K), the crude oil at atmospheric pressure was used as process medium, its convective heat transfer coefficient is 2358 W/(m^2 K), and the convective heat transfer coefficient of the insulation layer outer wall is 22.66 W/(m^2 K) by use of Eq. (1). The thermal conductivity of thermal cement is 10 W/(m K), the heat capacity 1200 W/(m^2 K), the density 1510 kg/m^3 respectively. The temperature distribution, heat flux distribution, and heat transfer rate of the tracing system are obtained by simulation calculation.

The highest temperatures which the process medium could be heated were shown in Table 2 under the conditions of 11.4 °C of ambient temperature, 90 and 100 °C of hot water, and a nominal diameter of 15 mm of heat pipe with thermal cement.

The calculated highest temperatures which the process medium could be maintained were also shown in Table 3 under the conditions of 11.4 °C of ambient temperature, 70 and 80 °C of hot water and a nominal diameter of 15 mm of heat pipe with tracing cement.

Similarly, the highest temperatures which the process medium could be maintained were shown in Table 4 under the conditions of 90 and 100 °C of hot water, a nominal diameter of 10 mm of heat piper with tracing cement.

3.2 Analysis on Results

3.2.1 Energy-Saving Effect of Hot Water Heating with Thermal Cement

Table 1 showed that the highest process medium temperature maintained with one heating pipe of 15 mm nominal diameter were 60, 60, 60, 60, 55, and 55 °C respectively, which respond to the process pipe diameters of 50, 80, 100, 150, 200, and 250 mm respectively at 90 °C hot water without thermal cement. When the heating water temperature is 100 °C, while the other conditions remain unchanged, the highest process medium temperature were 70, 70, 70, 65, 65, and 65 °C for the process pipe diameters of 50, 80, 100, 150, 200, and 250 mm respectively.

The highest process medium temperatures maintained by hot water with thermal cement were shown in Table 2. Comparing Table 2 with Table 1, we could know that the process medium temperatures maintained with thermal cement were 20 °C higher than those without thermal cement, under the conditions of same heating hot water temperature, the same heat pipe diameter, and number. So, there is significant energy-saving effect for the thermal tracing with thermal cement.

Table 3 showed the highest process medium temperature maintained by heating pipe of 15 mm nominal diameter with thermal cement at 70 and 80 °C hot water respectively. Comparing Table 1 with Table 3, we can obtain that the heating pipe with

Table 1. Simulated calculation results of heating pipe with hot water without thermal cement

Nominal diameter, mm	Ambient temperature, °C	Heat pipes number and nominal diameter (n × DN, mm)				Heat pipes number and nominal diameter (n × DN, mm)				
		Hot water temperature, 90 °C				Hot water temperature, 100 °C				
		Temperature of process medium maintain, °C				Temperature of process medium maintain (°C)				
	11.4	45	50	55	60	50	55	60	65	70
	Insulation thickness, mm									
50	40	1 × 15	1 × 15	1 × 15	1 × 15	1 × 15	1 × 15	1 × 15	1 × 15	1 × 15
80	40	1 × 15	1 × 15	1 × 15	1 × 15	1 × 15	1 × 15	1 × 15	1 × 15	1 × 15
100	40	1 × 15	1 × 15	1 × 15	1 × 15	1 × 15	1 × 15	1 × 15	1 × 15	1 × 15
150	50	1 × 15	1 × 15	1 × 15	1 × 15	1 × 15	1 × 15	1 × 15	1 × 15	2 × 15
200	50	1 × 15	1 × 15	1 × 15	2 × 15	1 × 15	1 × 15	1 × 15	1 × 15	2 × 15
250	50	1 × 15	1 × 15	1 × 15	2 × 15	1 × 15	1 × 15	1 × 15	1 × 15	2 × 15

Table 2. Simulated calculation results of heating pipe of hot water with thermal cement

Nominal diameter, mm	Ambient temperature, °C	Heat pipes number and nominal diameter (n × DN, mm)				Heat pipes number and nominal diameter (n × DN, mm)				
		Hot water temperature, 90 °C				Hot water temperature, 100 °C				
		Temperature of process medium maintain, °C				Temperature of process medium maintain, °C				
	11.4	65	70	75	80	70	75	80	85	90
	Insulation thickness, mm									
50	40	1 × 15	1 × 15	1 × 15	1 × 15	1 × 15	1 × 15	1 × 15	1 × 15	1 × 15
80	40	1 × 15	1 × 15	1 × 15	1 × 15	1 × 15	1 × 15	1 × 15	1 × 15	1 × 15
100	40	1 × 15	1 × 15	1 × 15	2 × 15	1 × 15	1 × 15	1 × 15	1 × 15	2 × 15
150	50	1 × 15	1 × 15	1 × 15	2 × 15	1 × 15	1 × 15	1 × 15	1 × 15	2 × 15
200	50	1 × 15	1 × 15	2 × 15	2 × 15	1 × 15	1 × 15	1 × 15	2 × 15	2 × 15
250	50	1 × 15	1 × 15	2 × 15	2 × 15	1 × 15	1 × 15	2 × 15	2 × 15	2 × 15

Table 3. Simulated calculation results of heating pipe of hot water with thermal cement

Nominal diameter, mm	Ambient temperature, °C	Heat pipes number and nominal diameter (n × DN, mm)				Heat pipes number and nominal diameter (n × DN, mm)				
		Hot water temperature, 70 °C				Hot water temperature, 80 °C				
		Temperature of process medium maintain, °C				Temperature of process medium maintain, °C				
	11.4	45	50	55	60	50	55	60	65	70
	Insulation thickness, mm									
50	40	1 × 15	1 × 15	1 × 15	1 × 15	1 × 15	1 × 15	1 × 15	1 × 15	1 × 15
80	40	1 × 15	1 × 15	1 × 15	1 × 15	1 × 15	1 × 15	1 × 15	1 × 15	1 × 15
100	40	1 × 15	1 × 15	1 × 15	1 × 15	1 × 15	1 × 15	1 × 15	1 × 15	1 × 15
150	50	1 × 15	1 × 15	1 × 15	1 × 15	1 × 15	1 × 15	1 × 15	1 × 15	2 × 15
200	50	1 × 15	1 × 15	1 × 15	2 × 15	1 × 15	1 × 15	1 × 15	1 × 15	2 × 15
250	50	1 × 15	1 × 15	1 × 15	2 × 15	1 × 15	1 × 15	1 × 15	1 × 15	2 × 15

Table 4. Simulated calculation results of heating pipe of hot water with thermal cement

Nominal diameter, mm	Ambient temperature, °C	Heat pipes number and nominal diameter (n × DN, mm)				Heat pipes number and nominal diameter (n × DN, mm)				
		Hot water temperature, 90 °C				Hot water temperature, 100 °C				
		Temperature of process medium maintain, °C				Temperature of process medium maintain, °C				
	11.4	55	60	65	70	60	65	70	75	80
	Insulation thickness, mm									
50	40	1 × 10	1 × 10	1 × 10	1 × 10	1 × 10	1 × 10	1 × 10	1 × 10	1 × 10
80	40	1 × 10	1 × 10	1 × 10	2 × 10	1 × 10	1 × 10	1 × 10	1 × 10	1 × 10
100	40	1 × 10	1 × 10	1 × 10	2 × 10	1 × 10	1 × 10	1 × 10	1 × 10	2 × 10
150	50	1 × 10	1 × 10	2 × 10	2 × 10	1 × 10	1 × 10	1 × 10	1 × 10	2 × 10
200	50	1 × 10	2 × 10	2 × 10	2 × 10	1 × 10	1 × 10	1 × 10	2 × 10	2 × 10
250	50	1 × 10	2 × 10	2 × 10	2 × 10	1 × 10	1 × 10	1 × 10	2 × 10	2 × 10

heat clay at the 20 °C hot water lower than one without heat cement could achieve the same heating effect, that is, the lower temperature hot water can be used in tracing heat with thermal cement. Because the temperature difference between hot water and the process medium was reduced, leading in the decrease of the exergy energy loss of the tracing heat system, there is a good energy-saving effect.

On the other hand, Table 4 showed the highest temperature that tracing hot water can maintain in the conditions of 90 and 100 °C hot water, the heating pipe with smaller diameter (10 mm). Compared Table 4 with Table 1, we know that the process medium temperatures with tracing cement and the diameter of 10 mm heating pipe were higher 10 °C than those without tracing cement and 15 mm heating pipe in the same heating hot water temperature and heat pipe number, resulting in the decrease of investment costs of heat pipe, energy-saving effect is significantly.

3.2.2 Heat Transfer Characteristics of Tracing Heat with Thermal Cement

Figure 3 showed that the heat balance temperature contribution of tracing system without thermal cement at 90 °C heating water and one heat pipe with the diameter of 15 mm.

Similarly, Fig. 4 showed the heat balance temperature contribution of tracing system with thermal cement at 90 °C heating water and one heat pipe with the diameter of 15 mm.

Each curve represents the isotherm in Figs. 3 and 4, the color of the isotherm from blue to red represents that the temperature of the tracing system increases gradually.

In the heating system, Figs. 3 and 4 showed that the air near the heat pipe or thermal cement was heated, its temperature rose and its density reduced; air near the

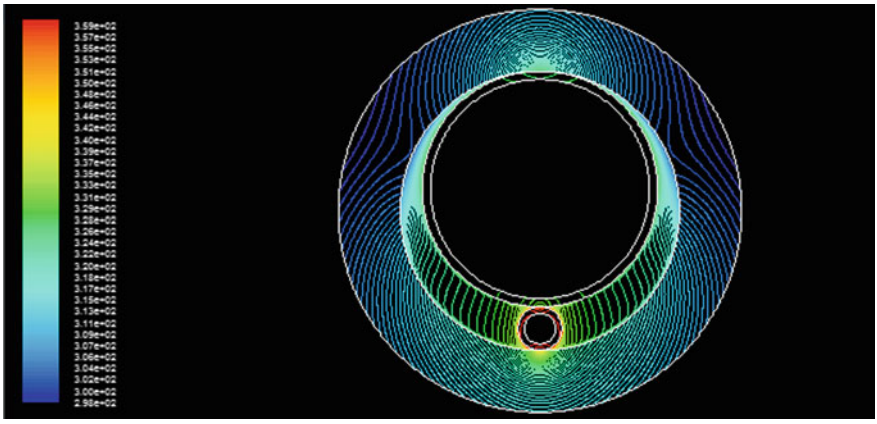

Fig. 3. Temperature field of tracing system without thermal cement at 90 °C heating water

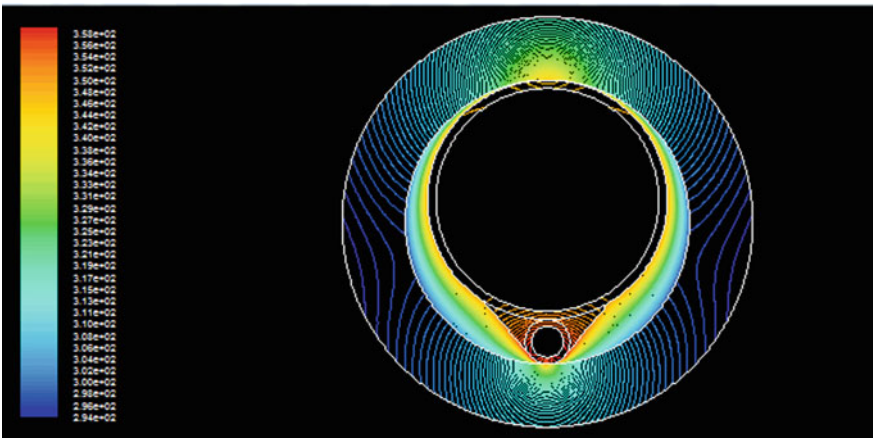

Fig. 4. Temperature field of tracing system with thermal cement at 90 °C of heating water

outer surface of the process tube flowed upwards and the heat was transferred to the process tube. The density of cooled air increased along the inner surface of the insulation layer, the cooled air flowed downwards, and afterwards it was reheated when the air flowed back to the heat pipe or near the thermal cement.

Compared Fig. 3 with Fig. 4, the temperature of air interlayer with thermal cement (Fig. 4) was higher obviously than those without thermal cement (Fig. 3) for heating water tracing system, and the area of high-temperature region with thermal cement also increased significantly. In addition, the density of isothermal lines with thermal cement rose greatly. The above phenomena indicated that the heat transfer property with thermal cement was better than one with no thermal cement in the same heating hot water temperature, so the temperature of the medium maintained by the heating water can rise greatly.

The reason which the thermal cement heating system has a high thermal tracing efficiency is that the thermal cement is filled between heat pipe and process pipe, so the line contact between the heat pipe and process pipe is changed into surface contact, which could increase the heating area on the one hand, on the other hand, increase the heat transfer efficiency because of heat transfer cement with high thermal conductivity instead of air of the low thermal conductivity. Therefore, the simulation results showed that the heating effect with heat cement tracing system was significantly better than one without thermal cement, the tracing system with heat cement is an optimization improvement to the traditional tracing system. With the deepening of energy saving, the tracing system with thermal cement will gradually replace the traditional one without thermal cement.

4 Conclusions

(1) The simulation results showed that the tracing heat effect of hot water heating system with thermal cement was better than one without thermal cement, the tracing system with heat cement is an optimization improvement to the traditional tracing system.
(2) At the same heating hot water temperature, the medium temperatures maintained with thermal cement were 20 °C higher than those without heat cement.
(3) At the same heating hot water temperature, we can use nominal diameter of 10 mm of heat pipe with thermal cement to obtain the process medium temperatures maintained by hot water those were 10 °C higher than ones without thermal cement by use of the nominal diameter of 15 mm heat pipe. This not only saves the investment cost of the heat pipe but also reduce the exergy energy loss of the heat tracing system.
(4) The hot water heating system with thermal cement can use lower temperature hot water (reduced by about 20 °C) to achieve the same heating effect without thermal cement. That is, the low-temperature hot water of 70 °C can be used to heat the process medium, which could make full use of the low-temperature heat of the petrochemical enterprise, and could reduce the exergy energy loss of the heat tracing system, obtaining the better energy-saving effect.

References

1. Barth RE, Bonorden CM, House PA, Johnson BC (2001) Heat tracing technology for the 21st century, vol 8, issue no 1. Pulp & Paper Industry Technical Conference, pp 174–179
2. Lan G, Li X (2000) Technology of special shaped heat pipe. Pipeline Tech Equip 4:20–21 (Chinese)
3. Li H (2000) The cold and thermal insulation of equipments and pipes. Chemical Industry Press, Beijing (Chinese)
4. Pan C, Mamat M, Zhang K et al (2013) On the application of energy-saving heat transfer cement in asphalt mixing tank. Petrol Chem Energy Conserv 1:28–30 (Chinese)
5. Qi X, Tan X, Xu Hong et al (2007) Review of performance optimization techniques for heat tracing system and external heat pipe system. Nat Gas Ind 27(4):108–111 (Chinese)
6. Pan H (2005) Study on heat transfer efficiency of heating tracer with heat transfer cement. Nat Gas Ind 25(2):172–175 (Chinese)
7. Zhang J, Yang Z, Zhang Z (2008) Numerical simulation of fluid dynamics and heat transfer process and application. Chemical Industry Press, Beijing, pp 13–25 (Chinese)
8. Wang F (2004) The principle and application of CFD software of computational fluid dynamics analysis. Tsinghua University Press, Beijing (Chinese)
9. Cai E (2002) The design of petrochemical pipelines. Chemical Industry Press, Beijing (Chinese)

Attaining and Sustaining Operational Excellence: A Best Practice POC

Scott. M. Shemwell(✉)

The Rapid Response Institute, Houston, TX, USA
sshemwell@theRRInstitute.com

1 Introduction

Following the Deepwater Horizon disaster in 2010, the United States government, the offshore industry, and other constituent groups rapidly put in place processes meant to reduce if not eliminate the risk of another disaster of this magnitude [1]. Many studies were undertaken with the goal of finding the root cause and changing the technological and business models used to drill oil and gas wells in deepwater [2].

Several engineering and process errors were uncovered, including poor contractor management on the part of the operator, drilling contractor and others. Moreover, the US regulatory agency changes resulted in the creation of the Bureau of Safety and Environmental Enforcement (BSEE).

BSEE mandated a new Safety and Environmental Management System (SEMS) when drilling in US Federal waters (mostly Deepwater Gulf of Mexico and offshore Alaska). SEMS is based on API-RP 75, Recommended Practice for Development of a Safety and Environmental Management Program for Offshore Operations and Facilities [3].

Initially, the goal of the research was to assess how the industry would change to meet these new realities. However, it appeared that the sector was taking incremental steps and most were not meeting the regulatory requirements. Moreover, at many levels, personnel did not know they had new responsibilities!

This casual approach morphed into a formal research project with the intent to better understand the systemic and disruptive transformation required of the sector. This is fundamentally applied research and is about human behavior and not technology although technology plays a major role enabling this new process.

In other words, this research tests a psychological hypothesis. How will human behavior be changed to manage complex interrelated systems where failure can be catastrophic? Conversely, the null hypothesis is that accidents will always happen—the Normal Accident Theory [4].

S. M. Shemwell and J. Lin (eds.), *Proceedings of the International Petroleum and Petrochemical Technology Conference 2018*,
https://doi.org/10.1007/978-981-13-2173-3_22

2 Methodology

In 2012, an extensive literature review of current Operations Management Systems (OMS) practices throughout the industry was undertaken. This study was later updated to reflect changes the sector made as this new management model became more widely adopted [5].

It became clear that the industry needed to substantially transform the way work was performed to become one of a Safety Culture and meet the BSEE requirements. Additionally, and importantly, contractors were placed under additional and formal scrutiny.

2.1 WCID-SEMS

API Bulletin 97, Well Construction Interface Document (WCID) Guidelines was first released in 2013. It is intended to, "Provide guidance on information that is to be shared regarding well construction and rig specific operating guideline." The Bulletin goes on to state, "The WCIS-SEMS is a bridging document that includes the elements identified in API RP 75 within the context of well construction activities [6] (Fig. 1)."

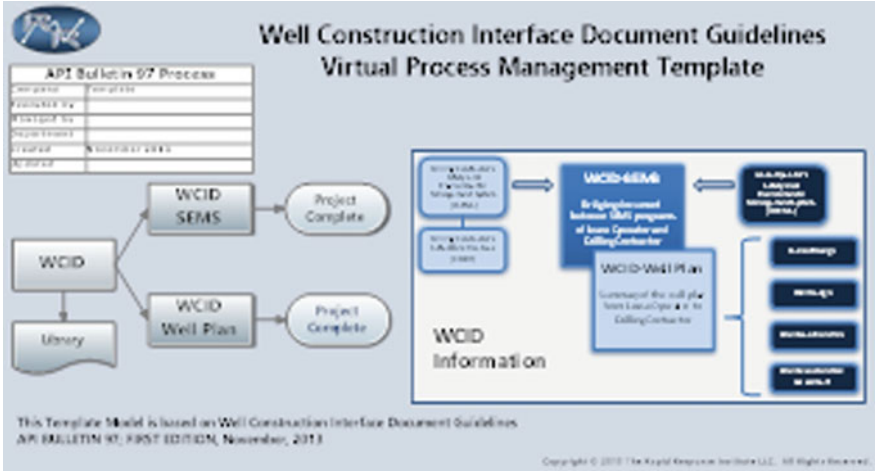

Fig. 1. WCID-SEMS template

The bridging document was originally designed to be used between the operator and the drilling contractor. However, to meet the BSEE requirements operators began requiring that all contractors (other than kitchen and housekeeping) use and adhere to these requirements. These represented considerable challenges for the thousands of smaller organizations now faced with significant new paperwork and reporting requirements.

Working with a large US independent operator, all of the workflows required from API RP 75, API Bullen 97 and associated other standards and regulatory compliance

were identified and mapped to actual field operations tasks. This was accomplished through many surveys and business process assessments.

In 2015, a Culture of Safety Maturity Model was developed based on accepted maturity model methodologies [7]. This model is a proxy to identify the state of WCID-SEMS adoption.

An online survey (n = 197) of industry executives (operators and supply chain) was statistically significant. As shown in the following figure, only a small percentage met all maturity level requirements (Fig. 2).

Fig. 2. COS maturity survey results

This suggests that the industry did not have the policies, process, and tools in place to meet the BSEE requirements. Effectively, since if one supplier is out of compliance, the entire project is also out of compliance. This created a non-tenable situation for the entire sector.

2.2 IT/OT Convergence

In the second phase of this research, the available technology landscape was assessed. As shown in the following figure, this included typical Information Technology (IT) as well as Operational Technology (OT). Often traditional research of this nature does not address the human–machine interface.

The nature of WCID-SEMS requires humans to manage complex, interrelated systems where a failure can be catastrophic. Moreover, since major disasters such as Deepwater Horizon are often the result of a number of issues simultaneously traditional Normal Accident Theory (NAT) solutions are not adequate.

The industry has been a late adopter of methods that have been available and deemed to be necessary to effectively manage Critical Infrastructure such as with

sectors such as medicine and public health, power generation and distribution as well as oil and gas processes. For these processes, traditional process safety can fall short.

High Reliability Management along with associated Human Factors and Human Systems Integration models should be coupled to the traditional IT/OT often put forth with Internet of Things (IoT) models (Fig. 3).

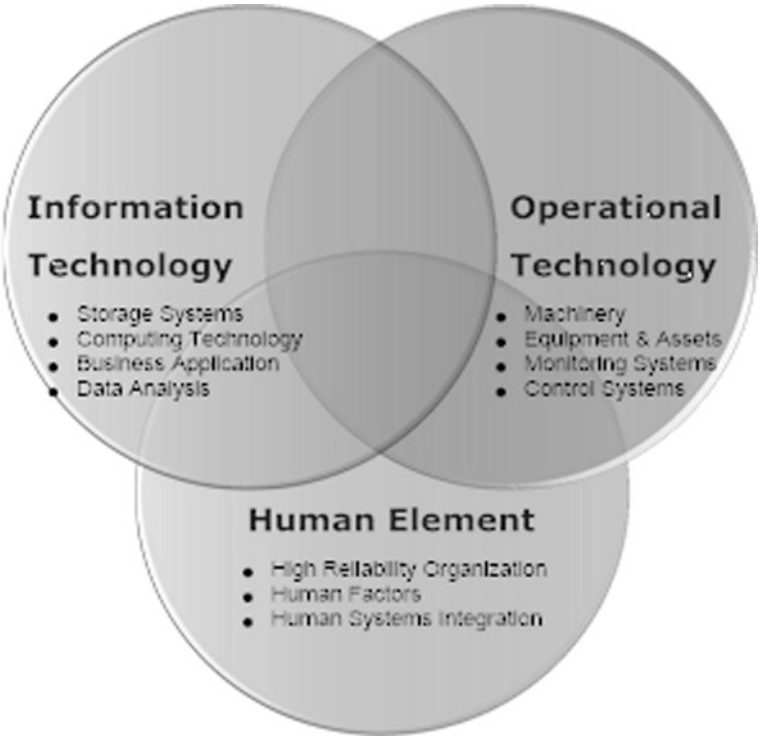

Fig. 3. Extended IT/OT convergence Venn diagram

The roles, responsibilities, and competencies necessary for WCID-SEMS were mapped to the previously identified tasks and processes. Moreover, workshops and interviews (primary research) with other critical infrastructure sectors such as nuclear power and medicine were undertaken on a global scale.

There is an extensive body of work readily available regarding critical system failures such as Deepwater Horizon, US Space Shuttles, Nuclear Power and Public Health incidents. An extensive literature review was undertaken and catalogued.

However, since these aspects of WCID-SEMS management systems are relatively new to the upstream sector, there is a dearth of data readily available. The traditional process safety organizations have not adequately addressed these issues yet.

While this research continues, the bulk of efforts specifically as it relates to WCID-SEMS is now fairly mature. That said, major incidents continue so it became clear that the traditional IT/OT model is still insufficient.

Issues around the Human Element remain immature and poorly understood by many. Moreover, this research has shown this is not limited to the oil and gas sector but is widespread in other critical infrastructure sectors as well.

2.3 Human Element

There is a well-documented body of knowledge regarding Change Management and Organizational Transformation. These generally accepted practices were incorporated into the (then) emerging Operational Excellence model. However, significant gaps were quickly revealed and included:

- Traditional organizational Governance and Risk Management models were inadequate and largely focused on financial transparency or IT delivery
- Most OE models involved limited involvement of third parties such as contractors who often have significant roles in field operations
- Process safety models were not as systemic as projects such as Deepwater Horizon required
- Risk management was often deterministic and frequently too simple
- There were few ways to test these large complicated systems without significant costs and negative impact on production
- Training and knowledge transfer were often traditional instructor-led and did not take full advantage of current e-learning methods.

These and other gaps and omissions are often explained due to the conservative nature of the sector with its boom-bust cycles that limit investment of this nature. Given the nature of today's "bet your company" and "bet your career" risk model, this business model seems short-sighted and perhaps in some cases irresponsible.

These and other gaps/shortcomings were addressed concurrently as they were uncovered. In some cases, such as the use of Serious Games and Process Simulation, solutions and technologies were already available and incorporated as appropriate.

The model depicted in the following figure addresses the full solution at its current level of maturity. The model is broadly documented by primary and secondary research along with extensive testing of the resulting products and processes by the industry (Fig. 4).

First put forth in 2014, Strong Bond Governance is enabled by current IoT and mobility tools. This allows management to tightly control critical processes using a High Reliability Management business model [8]. It directly addresses the gaps discussed previously (Fig. 5).

By definition, WCID-SEMS requires that the operator's ecosystem provide competent personnel who deliver a high-quality work product. Prior to this regulatory requirement, contractual obligations were the primary instrument to assure good timely project delivery.

Stochastic risk management tools are available and should be used in these complex projects [9]. However, the research revealed that few individuals were aware or could use these tools.

Fig. 4. Full operational excellence model

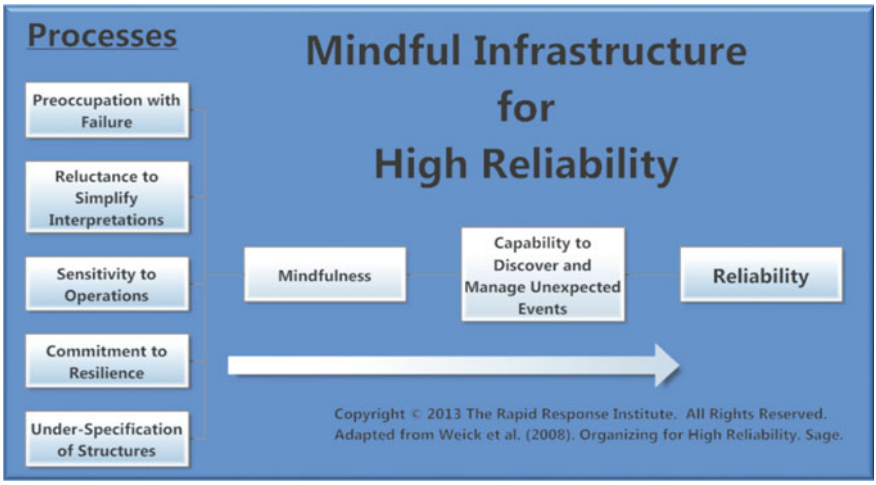

Fig. 5. High reliability model

The final model is extensive. Each component was assessed individually and integrated into the ultimate model as appropriate. This approach was driven by the research program.

As noted, the research began as an informal inquiry into the changes in human behavior that would be required post-Deepwater Horizon. It was quickly discovered that the gaps, lack of industry knowledge, and missing tools demanded that a more formal approach be taken using the generally accepted research methodologies.

3 Results

This longitudinal and multifaceted study effectively began in late 2010 albeit not formally until 2011. As noted herein, both primary and secondary research was conducted within the oil and gas sector as well as other relevant sectors. Best/good practices were identified and adapted to the specific requirements of the upstream oil and gas sector.

While the model has been extensively tested, as with all early versions more work is necessary to continue to support the hypothesis. More tools are likely necessary to transform critical infrastructure sectors such as oil and gas exploration and development (E&P).

There remain areas where additional work is to be done, including IT/OT where the technology model is new and not widely used at this point. Serious Games and Simulation, while robust still do not have many oil and gas specific applications.

WCID-SEMS is deemed to be relatively mature in terms of its documentation and regulatory requirements. However, BSEE is still fining organizations for noncompliance.

The SaaS solution developed to support WCID-SEMS is robust and currently fit for purpose. Technological changes will continue to march forward and it will need to be updated continuously.

One of the unintended consequences of this effort is a recognition that while this development was intended to US federal waters, it is applicable across all upstream operations including unconventional as well. This is potentially high value added.

4 Conclusion

The development of the initial Proof of Concept for Operational Excellence Best Practices was initially available in 2015. Prior to that date component parts were developed, tested and made available.

The full model was first published in two parts titled, Assuring Operational Excellence from Contractors and their Subcontractors in 2017. These two documents are available online [10, 11].

This is a relatively new field for the upstream sector and little academic research has been undertaken. Assessments of incidents typically posit changes; however, most are not disruptive but incremental steps in process safety management.

As part of the research program, practices from other industry segments of other the global industries managing critical infrastructures were assessed. Notable issues were identified which suggest that this or similar solutions are applicable there as well.

Additionally, the emerging IT/OT (digitalization) models can be very complex and somewhat daunting at first glance. This model for changing human behavior may have applicability there as well.

As the rate of change grows exponentially, organizations and entire industries will have to constantly reevaluate their business models and strategies. It is critical that the

ecosystem transform at the same rate as their customers. This includes the smallest subcontractors providing even the minimum of tasks.

For example, during this research, an eight-man geoscience firm (all Ph.D.) was interviewed and revealed that they had lost a long-time contract because they were deemed not compliant with BSEE requirements. A lesson learned for all in the ecosystem.

This is the new way of doing business. There is now too much at stake for societies to continue to tolerate Deepwater Horizon or Bhopal type incidents.

Normal Accident Theory is no longer relevant. High Reliability Management is now the appropriate model in an IoT world.

Acknowledgements. The author has worked closely with industry leaders over the course of the development of this methodology. Early guidance was provided by many including the American Petroleum Institute's Centre for Offshore Safety. Denise Brooks, Ph.D. provided extensive guidance in the development of Human Factors programs applicable to the oil and gas sector. The late "Dutch" Holland, a world-renowned Change Management expert was coauthor of the book titled, implementing a Culture of Safety: A Roadmap for Performance Based Compliance, and I own a great deal of gratitude for his advice and consult over the years I knew him [11].

An extensive set of interviews, surveys, and questions took place over several years and the many individuals who took their valuable time and provided key materials are greatly appreciated. The fidelity of the program would not be what it is without their help.

Finally, this work would not have been possible without the support of my family, colleagues, mentors, especially Tim Coburn, Ph.D. at the University of Tulsa and PennEnergy. Finally, the thoughts, ideas, concepts, and inputs of the many are greatly appreciated; however, ultimately any errors, omissions, or inconsistencies are my own.

References

1. http://www.centerforoffshoresafety.org/
2. https://www.niehs.nih.gov/research/supported/centers/gulfconsortium/index.cfm
3. https://www.bsee.gov/resources-and-tools/compliance/safety-and-environmental-management-systems-sems
4. https://en.wikipedia.org/wiki/Normal_Accidents
5. http://pennwellknowledge.com/products/the-state-of-sems-the-industry-transformation-to-a-culture-of-safety.html
6. https://www.bsee.gov/sites/bsee.gov/files/public-comments/public-comments-notices/rick-graff-api-standards-110811.pdf
7. http://cmmiinstitute.com/capability-maturity-model-integration
8. http://www.pennenergy.com/articles/pennenergy/2014/11/high-reliability-management-in-process-industries-sustained-by-human-factors.html
9. https://www.youtube.com/watch?v=WvU7S4ncLP4
10. http://insights.btoes.com/assuring-operational-excellence-from-contractors-and-their-subcontractors
11. http://insights.btoes.com/achieving-sustaining-operational-excellence-from-contractors-and-their-subcontractors-2
12. https://www.amazon.com/Scott-Shemwell/e/B00KNBEQS8